LCP MEMS SENSOR AND PACKAGE DESIGN FOR CPAP DEVICES

William Thorby

Bachelor of Engineering (Honours)
Mechatronics Engineering

Department of Engineering
Macquarie University

November 6, 2017

Supervisor: Mohsen Asadnia

ACKNOWLEDGMENTS

I would like to acknowledge a number of people who have helped and supported me throughout my time at university as an undergraduate student and throughout my thesis.

I would like to thank Dr. Mohsen Asadnia for giving me the opportunity to work on this project, for the guidance throughout the project and allowing me to explore the field of microsensor technology and its applications in the medical industry.

I would like to thank the past and current teachers and tutors within the engineering department for all the help and support they have given me throughout my time as an undergraduate.

Thank you to all my friends and family for the love and support they have given me throughout this journey and a special thank you to Lissandra Larobina for supporting me and motivating me to be the best I can be.

STATEMENT OF CANDIDATE

I, William Thorby, declare that this report, submitted as part of the requirement for the award of Bachelor of Engineering in the Department Engineering, Macquarie University, is entirely my own work unless otherwise referenced or acknowledged. This document has not been submitted for qualification or assessment at any academic institution.

Student's Name: William Thorby

Student's Signature: William Thorby (Electronic)

Date: 6th November 2017

ABSTRACT

The ability to accurately measure fluid flow velocity and direction are important measures for data collection in a variety of industries including environmental science, biotechnology, aerospace and emergency response organisations. As a result of extensive research and development into micro-electromechanical systems (MEMS), a low cost, miniaturized, biomimetic piezoresistive sensor inspired by the lateral line sensory system has been developed to be more durable, flexible, robust to harsh environments, more cost effective to manufacture and is more sensitive than traditional MEMS flow sensors on the market today. This thesis, aims at designing, simulating, assembling and testing different packaging designs and configurations to the LCP sensor to determine its usability and performance in air flow monitoring within the medical industry by comparing the air flow velocity detection capabilities of the system against a commercially available sensor implemented inside a Continuous Positive Airway Pressure (CPAP) device, used to treat patients with sleep apnea.

It is demonstrated in this thesis that the pressure sensor configuration and flow sensor configuration outperform the commercial sensor in low flow velocity detection, reduced signal noise and the ability to show a measurable voltage change per 1LPM change in flow rate, but lack in response time due to the mechanical nature of the sensor. A variety of future work suggestions are recommended with preliminary testing of the flow sensor in a nasal mask completed.

Contents

List of Figures

List of Tables

Chapter 1

Introduction

The ability to accurately measure fluid flow velocity and direction are important measures for data collection for a variety of uses in many industries including environmental science, biotechnology, aerospace and emergency response organisations. Capabilities such as monitoring, process control, and sensing changes in fluid flow velocity and direction are evident in systems found in aircraft and underwater vehicles, emergency response vehicles, weather monitoring equipment, plant control systems and medical devices. Traditionally, sensing equipment utilized for these sensing capabilities have had inherent limitations such as their large power consumption requirements as they utilize active sensing capabilities to detect changes in fluids; furthermore, many offer low response, low sensitivity can be large in both weight and physical size [5].

The majority of flow sensors developed can be categorized as either thermal or non-thermal sensors, based on the mechanism of flow sensing [6, 9, 11]. Thermal flow sensors work on the principle of the fluid flow interacting with a hot body; this interaction causes a change in the thermal energy on the hot body which is then measured [6]. Non-thermal flow sensors detect the mechanical change experienced when a fluid flows over its surface of the sensor; this change is converted into a measurable property of the sensor (such as a change in resistance) which is then detected and used as a means of measurement. In the world of micro-electromechanical systems (MEMS) the current limitation of flow sensors lies in its lack of repeatability and sensitivity to detect these changes. Research has found that there is an observed tradeoff between the mechanical strength and reliability of the device against its sensitivity capabilities [5].

The lateral line sensory organs found in aquatic vertebrae such as fish can detect the movement, vibration, and pressure changes in water through the use of individual sensors on their body called neuromasts which are standing cylindrical (hair-like) structures that extend into the surrounding flow of water [7, 8]. As water passes over their body these neuromasts bend due to changes in flow velocity and direction, this in turn causes an electrical impulse to fire via excitatory synapses which is then interpreted by the vertebrae. This system has been shown to allow some fish such as the blind cave fish (Astyanax

fasciatus) to swim adeptly at high speeds and avoid collision despite its atrophied eyes [8].

As a result of extensive research and development; a low cost, miniaturized, biomimetic, piezoresistive sensor inspired by the lateral line has been developed consisting of a liquid crystal polymer (LCP) membrane bonded to a silicon wafer with an integrated gold thin film piezoresistor strain gauge sputter-deposited on the membrane. From previous research, this sensor has shown to be more durable, flexible, robust to harsh environments, more cost effective to manufacture and is more sensitive than traditional MEMS flow sensors on the market today and can be used in a variety of real world applications, such as those examples previously mentioned.

The current research regarding the LCP piezoresistive MEMS sensor is to test its real-world applications and to determine its sensitivity, durability, and reliability for flow detection of flow velocity and flow direction under various environments (i.e. water, air). For this project , the proposed research involves the design, fabrication, implementation and testing of different packaging designs and sensor modifications to the the LCP MEMS sensor and housing to improve its system performance and usability for real world devices in particular this research will look at the systems ability to be comparable to a commercial flow sensor used in an continuous positive airway pressure (CPAP) device that is used to treat patients with sleep apnea. This paper will also comprehensively analyse the sensitivity, system response and other system performance properties and parameters for comparison against the performance of the commercially available flow sensor used in the CPAP device.

1.1 Project Goal

The overall project goal is to design, simulate, test and implement the most appropriate packaging and system design for the LCP MEMS sensor to be used in a medical air flow generator used to treat sleep apnea, due to particular constraints outside the scope of this thesis, the sensor housing design must allow the system to be fitted at the end of the tube used to connect the CPAP device and the mask. In order to achieve this overall goal a number of short term, long-term and non-goals have been identified.

Initial and short term goals of this project include understanding the fundamental principles of the LCP sensor such as the inspiration of its development, the fundamental principles of how it works, understanding the manufacturing process and methods used to develop the sensor which are critical to the project as suggestions to changes in the manufacturing process or modifications made may help to improve system performance in air flow specific circumstances as well as identifying current limitations of the device based on previously collected data and through finite element analysis (FEA) simulation of fluid-solid interaction.

Longer term goals for this project pertain to the final result and main objective of the thesis which include designing and creating a packaging for the LCP MEMS sensor as well as sensory configurations and possible design changes to the sensor itself ensuing that it has minimal negative impact on the flow through the CPAP system, the sensor remains highly sensitive to changes in air flow velocity, the design is simple to implement into the system as well as to identify if the packaging or sensor modifications can be used in alternate areas for air flow sensing and to ensure that the overall research positively contributes to the advancement in research of the LCP MEMS sensor.

An additional area includes non-goals and impacts on stakeholders; Throughout this project, the MEMS sensor will be tested and compared to the sensors used within the CPAP device designed by ResMed, a medical device manufacturer who create systems to treat sleep apnea. This research includes the comparison of key desirable parameters required in air flow sensing systems used in the engineering research and development department when reviewing, upgrading and implementing flow sensors in CPAP devices. Due to promising initial data collected, an open dialogue between the company and researchers of the LCP sensor have been established. This open communication has the potential to lead to further design and testing of the LCP sensor in a variety of their devices for higher quantitative data collection which can contribute to the analysis of its real-world capabilities and applications of the sensor in the medical field.

1.2 Outcomes and Impact

The main outcome of this project is to design and implement a simple to assemble housing and sensor configuration for the LCP MEMS sensor to be used in monitoring air flow velocities generated from a CPAP machine used to treat sleep apnea.

The deliverables of this project are both tangible and intangible in nature. A tangible set up which includes the packaging for the device and intangible deliverables such as simulated quantitative data, CAD drawings of optimal design and alternative designs, quantitative data from the experimentation and comparisons between LCP MEMS sensor and the commercially available sensor will be produced.

1.2.1 Deliverables

The main set of deliverables for this project include:

- Working prototype of packaging and sensor configuration for LCP MEMS sensor.
- Alternative designs for packaging - alternative designs may be usable in other scenarios.
- Data acquired from computer simulation.

- Data acquired from real work testing of the packaging and configuration.

1.3 Project Timeline

The gantt chart below shows the initial planned timeline of tasks that need to be completed with given specified dates as well as the estimated duration time required for each task to be completed. An additional gantt chart has been added to show the actual timeline used to complete the project, this will give some insight into milestone completion times and any changes that were made along the way. The weeks outlined in the timeline relate to the weeks of the university semester and do not include the mid semester break and therefore there will be an extra two weeks that will be utilised and act as a buffer in case time management becomes an issue due to unforeseen circumstances.

The first timeline shows the proposed timeline for the thesis project, however there were changes made to the approach of the project and the timeline had to be adjusted, the proposed and adjusted timelines can be seen in Figures 1.1 and 1.2.

1.4 Project Cost

The project was allocated a budget of $300. Due to the nature of the project, most of the equipment and software required for this project has previously been obtained by Macquarie University and therefore the allocated funds were pooled together to cover any additional costs of this and other related projects.

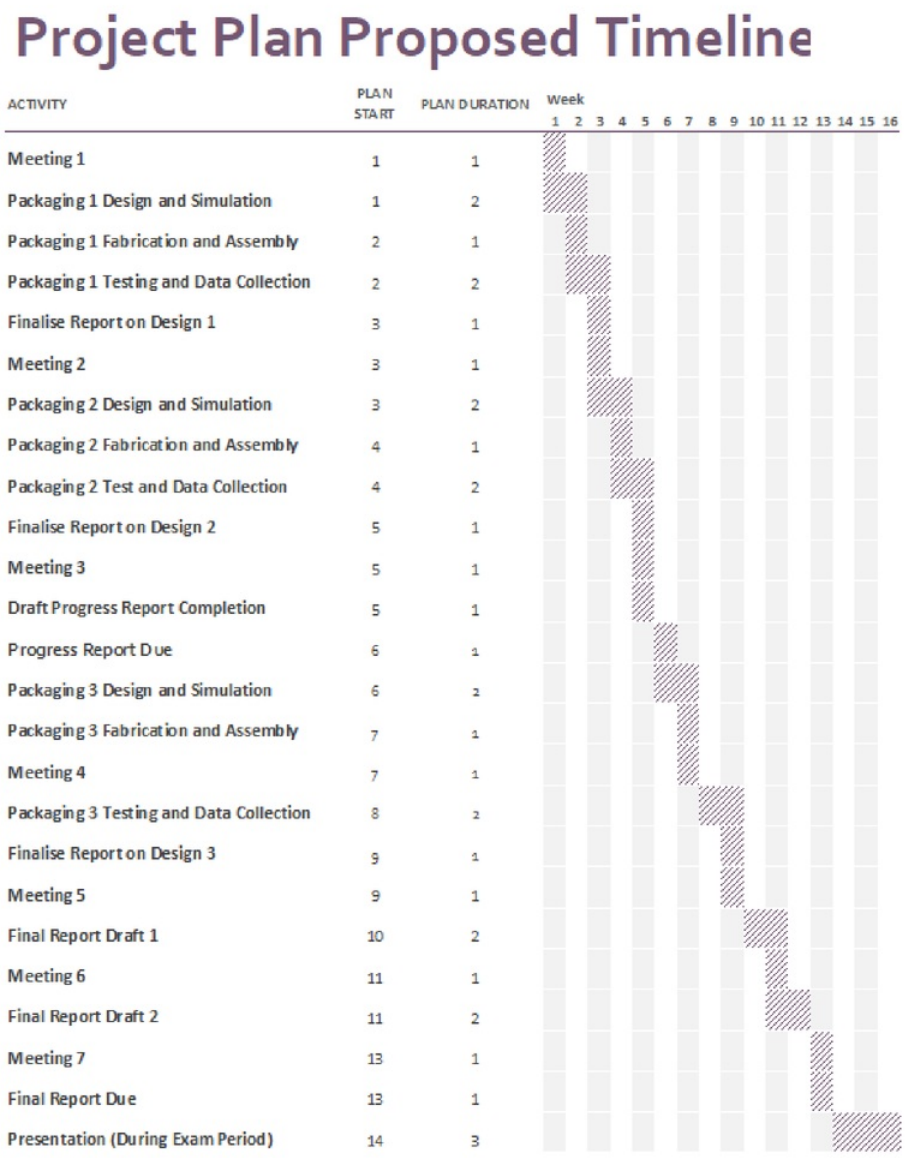

Figure 1.1: Proposed Gannt Chart

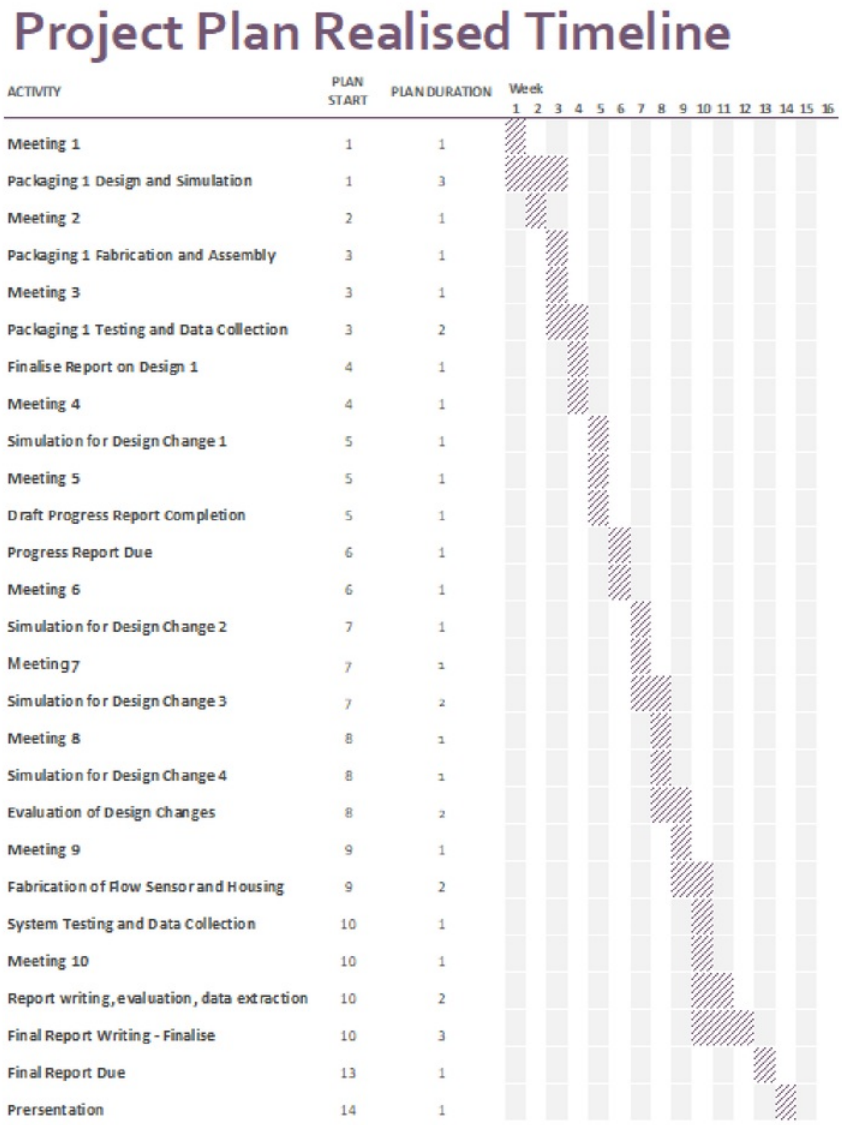

Figure 1.2: Realised Gannt Chart

Chapter 2

Background and Related Work

This chapter details the conception of the LCP MEMS sensor and expands upon this into its modelling and then manufacturing processes used to fabricate the device as well as the real-world applications tested, including some of the data collected from previous experiments. This chapter also outlines some of the principles that have been applied and considered throughout the thesis as well as the software and hardware utilised in the project.

2.1 Introduction to LCP MEMS Sensor

The ability to accurately measure fluid (air, water, etc.) flow velocity and direction are important measures in a variety of applications in fields such as environmental monitoring, process control and sensing systems used in vehicles such as aircraft and underwater vehicles. Fluid flow characteristics can also be used in emergency response monitoring such as weather forecasting and in the biomedical industry. According to Kottapalli, et al. traditionally, large mechanical flow sensors that were first used as means of fluid flow measuring included turbines, pitot tubes and metal filament anemometers which have limitations including large power consumption requirements, poor response, low sensitivity, and are large in size [5]. Today there are a number of MEMS flow sensors which utilise various methods for flow sensing. Furthermore, from a review of the literature, Kottapalli and others categorise flow sensors as either thermal or non-thermal sensors based on the mechanism in which they detect the flow [5, 6, 11].

Thermal flow sensors work on the principle of the fluid flow interacting over a hot body; this interaction causes a change in the thermal energy on the body, and it is this change of thermal energy acted on the body that is measured [6]. The disadvantage of thermal sensors in that they require 'active sensing', meaning they have high power consumption requirements and can be difficult to integrate with other systems on a microscale level. Non-thermal flow sensors detect the mechanical change experienced when a fluid flows over the surface of the sensor; this change is converted into a measurable property of the sensor,

such as a change in resistance in the case of LCP MEMS sensor. This change in measurable property is then detected and used as a means of measurement and this technique of 'passive sensing' is far more energy efficient than active sensing systems. In the world of MEMS (micro-electromechanical systems) the current limitations of flow sensors reside in their lack of repeatability and sensitivity to detect these changes. Research has found that there is an observed tradeoff between the mechanical strength and reliability of the device against its sensitivity capabilities [5].

In the field of airflow sensing, material used in MEMS sensors have predominantly focused on the use of silicon as the structural material which has limitations of a lower mechanical yield strain which results in a decrease in robustness to large fluctuations of fluid flow, resulting in a decrease in the structural integrity of the device if large changes occur. Liquid crystal polymer (LCP) in the past has been used in electronic packaging applications [13]. The sensor used in this project uses LCP as the structural material as it offers a greater sensitivity over silicon due to its lower Youngs modulus without compromising the sensors structure. The fabrication of an LCP structured sensor also has financial benefits as the costs are lower than that of a silicon based sensor [2,3,5]. An LCP sensor is also described as being more chemically robust due to its lower moisture absorption capabilities which also makes it a candidate for use in harsh environments such as in water. Kottapalli summarises that the key advantages of manufacturing a LCP structures MEMS sensor over a silicon sensor is that it has *[an] increased sensitivity over silicon counterpart, [an] increased robustness for harsh environment, low temperature processing [and] its a simple device with low fabrication costs and has low noise due to electrical leakage* [2,3,5].

2.2 Inspiration and Sensor Design:

The sensors conceptive design is based on the lateral line sensory system found in aquatic vertebrae which can detect the movement, vibration, and pressure changes in water through the use of individual sensors on their body called neuromasts [7,8]. These neuromasts are standing cylindrical (hair-like) structures made of a soft polymer-like material that extend into the surrounding flow of water. As water passes over, the neuromasts bend due to changes in flow velocity and direction, this in turn causes an electrical impulse to fire via excitatory synapses to the animals brain. The lateral line consists of two sub modulates: the velocity sensitive neuromasts which are located on the surface of the skin - which respond to flow variations; and the canal neuromasts - which are submerged in fluid filled canals and communicate with the surrounding water through pores and work by actuating the neuromasts between the pores through means of pressure differences within each pore; This function allows canal neuromasts to respond to pressure variations. The lateral line sensory system has been shown to be such a sophisticated system that some fish such as the blind cave fish (Astyanax fasciatus) are able to swim adeptly at high speeds and avoid collision despite its atrophied eyes [8].

In many of the literature papers regarding LCP based MEMS sensors, the manufacturing process of the device remains consistent; The structure of the device consists of a 25m LCP (3908) thin film membrane membrane bonded to a silicon wafer with SU-8; A deep reactive ion etching (DRIE) through-hole is used to release the LCP membrane from the silicon wafer, A gold (AU) strain gauge is then sputter deposited onto the membrane [2, 3, 5]. This strain gauge consists of radian strain gauges placed around the periphery of the membrane to allow maximum stress to be applied, the gauge is sputtered on in a zig zag pattern which consists on long radial and short tangential elements. The wires linking the radial wires are created short and wide as they are strained perpendicular to the electric current and reduce the strain gauge signal.

2.3 Working Principle

The design of the sensor consists of radian strain gauges placed at the periphery of the membrane due to maximum stress being generated at these point due to pressure applied to the membrane from laminar airflow. A serpentine pattern of a resistor consisting of long radial and short tangential elements was designed. Traditionally, MEMS flow sensors use piezoresistor formed by controlled doping, however in this LCP MEMS flow sensor, a gold deposited strain gauge is used due to their low temperature deposition and compliance with a variety of materials. Kottapalli notes that strain gauges made of metal do not compare favorably with silicon piezoresistors in terms of their gauge factor (ratio of relative change in resistance due to mechanical strain) as seen by the gauge factor of $K_{si} = 140$ compared to $K_{Au} = 2$. Despite this, the metal strain gauge on LCP offers an increased sensitivity compared to piezoresistors on a silicon membrane despite having a low gauge factor. This sensitivity is calculated by their K/E ratio where E is Youngs modulus and K is gauge factor.

$$\frac{\Delta(R)/R}{\sigma} \approx \frac{K}{E} \tag{2.1}$$

Where $E_{Si} = 185GPa$ and $E_{LCP} = 2.16GPa$ and σ representative of stress.

When comparing two strain gauge sensors of the same size and thickness, the sensitivity of the LCP membrane is 19% more sensitive compared to one with a silicon membrane; furthermore, LCP membranes can be as thick as 25m and offer comparable sensitivities to silicon membranes which range from $2 - 10\mu m$ in thickness. An LCP membrane therefore has an adherent advantage of a higher fracture strength due to its ability to be over twice as thick as their silicon counterpart.

The deflection (w) at any point on the diaphragm under uniform pressure is governed by the following differential equations:

$$\nabla^4 w = \frac{P}{D} + \frac{h}{Dr}\frac{\partial\phi}{\partial r}\frac{\partial^2 w}{\partial r^2} \tag{2.2}$$

$$\nabla^4 \phi = -\frac{E}{R}\frac{\partial w}{\partial r}\frac{\partial^2 w}{\partial r^2} \tag{2.3}$$

Where ϕ is the Airy stress function and the biharmonic ∇^4 is given by

$$\nabla^4 = \left(\frac{\partial^2}{\partial r^2} + \frac{1}{r}\frac{\partial}{\partial r}\right)^2 \tag{2.4}$$

Since most micromachined diaphragms are considered to have clamped boundary conditions, that is:

$$w\left(r = edge\right) = 0, \frac{\partial w}{\partial r}|_{r=edge} = 0 \tag{2.5}$$

The Laplacian for a circular place from equations 2.2 and 2.4 give:

$$\nabla^2 = \frac{\partial^2}{\partial r^2}\frac{1}{r^2}\frac{\partial^2}{\partial \phi^2} + \frac{1}{r}\frac{\partial}{\partial r} \tag{2.6}$$

This gives us the solution for small deflection of a clamped circular plate under uniform pressure (P) to be:

$$w\left(r\right) = \frac{Pa^4}{64D}\left[1 - \left(\frac{r}{a}\right)^2\right]^2 \tag{2.7}$$

Where r is the position along the radial direction and a is the radius of the diaphragm. D is the flexural rigidity and is given as a measure of stiffness from:

$$D = \frac{Eh^3}{12\left(1 - v^2\right)} \tag{2.8}$$

Where E is the Youngs modulus, h is the plate thickness and v is Poissons ratio. Maximum displacement of the membrane occurs at the centre of the membrane w_0 given by:

$$w_0 = \frac{P_{air}a^4}{64D} \tag{2.9}$$

Furthermore, radian and tangential strains on the membrane are given by:

$$\epsilon_r = 2\left(\frac{w_0}{t}\right)\left(\frac{t}{2}\right)^2\left[3\left(\frac{r}{a}\right)^2 - 1\right] \tag{2.10}$$

$$\epsilon_t = 2\left(\frac{w_0}{t}\right)\left(\frac{t}{2}\right)^2\left[\left(\frac{r}{a}\right)^2 - 1\right] \tag{2.11}$$

Where ϵ_r and ϵ_t are the radial and tangential directions.

Maximum strain ϵ_{rmax} can then be calculated as:

$$\epsilon_{rmax} = \left(\frac{3}{4}\right)\left(\frac{P_{air}}{E}\right)\left(\frac{a}{t}\right)^2\left(1-v^2\right) \tag{2.12}$$

The relative change in resistance for a resistor deformed by being bonded to the top of a plate can be represented as:

$$\frac{\Delta R}{R} \approx \frac{1}{1-v}\epsilon_r + \frac{2v-1}{1-v}\epsilon_t \tag{2.13}$$

Substituting values E = $2.1GPa$ (LCP), a = $100\mu m$, v = 0.3 and t = $25\mu m$ we can simplify the equation above to:

$$\frac{\Delta R}{R} = 7.42857 \times 10^{-7} P_{air} \tag{2.14}$$

Where P_{air} can be calculated using Bernoullis equation:

$$P_{air} = \frac{1}{2}\rho_{air} V_{air}^2 \tag{2.15}$$

Where ρ_{air} and V_{air} are the density and velocity of air; $\rho_{air} = 1.25kgm^{-3}$.

Further calculations show that the resistance change in the LCP MEMS sensor is:

$$\frac{\Delta R}{R} = 4.643 \times 10^{-7} V_{air}^2 \tag{2.16}$$

2.4 Fabrication

The fabrication process begins by stripping the $18\mu m$ of copper cladding that is attached to both sides of the LCP (3908) film, leaving fresh LCP exposed on both sides. The LCP is then bonded to a silicon wafer using an SU-8 adhesion layer this SU-8 layer is used as an intermediate layer for bonding to avoid the bucking issues that occur due to the mismatch in thermal expansion properties; 18ppm $^\circ C^{-1}$ for LCP and 3.2ppm $^\circ C^{-1}$ for Silicon.

Prior to SU-8 spin coating onto the silicon wafer, the wafer is cleaned in a piranha solution to avoid contamination from foreign particles, the wafer was then dehydrated at 130 °C for 20min to improve the SU-8 adhesion. SU-8 2005 is then spin coated at 2500rpm for 30 seconds onto the silicon wafer to form a $5\mu m$ thick layer; the LCP thin film is then cut to fit the silicon wafer and then adhered to each other through pressure applied through a uniform load to ensure no air is trapped in the bonding process; this wafer pair is then heat treated to enhance the bonds strength as well as a uniform pressure being applies at 5KPa by placing uniform circular wafers on the bonded wafer pair.

The heat treatment process occurs in steps of increasing temperature starting at 45°C for 20 mins, 80 °C for 10 mins and finally 120 °C for 20 mins; during this process, the SU-8 layer hardens to enhance the bond strength. DRIE holes are then etched into the other side of the silicon wafer to release the LCP diaphragm, in order to protect the LCP during this process a silicon wafer with $7\mu m$ resist was bonded onto the other side of the LCP; this silicon wafer can be removed by dipping in acetone after etching DRIE holes - during this step, the LCP silicon bonding remains intact due to the SU-8 layer that was hardened during heat treatment and is not impacted by the acetone.

Following this, the thin film resistor is to be formed on the diaphragm - Gold (AU) was chosen to be used as the strain gauge material due to its conformal deposition properties in comparison to other materials (such as Ni, NiCr and Al) and its higher gauge factor. A $5\mu m$ thick resist is then spin coated on the LCP for lift off. A mask containing the serpentine resistor features is aligned with the DRIE holes using back alignment. The resist is then exposed and patterned - a 100nm AU layer with a 10nm CR layer (Cr used to enhance the AU adhesion) was sputter deposited on the patterned resist. Following this step the list off process was performed by etching the resist layer underneath the Au layer. The wafer was then dipped in an acetone solution and agitated ultrasonically for 20 seconds [2, 3, 5]. It is important to note that a key driver in the device fabrication was to create a simple, low cost and repeatable fabrication process that employs low temperatures. Figures 2.1 - 2.4 below show a visual systematic process of the fabrication of the device with Figures 2.5 and 2.6 showing the LCP sensor under microsope.

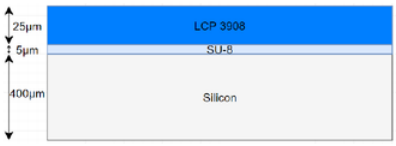

Figure 2.1: Step 1 Wafer Bonding

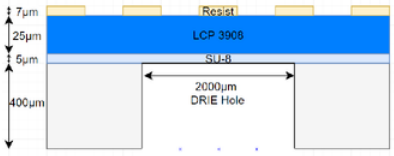

Figure 2.2: Step 2 DRIE Etching

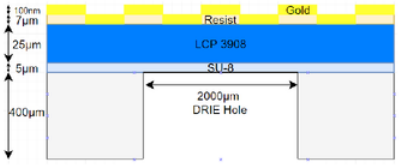

Figure 2.3: Step 3 Gold Sputter

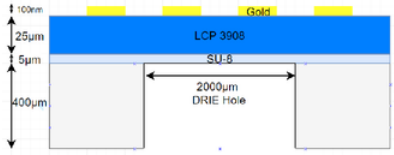

Figure 2.4: Step 4 Gold Liftoff

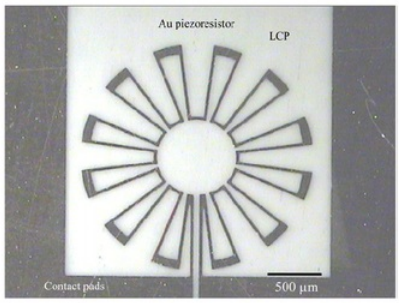

Figure 2.5: Optical Image of Front of LCP Sensor [5]

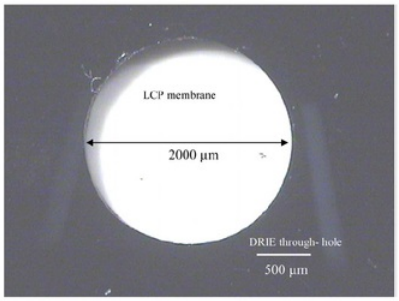

Figure 2.6: Optical Image of back of LCP Sensor [5]

2.5 Real World Application and Testing

2.5.1 Air Flow Testing

Kottapalli states in one of his papers that the sensor is characterized and tested as an airflow sensor with the ability to detect air flows of human breathing $0.1ms^{-1}$ to high air flows of $10ms^{-1}$ showing that it can be used in a variety of fields such as the medical field where human breathing rates require monitoring to weather monitoring for emergency response [5]. Kottapalli also notes that the front side of the membrane can be coated with a thin polymer such as Parylene or PDMS to protect the device when placed in harsh environments. In order to collect the data from the device in all papers where testing has taken place, a National Instruments data acquisition (NI-DAQ) device has been used and the signal has been acquired through LABVIEW (at varying sample rates). The system also comprises of an external Wheatstone bridge circuit with a bias voltage of 5V to convert the small change in resistance of the LCP sensor into a measurable voltage change and a gain of some amount (varies from paper to paper). In Kottapalli's testing, the sensor demonstrated nano-volt levels of noise whereas the order of change in voltage due to airflow was in the milli-volts. Kottapalli first demonstrated the LCP sensors capabilities for air flow sensing through the use of a wind tunnel for velocities ranging from 1 to $10ms^{-1}$ with the sensor mounted perpendicular to the direction of airflow; the results showed that the experimental data was very similar to the results that were theoretically predicted as seen in Figure 2.7 [5].

The sensor demonstrated a 3.6% average error and showed sensitivity of $3.695mV(ms^{-1})^{-1}$ to air flow velocity. Kottapalli also notes the limitation of the sensor being as pressures reach $1.5KPa$, the diaphragms displacement reaches its maximum displacement.

The Sensor was also tested for directional air flow capabilities by placing the sensor on rotatable fixture in the wind tunnel, which was then rotated from $0\,^\circ$ to $90\,^\circ$ with respect

to the air flow direction (0° is parallel to flow direction). The results showed a change in resistance was detectable at all angles up to the maximum angle of 90° to the air flow direction - the membrane being perpendicular to the flow direction.

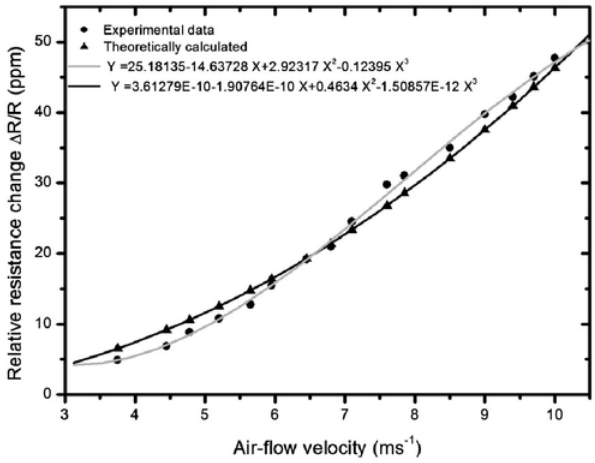

Figure 2.7: Kottapalli Airflow Test [5]

Further testing also demonstrated the sensors use in the clinical field to determine the flow velocities at various points in the nasal cavity, the results showed it could detect the exhaling action of the nostril.

2.5.2 Water Flow Sensing

When it comes to water flow sensing capabilities, there are a number of alternatives such as sonar and optical sensors, however they have their inherent disadvantages, predominantly due to the fact they require active sensing which isnt an energy efficient system as well as the fact these systems can be quite bulky, other disadvantages include: the fact sonar has poor resolution of detection and causes deaths in some aquatic fauna due to noise of sonar signal and optical cannot work in dirty/ cloudy waters [2, 4].Therefore, a need to develop a low powered, low cost sensor that is robust and able to withstand harsh environments is required, and based on the developments of LCP MEMS sensors, it fulfills the majority of these requirements.

Water fluid flow detection was tested by Kottapalli et al in multiple instances, the first experiments were means to test the sensors ability to detect near field flow patterns generated as an object moved through the water passed the sensor via means of detecting the pressure changes [5]. In one experiment, the sensor was mounted to a wall in a container filled with water, a 10mm cylinder was used to pass the device at a distance

of 4 inches and moved passed the sensor in a straight line, the signal was given a gain of 500 and data was acquired. In Figure 2.8, the drop in the graph indicates a drop in voltage that occurred each time the diaphragm was displaced by the hydrostatic pressure generated by the passing object.

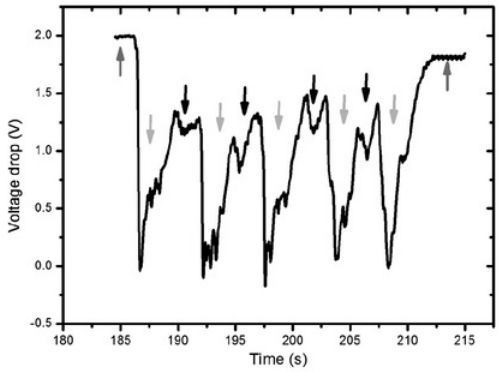

Figure 2.8: Underwater Detection Results [5]

In Kottapallis et al second paper, an array of 10 sensors with a total footprint of $60mm \times 24mm \times 0.4mm$ $(L \times W \times H)$ was created and tested which demonstrated a pressure sensitivity of $14.3\mu VPa^{-1}$, a resolution of $25mms^{-1}$ with a high accuracy with only a 2.5% error [2]. Similarly to the first experiment, an object was moved passed the array of sensors to collect data. The array of sensors also allowed the researchers to determine the velocity of the object moving passed as seen in Figure 2.10.

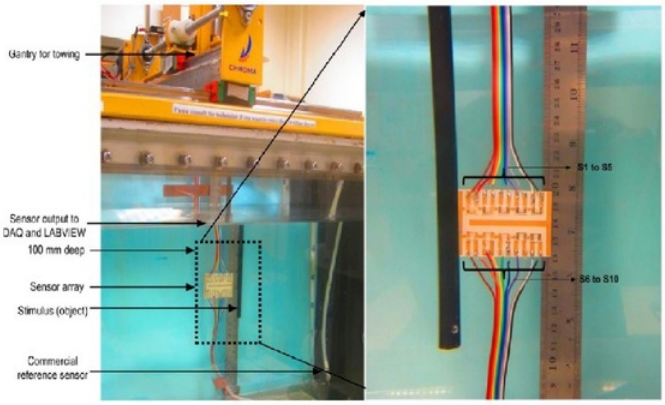

Figure 2.9: Underwater Array Setup [5]

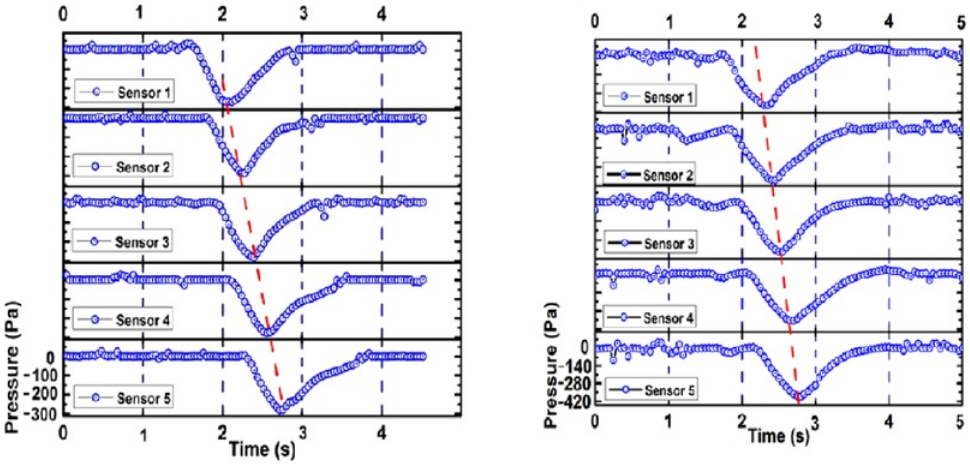

Figure 2.10: Underwater Array Results [5]

In another experiment looking at real world implementations, the LCP sensor showed its ability monitor the fluid flow in an infusion pump, the sensor was packaged in such a way that it could detect the current flow to ensure correct dosage as well as to detect if there is a blockage within the intravenous (IV) line [4, 10]. The setup was essentially identical to all previous set ups (Wheatstone bridge with some gain on the signal). The sensor showed that it can detect flows through the IV set up from as a low as 2mL/Hr which is 20 times below the suggested keep vein open (KVO) rate of 25-50ml/Hr showing that it has great promise in this area of clinical work.

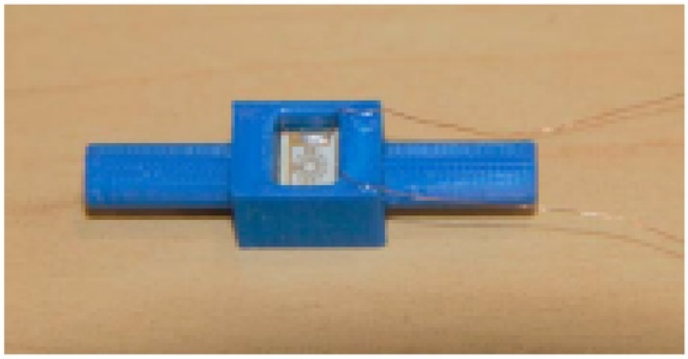

Figure 2.11: Infusion Housing with LCP MEMS [4]

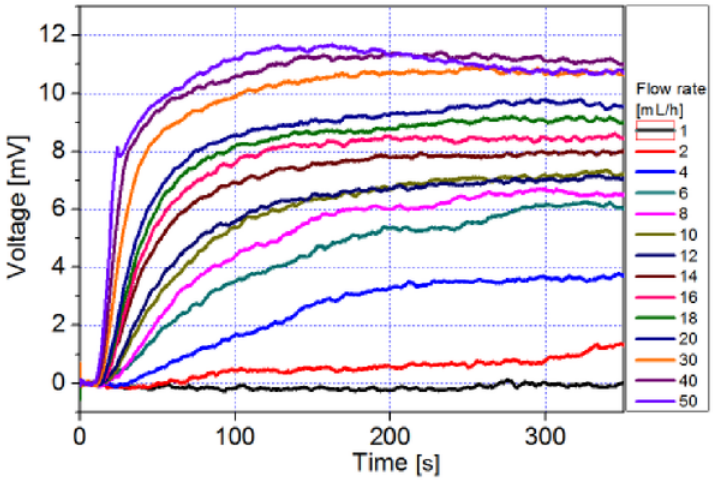

Figure 2.12: Infusion Flow Results [4]

2.6 Fluid Dynamics

Throughout this thesis project, an understanding of fluid dynamics is required in particular the aerodynamics and the interactions of air in a tube with the LCP sensor and housing respectively. Some of the laws and principles that will be studied throughout this project include the following.

2.6.1 Bernoullis Principle

Bernoullis principle states that an increase in the speeds of a fluid occurs simultaneously with a decrease in pressure or a decrease in the fluids potential energy; this principle has resulted in a number of forms of Bernoullis equations which relate to various types of fluid flow such as incompressible and compressible fluids at various speeds. Bernoullis principle can be derived from Newtons second law of motion in that a rate of change in momentum of a body is proportional to the force applied and this change takes place in the direction of the force applied as well as the principle of conservation of energy, in that the sum of kinetic energy, potential energy and internal energy must remain constant. Therefore, an increase in the fluids speed implies and increase in both dynamic pressure and kinetic energy and a decrease in static pressure, potential energy, and internal energy [1].

2.6.2 Hagen-Poiseuille

Hagen-Poiseuille law or Poiseuille equation is a law that gives the pressure drop in an incompressible and Newtonian fluid in laminar flow through a long cylindrical pipe of

constant cross section which can be derived from Naiver-Stokes momentum equations. The equation assumes the fluid is incompressible and laminar in flow through a pipe of constant cross section that is substantially longer than the diameter of the pipe and there is no acceleration of fluid within the pipe itself. The change in pressure can be represented in the following equation:

$$\Delta P = \frac{8\mu LQ}{\pi R^4} \tag{2.17}$$

Where ΔP is the pressure difference between the two ends, L is the length, μ is the dynamic viscosity, Q is the volumetric flow rate and R is the radius of the pipe

2.6.3 Viscosity

Viscosity by definition is the measure of resistance of a fluid due to shear stress or tensile stress. Viscosity is a property of which the fluid wishes to oppose the relative motion between the two interacting surfaces of fluid which are moving at differing velocities. In the case of through a tube in the project, the particles which compose the air flow move more quickly near the tubes axis and slower near the walls due to boundary layer formation thus creating a parabolic fluid velocity profile, therefore a pressure difference between two ends of a pipe is required to overcome friction produced in laminar flow.

2.7 Software Packages

Throughout the thesis project a number of software packages are required to complete the necessary steps of drawing designs, computing finite element analysis (FEA) simulations as well as collecting and recording real world data, the following subsections give a brief outline of the type of software and its purpose in this thesis.

2.7.1 SOLIDWORKS

SolidWorks (SOLIDWORKS) is a solid modelling, computer automated design (CAD) and computer-aided engineering (CAE) software tool used by engineers to create and design 2D and 3D models in a fast and cost effective manner. Solidworks can be used to design and create single parts or whole assemblies ranging from simple constructions to complex, multi-part assemblies. Solidworks also comes with the ability to simulate designs made to help the user understand their constructions interactions in a given environment.

For this project Solidworks has been used to model the LCP MEMS sensor - breaking it down into its three basic layers (excluding the SU-8 bonding material) of the Gold piezoresistor, LCP membrane and the silicon wafer with DRIE through hole; it has also been used to desgin and draw the housing alternatives.

2.7.2 COMSOL Multiphysics

COMSOL Multiphysics is a cross platform simulation software and finite element analysis solver. Within the platform there are many modules that allow the user to use such as electrical, mechanical, fluid, chemical environments - each with its own sub-modules accordingly; COMSOL Multiphysics also includes multipurpose modules which allow optimisation with other COMSOL products, the ability to integrate a material library to be applies to designs and a particle tracing module as well as an interfacing module which allows the user to import designs from different platforms or to sync in real time with changes made to the design in another software package.

In this project, COMSOL Multiphysics finite element analysis simulation software has been used to simulate laminar fluid flow around the packaging design to identify areas of fluid flow inefficiencies such as unwanted pressure or air flow velocity drops. It is also being used to observe the fluid-solid interactions with fluid flow and the packaging as well as the LCP sensor itself.

Due to difficulties in applying fluid-structure interactions with the 3D models, a 2D model was created and simulated in COMSOL, due to this change from 3 dimensions into 2 dimensions the results vary due to the simulations inability to calculate the 3rd dimension of the model.

2.7.3 ANSYS

Similar to COMSOL Multiphysics, ANSYS is a computer aided engineering software that completes analysis on a range of areas such as finite element analysis, structural, fluid dynamics and heat transfer.

In this project ANSYS is used as a second method of data collection for laminar fluid flow simulation and to collect data on fluid flow velocities, pressure differences and fluid-solid interactions.

Due to the desire to have fluid-structure interaction simulation working correctly ANSYS was only used to compare fluid flow due to changes in packaging as means to double check the fluid flow against COMSOL, in the design changes chapter of this thesis, due to similarities in results and time constraints, COMSOL was predominantly used.

2.7.4 NI Signal Express

Signal Express is a software package created by national instruments that allows the user to quickly acquire, analyse and present data from a number of data acquisition devices without requiring any programming.

For this work, Signal Express is used to collect, store and graph the data acquired from the data acquisition (DAQ) device used in the experimental section of the project.

2.7.5 Matlab

Matlab or matrix laboratory is a mathematical computing software used globally for a number of uses. In this project Matlab is used to translate excel data files created from Signal Express and to plot this data into meaningful graphs which were used to make meaningful analysis'.

2.7.6 Origin

Origin is a software used for interactive scientific graphing and data analysis. Origin has been used to extract and plot some of the data used in this thesis work.

2.8 Hardware

2.8.1 CPAP Machine/ Air Flow Generator

Throughout the testing stages of this thesis, a continuous positive airway pressure (CPAP) machine was used to test the system response to air flow velocities as well as using the commercially available sensor built into the device for a direct comparison of key performance measures.

During the testing stages the flow rates were varied from 8LPM to 200LPM from the user interface on the device itself and results were captured from both the LCP sensor and the sensor built in.

2.8.2 National Instruments Data Acquisition (NI-DAQ)

Voltage data outputted from both the ResMed Air10 flow sensor and the LCP sensor were collected through a data acquisition system from National Instruments. Data Acquisition (DAQ) allows users to measure and collect electrical or physical phenomenon such as voltage, current, temperature, sound, etc.

For this thesis the cDAQ 9174 was used as means for collecting the voltage reading which was passed through National Instruments Signal Express running on a laptop.

2.8.3 Noise Filter and Preamplifier

A Standford Research System Model SR560 Low Noise Preamplifier was used during the testing stages of this thesis to remove signal noise and amplify the signal.

Chapter 3

LCP MEMS Pressure Sensor

3.1 Packaging Design

The first design of the housing for the LCP sensor was designed based on a few basic considerations:

- Allow the LCP sensor to be subjected to maximum membrane displacement - the sensor is required to be positioned perpendicular to the laminar flow of air through the tube to maximise uniform membrane displacement across the entirety of the membrane.
- The ability to securely hold the sensor inside the tube without it falling out.
- Ease of assembly/manufacturing.

In order to meet these requirements, the housing required a block-like object to hold the sensor in place perpendicular to the laminar flow and a ring structure to allow the design to be held inside the tube to remain fixed in place, therefore the diameter of the ring portion of the housing was required to have a diameter of 20mm, equaling the diameter of the tube. It was noted that since the tube used was made of a material that contains some elastic properties, there was not going to be any issues in placing the ring inside the tube as it would stretch to fit the housing.

To achieve maximum displacement on the membrane of LCP sensor, the sensor is required to face perpendicular to the direction of the fluid flow, this set up will allow the maximum displacement to occur at each varying flow rate as well as allowing a more accurate and sensitive resistance to occur at each flow rate due to uniform force applied across the entirety of the membrane, allowing the utilization of all strain gauges on the sensors membrane. The placement of the sensor is required to be as close to the centre of the pipe as possible due to viscosity on laminar flow and friction caused with the interaction of the inner walls and laminar flow, creating a boundary layer extending from the walls.

Due to the boundary layer forming at the walls due to the no slip condition, a beam like structure and block with a small extrusion cut for the LCP sensor to be placed into were created. Furthermore, taking into consideration the easy of assembly, the beam and block was position is slightly lower than the exact centre of the tube, although not at the exact centre of the tube, this position was still above the boundary layer created.

In the figures below a design of the LCP sensor was drawn in Solidworks as well as the first design iteration these models are also shown together to give a visual representation of the design.

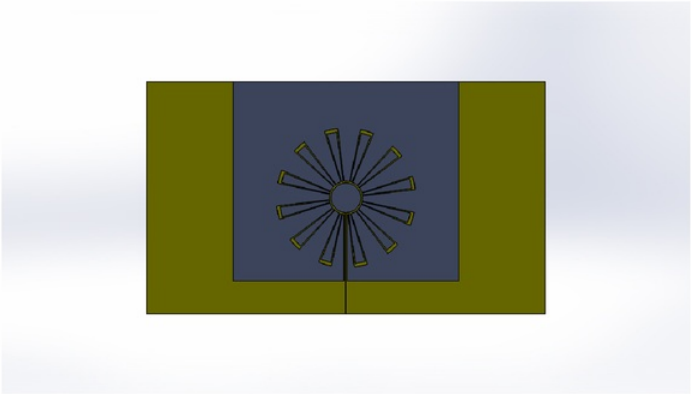

Figure 3.1: LCP MEMS Sensor Front

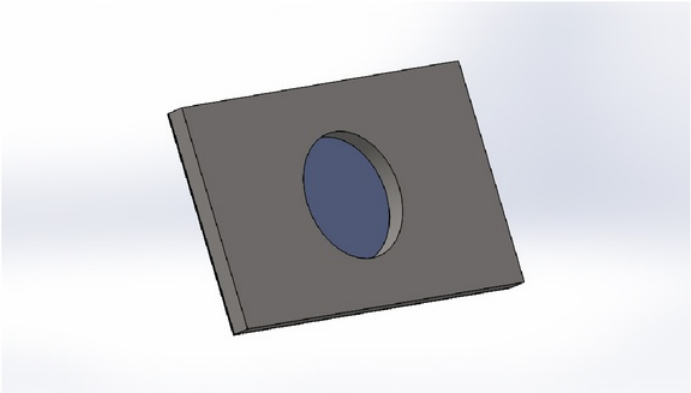

Figure 3.2: LCP MEMS Sensor Back

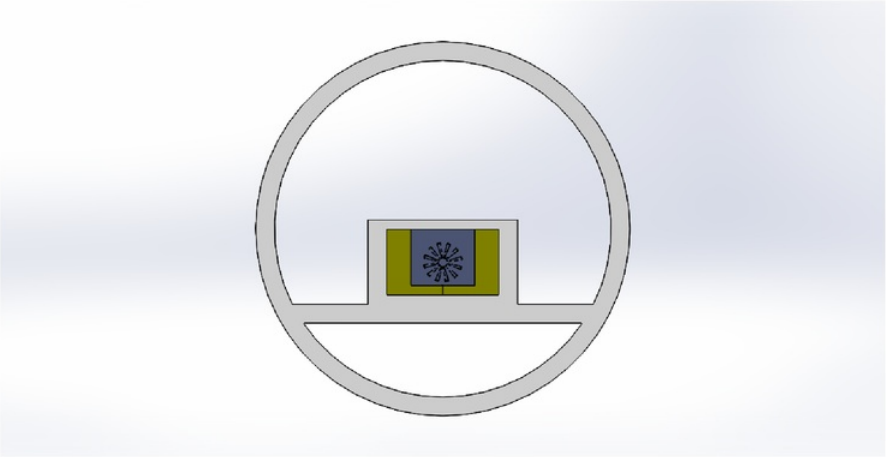

Figure 3.3: Front view of Design 1

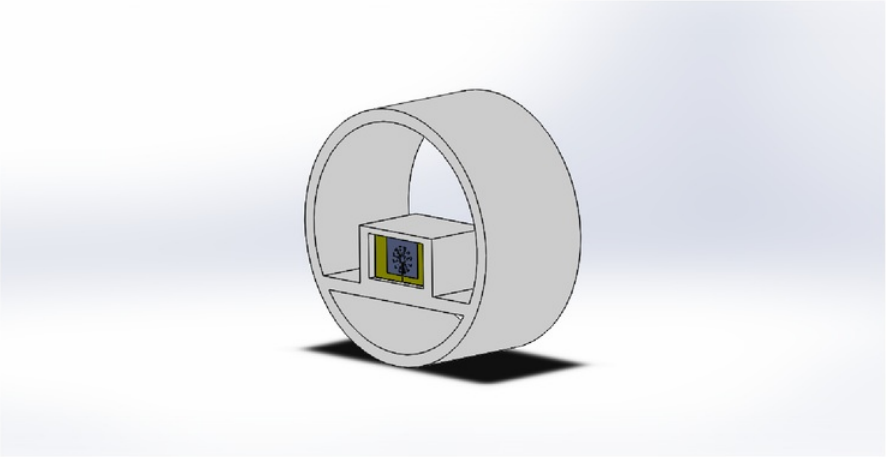

Figure 3.4: Isometric view of Design 1

3.1.1 Simulation

For the simulation testing of this design the objective was to analyse the fluid-flows interaction with the housing by looking at the flows movement, changes in pressure as the laminar fluid flow passed through the housing and the air velocity changes. The simulations were done on both ANSYS and COMSOL Multiphysics, however due to limitations, fluid-solid interactions in the 3D space was unsuccessful and therefore simulations had to be completed in 2D space, therefore design changes were made based on the results of the 2D simulation rather than 3D simulations.

As the air flow generator used has a varying number of air flow rates - measured in litres per minute (LPM), the simulation was run assuming an air flow of 100LPM, which is the median flow rate in actual testing of the device. In order to calculate the velocity of airflow entering the system, 100LPM was converted into an air velocity of $5.31ms^{-1}$ based on the following calculation:

$$Q = Av \tag{3.1}$$

Where Q is the volumetric flow rate, A is the cross-sectional area and v is the average flow velocity

$$v = \frac{FlowRate(LPM) * 0.001}{60\pi \left(\frac{d}{2}^2\right)} \tag{3.2}$$

Where v is the velocity, Flow Rate in Litres Per minute (LPM $\times 0.001$ is used to convert to m^3/min then dividing by 60 to attain m^3/s, d is the diameter of the pipe (m).

$$v = \frac{100 * 0.001}{60\pi \left(\frac{0.02}{2}^2\right)} \tag{3.3}$$

$$v = 5.31ms^{-1} \tag{3.4}$$

The pressure set at the exit point of the tube for flow simulation was set to 0Pa

Pressure

The pressure data collected from both ANSYS and COMSOL simulations are shown in the figures below:

ANSYS Simulation

Although the main areas to run simulation are regarding air flow velocity, it is also important to study the effects of pressure as they can give an indication of where the most force is being applied to the housing due to the interrelation between Force, Pressure and Area; Furthermore, pressure drops in simulation such as negative pressure can cause backflow, creating turbulence in the system.

The simulation results from both ANSYS and COMSOL are shown in the figures below:

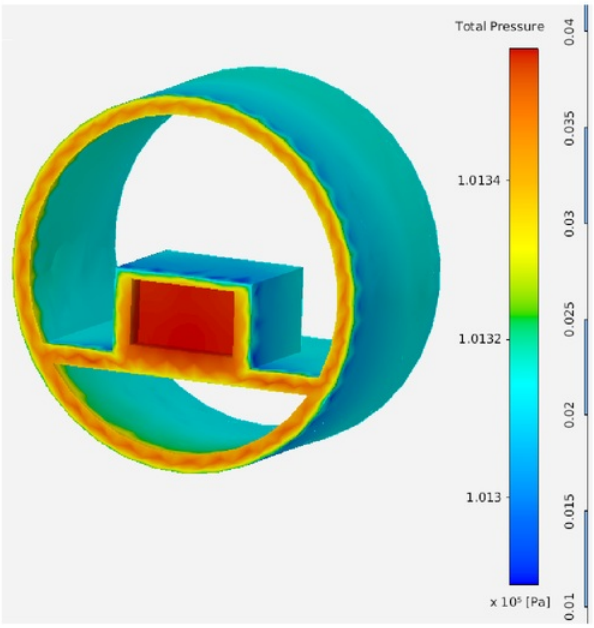

Figure 3.5: Ansys Pressure on Package - Isometric View

As we can see from Figure 3.5 and Figure 3.6 , the maximum total pressure applied to the surface of the packaging structure occurs in the forward-facing hole at the centre of the blocks face, situating in the centre of the pipe, this is due to the airs inability to continue it flow through the exit, whereby increasing the static pressure component of the total pressure; as total pressure is a combination of static pressure and dynamic pressure.

$$P_T = P_S + P_V \tag{3.5}$$

Where P_T is the Total Pressure, P_S is the Static Pressure and P_V is the Dynamic (Velocity) Pressure

From Figures 3.5 and 3.6 we can see that the total pressure where the LCP sensor is located is approximately 1.0136×10^5 Pa. we can also see from Figure 3.7 that there is a notable pressure drop around the walls of the inside of the tube, the cross beam and the block that holds the sensor in the tube; this pressure drop around the walls of these sections is due to head loss caused by the friction between the laminar flow of air and internal walls.

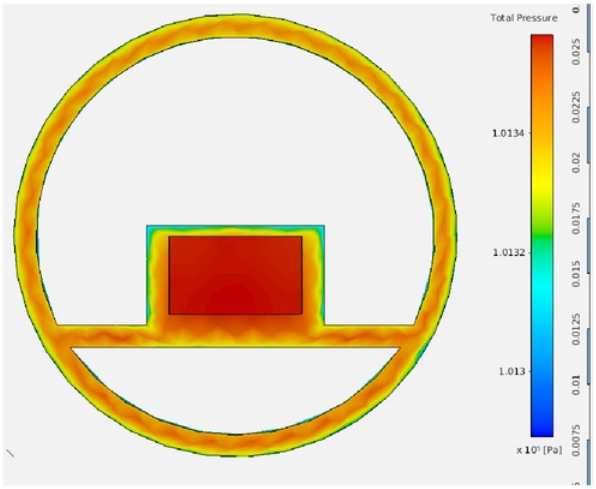

Figure 3.6: Ansys Pressure on Packaging - Front View

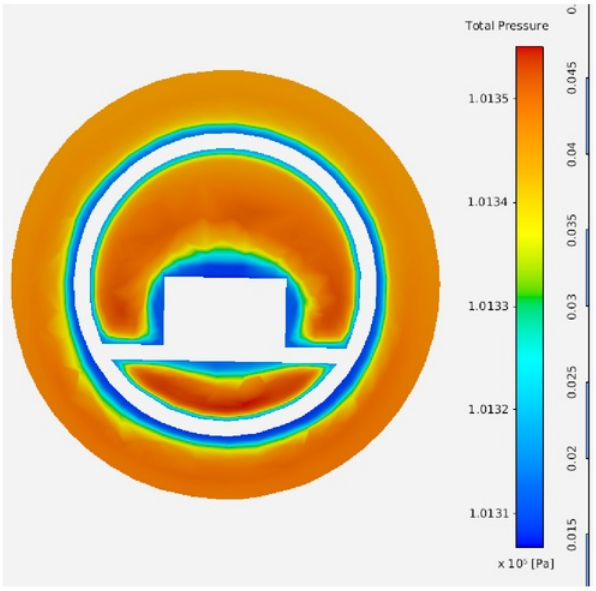

Figure 3.7: Ansys Pressure Through Package

COMSOL Multiphysics Simulation

When looking at the simulation results from COMSOL Multiphysics, we can see a larger pressure value in the forward-facing extrusion where the LCP sensor is located, the value is similar to that in the ANSYS simulation above. If we look at the X-Y plot in figure 3.9 we can see there is a maximum pressure at the wall there the LCP sensor is located, approximately 1.022×10^5Pa.

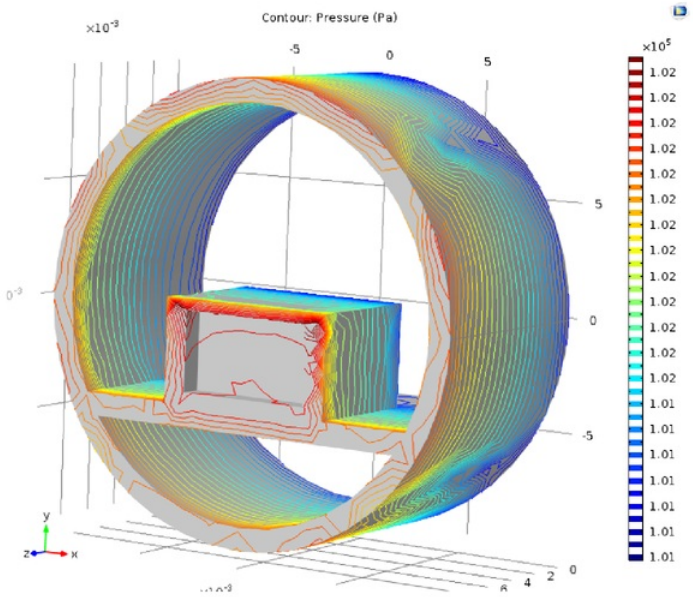

Figure 3.8: Comsol Pressure on Packaging - Isometric View

When comparing the two simulation software packages, there is a discrepancy of 0.82% in the calculation for pressure at the location of the LCP and therefore either software package can be used for further study, due to its ease of use, COMSOL will be the primarily used FEA software.

As previously noted, due to an inability to successfully run fluid- solid interactions in 3 dimensions, a 2D model was created to compare design changes, furthermore it is important to note that values for pressure and flow velocity will vary between the 2D and 3D simulations as shown between pressure differences between the 3D simulation in Figure 3.8 and the 2D simulation in figure 3.10 below.

In Figure 3.10, we can see the changes in pressure due to changes in air flow cross sectional area, validating Bernoullis principle. The maximum point located on the figure shows the location of most displacement in this model this occurs at the centre of the membrane.

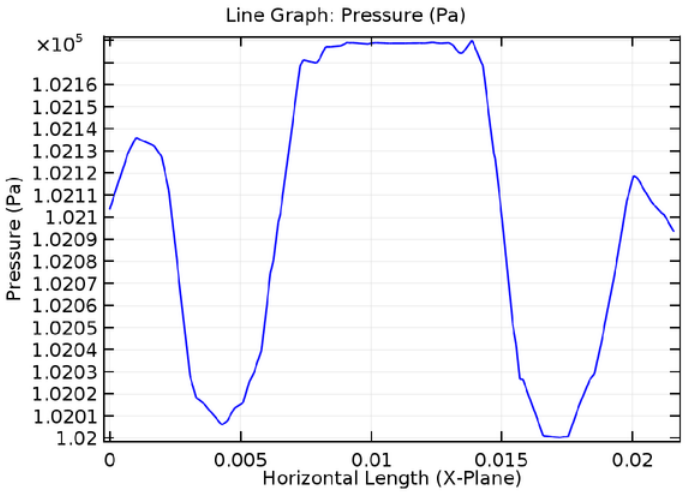

Figure 3.9: Pressure Graph at LCP

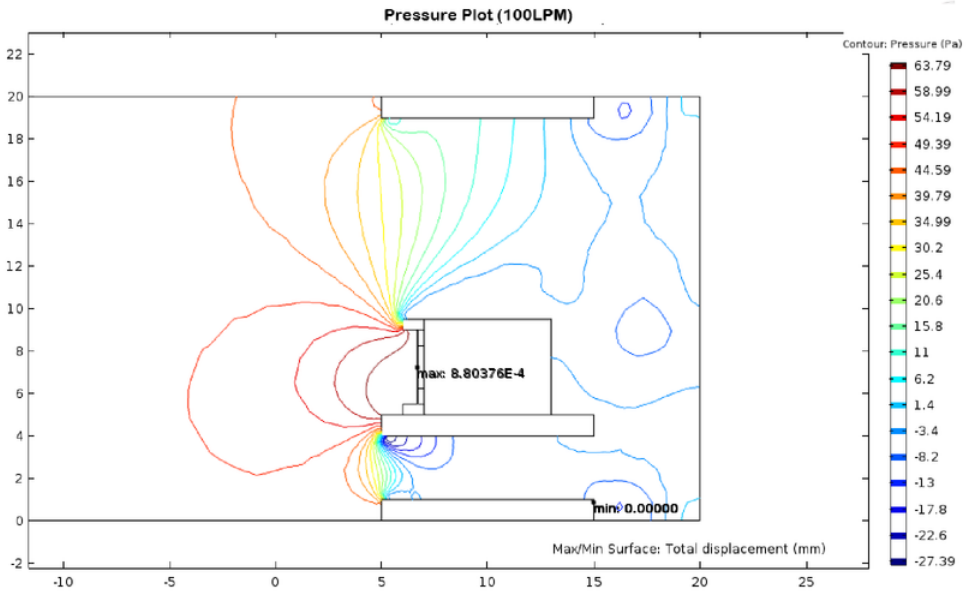

Figure 3.10: 2D Simulation Pressure Plot

Flow Velocity

One of the main areas of investigation within this thesis is to investigate the sensors response to various air flow velocities from an air flow generator used in the medical field, therefore the majority of simulations and design considerations will be optimising a configuration that will allow maximum air flow velocity to interact with the LCP membrane for maximum displacement.

From the ANSYS simulation results in Figure 3.11 and 3.12 we can clearly see the boundary layer forming between the fluid flow and walls of the housing due to the no-slip condition. Although there appears to be next to no flow velocity at the extrusion where the sensor is located, the force being applied to the sensor is however evident from the pressure plots previously detailed.

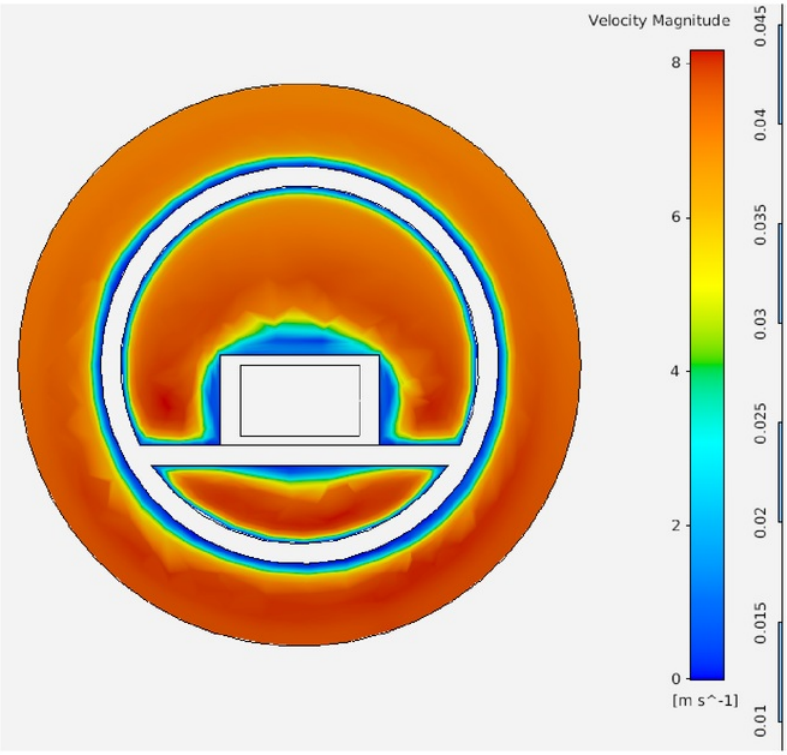

Figure 3.11: Velocity Profile Through Housing - Front View

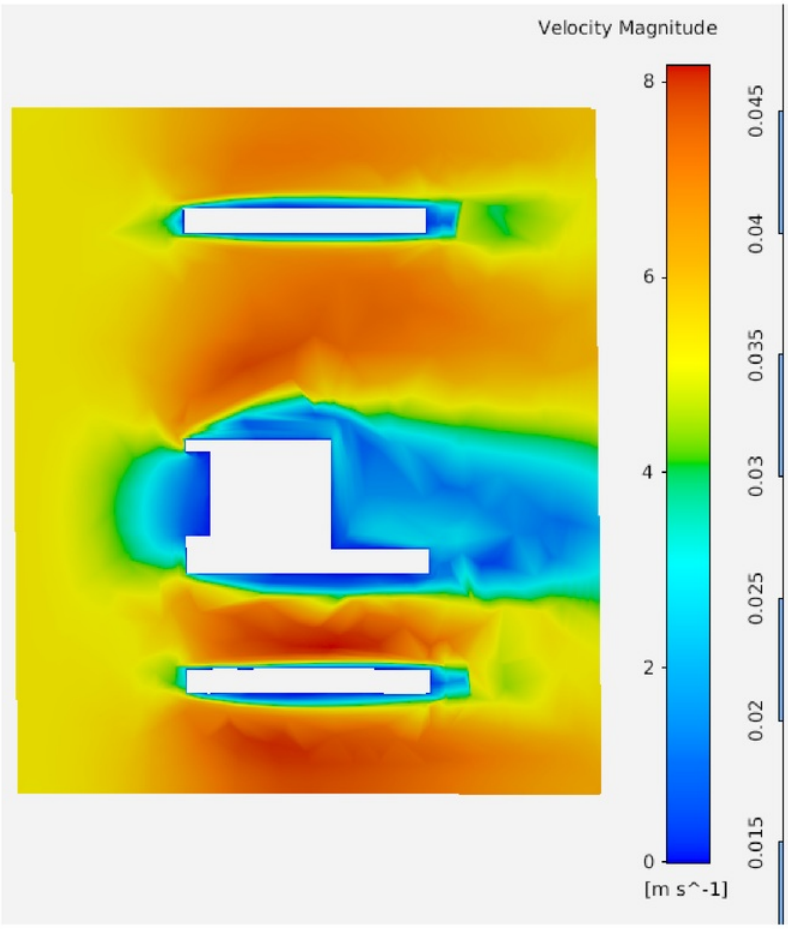

Figure 3.12: Velocity Profile Through Housing - Side View

When running the 2D simulation in COMSOL we see very similar results in air flow velocity. In Figure 3.13 below we can see the simulation setup has the housing and sensor located at the end of a tube of $10cm$ in length in order to replicate the length of the tube attached to the CPAP device.

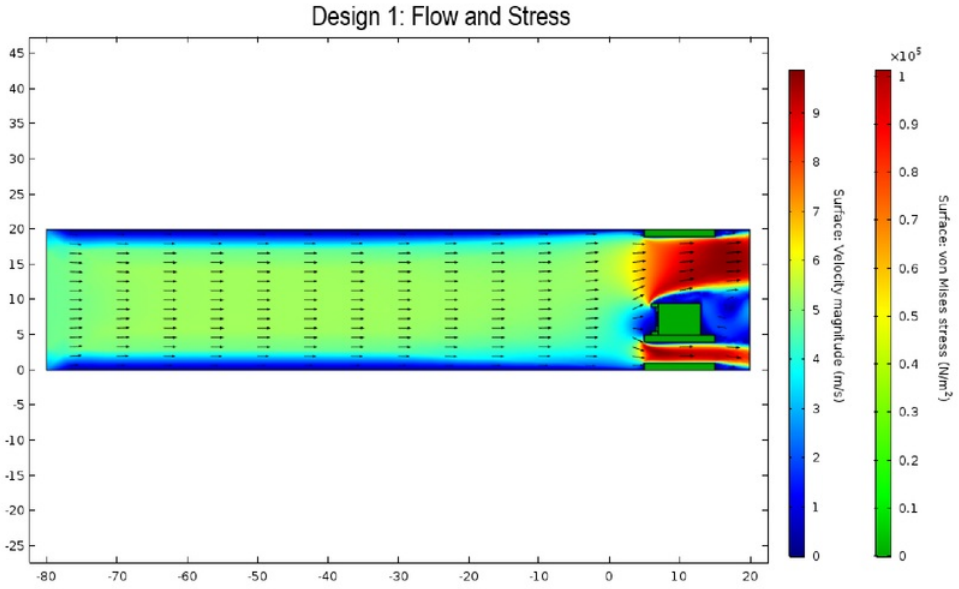

Figure 3.13: Pressure Sensor Flow and Stress Simulation - Full View

In Figure 3.14 we see a zoomed image to better see how the air flow interacts with the housing structure, again in the COMSOL simulation we can see the boundary layers forming from the walls of the tube in Figure 3.13 as well as in Figure 3.14

Figure 3.15 shows the deformation and stress applied to the membrane due to force applied by the air flow at its given velocity. In order to see the deformation more clearly the deformation model was scaled 20 times to give a visible demonstration of the membranes response.

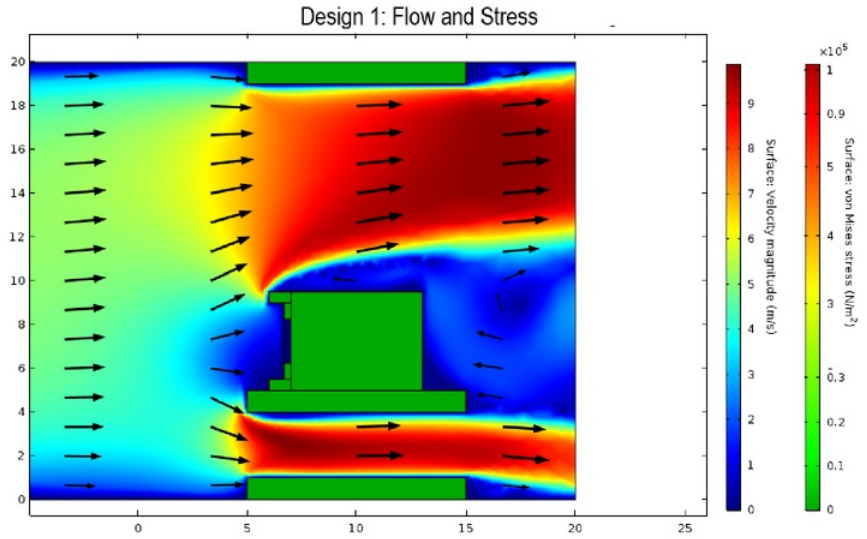

Figure 3.14: Pressure Sensor Flow and Stress

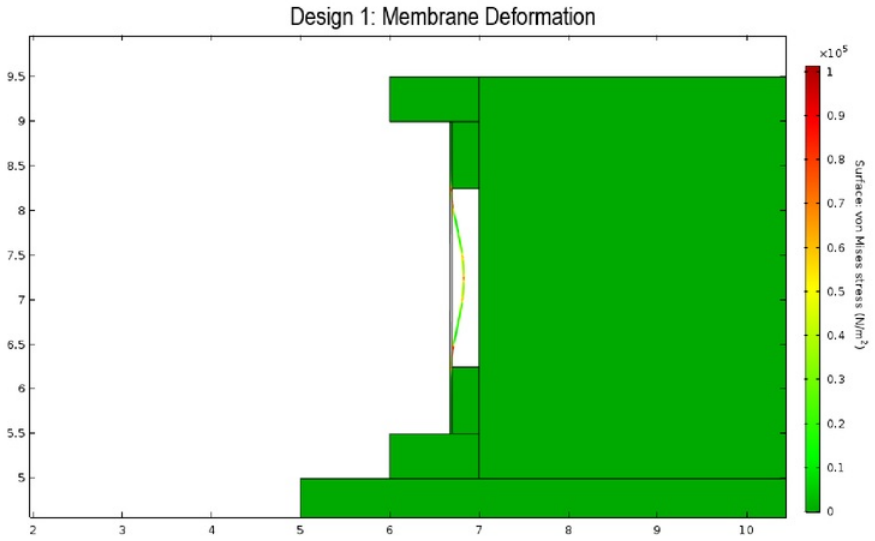

Figure 3.15: Pressure Sensor Membrane Displacement

A parametric sweep was applied to the flow velocity at the inlet of the simulation to replicate different flow rates generated by the CPAP device, Figure 3.16 shows the membrane displacement results from this simulation.

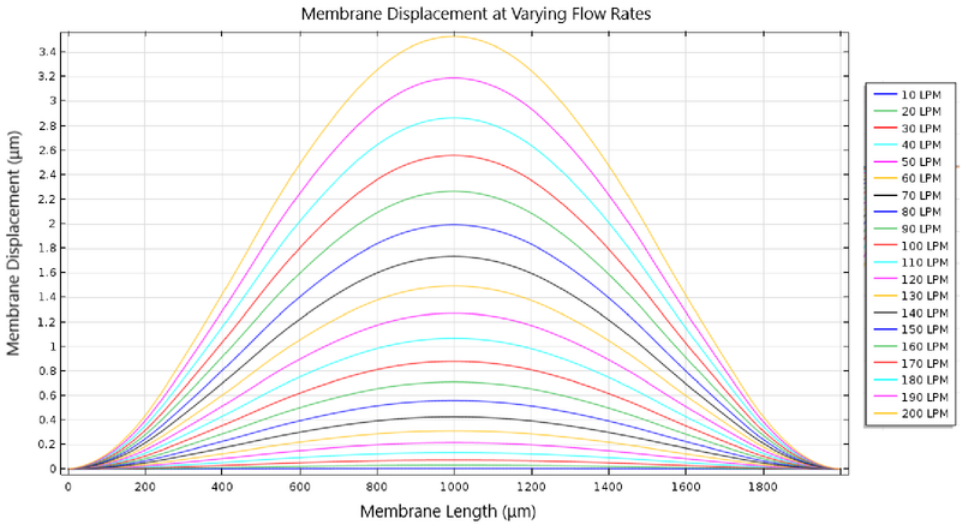

Figure 3.16: Pressure Sensor Displacement

Based on the simulation of membrane displacement, there are distinct, measurable membrane displacement for each 10LPM flow rate step; it is important to note that the difference is membrane displacement between each flow rate increases in a non-linear fashion, indicating that the difference in sensitivity may be difficult to distinguish at lower flow velocity changes compared to higher flow rate changes.

3.1.2 Construction and Assembly

The packaging design was printed with a 3D printer using polylactic acid (PLA), a commonly used bioplastic known for its biodegradability, ease of use and its versatility of uses such as its uses as a resin or filament.

Once 3D printing was completed, the LCP sensor was adhered to the wall inside the extrusion hole with EPO-TEK H70E epoxy, with the gold strain gauges facing outwards, perpendicular to the air flow. The epoxy required was applied using the tip of a hypodermic needle, the epoxy was evenly distributed, and the sensor was placed on the wall with tweezers with the assistance of a microscope. This was then placed into an oven at 100°C for 40mins to dry.

Thin wires were then stripped using a soldering iron to improve conductivity and glued using Polytec EC 101, a two-part conductive adhesive to the gold piezoresistive contact pads on the sides of the LCP sensor. The difficulties in construction occurred when testing the two-part conductive adhesive as the ratios of the two parts needed to be exact, this mix had to be dried in an oven and tested for conductivity before adhering the wires on. A separate microscope slide from the one used to dry and test was used to mix the two parts.

Once the correct mixture was created the adhesive was applied with the tip of a hypodermic needle under a microscope. Once this was adhered correctly and the wires in place, the housing with wires connected were placed in an oven at 100°C for approximately 1 hour to allow the epoxy holding the sensor to the wall as well as the conductive adhesive to dry. These wires were then used to connect to the external circuitry which is detailed in the testing section of this project. Figure 3.17 shows the assembled sensor and packaging.

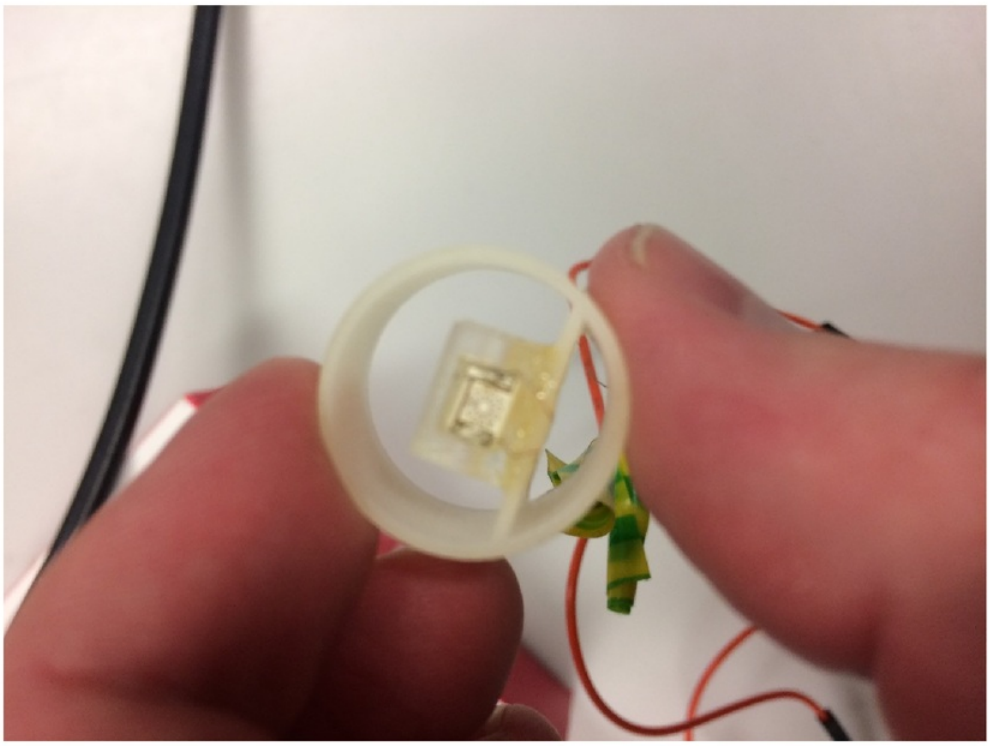

Figure 3.17: Pressure Sensor Packaged

3.1.3 Testing

In the testing phase, the purpose was to conduct experimental work to identify the LCP response to a variety of airflow rates produced by the air flow generator and to detail the experimental results derived from experimental work with LCP MEMS pressure sensor. A comparison between key parameters of a commercially available flow sensor against the LCP piezoresistive pressure sensor was also investigated.

Key parameters that are outlined in this section include flow range from flows of 8LPM to 200LPM as well as resolution graphs of flow rates of 8 - 10LPM, 47-50 LPM, 97 - 100LPM, 147 - 150LPM and 197 - 200LPM, accuracy of peak to peak voltages on flow rates from 10 - 200LPM, and an overview of response time on flow rates of 10, 50, 100, 150 and 200LPM for both sensors.

Experiment

The experiments tested, both the LCP MEMS pressure sensor and the commercial sensor simultaneously. The LCP sensor, located at the end of the flexible tube attached to the air flow generator, was connected to an external Wheatstone bridge biased with 5V and connected to an amplifier and filter with a gain of 50 and a 3Hz low pass filter. The output signal from the amplifier/low pass filter system as well as the output signal directly from the commercial sensor were then used as inputs into a National Instruments data acquisition (NI-DAQ) system cDAQ 9174 series.

Data was then captured and recorded in National Instruments Signal Express 2015 software, where 1000 samples were taken at a rate of 2KHz. All experiments were conducted using the air flow generators default period of 3000ms and set low point of 0LPM. A basic set up diagram is shown below.

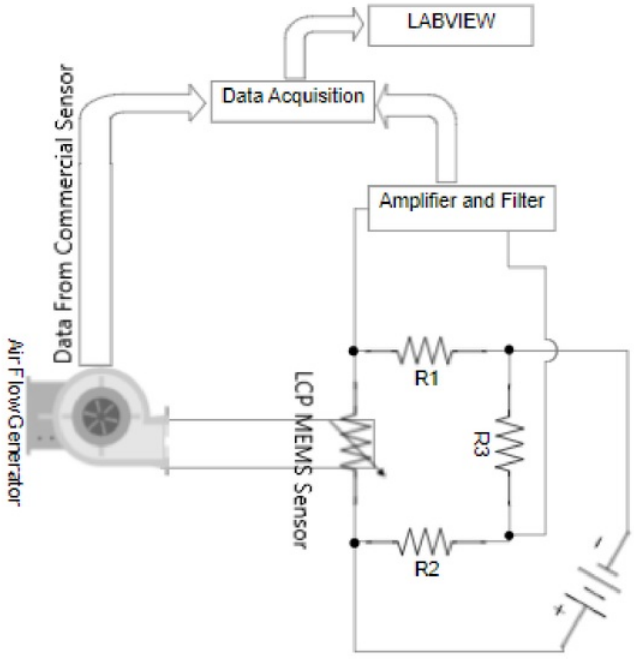

Figure 3.18: Testing Setup

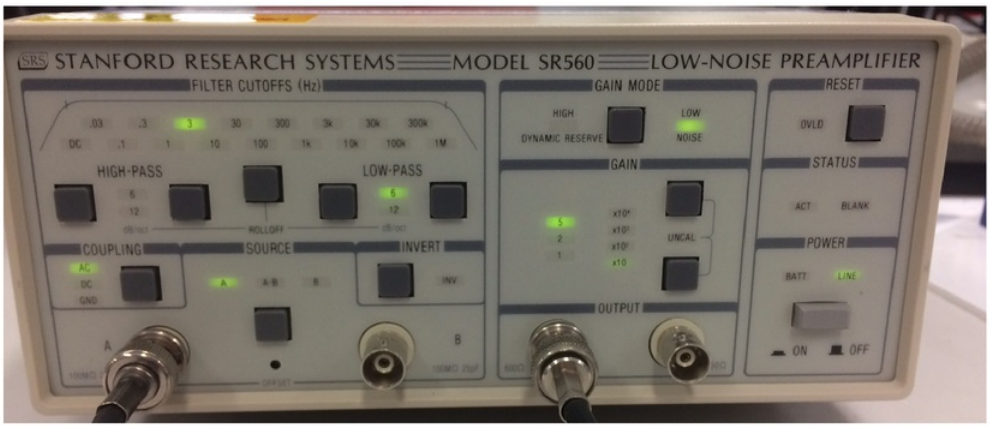

Figure 3.19: Stanford Research Systems Low-Noise Preamplifier

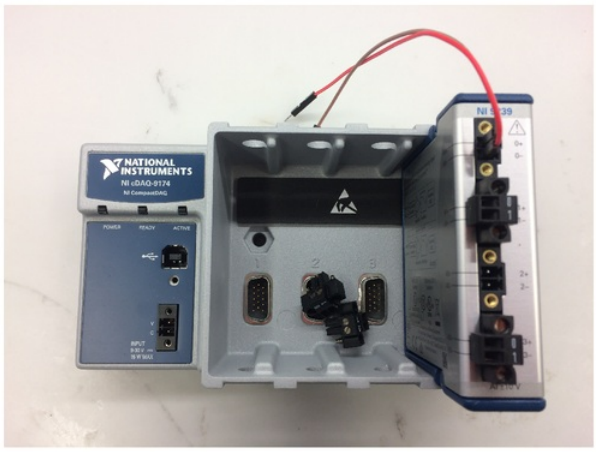

Figure 3.20: NI-DAQ Used To Collect Data

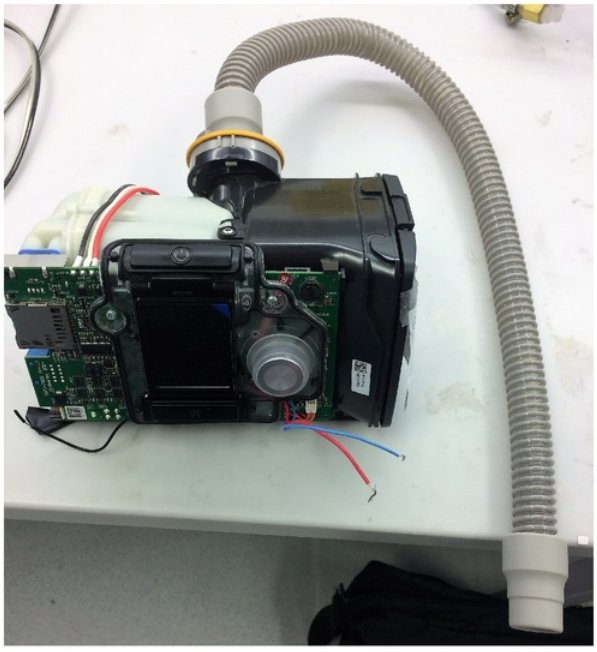

Figure 3.21: ResMed Air 10 CPAP Device

3.1.4 Results

Flow Ranges and Calibration Plot

For flow ranges, the system was set up as outlined and recorded using National Instruments Signal Express 2015, the data was then exported to excel and plotted using Matlab.

Figure 3.21 and Figure 3.22 show and overview of the results from the experiments performed and recorded from both sensors outputs ranging from 10 to 100LPM.

Figure 3.23 shows the calibration plot of the LCP sensor; the graphed points show the average peak to peak voltages gathered from 4 to 5 periods of air flow, with error bars giving the standard deviation of these results.

When fitting a linear line of best fit we can see that for voltage increase by 0.0026V for every 1LPM increase in flow rate.

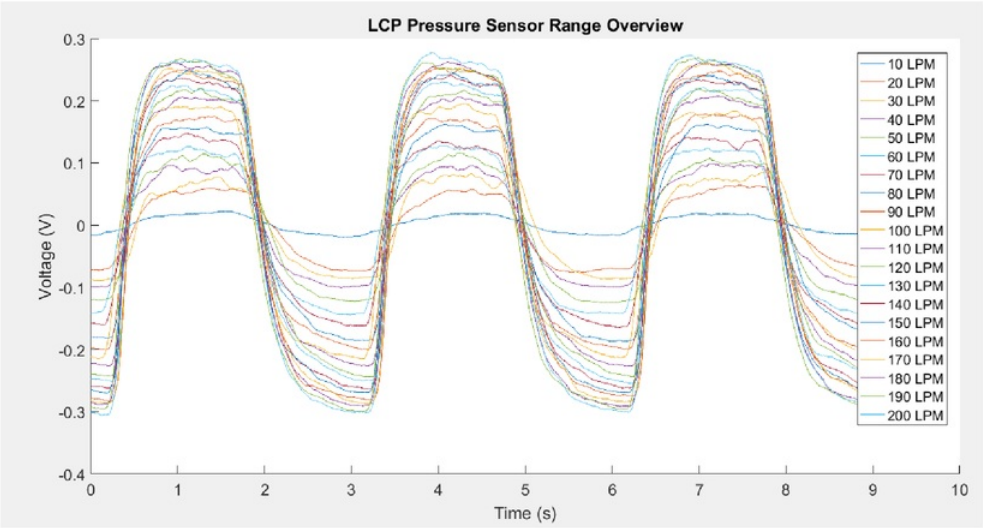

Figure 3.22: LCP Pressure Sensor Overview

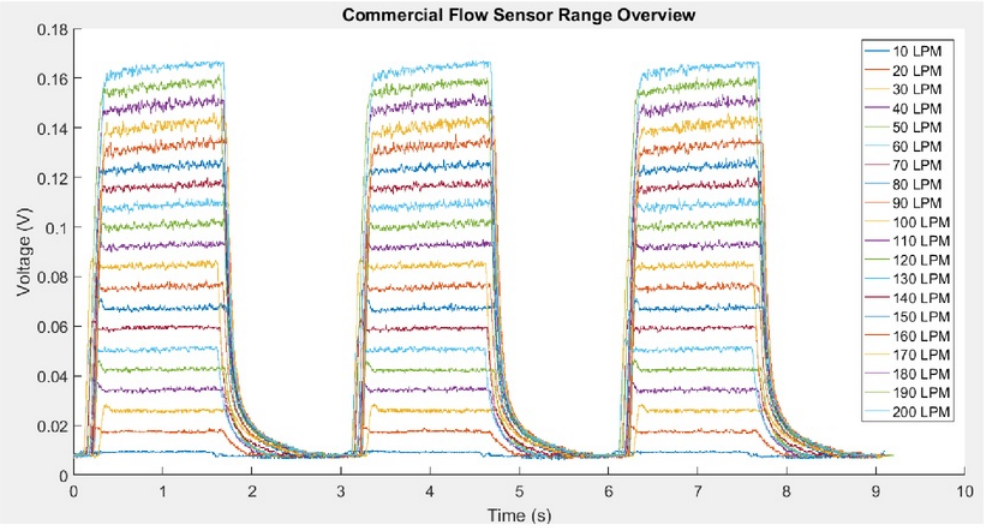

Figure 3.23: Commercial Flow Sensor Overview

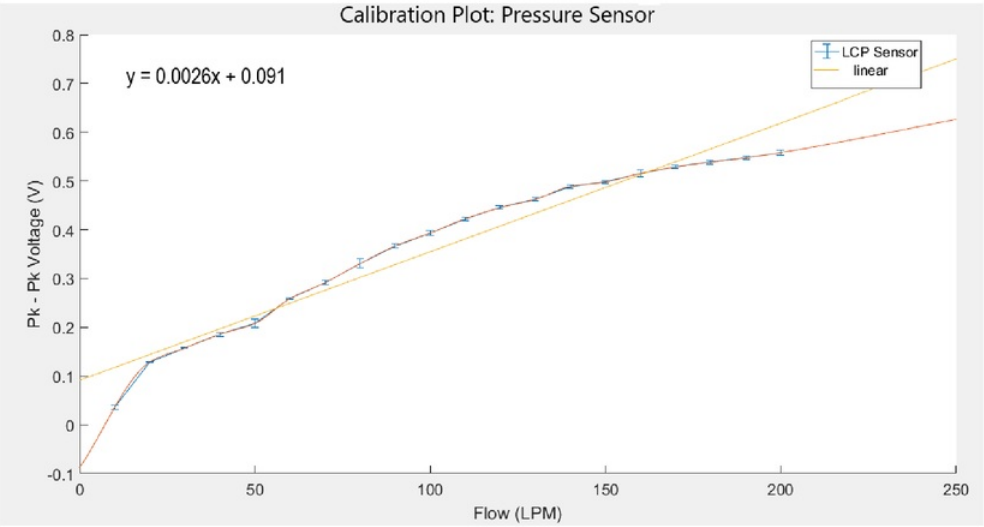

Figure 3.24: Pressure Sensor Calibration Plot

Commercial Flow Sensor and LCP Pressure Sensor Comparison

Figures 3.24 - 3.34 give a direct comparison between the commercial sensor and the LCP sensor at various flow rates.

It is important to note that the observed delay between the rise time of the commercial sensor and the LCP sensor is due to its positioning of the sensor in the air flow generator system. The commercial sensor is located at the initial flow velocity location, whereas the LCP is located at the end of the pipe and therefore the last location in the system and resulting in a delay to respond to flow velocity.

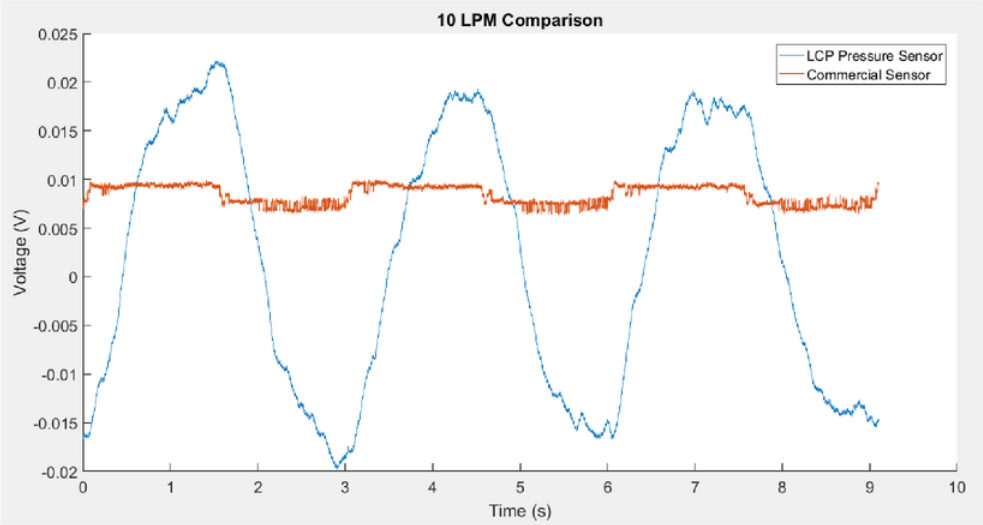

Figure 3.25: Pressure Sensor Vs Commercial Sensor 10LPM

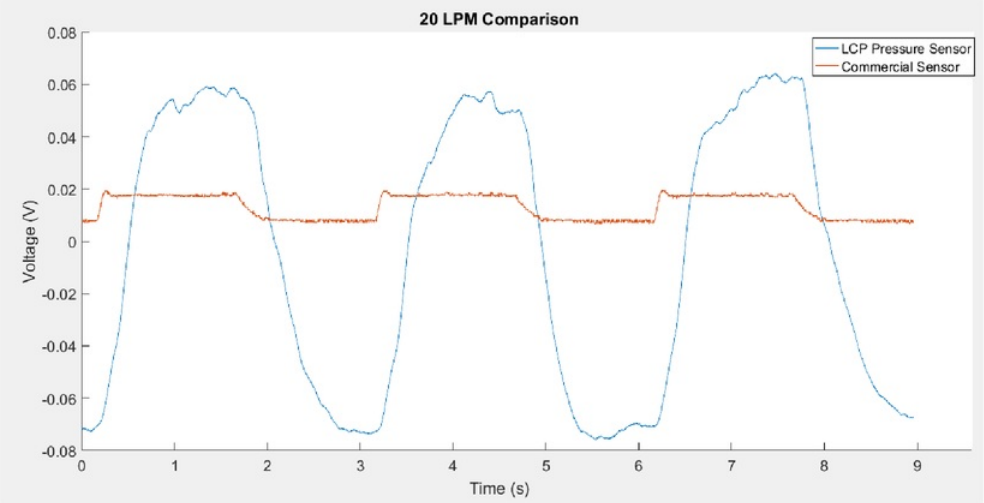

Figure 3.26: Pressure Sensor Vs Commercial Sensor 20LPM

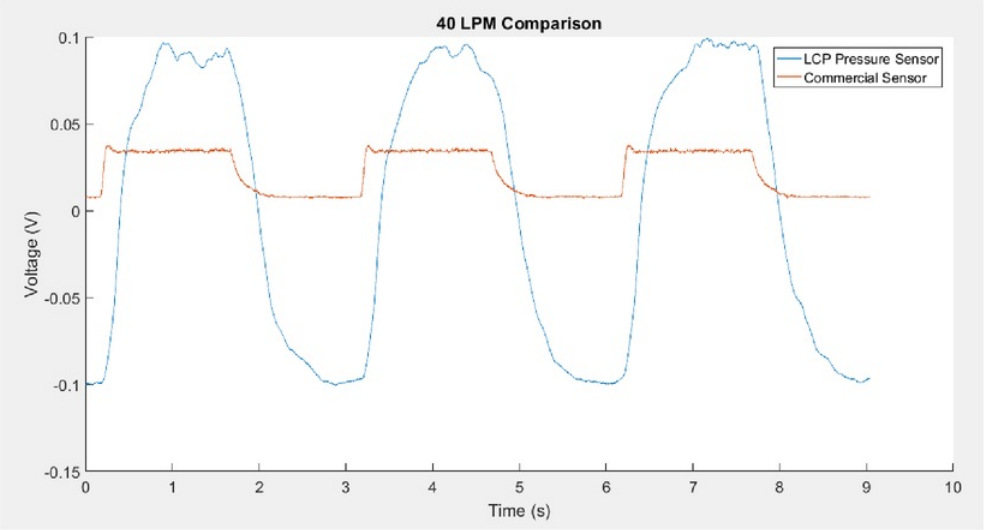

Figure 3.27: Pressure Sensor Vs Commercial Sensor 40LPM

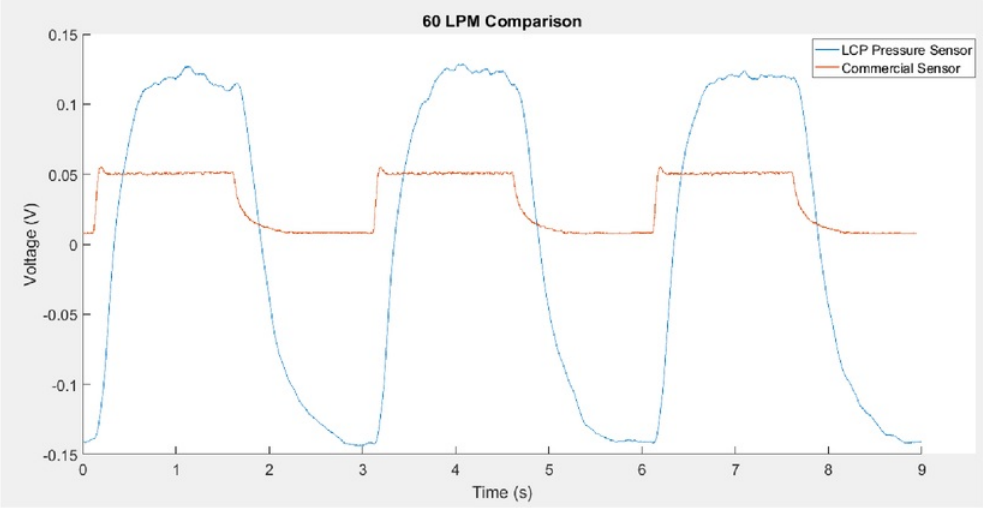

Figure 3.28: Pressure Sensor Vs Commercial Sensor 60LPM

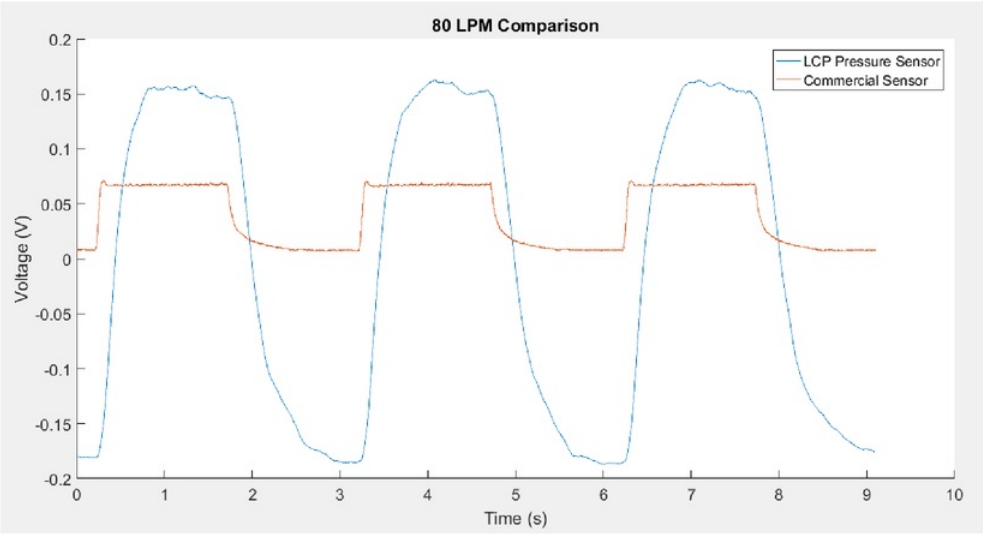

Figure 3.29: Pressure Sensor Vs Commercial Sensor 80LPM

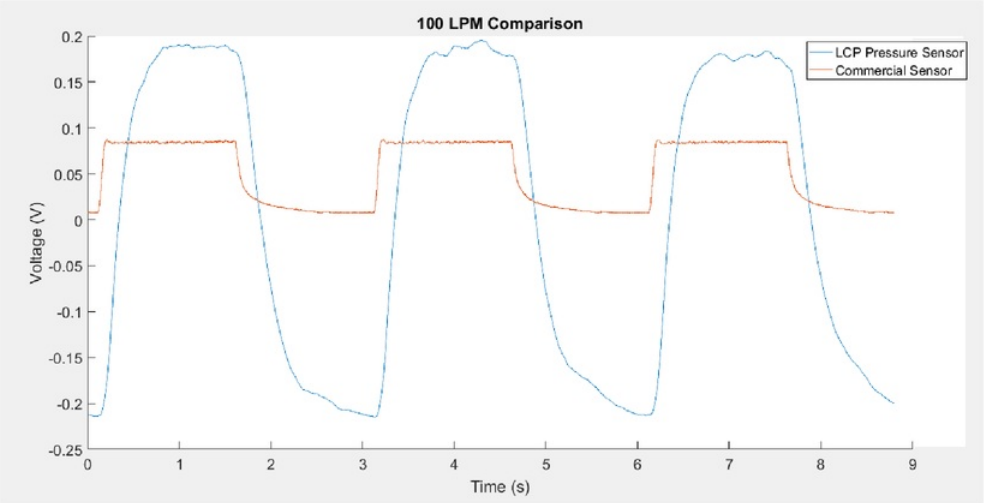

Figure 3.30: Pressure Sensor Vs Commercial Sensor 100LPM

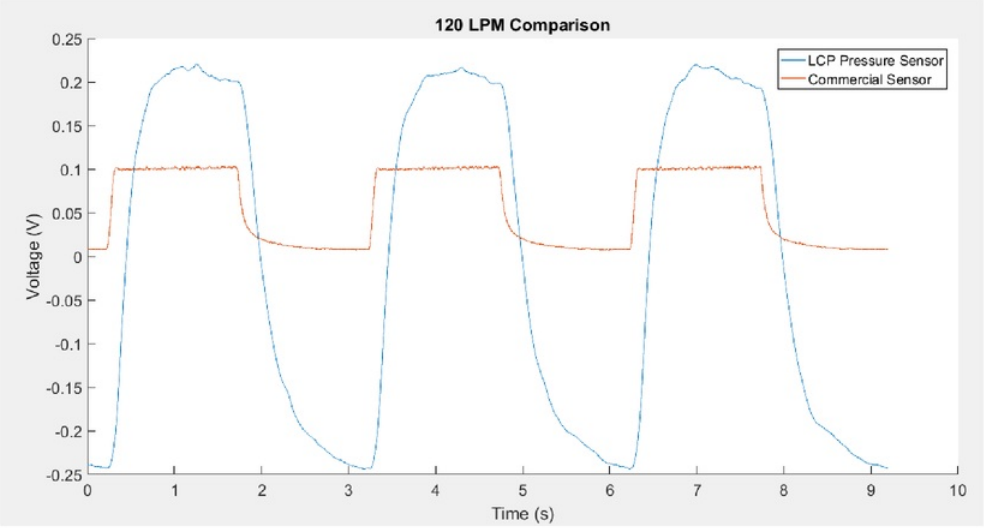

Figure 3.31: Pressure Sensor Vs Commercial Sensor 120LPM

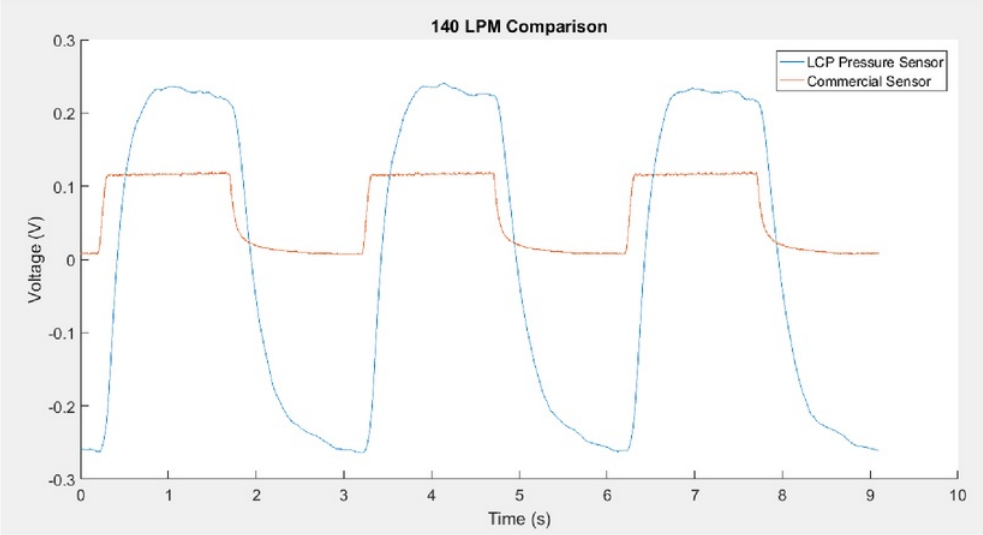

Figure 3.32: Pressure Sensor Vs Commercial Sensor 140LPM

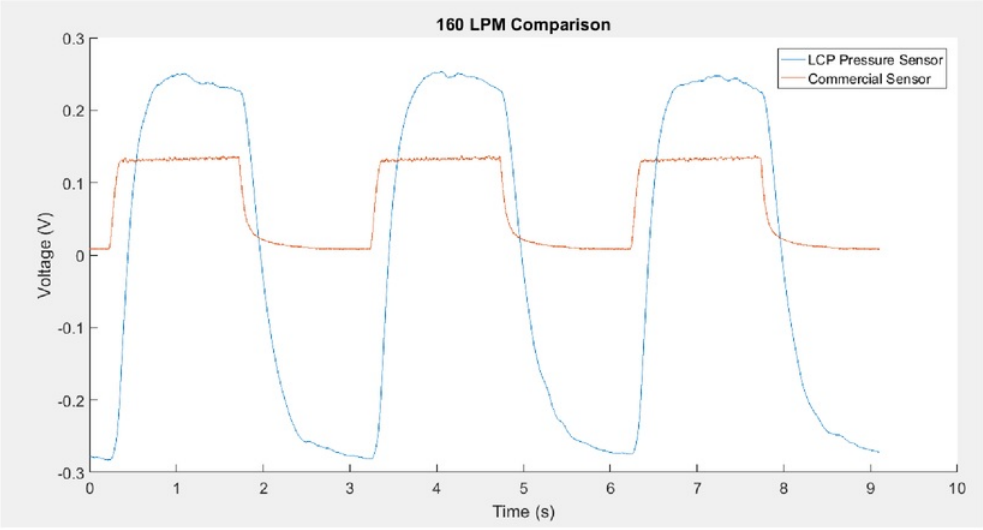

Figure 3.33: Pressure Sensor Vs Commercial Sensor 160LPM

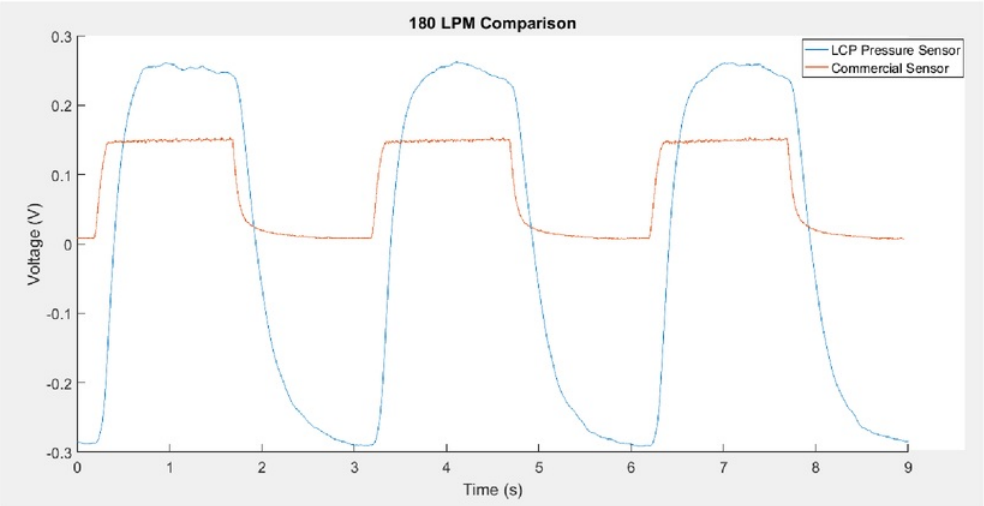

Figure 3.34: Pressure Sensor Vs Commercial Sensor 180LPM

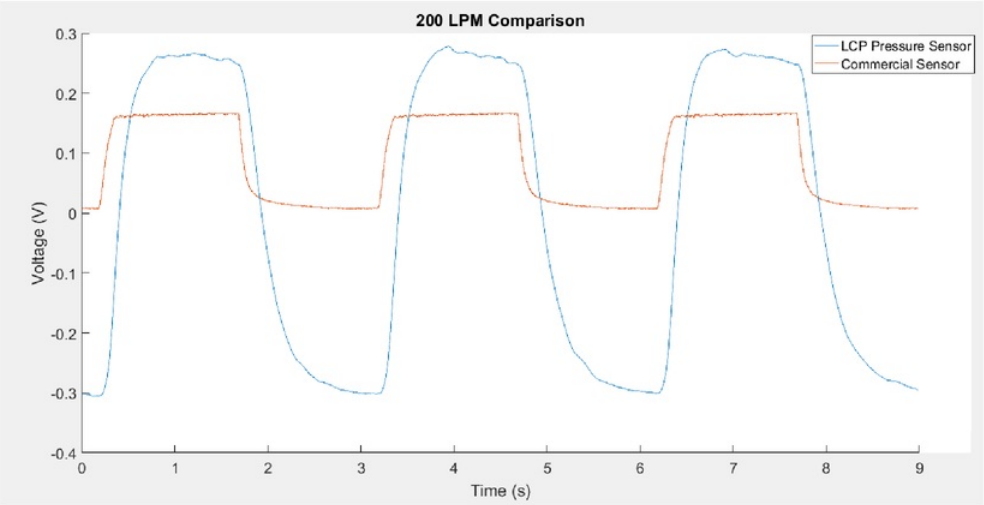

Figure 3.35: Pressure Sensor Vs Commercial Sensor 200LPM

Low Flow Rate Sensing

Experimentation was also conducted to observe the capabilities of the LCP sensor to detect low flow rates. Figure 3.35 below shows that the LCP pressure sensor was able to demonstrate clear sensing capabilities at flow rates as low as 8LPM; furthermore, Figure 3.35 shows the comparison between the data collected from both the LCP pressure sensor and commercial sensor at 8LPM, showing that the LCP sensor is significantly more sensitive to low flow velocities with less signal noise. The pressure sensor does however product some noise despite the low band pass filter applied to the signal.

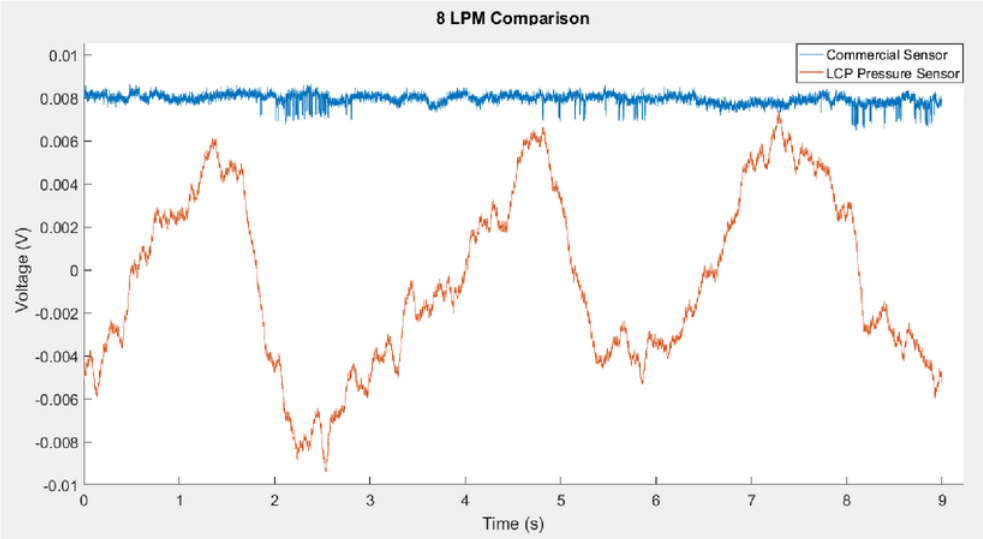

Figure 3.36: Pressure Sensor Vs Commercial Sensor 8LPM

Sensitivity/ Resolution

A set of experiments were conducted to determine if there was a measurable difference between flow rates at 1LPM intervals at various flow rates. These tests were done in flow ranges of 8 10LPM, 47 - 50LPM, 97 100LPM, 147 150LPM and 197 200LPM.

It is evident visually, the LCP sensor demonstrates a measurable resolution of 1LPM from all flow rates tested from 8 - 120 LPM, it is however difficult to differentiate the response from 1LPM variations given the noise in the signals and therefore may be difficult to determine which the exact flow rate, for example, the ability to differentiate the response at 97LPM and 98LPM.

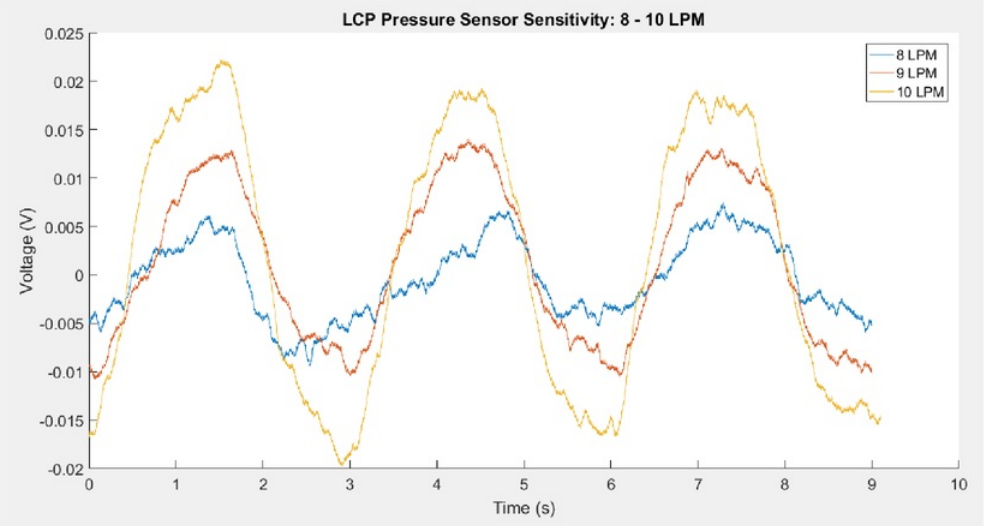

Figure 3.37: LCP Pressure Sensor Sensitivity 8 - 10LPM

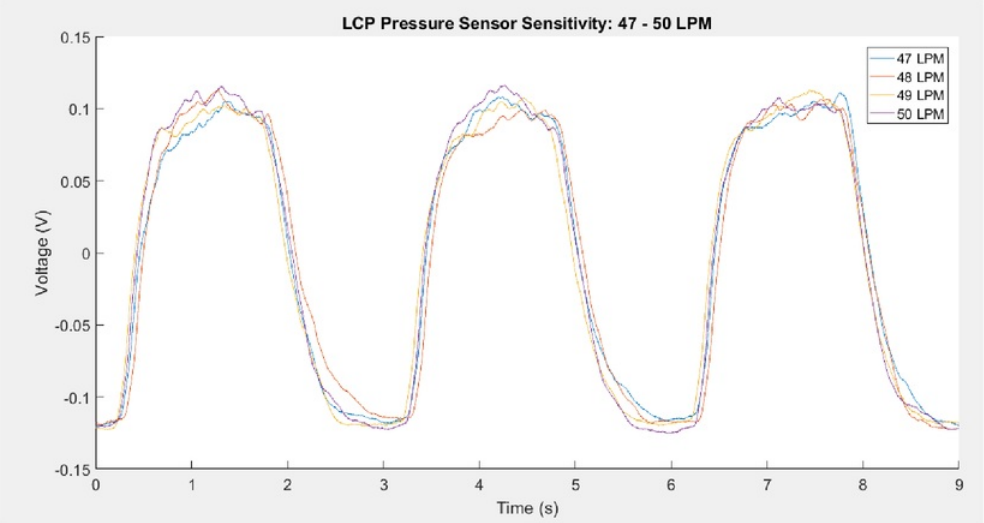

Figure 3.38: LCP Pressure Sensor Sensitivity 47 - 50LPM

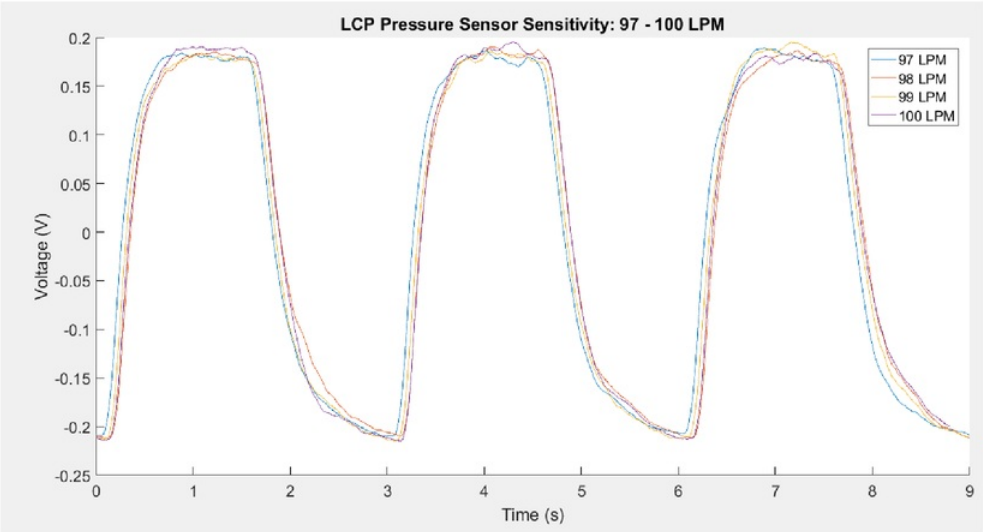

Figure 3.39: LCP Pressure Sensor Sensitivity 97 - 100LPM

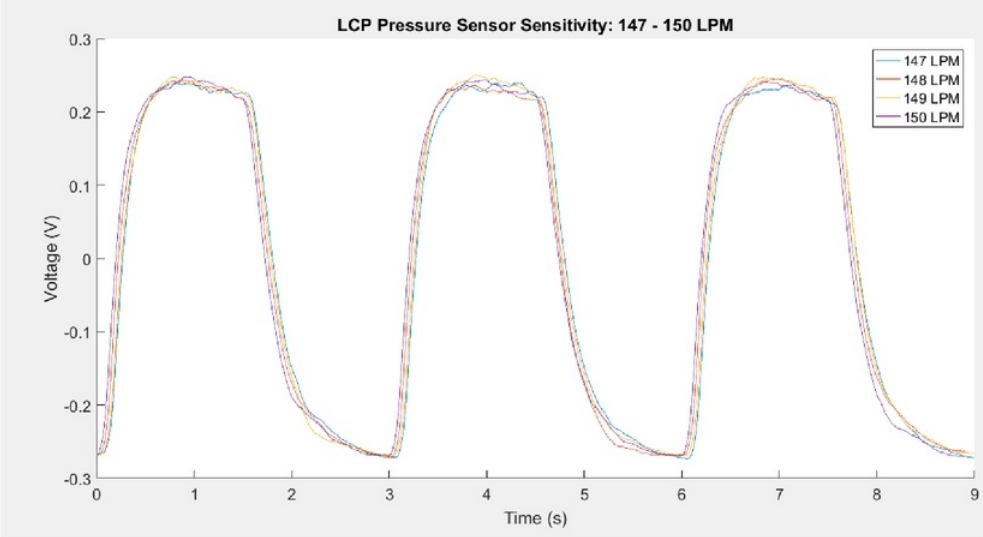

Figure 3.40: LCP Pressure Sensor Sensitivity 147 - 150LPM

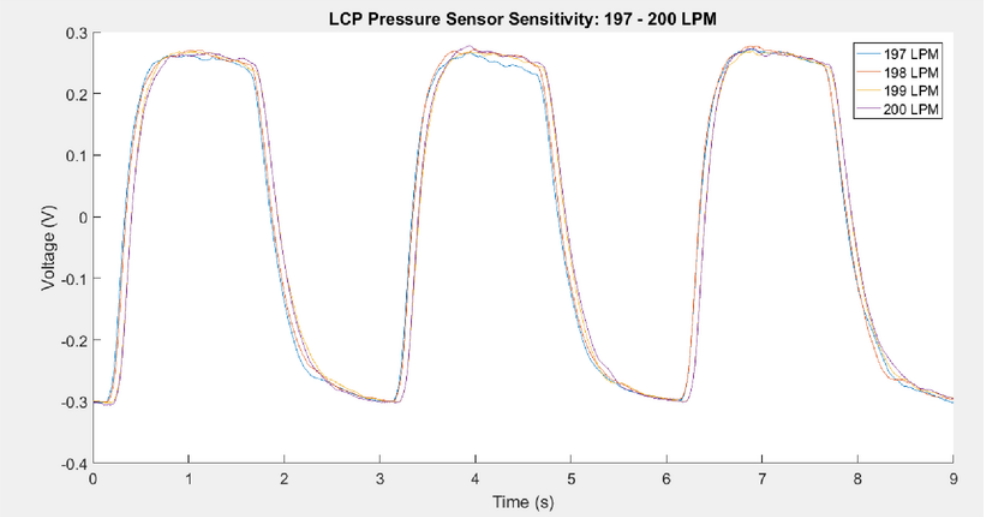

Figure 3.41: LCP Pressure Sensor Sensitivity 197 - 200LPM

Band Gap/Response Time

Throughout the experiments, the response time was also inspected to determine how fast the LCP will reach its peak value which is then compared against the commercial flow sensor Figures 3.41 - 3.44 show visually the response times for varying flow rates; Table 3.1 details the response times of each.

Flow Rate (LPM)	Pressure Sensor Response (s)	Commercial Sensor Response (s)
10	1	N/A
50	0.4	0.15
100	0.4	0.1
150	0.4	0.1
200	0.4	0.1

Table 3.1: Response Time of Sensors

From Table 3.1 above the response time on average for the commercial sensor was 0.1s compared to the LCP pressure sensor which was on average 4 times slower at 0.4s, this slower response time is due to the design and physical limitations of the sensor; a polymer based sensor requires time to undergo mechanical stress at the membrane resulting in membrane displacement. For a change in resistance to occur, the membrane must undergo mechanical stress caused by fluid flow, this requires time for the maximum stress to be applied at each respective flow rate; as the flow rate increases the faster the response time, however at these flow rate, the increased response time is almost negligible.

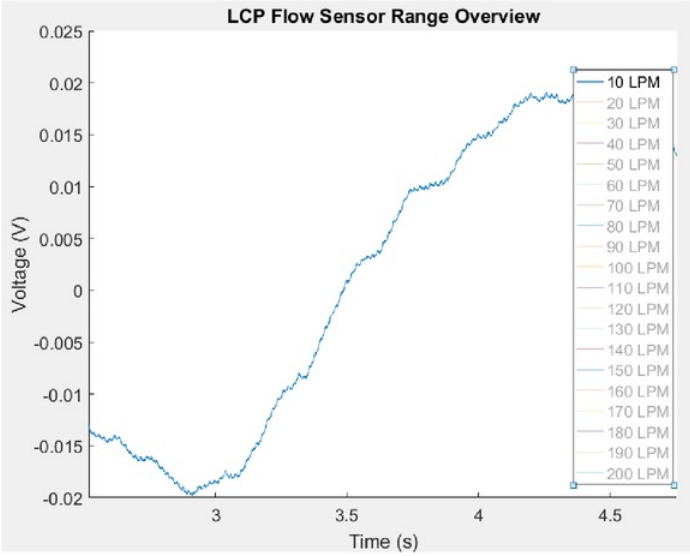

Figure 3.42: LCP Pressure Sensor Response Time 10LPM

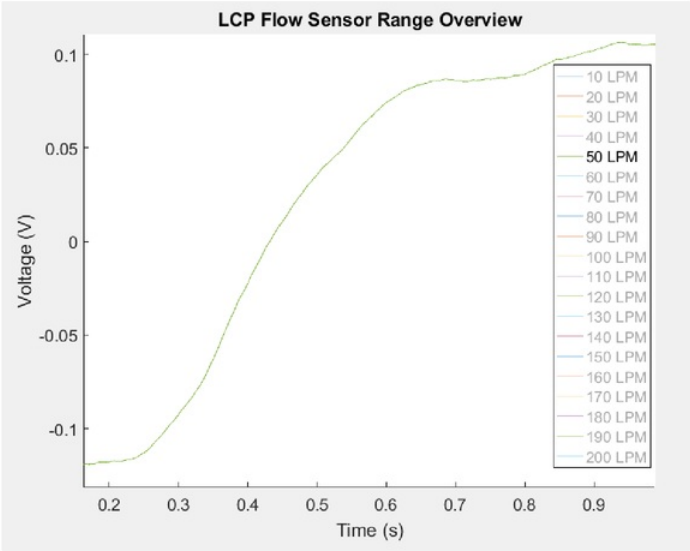

Figure 3.43: LCP Pressure Sensor Response Time 50LPM

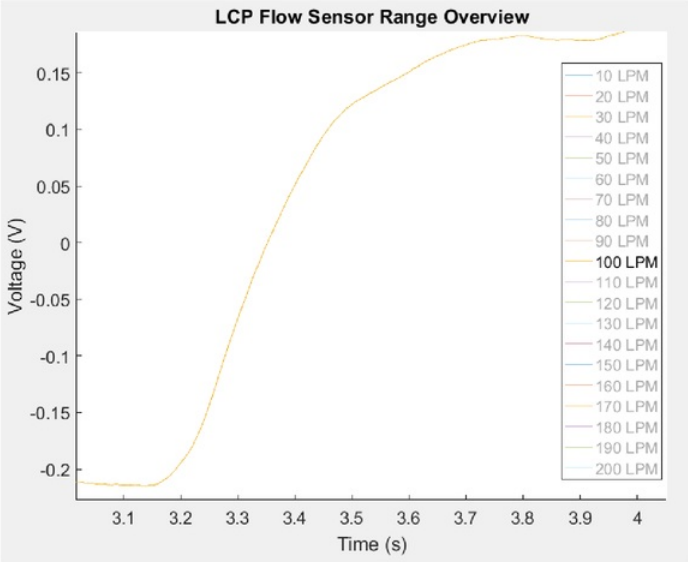

Figure 3.44: LCP Pressure Sensor Response Time 100LPM

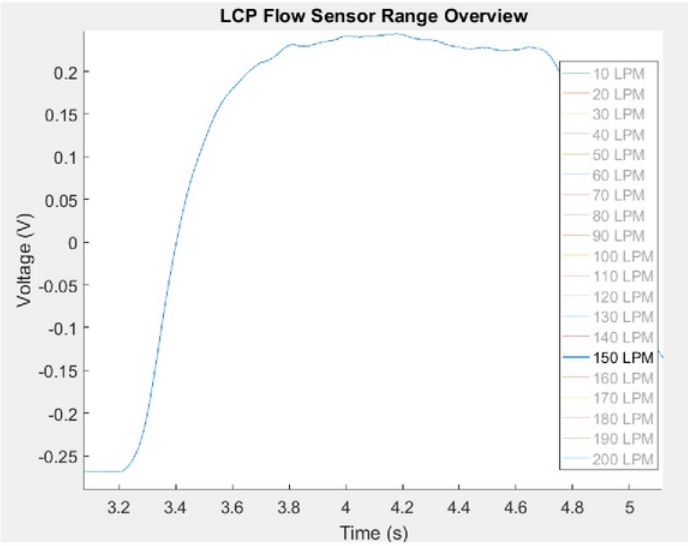

Figure 3.45: Pressure Sensor Response Time 150LPM

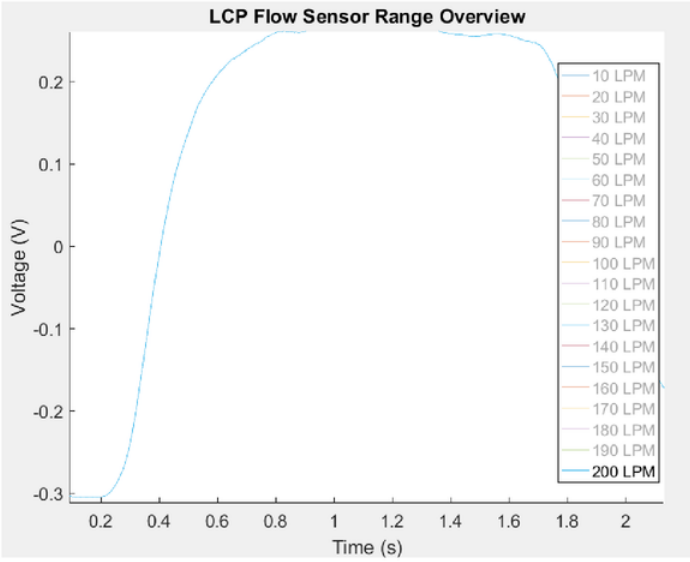

Figure 3.46: Pressure Sensor Response Time 200LPM

Summary of Experimental Work

A number of tests have been conducted to compare the properties of the LCP MEMS pressure sensor against a commercially available flow sensor. The main areas of focus of study for these experiments have been at the flow range sensitivity, resolution, accuracy and response time of the LCP sensor. We can see from Figure 3.21 that the sensor is capable of detecting air flow rates from 10 - 200LPM and even as low as 8 LPM from Figure 3.24. From the calibration plot in Figure 3.23 we can see an average voltage response of 0.0026V per 1LPM flow rate change with an average standard deviation of 0.0047 across flow rates of 10 200LPM; Figures 3.36 3.40 show that there is a measurable difference in voltage given each 1LPM changes in air flow at various flow rates; Figures 3.41 - 3.44 show that the response time for the LCP sensor is approximately 4 times slower than the commercial sensor at 0.4s.

3.1.5 Changes and Improvements

The next design will have some significant changes in both the design of the housing and the way the sensor is packaged. Firstly, the sensor will be modified to include a hair cell-like standing structure attached to the LCP membrane. From previous work by Kottapalli, a hair cell-like standing structure was attached to the membrane with a Youngs modulus of 2.5 - 3GPa, a high aspect ratio of approximately 7.5 and dimensions $3000\mu m$ tall and $400\mu m$ in diameter and comprised of Si60 [3]; this standing structure was attached to the membrane through stereolithography.

The reasoning for adding this hair cell is that it allows the sensor to extend outside the boundary layer generated due to no-slip conditions at the fluid-solid boundary and showed that this made the sensor more sensitive to flow flow velocities and accurate as it was able to detect flow velocities in air as low as $0.01ms^{-1}$ with the standing structure compared to $0.1ms^{-1}$ without and accuracy of 1% deviation compared to 3.6% error in results from LCP pressure sensor, there is however a trade-off as the LCP sensor with standing structure produced $1.3mV/ms^{-1}$ for airflow compared to $3.695mV/ms^{-1}$ without the standing structure [3, 5].

With this modification applied to the LCP sensor in this thesis, the sensor can now be positioned parallel to the flow direction, allowing the hair cell to stand perpendicular to the air flow from which a drag force generated from the fluid-structure interaction is applied to the standing structure thereby displacing the standing structure thus causing deformation on the LCP membrane through mechanical stress of the membrane buckling. This induced displacement will cause a change in resistance applied via the strain gauges. This simple change will also remove the need to the block to be placed in the housing of the sensor, thus reducing the overall obstructions inside the tube and the overall pressure and flow velocity variations that may occur and will also allow the standing structure to be positioned closer to the centre axis of the tube where the flow velocity is least affected by the boundary layer.

Considerations for design changes will also include making the cross beam (that holds the hair cell in place) more aerodynamic for laminar flow as well as looking into the ideal location for the beam to be placed inside the tube. Due to the similarities in simulated results between ANSYS and COMSOL and to avoid any additional double handing of information, COMSOL will be the primary tool used to model these design changes.

Chapter 4

Design Change Considerations

In the following chapter of this thesis, the design change considerations will be outlined and the 2D COMSOL simulations will be shown as well as an evaluation of each design change and whether the change will be implemented in the final design of the housing.

4.1 Design Change I - Pressure to Flow Sensor

4.1.1 Design

As mentioned in the changes and improvements section of the last chapter, the first design change considered was the implementation of a standing structure on the LCP sensor.

Based on previous work by Kottapalli, [3], a hair cell-like standing structure was attached to the membrane with a Youngs modulus of 2.5-3GPa, a high aspect ratio of approximately 7.5 and dimensions $3000\mu m$ tall and $400\mu m$ in diameter and comprised of Si60 was attached to the membrane through stereolithography. The results of his experimentation showed that the sensor was more sensitive to changes in air flow velocity from $3.695mV/ms^{-1}$ to $1.3mV/ms^{-1}$ with an accuracy of $0.05ms^{-1}$. The reasoning for this design change is that it allows the sensor to reach outside the boundary layer created between the air flow and the walls due to no-slip conditions.

By implementing this change, the block that holds the LCP perpendicular to the air flow direction becomes redundant and is no longer required in the housing setup, thereby reducing the amount of obstructions within the pipe and reducing the overall changes in air flow velocity and pressure which can be derived from Bernoullis principle and formalised in Naiver-Stokes equations as the radius of the pipe (respective of the outer ring of the housing) decreases and splits into two pathways with the introduction of beam.

The height of the standing structure was maintained at 3mm similar to the Kottapallis research. In his PhD thesis Kottapalli investigated the system response of the LCP sensor

with varied standing structure heights and thickness as well as determining the boundary layers created from the distance between the leading edge of the LCP sensor and the standing structure. If we denote the velocity as U, distance from the leading edge of the plate (sensor), Reynolds number based on the free stream velocity and the length along the plate Re_x, ($Re_x = Ux/v$) where v is the kinematic viscosity of fluid, then δ the outer limit of the boundary layer for laminar flow occurs at:

$$\delta = \left(\frac{5}{\sqrt{Re_x}}\right) x \tag{4.1}$$

And for turbulent flow:

$$\delta = \left(\frac{0.16}{Re_x^{\frac{1}{7}}}\right) x \tag{4.2}$$

With the leading-edge x = 2mm and an air flow range from $0.1ms^{-1}$ to $10ms^{-1}$, the Reynolds number Re_x is 13 and 1276 respectively, thus giving the boundary layer heights of $280\mu m$ and $2800\mu m$.

When testing various standing structure heights and thicknesses using finite element analysis (FEA), Kottapalli optimised the standing structure to be $2500\mu m$ in height and $350\mu m$ in diameter for use in both air and water. As our experimentation is only in air flow, this thesis has opted for using a $3000\mu m$ (3mm) standing structure with a thickness of $400\mu m$, the maximum diameter without drastically reducing membrane displacement. Furthermore, due to limitations in manufacturing and material availability, SU-8 was not a viable material for the standing structure and therefore Polytetrafluoroethylene (PTFE) was used as a substitute.

The images below give a visual representation of the result of the first design change drawn in SolidWorks

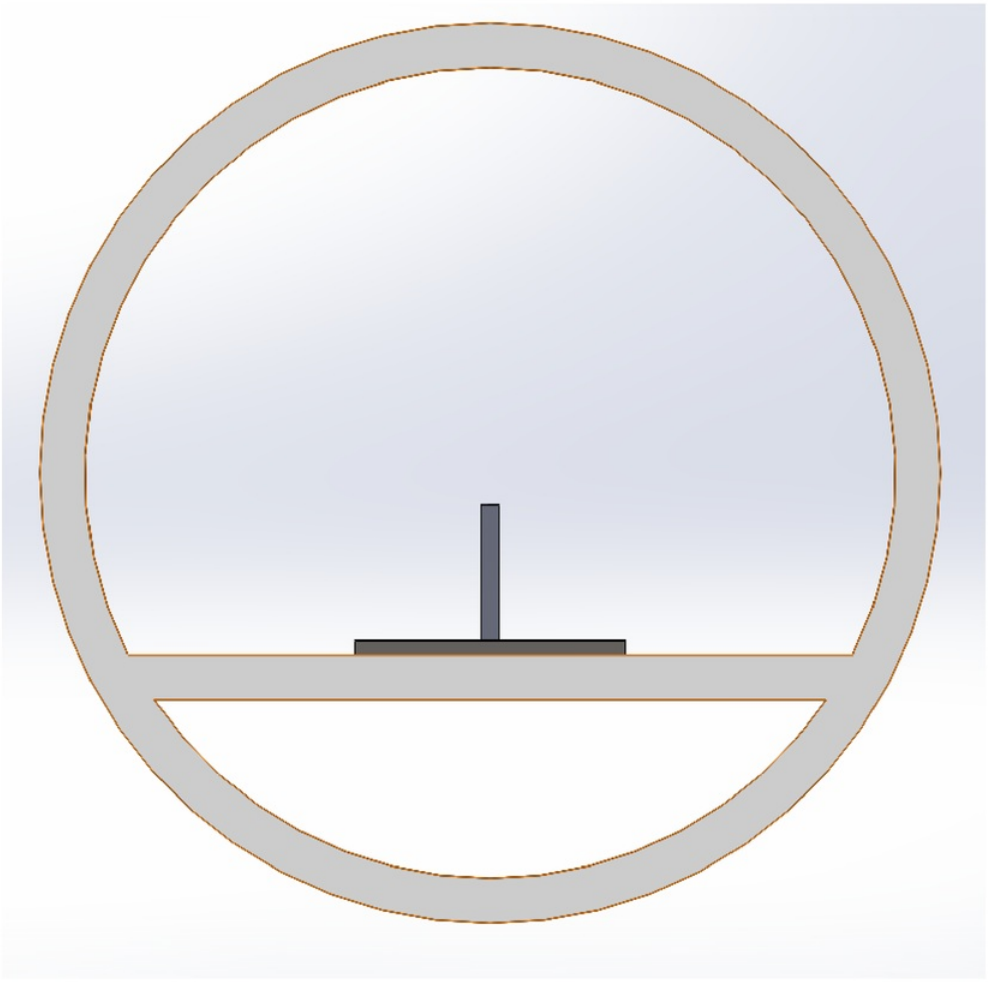

Figure 4.1: Design Change I - Front View

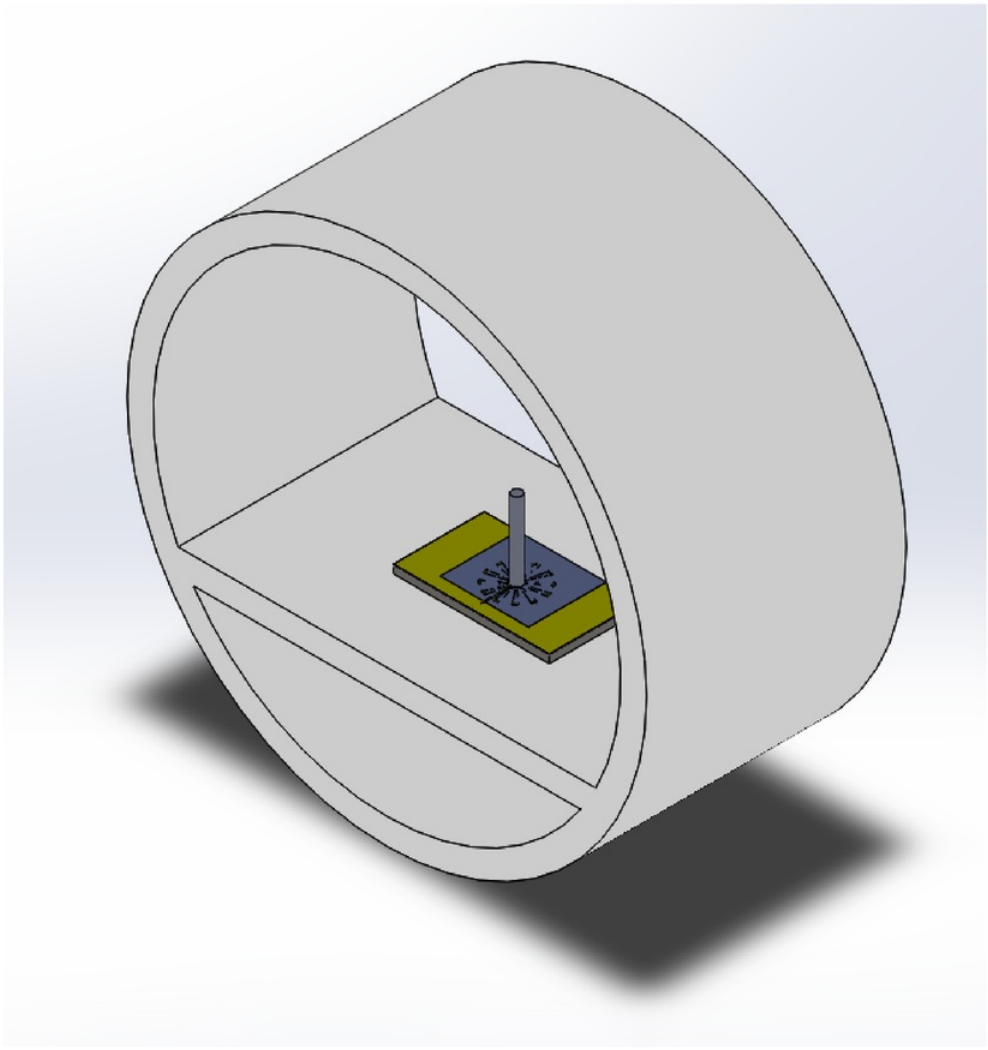

Figure 4.2: Design Change I - Isometric

4.1.2 Simulation

A 2D simulation was conducted using COMSOL, again, using the median 100LPM ($5.31ms^{-1}$) flow rate at the inlet and a pressure of 0Pa at the outlet, as seen in the flow and pressure figures below.

In Figure 4.5 the deformation on the membrane and standing structure has been scaled 20 times to show visually the bend of the standing structure and deformation of the membrane.

In the Figure 4.4, there is evidence of a turbulent flow behind the standing structure, which can be seen in the pressure plot in Figure 4.6 as an area of negative pressure, this backward flow of air may affect the simulated results due to its limitations in the 2D space and therefore cannot analyse the large gap between the standing structure and the wall in the 3rd dimensional plane.

A parametric sweep was also conducted to compare the displacement of the membrane at flow rates from 10 PM to 200LPM as shown in Figure 4.7.

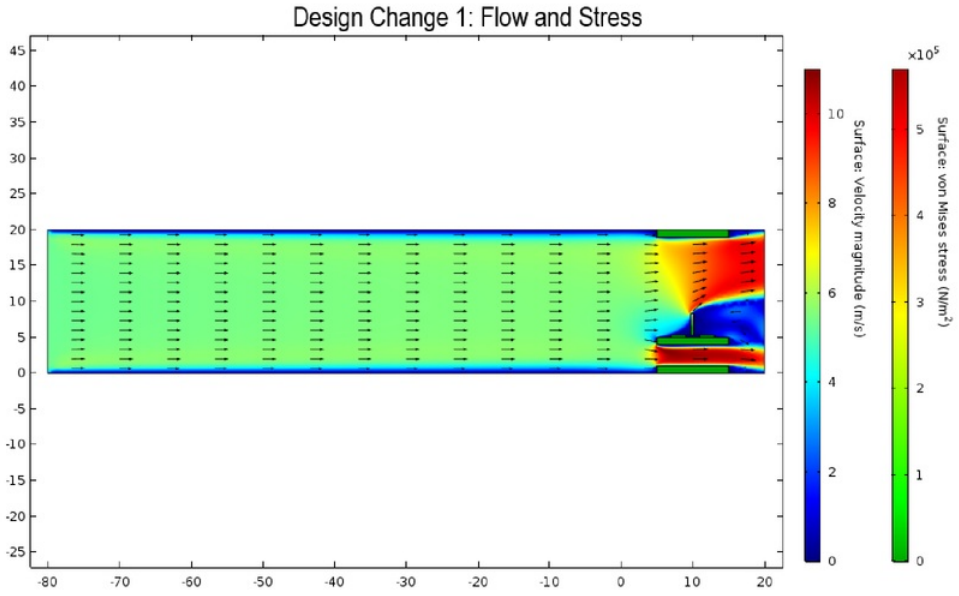

Figure 4.3: Design Change I - Flow and Stress

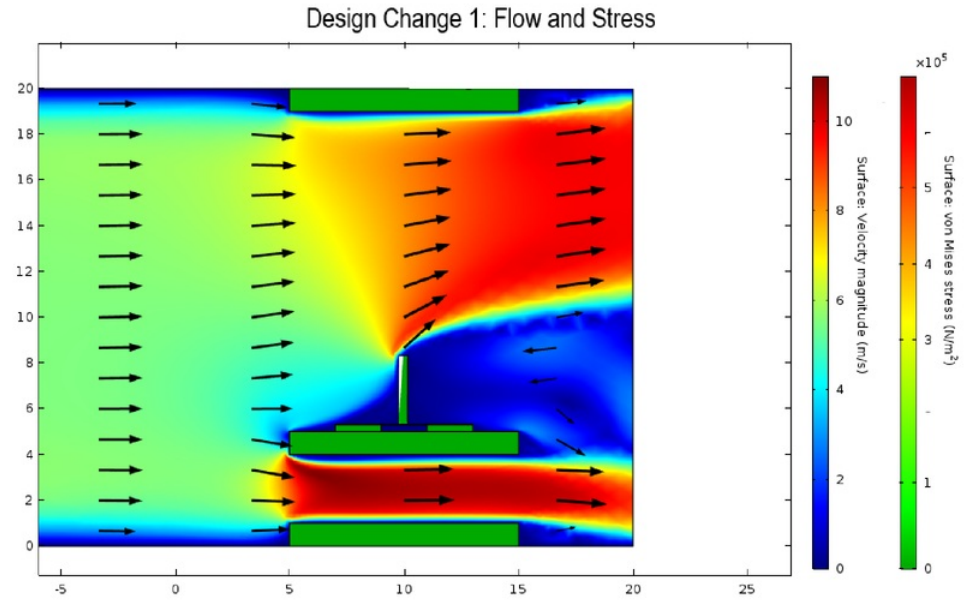

Figure 4.4: Design Change I - Flow and Stress

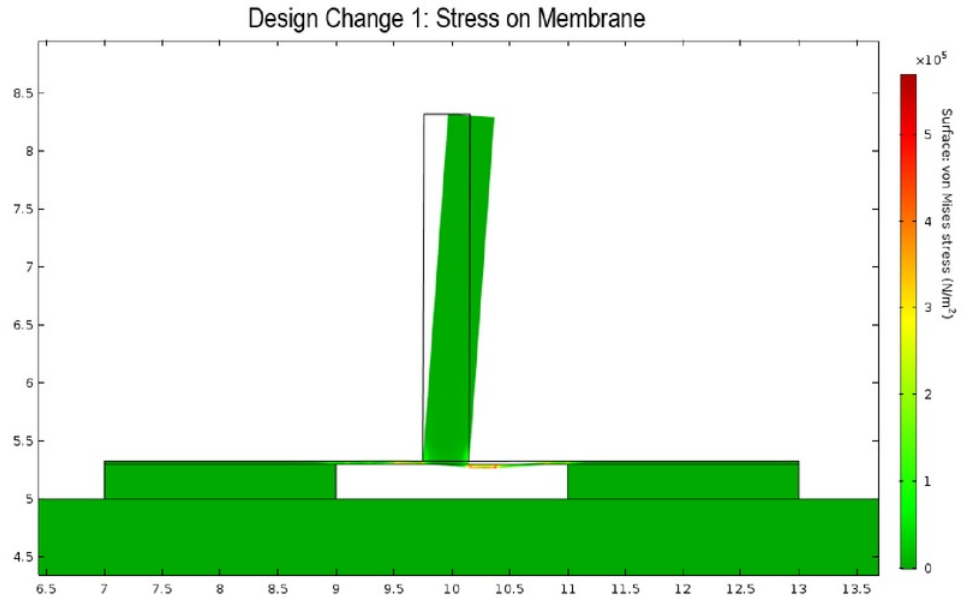

Figure 4.5: Design Change I - Membrane Deformation

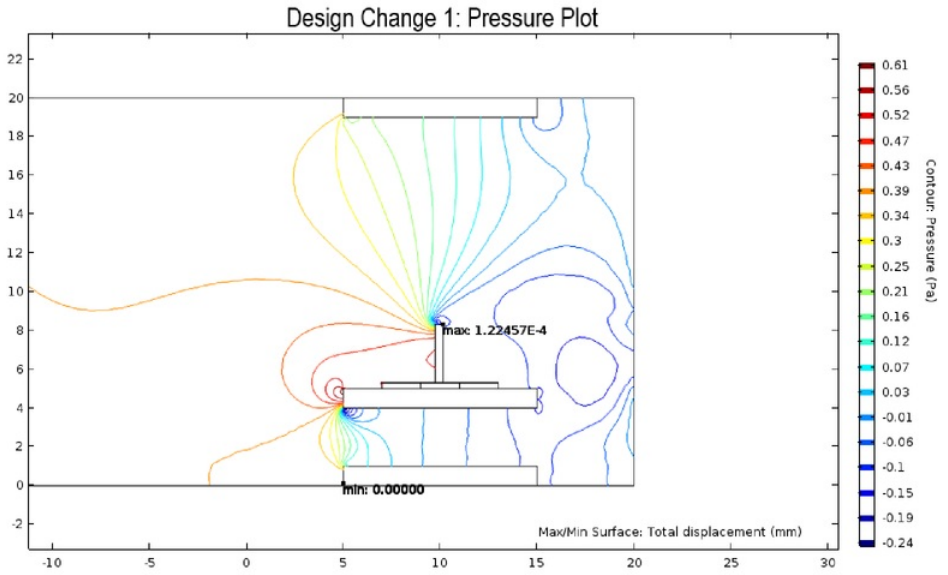

Figure 4.6: Design Change I - Pressure

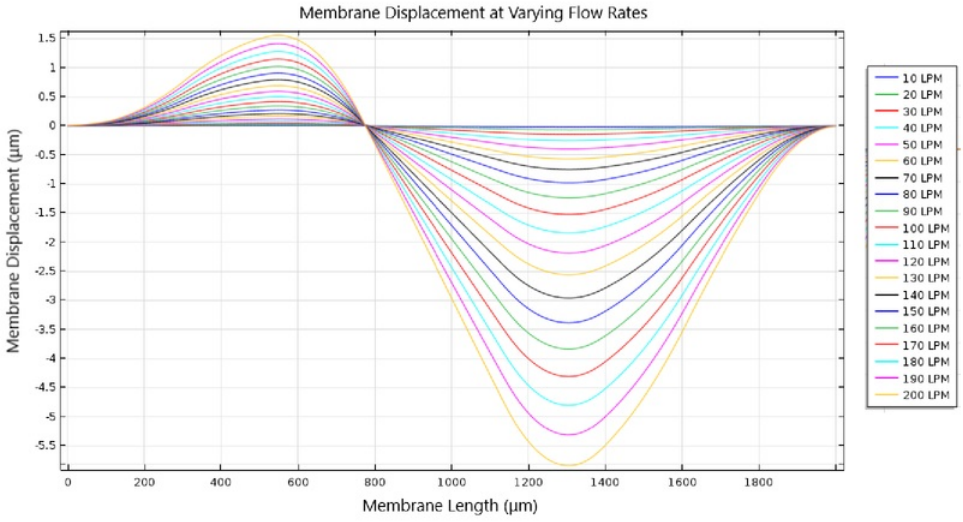

Figure 4.7: Design Change I - Displacement at Various Flow Rates

4.1.3 Evaluation

This design change is the most significant design change that will be implemented into this project as it essentially converts a LCP MEMS pressure sensor to an LCP MEMS flow sensor, we can see in the simulation that the deformation of the membrane is not uniform in that the displacement of the membrane that deforms upwards on the left side of the membrane does not equal to the displacement of the membrane downwards on the right side of the membrane. This non-uniformity of membrane displacement on both sides as well as asymmetrical displacement across the entirety of the round membrane in three dimensions changes the impact on the overall effectiveness of the strain gauges being influenced by membrane deformation.

When comparing the overall displacement of the membrane on both the new design and old design at 100LPM flow rate, we can see that the total absolute area displacement along the membrane is larger in the design change than in the first design.

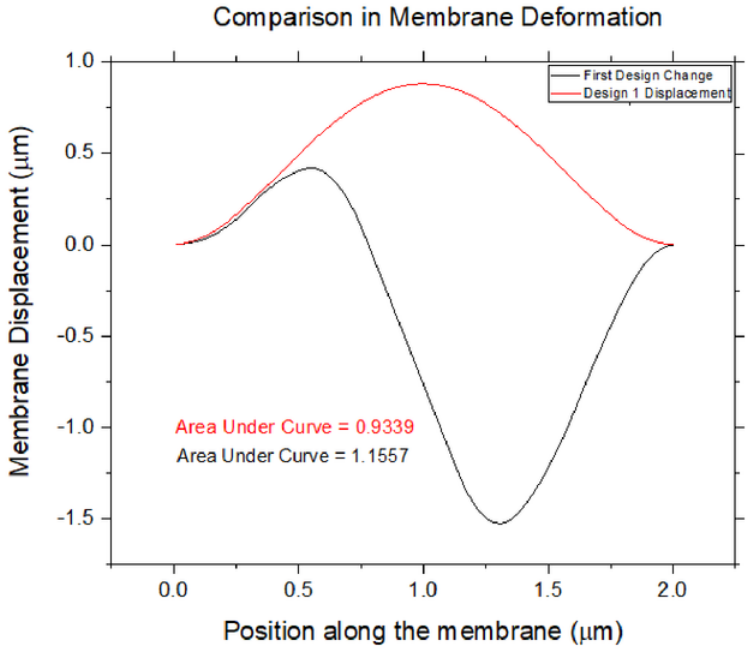

Figure 4.8: Pressure Sensor Vs Flow Sensor (Design Change I) Displacement

The next design change that will be explored will be the thinning of the cross beam and outer ring that holds the housing in place in the tube. By thinning the structures in

the housing, the changes in flow velocities and pressure will be minimised to give a more accurate response based on actual air flow through the pipe.

4.2 Change II - Thinning the Structures

4.2.1 Design

The second design change that was explored was the idea of thinning the ring structure and support beam that holds the LCP sensor in place. By doing so, this would reduce the change in air flow velocity and pressure that occurs, as explained by Bernoullis principles, thereby resulting in a more accurate resistance change for the air flow velocity generated by the CPAP device.

4.2.2 Simulation

Similar to the last design change, the model was created in COMSOL using the previous model and changing the thickness of all beams from 1mm in height to 0.5mm in height. The simulation was run in the same manner as the previous design changes, the images of flow and pressure are the results of the fluid structure interaction at 100LPM ($5.31ms^{-1}$ inlet flow) with the pressure of the outlet set to 0Pa. The simulated results are shown in Figures 4.9 - 4.13.

A parametric sweep was again conducted to observe the LCP membrane deformation from flow rates ranging from 10LPM to 200LPM shown in Figure 4.13

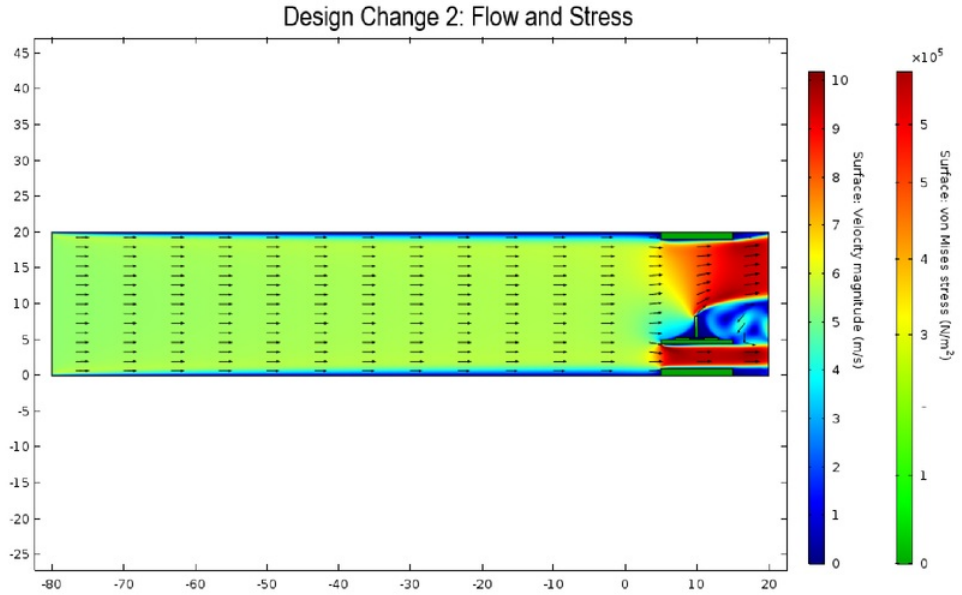

Figure 4.9: Design Change II - Flow and Stress

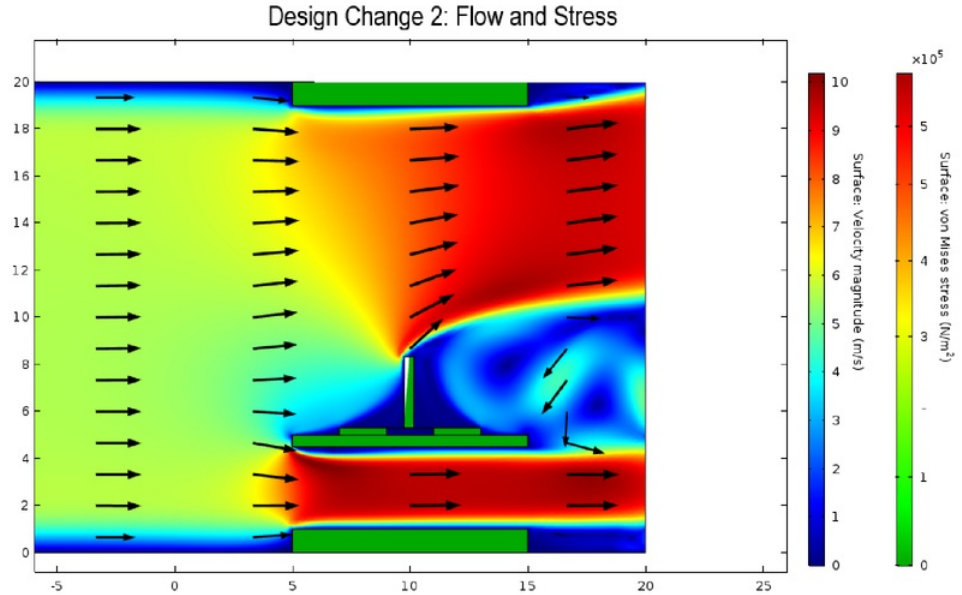

Figure 4.10: Design Change II - Flow and Stress

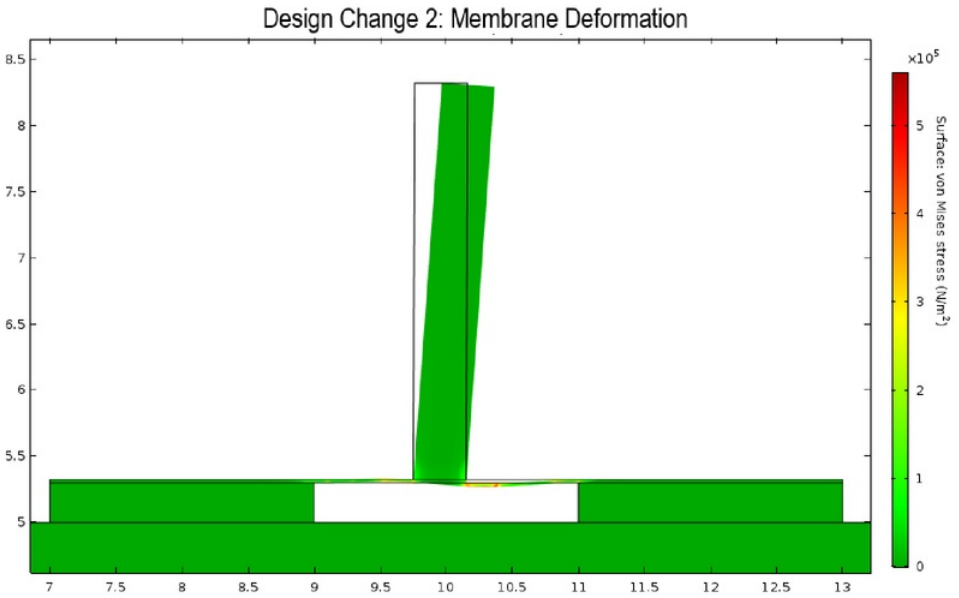

Figure 4.11: Design Change II - Membrane Deformation

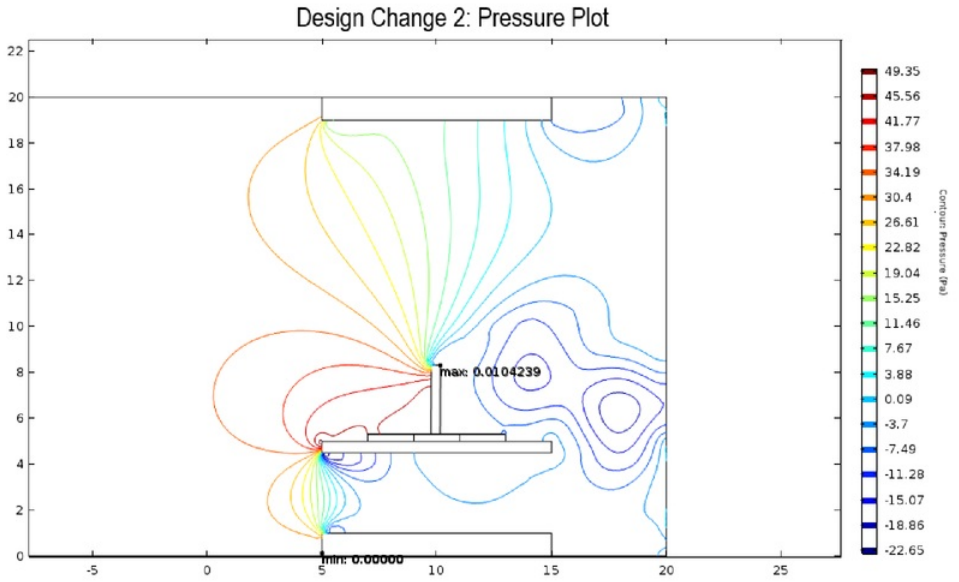

Figure 4.12: Design Change II - Pressure

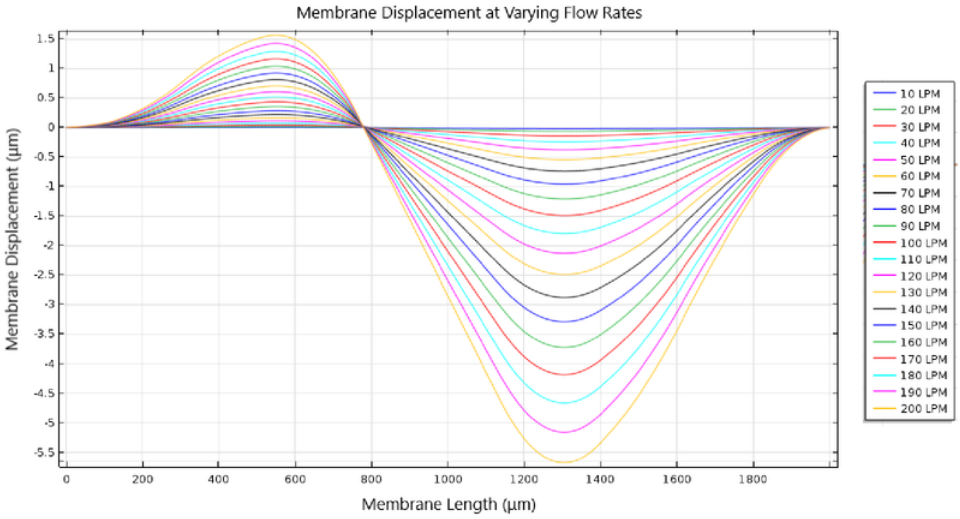

Figure 4.13: Design Change II - Membrane Displacement at Varying Flow Rates

4.2.3 Evaluation

When evaluating the displacement of the membrane at 100LPM between Design Change I and Design Change II the peak to peak values of the 1mm thick housing is larger than the 0.5mm thick housing. The reason for this lies in air flow velocity properties of a narrowing pipe; a 1mm thick housing restricts the surface area available to the air flow compared to a 0.5mm thick housing, this increase in air flow velocity results in a greater drag force applied to the standing structure which bends the LCP membrane.

By reducing the air flow velocity experienced by the standing structure a lower membrane displacement occurs, this has some advantages and disadvantages by allowing the air flow velocity experienced by the standing structure to be closer to the actual air flow generated by the flow generator, we can attain a more realistic system response to the air flow, however this may also reduce the systems sensitivity to lower flow velocities. Put simply, the small increase in flow velocity can act as an amplification of sorts for the standing structure to interact with which may allow the system to detect a flow rate lower than what it may be able to without the increase in velocity.

It is important to note the limitations of a 2D simulation as it does not account for the area on each side of the standing structure between it and the wall and the effects that would have on minimising the flow velocity increases that are represented in these simulated figures above.

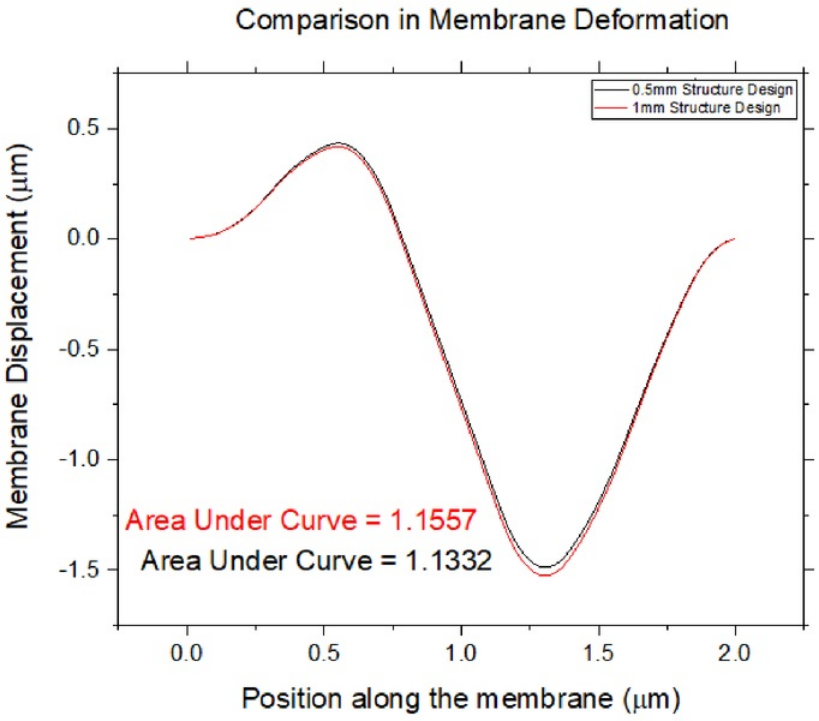

Figure 4.14: Membrane Displacement: Design Change I Vs. Design Change II

When evaluating the differences in displacement between the two design changes, shown in Figure 4.14, there is a near negligible difference in total area deformation in the membrane, meaning there may be no real change in the output voltage attained in real world testing, furthermore due to 3D printing resolution restrictions, the design will be difficult to print without the use of a high quality printer which is unable to be attained within the relative time constraints of this project, it is therefore recommended that the thickness of the housing remain at 1mm.

The next design change that will be investigated is the effects of filleted edges and their impacts on reducing the turbulent flows that may arise between the interaction of the laminar flow and the start of the housing. By reducing the possibility of turbulent flows arising in front of the housing, the reduction in in changes in pressure and flow velocities may improve system response.

4.3 Design Change III - Fillet Edges

4.3.1 Design

The next design change idea was to fillet the leading edges of the housing respective of the airflow; by doing so, the turbulent air flow that is produced when the laminar flow interacts perpendicular to the face of the housing is reduced and/or redirected as well as assisting in redirecting the laminar flow through the housing. Furthermore, by changing the laminar flow profiles there may be a change in pressure variations interacting with the system. A COMSOL simulation will better explore the fluid-solid interaction and identify if any positive or negative affects result from this design change.

Figure 4.15 gives a 3D model of the filleted design drawn in SolidWorks.

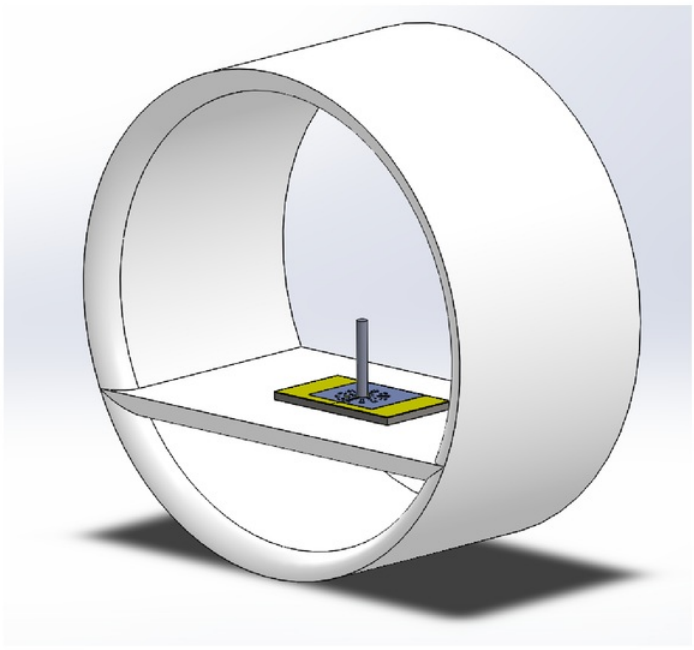

Figure 4.15: Design Change III - Fillet Edges

4.3.2 Simulation

The simulation was remodelled and run in COMSOL using the previous model but including a 1cm fillet on the edges of the housing ring and a filleted beam directing the flow downwards, reducing the turbulent flow generated in front of the standing structure. The simulation was run in the same manner as the previous design changes, the images of flow and pressure are the results of the fluid structure interaction at 100LPM ($5.31ms^{-1}$ inlet flow) with the pressure of the outlet set to 0 Pa.

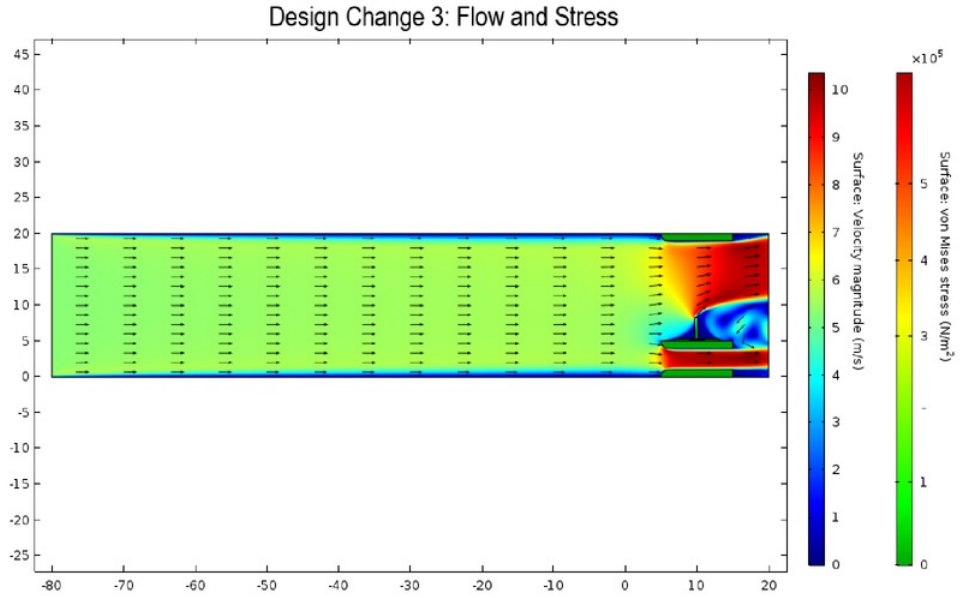

Figure 4.16: Design Change III - Flow and Stress

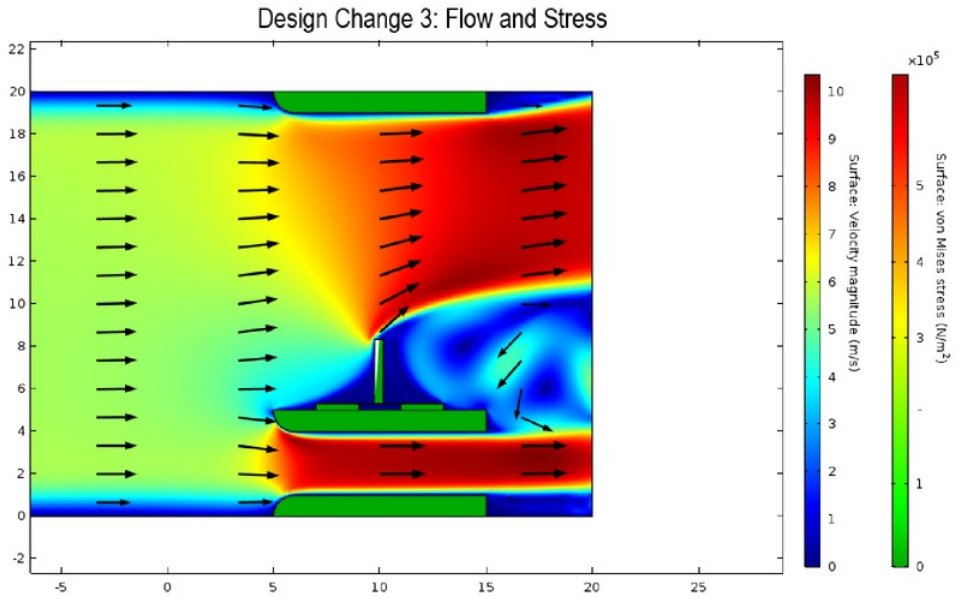

Figure 4.17: Design Change III - Flow and Stress

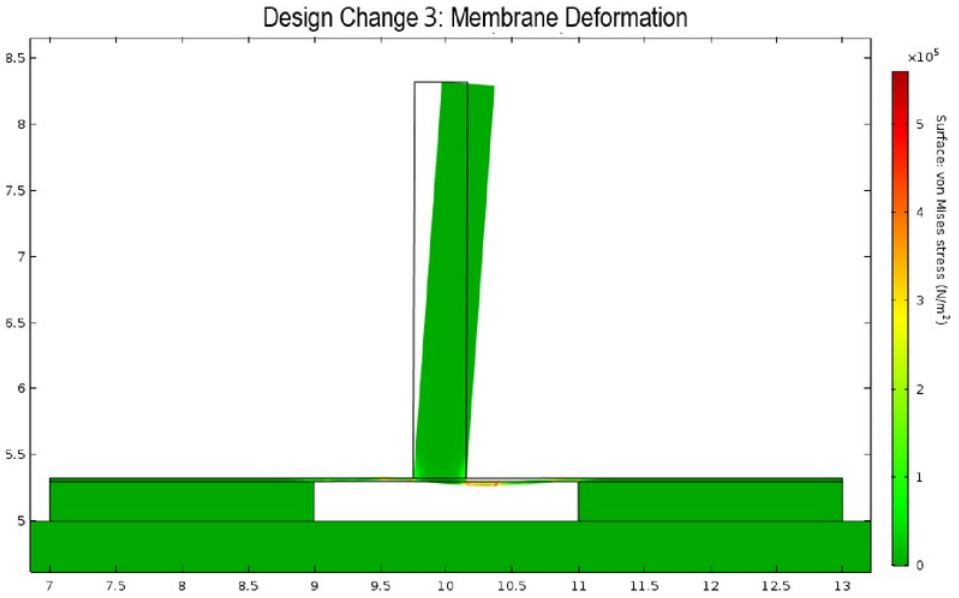

Figure 4.18: Design Change III - Membrane Deformation

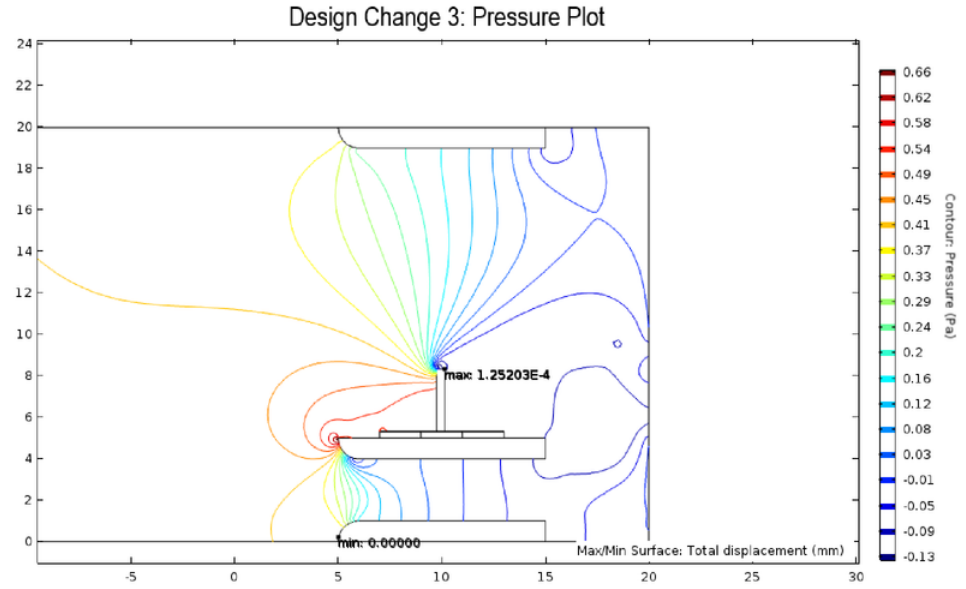

Figure 4.19: Design Change III - Pressure

4.3.3 Evaluation

Based on the FEA completed in COMSOL we can see that by implementing a filleted edge at the edges facing the fluid flow, we can see that the boundary layers that form at the edges of the ring portion of the housing are reduced as well as at location on the underside of the crossbeam holding the sensor in position. Furthermore, we can see by comparing the pressure plot with the pressure plot from Design Change I that the pressure drops are less significant in the curved edge model. We can see the large pressure drop at the back of the beam and behind the standing structure is less also at -0.09 Pa compared to -0.15 Pa and -0.19Pa when comparing the same pressure contour size. Due to this decrease in negative pressure occurring in the simulation, we can also see there is a reduced backflow occurring in the flow and stress model. This reduced backflow could be the root cause to the larger bending on the standing structure as there is less air flow (produced by the backflow) impacting on the standing structure.

Again, it is important to note that a 2D simulation may not be truly representative of real world experimentation since it cannot distinguish the large spatial gaps in the z-plane between the ring housing and sides of the standing structure, which would likely minimise completely this backflow occurrence.

Due to limitations in resolution of the 3D printers available, a design with 1cm filleted edges on objects with 1mm thickness is difficult to create due to the level of detail required in the printing process.

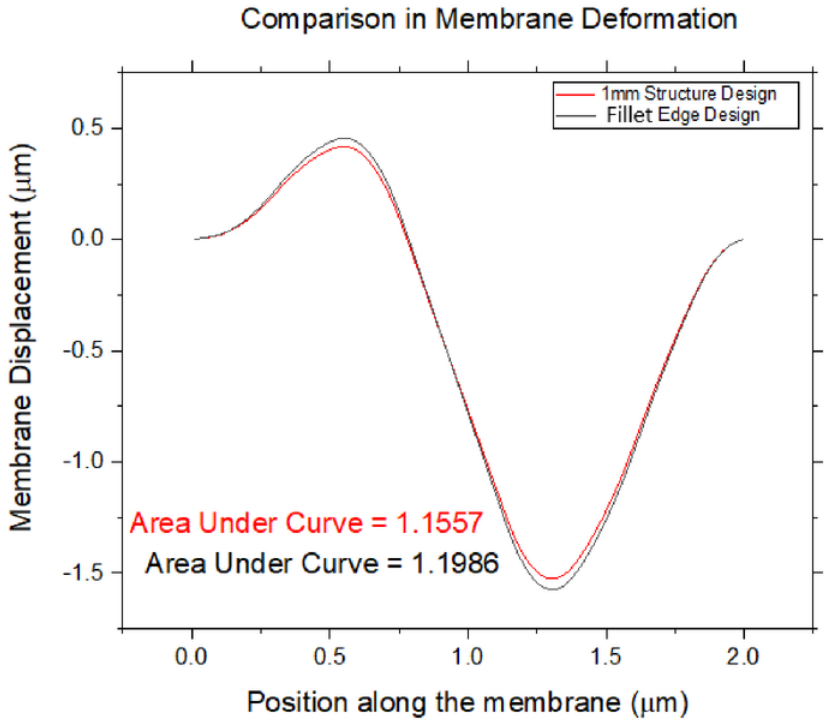

Figure 4.20: Membrane Displacement: Design Change II Vs. Design Change III

When comparing the total area displaced on the membrane there is less than a 4% difference in the total area displacement between the two designs. Since there is not a large enough difference in membrane deflection and due to 3D printing resolution issues, there if not a significant enough advantage to sourcing a higher quality printer (which may impose further time constraints on the project) to print the design and implement.

The next design consideration that will be studied is the effects of varying the height of the beam; by varying the height of the beam, the standing structure may be affected due to boundary layers created from the tube or ring portion of the housing, furthermore by changing the height of the beam, the air that passes through the top portion of the housing (where the standing structure is location) may change in velocity or pressure due to principles of conservation of energy in changing pipe diameters and Y junction type pipe splitting. These effects will be investigated in the next FEA.

4.4 Design Change IV - Height Variation

4.4.1 Design

In this section of the project, the height of the beam and by association, the position of the LCP flow sensor with standing structure and its interaction with the fluid flow will be investigated. Through the effects of the conservation of energy and Bernoullis principles applied to varying the diameter of a pipe. As the (assumed) laminar air flow reaches the housing, the cross-sectional area of the opening decreases from

$$A_1 = \pi \left(\frac{d}{2}\right)^2 \tag{4.3}$$
$$= 0.000314m^2\,(314mm^2)$$

to a cross-sectional area of

$$A_2 = \pi \left(\frac{d}{2}\right)^2 \tag{4.4}$$
$$= 0.000227m^2\,(227mm^2)$$

where d = 0.017m

This calculation accounts for the for the 1mm edge at the top and bottom and the 1mm beam in a 2D simulation and not the z-plane in 3D.

$$A_1 v_1 = A_2 v_2 \tag{4.5}$$
$$0.000314 \times 5.31 = 0.000227 v_2$$
$$v_2 = 7.345 ms^{-1}$$

The idea behind this investigation is to see if the positioning of the sensor relative to the fluid flow profile created in the tube has a significant impact on the deflection of the membrane. In theory the boundary flow at the walls should create a parabolic velocity flow profile with the fastest flow velocities originating closest to the centre axis of the pipe (ie. In the middle of the pipe) as shown in Figure 4.21.

In order to maximise the membrane deformation, maximum drag must be produced along the standing structure which will translate to maximum moment at the base of the standing structure, similarly to reaction forces demonstrated with a cantilevered beam with some load at the end. In theory the largest bending moment on the beam will occur the closer the highest flow velocity in the velocity flow profile interacts with the top or furthest end of the standing structure away from the membrane. This moment about the end fixed to the membrane will cause a buckling effect on the membrane, this results in deformation and displacement along the membrane resulting in a change in resistance.

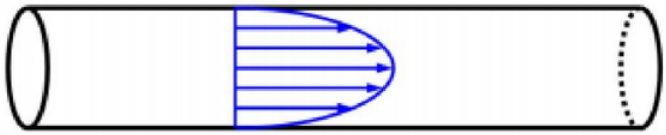

Figure 4.21: Fluid Velocity Profile

The simulations designed will vary the height of the beam and sensor to see if there is any significant change in membrane displacement by varying heights.

4.4.2 Simulation

Within this COMSOL simulation a parametric sweet was done with the y-coordinates of the geometries which was then re-meshed though each iteration and subjected to the same 100LPM inlet flow with 0Pa outlet pressure to allow the simulation to remain consistent.

The main areas of investigation were the fluid-structure interactions occurring at:

1. The original crossbeam height of the system - noted as **Standing Structure at 5mm** in Figure 4.22.
2. The height at which the middle of the standing structure is located at the midpoint of the tube, where the velocity flow profile shows the highest fluid flow velocity - noted as **Standing Structure at 8.5mm** in Figure 4.23.
3. The height at which the middle of the crossbeam is located across the central axis of the pipe - noted as **Standing Structure at 10.5mm** in Figure 4.24
4. Any positions higher that reduce the gap between the top of the standing structure and the upper portion of the housing to observe if the boundary layer between the fluid flow and wall interact with the top of the standing structure these positions are noted as **Standing Structure at 12mm** in Figure 4.25 and **Standing Structure at 13mm** in Figure 4.26.

The membrane displacement graphs are then compared and plotted in origin and the integral of each was taken to determine the total absolute area of displacement across the membrane, shown in Figure 4.27.

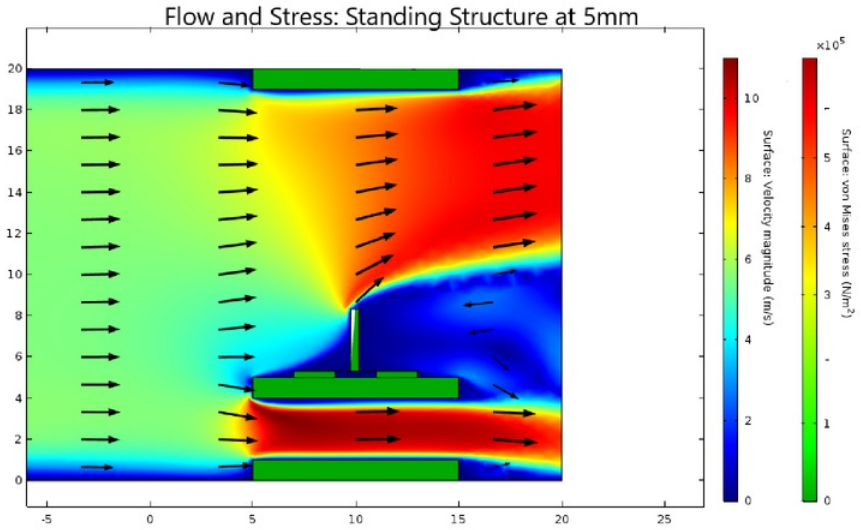

Figure 4.22: Standing Structure at 5mm

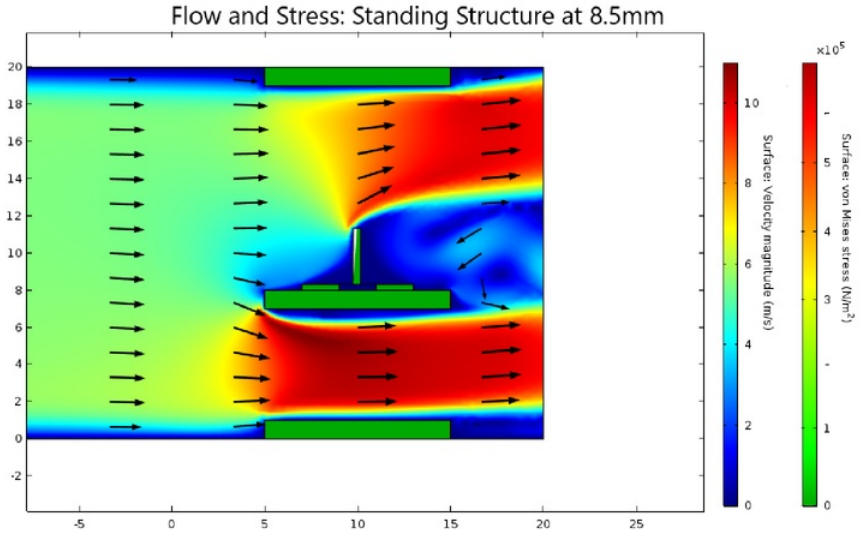

Figure 4.23: Standing Structure at 8.5mm

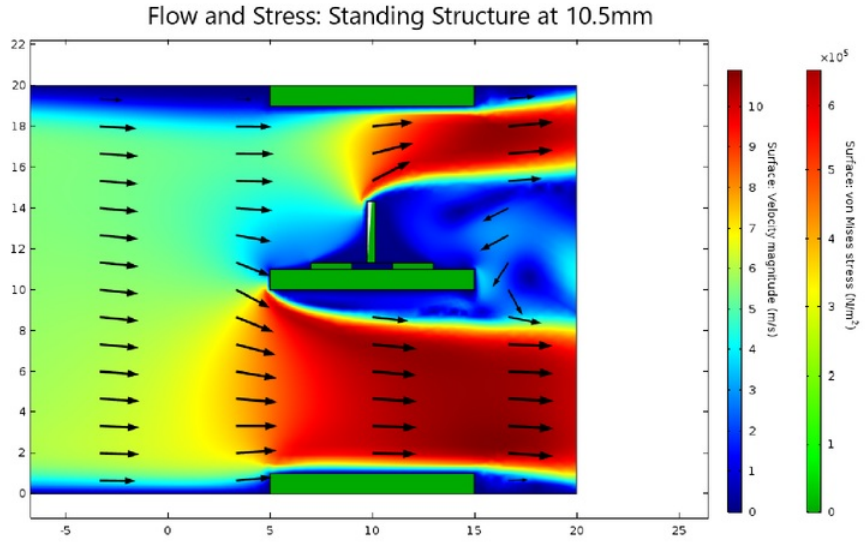

Figure 4.24: Standing Structure at 10.5mm

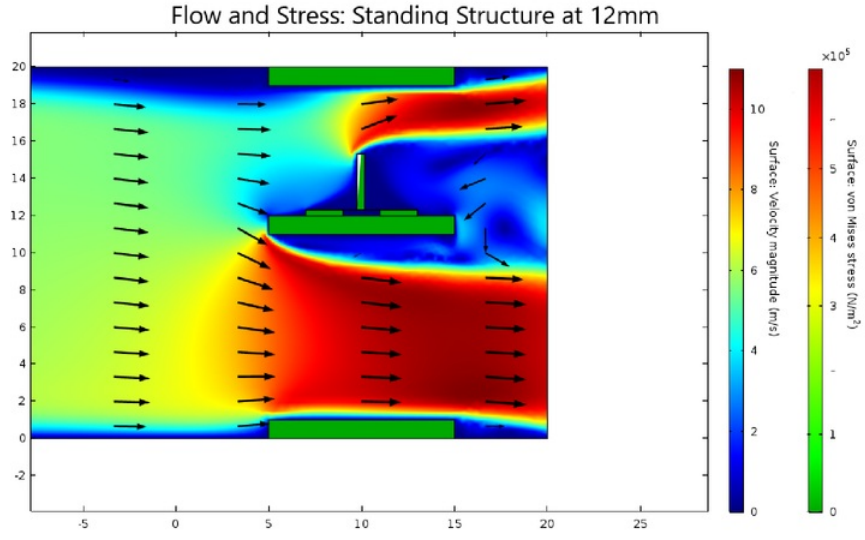

Figure 4.25: Standing Structure at 12mm

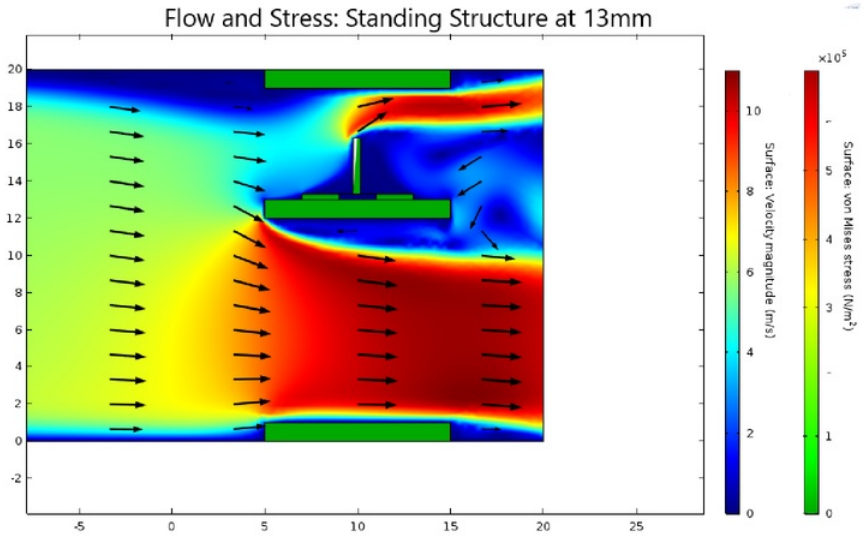

Figure 4.26: Standing Structure at 13mm

4.4.3 Evaluation

We can see from Figure 4.27 that configuration that allows the most displacement across the membrane is the configuration "'Standing Structure at 12mm"'; the next best membrane displacement simulation is configuration labelled "'Standing Structure at 10.5mm"' which is the design that with the cross-beam through the centre axis of the pipes diameter. We can also see from the data that as the standing structure is located higher than 12mm in the y-axis (relative to the tube) we can see that performance decreases as the standing structure is affected by the boundary layers forming from the ring portion of the housing, shown as it is comparable to the "'Standing Structure at 10.5mm"' simulation.

When comparing the two best performing design simulations against the height used in the previous design changes, we can see that there is a 7.8% increase in membrane displacement by positioning the cross-beam in the middle of the tube (where the standing structure is located at 10.5mm) and a 9.7% increase in membrane displacement if the standing structure is moved upwards towards the wall at a position of 12mm.

When comparing these two best performing designs against our criteria we see that in order to place the sensor in the correct position with the standing structure located at 12mm, there are inherent difficulties in the manufacturing process such as the ability to attach the standing structure with only 4mm of clearance between the sensor and the ring portion of the housing, compared so a significantly easier means of installing the sensor in the configuration where the beam is located at the centre.

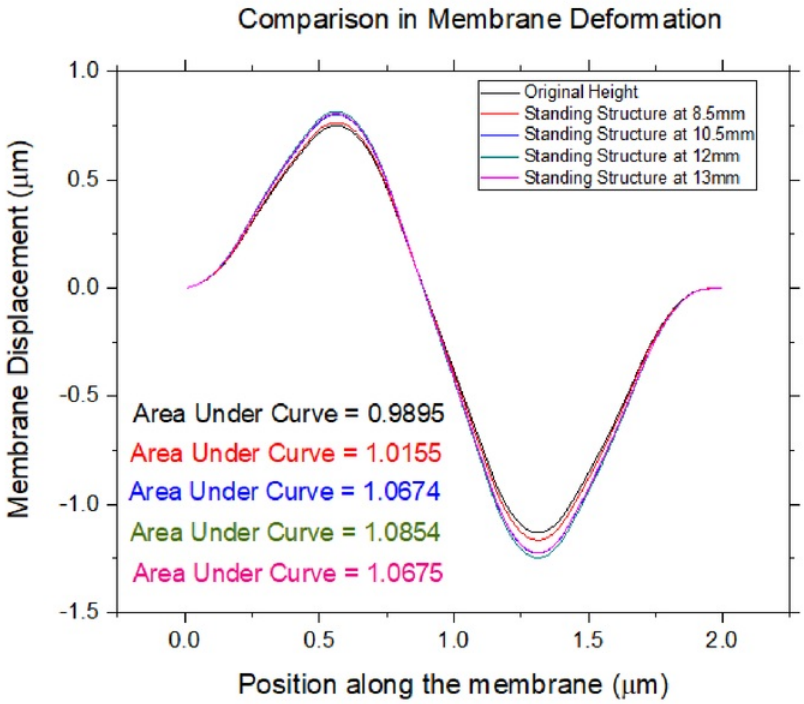

Figure 4.27: Flow Sensor Displacement at Varying Heights

When comparing the difficulties of manufacturing and packaging against a 2% increase in system performance, there is not enough of a improvement in the system to warrant the "'best"' performing packaging design in terms of membrane displacement and therefore the design labelled as "'Standing Structure at 10.5mm"' was selected to be the optimal height for the packaging design.

It is also important to note the limitations of a 2D simulation and its translation to a 3D model as shown where values skewed due to the large changes boundary layer forming on the underside of the cross beam resulting from the simulation only being able to identify the standing structure as a wall that the air flow is only able to pass over the top rather than on each side (in the third dimension), which explains the increase in flow velocity to $10ms^{-1}$, shown if we continue the calculation previously computed to attain the increase flow velocity of $7.345ms^{-1}$ at the opening portion of the housing:

Using the velocity found previously;

$$V_2 = 7.345ms^{-1}$$

$$Q = Av \tag{4.6}$$

$$Q = \pi \left(\frac{d}{2}\right)^2 v \tag{4.7}$$

$$\mathrm{Q} = 0.000227 \times 7.345$$

$$\mathrm{Q} = 0.001667$$

$$0.001667 = \pi \left(\tfrac{d}{2}\right)^2 v_3$$

where d = 0.014 which is the total cross-sectional area available

$$v_3 = 10.83ms^{-1}$$

The simulation now recalculates the total cross-sectional area decreasing due to the "'wall"' that is the standing structure, this increase in flow velocity may also increase the membrane displacement plots as the simulation now sees a higher fluid flow velocity interacting with the standing structure.

4.4.4 Summary for Changes Implemented in Final Design

In the first design change it has been shown that the LCP pressure sensor will be altered and changed into an LCP flow sensor through the use of a standing structure to influence the displacement across the membrane. Considering this significant design change, it has been noted and demonstrated through simulation that the displacement will be caused by buckling resulting from force generated about the centre of moment located at the connection point of the standing structure and the LCP membrane. This significant design change is responsible for the sensors change from a pressure sensor which utilised uniform pressure across the entire membrane to a flow sensor which uses a standing structure to create drag, causing asymmetrical displacement across the membrane.

It has also been demonstrated that by thinning the housing for the sensor also impacts the laminar flow, by increasing the cross sectional area available to fluid flow, the velocity of air decreases when compared to the original thickness of the housing, this gives the advantage of allowing the system to respond at a value closer to the actual flow being generated by the pump however this decrease in flow velocity also reduces the ability for the system to detect lower flow velocities that are generated by the pump. Considering the limitations of the 3D printers available at the time of writing and the structural impacts of the housing in terms of usability and the significance of the design change; It was concluded that there is no real benefit added by attempting a housing design with thinner structures.

This same conclusion was also made for the design change with filleted edges at locations that first interact with air flow. By filleting the edges, the pressure gradients changes throughout the system are reduced and the negative pressure and backflow generated behind the crossbeam and standing structure are also reduced, however due to the simulations inability to model successfully in 3D it is, with relative probability that the backflow is insignificant when evaluating the air flow that passes on each side of the standing structure as well as the 3D printers ability to print with high resolution, the filleted edges required.

Finally, a study on varying the height of the location of the sensor was investigated to identify the locations which influenced membrane displacement the most. When considering the difficulties in packaging the sensor into the housing with only a potential 2% increase in membrane displacement, the second-best option was chosen to be the final height of the sensor, which gives a 7.8% increase in total area displacement across the membrane compared with the original height used when converting the pressure sensor to the flow sensor and a 14% increase in membrane displacement compared to original pressure sensor set up.

Figure 4.28 below shows the total area displacement between the first design with the LCP sensor acting as a pressure sensor and the final design where the LCP sensor acts as a flow sensor with a standing structure, we can see that the area of displacement has increased by 14% which should give a better system response to fluid flow velocities.

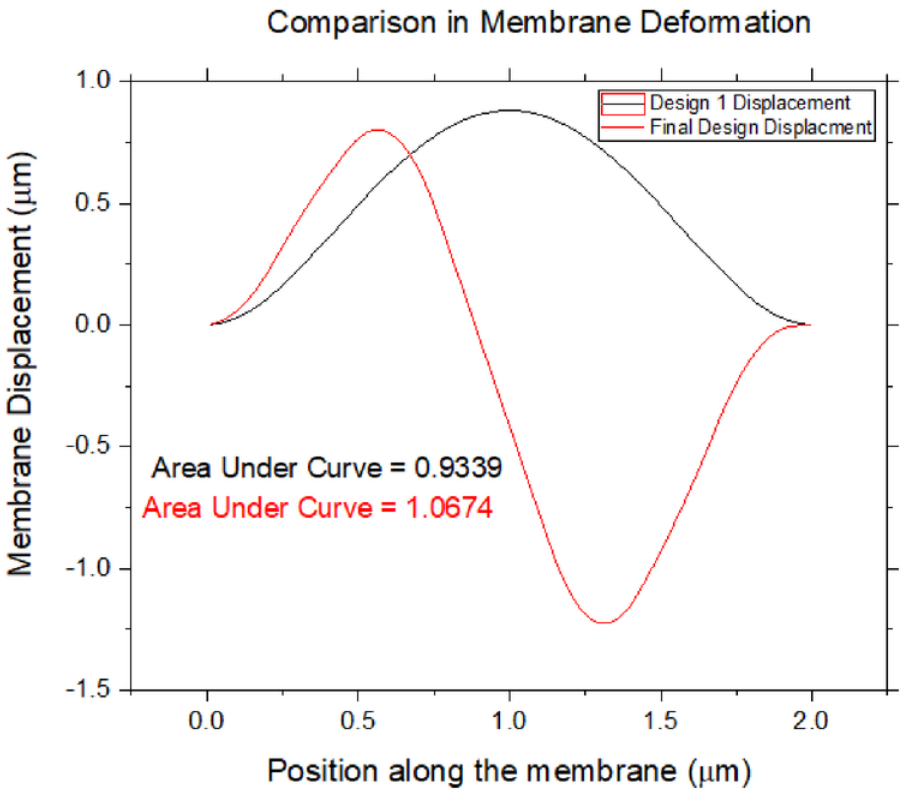

Figure 4.28: Membrane Displacement: Pressure Sensor Vs. Flow Sensor

Chapter 5

LCP MEMS Flow Sensor

5.1 Packaging Design

The final design of the housing for the LCP sensor was designed based on the same considerations as the first design:

1. Allow the LCP sensor to be subjected to maximum membrane displacement - to create a design configuration that will maximise membrane displacement
2. The ability to securely hold the sensor inside the tube without it falling out.
3. Ease of assembly/manufacturing.

The design changes from the LCP Pressure sensor to LCP Flow sensor have been outlined in the final section of the previous chapter see "'Summary for Changes Implemented in Final Design"'

The final SolidWorks models are shown in Figures 5.1 and 5.2

Like the first design, the housing in this model is created with an outer ring housing that is equal to the 20mm diameter of the pipe used on the airflow generator to hold the housing in place.

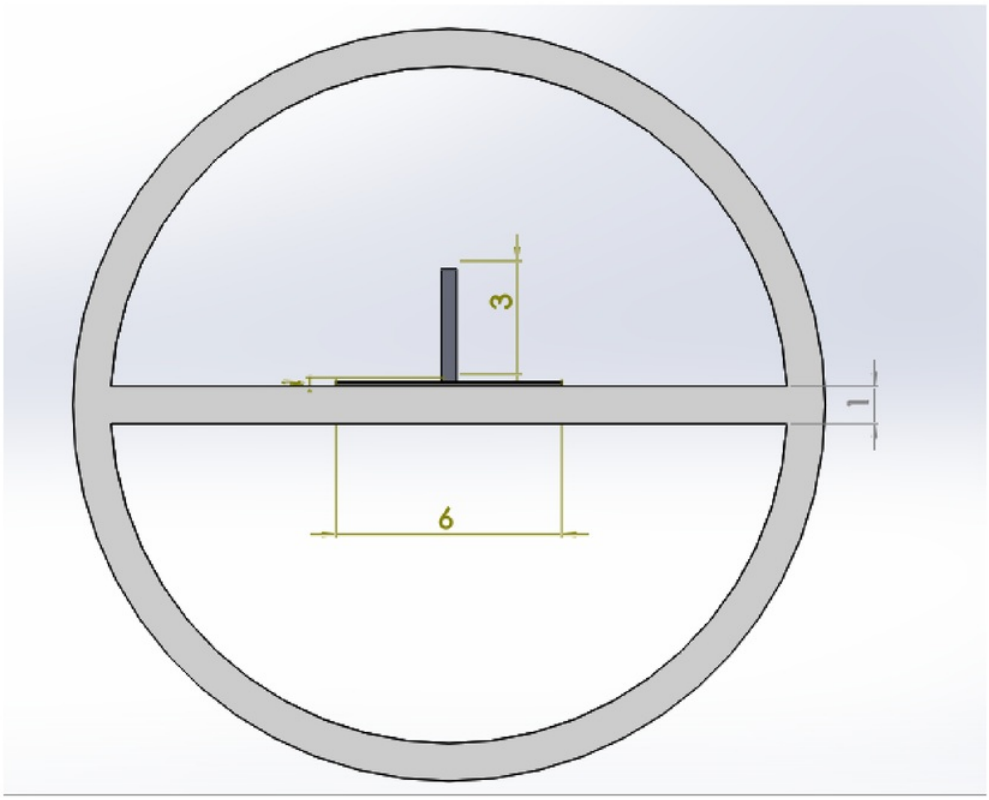

Figure 5.1: Flow Sensor - Front View

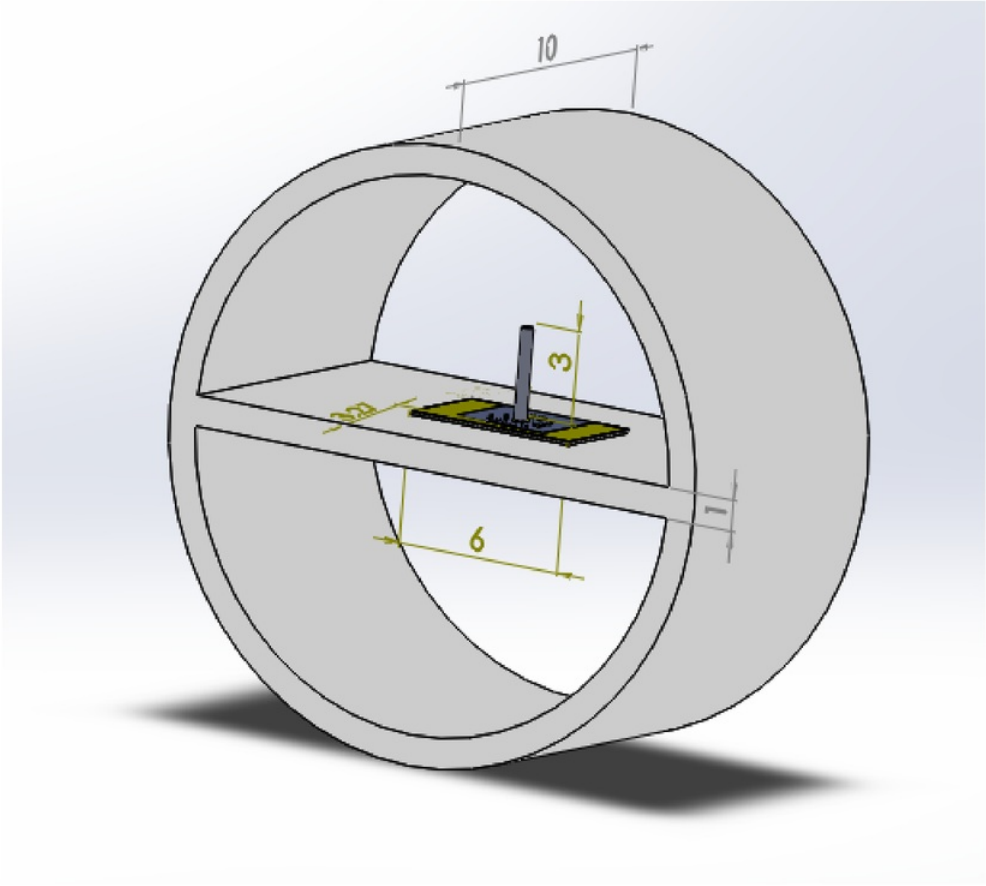

Figure 5.2: Flow Sensor - Isometric View

5.2 Simulation

Simulation again was performed using COMSOL Multiphysics, the images below are the fluid flow with inlet set to 100LPM or $5.31ms^{-1}$ and outlet pressure of 0Pa

A parametric sweep from 10LPM to 200LPM was also performed, there was however issues when computing 160LPM and therefore was omitted from the plot.

In the membrane deformation in Figure 5.5 has been scaled by a factor of 20 to demonstrate the fluid-solid interaction better visually.

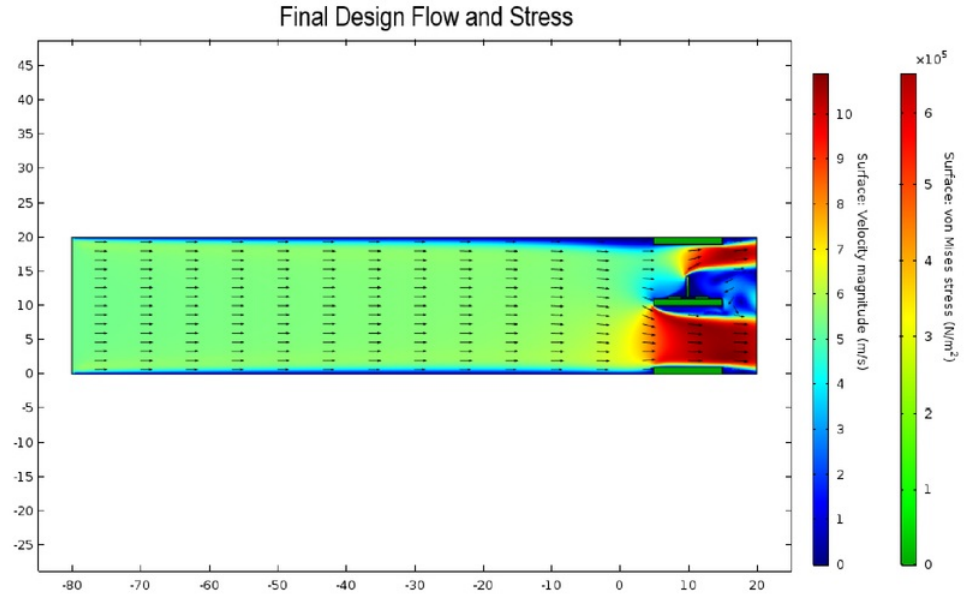

Figure 5.3: Flow and Stress: Flow Sensor

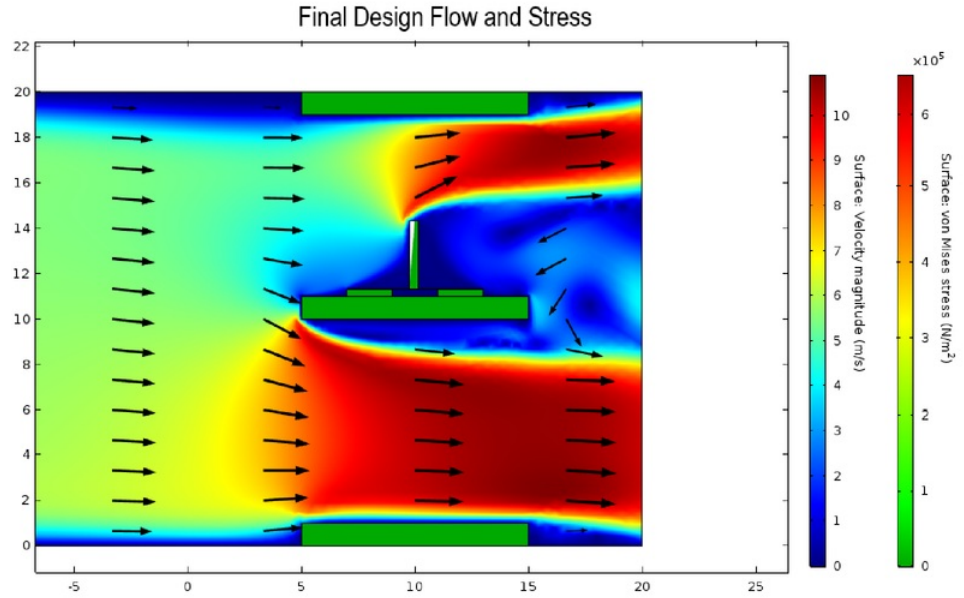

Figure 5.4: Flow and Stress: Flow Sensor

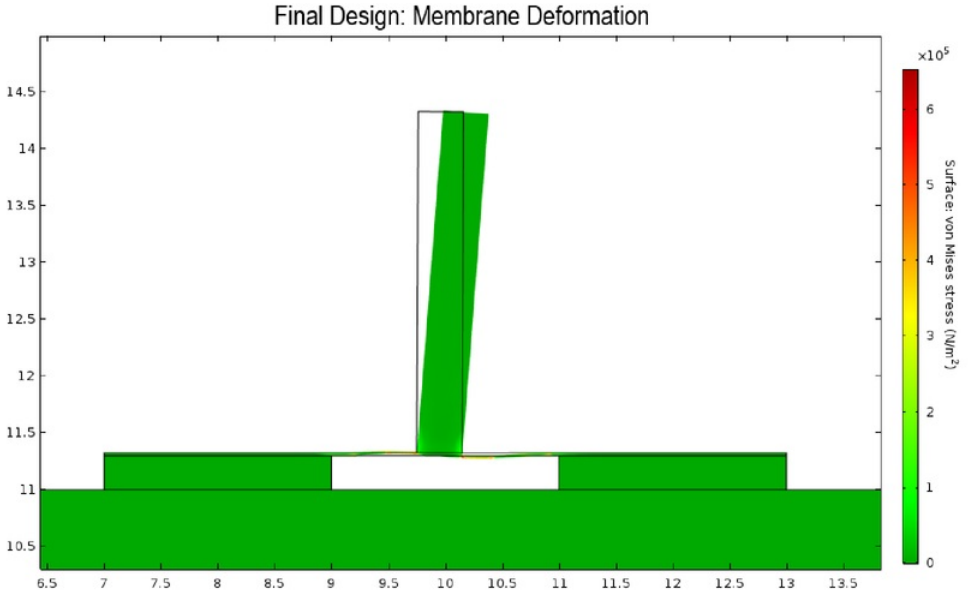

Figure 5.5: Membrane Deformation: Flow Sensor

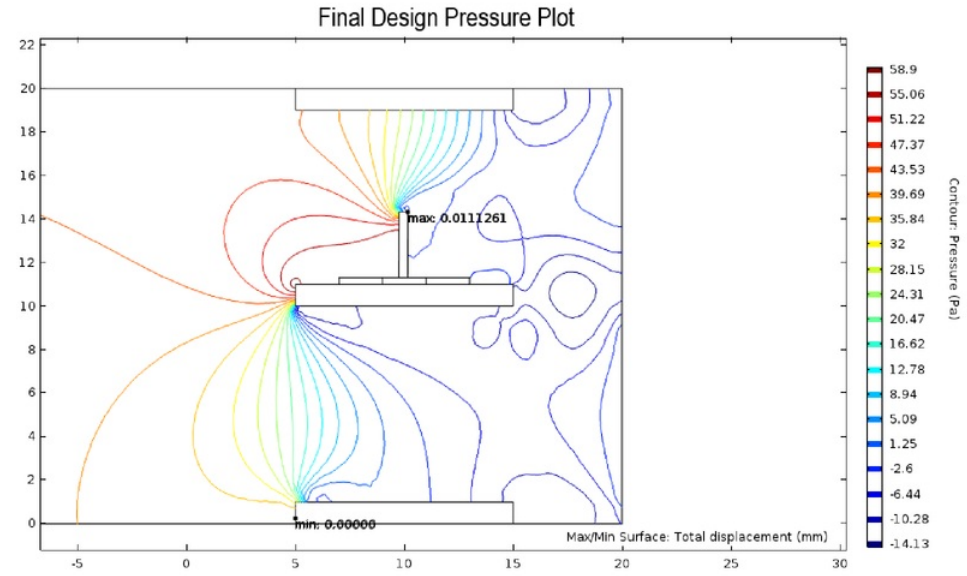

Figure 5.6: Pressure: Flow Sensor

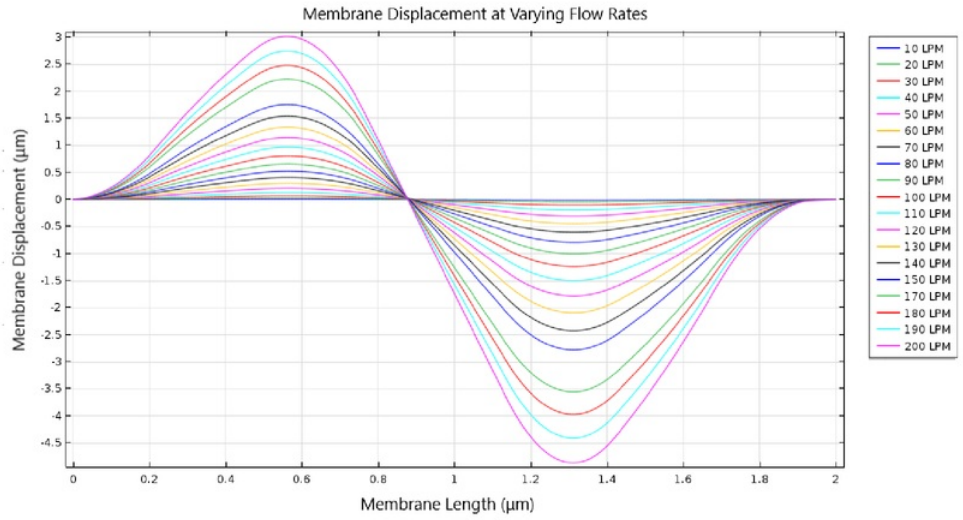

Figure 5.7: Flow Sensor Membrane Displacement at Varying Flow Rates

5.3 Construction and Assembly

The packaging design was printed again with a 3D printer using polylactic acid (PLA) the same material that was first used in the housing packaging.

Once 3D printing was completed, the LCP sensor was glued to the cross beam using EPO-TEK H70E epoxy, with the gold strain gauges facing upwards, parallel to the air flow. The epoxy required was applied using the tip of a hypodermic needle, the epoxy was evenly distributed, and the sensor was placed on the wall with tweezers with the assistance of a microscope. This was then placed into an oven at $100°C$ for 40 minutes to dry.

Thin wires were then stripped using a soldering iron to improve conductivity and glued using Polytec EC 101, a two-part conductive adhesive to the gold piezoresistive contact pads on the sides of the LCP sensor. The difficulties in construction occurred when testing the two-part conductive adhesive as the ratios of the two parts needed to be exact, this mix had to be dried in an oven and tested for conductivity before adhering the wires on a separate microscope slide used to mix the two parts.

Once the correct mixture was created the adhesive has to be applied with the tip of a hypodermic needle under a microscope. Once this was adhered correctly and the wires in place, the housing with wires connected were placed in an oven at $100°C$ for approximately 1 hour to allow the epoxy holding the sensor to the crossbeam as well as the conductive adhesive to dry. These wires were then used to connect to the external circuitry which is detailed in the testing section of this project.

A note is required to be made at this stage that there were difficulties in the manufacturing process in terms of ensuring the standing structure was directly straight as well as being correctly adhered to the membrane, the results from testing can therefore be improved if the use of packaging tools and equipment are used to remove the manufacturing issues created by human errors, these issues will be detailed further in the next chapter.

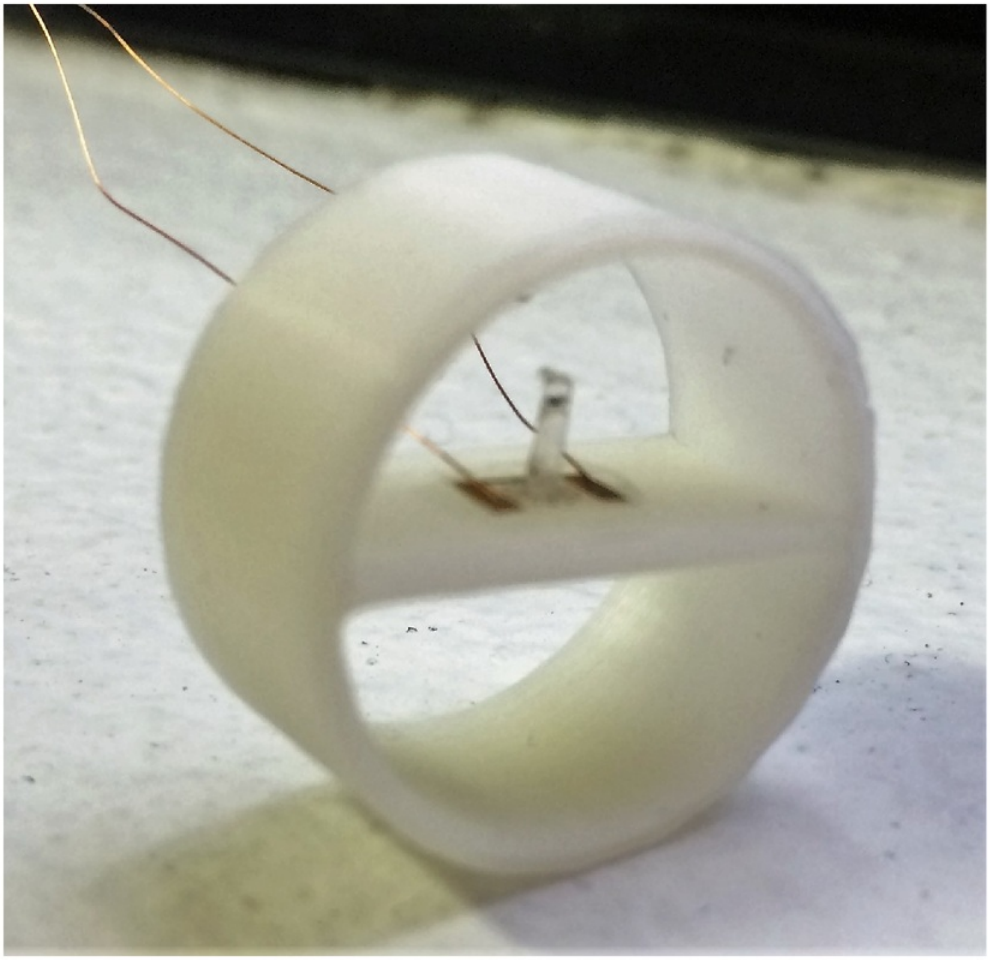

Figure 5.8: LCP Flow Sensor Assembled

5.4 Testing

In the testing phase, the purpose was to conduct experimental work to identify the LCP response to a variety of airflow rates produced by the air flow generator and to detail the experimental results derived from experimental work with LCP MEMS flow sensor. A comparison between key parameters of a commercially available flow sensor against the LCP piezoresistive flow sensor was also investigated. Testing is also used to compare the results of the LCP flow sensor against the LCP pressure sensor.

Key parameters that are outlined in this section include system response from flows of 8LPM to 200LPM as well as resolution graphs of flow rates of 8 - 10LPM, 47 - 50LPM, 97 - 100LPM, 147 - 150LPM and 197 - 200LPM, accuracy of peak to peak voltages on flow rates from 10 - 200 LPM, and an overview of response time on flow rates of 10, 50, 100, 150 and 200LPM for both sensors.

5.5 Experimentation

The experiments tested, both the LCP MEMS pressure sensor and the commercial sensor simultaneously. The LCP sensor, located at the end of the flexible tube attached to the air flow generator, was connected to an external Wheatstone bridge biased with 5V and connected to an amplifier and filter with a gain of 50 and a 3Hz low pass filter. The output signal from the amplifier/low pass filter system as well as the output signal directly from the commercial sensor were then used as inputs into a National Instruments data acquisition (NI-DAQ) system cDAQ 9174 series.

Data was then captured and recorded in National Instruments Signal Express 2015 software, where 1000 samples were taken at a rate of 2KHz. All experiments were conducted using the air flow generators default period of 3000ms and set low point of 0 LPM. A basic set up diagram is shown below.

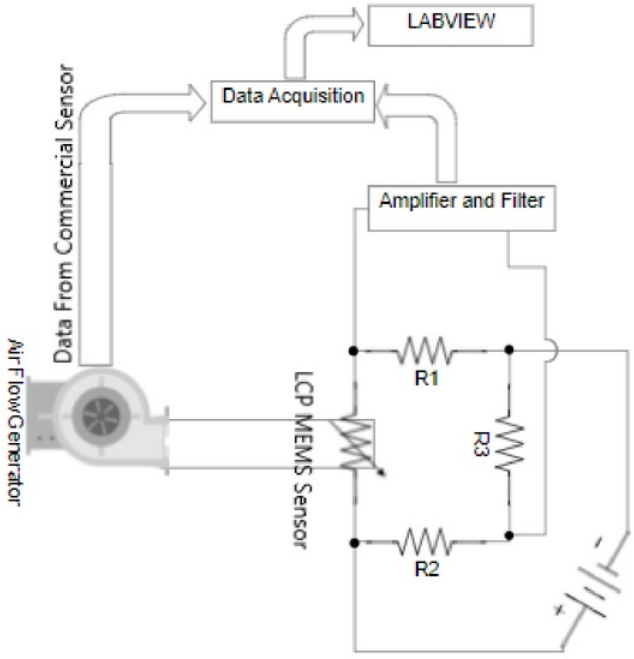

Figure 5.9: Testing Setup Diagram

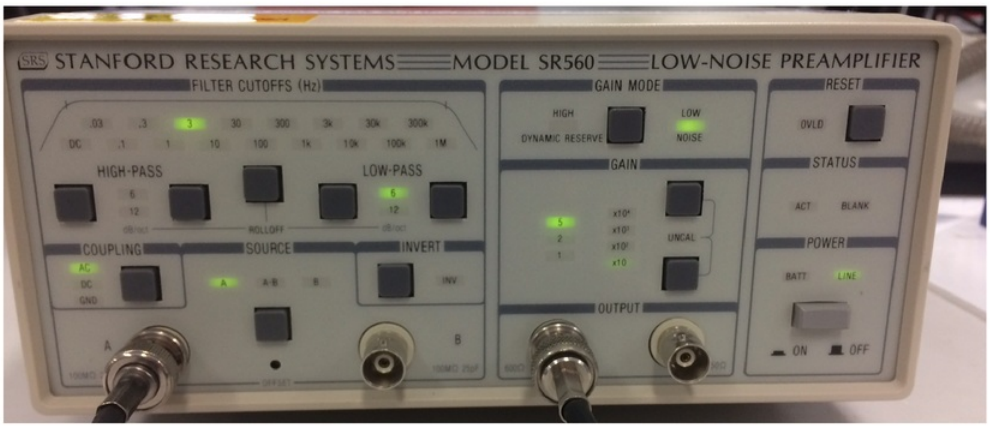

Figure 5.10: Stanford Research Systems Low-Noise Preamplifier

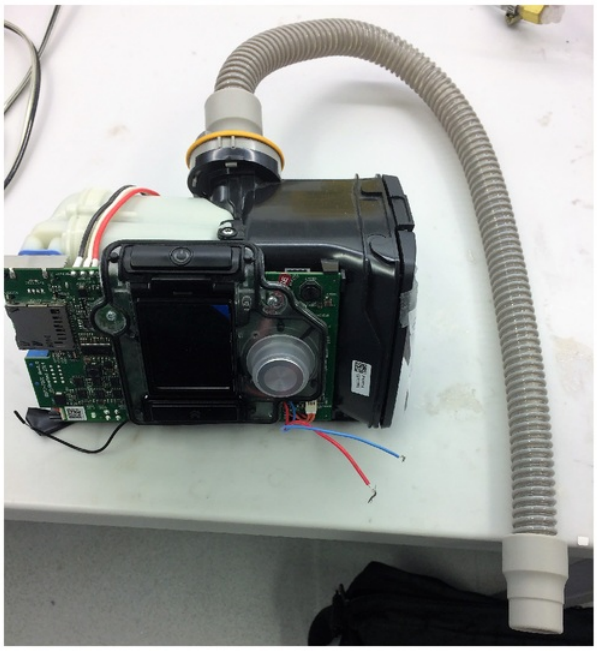

Figure 5.11: ResMed Air10 CPAP

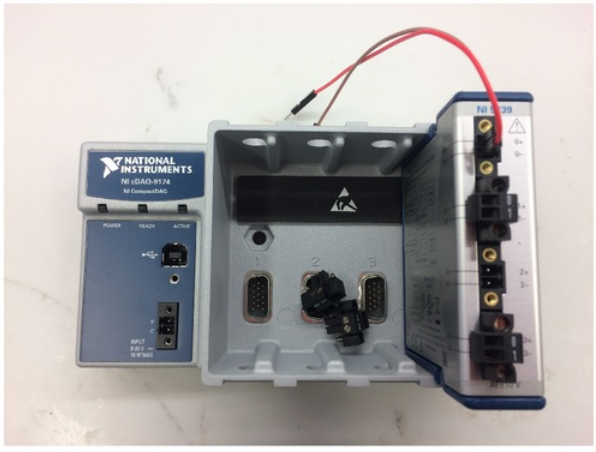

Figure 5.12: NI-DAQ

5.6 Results

5.6.1 Flow Ranges and Calibration Plot

For flow ranges, the system was set up as outlined and recorded using National Instruments Signal Express 2015, the data was then exported to excel and plotted using Matlab.

Figure 5.12 and Figure 5.13 show and overview of the results from the experiments performed and recorded from both sensors outputs ranging from 10 to 100LPM.

Figure 5.14 shows the calibration plot of the LCP sensor; the graphed points show the average peak to peak voltages gathered from 4 to 5 periods of air flow, with error bars from Table 3.1 giving the standard deviation of these results.

When fitting a linear line of best fit we can see that for voltage increase by 0.0016V for every 1LPM increase in flow rate.

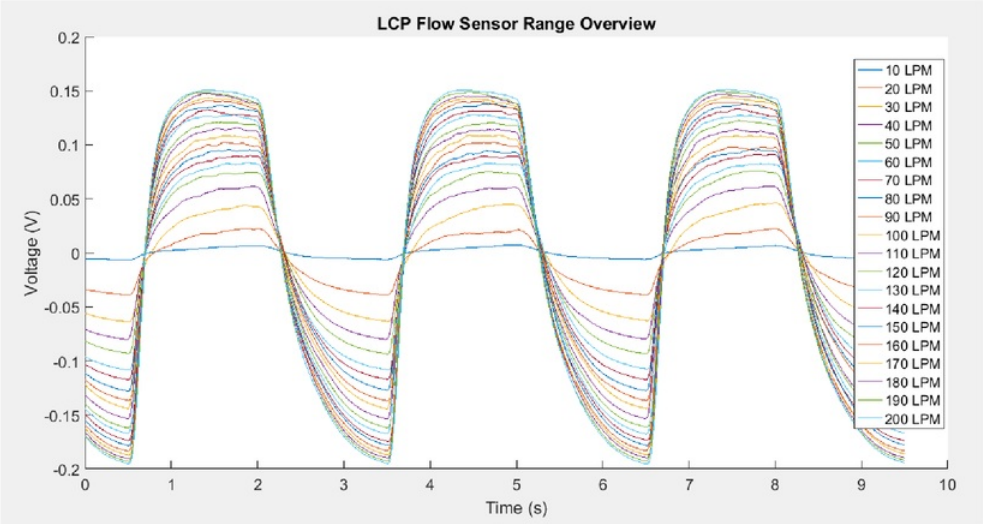

Figure 5.13: Flow Sensor Overview

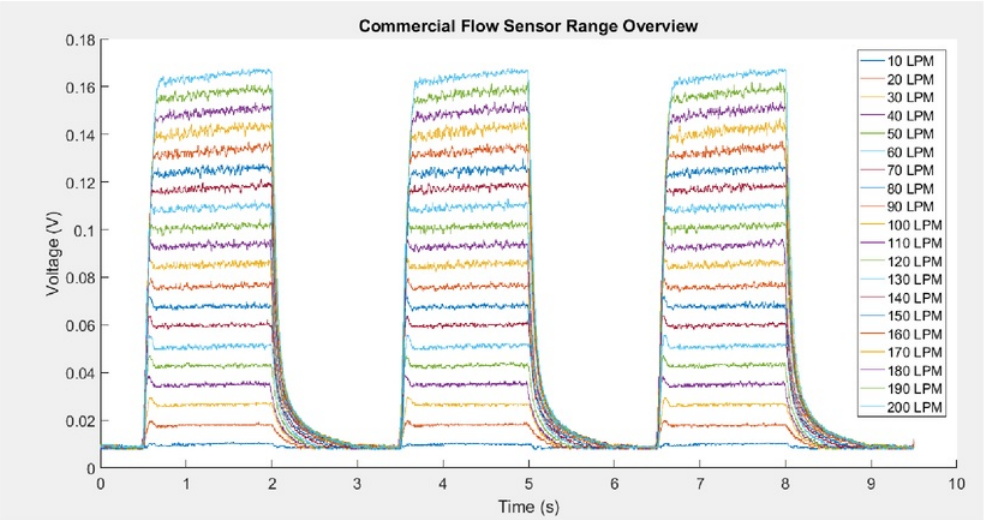

Figure 5.14: Commercial Flow Sensor Overview

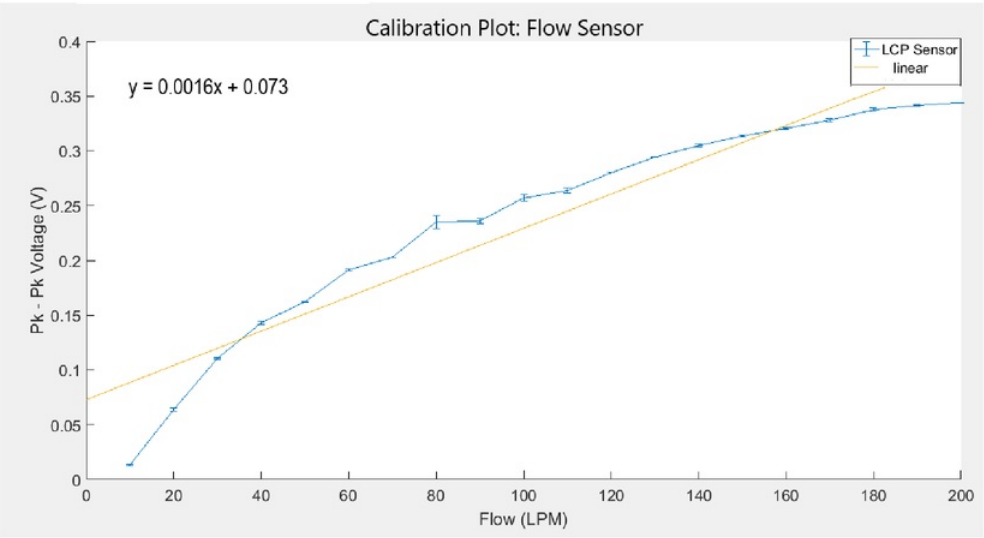

Figure 5.15: Flow Sensor Calibration Plot

5.6.2 Commercial and LCP Flow Sensor Comparison

Figures 5.15 - 5.25 give a direct comparison between the commercial sensor and the LCP sensor at various flow rates.

Similarly to the last experiment, there is an observed delay between the rise time of the commercial sensor and the LCP sensor is due to its positioning of the sensor in the air flow generator system. The commercial sensor is located at the initial flow velocity location, whereas the LCP is located at the end of the pipe and therefore the last location in the system and therefore a delay to respond to flow velocity.

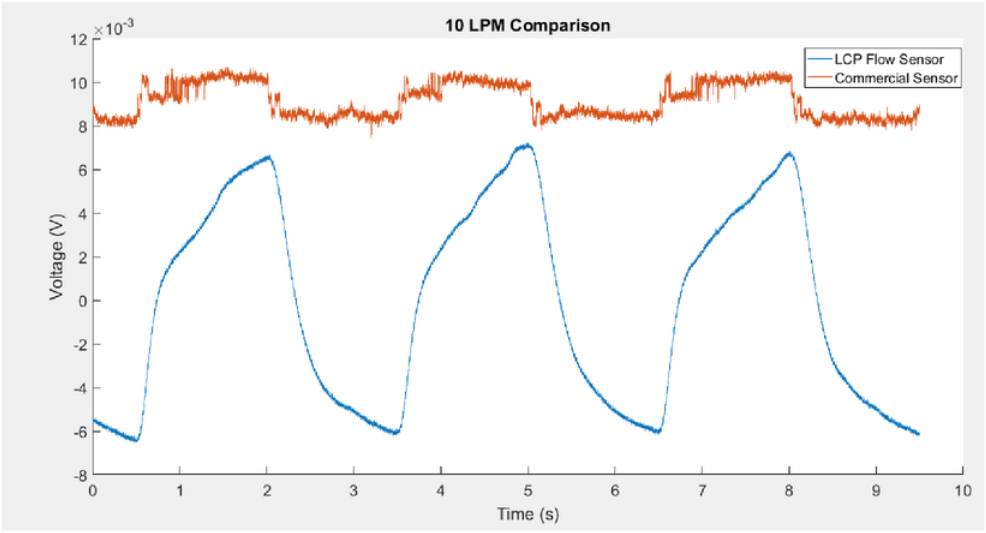

Figure 5.16: Comparison Plot 10LPM

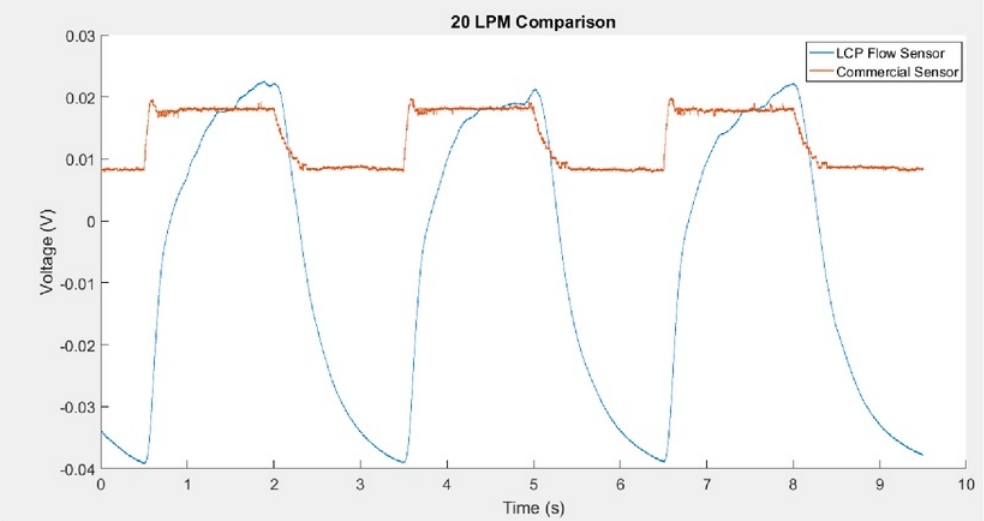

Figure 5.17: Comparison Plot 20LPM

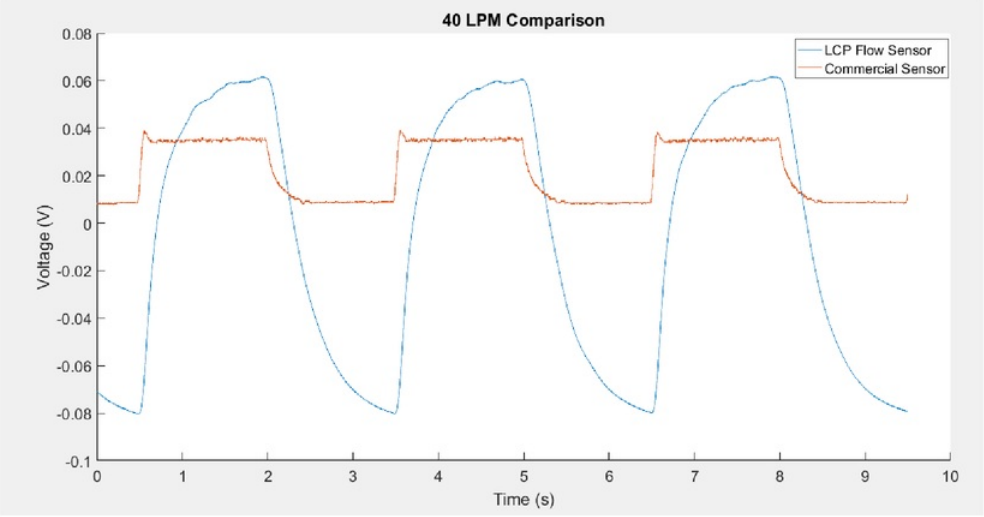

Figure 5.18: Comparison Plot 40LPM

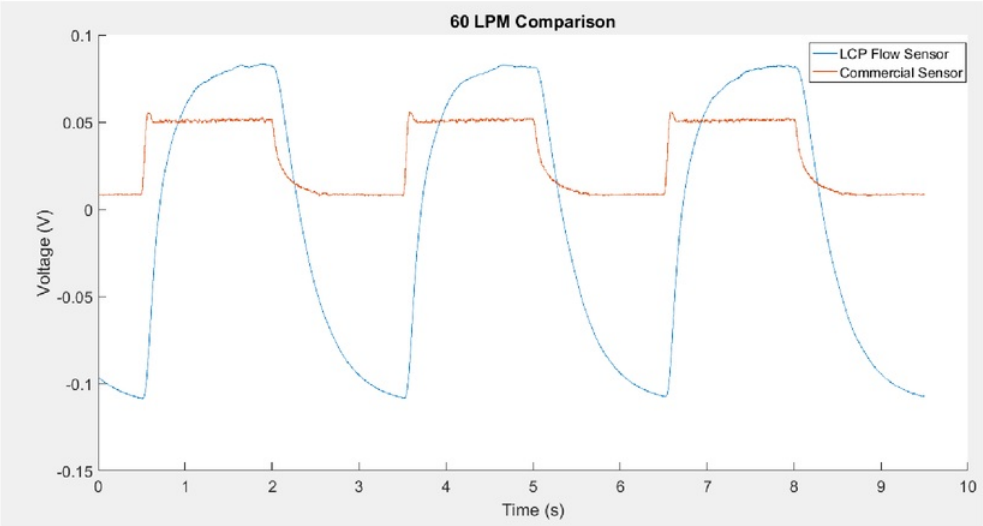

Figure 5.19: Comparison Plot 60

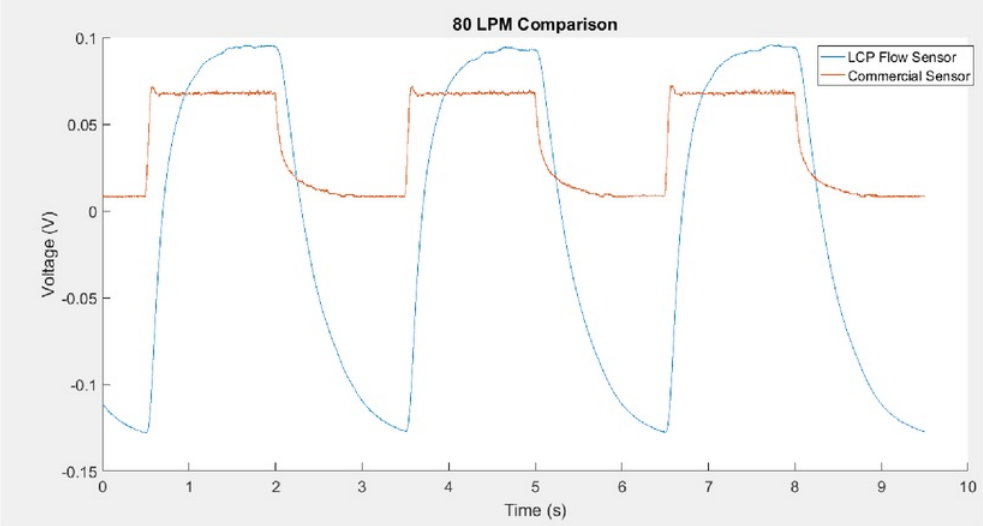

Figure 5.20: Comparison Plot 80LPM

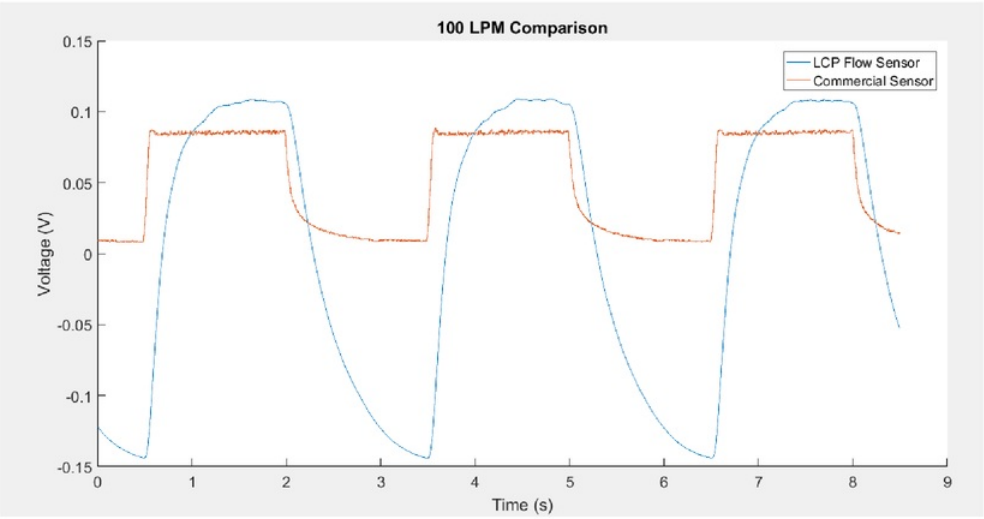

Figure 5.21: Comparison Plot 100LPM

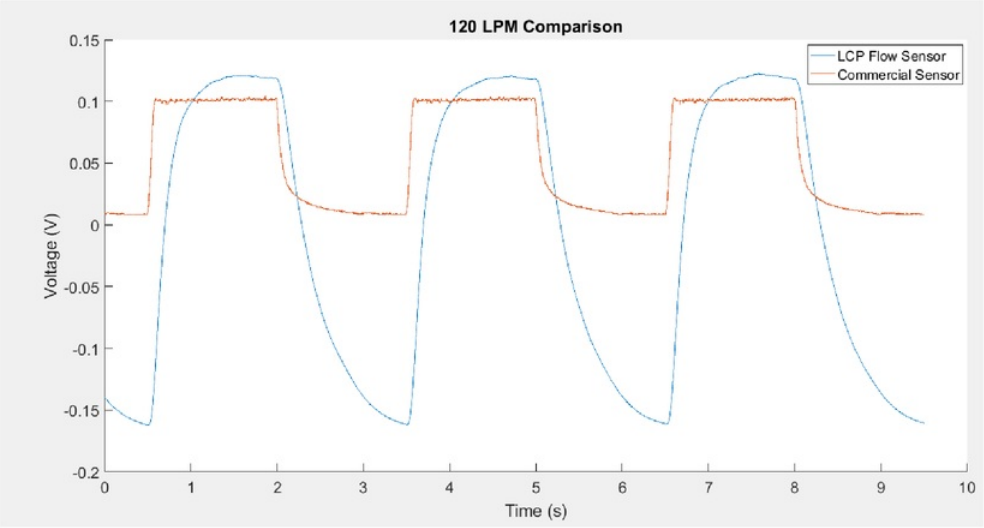

Figure 5.22: Comparison Plot 120LPM

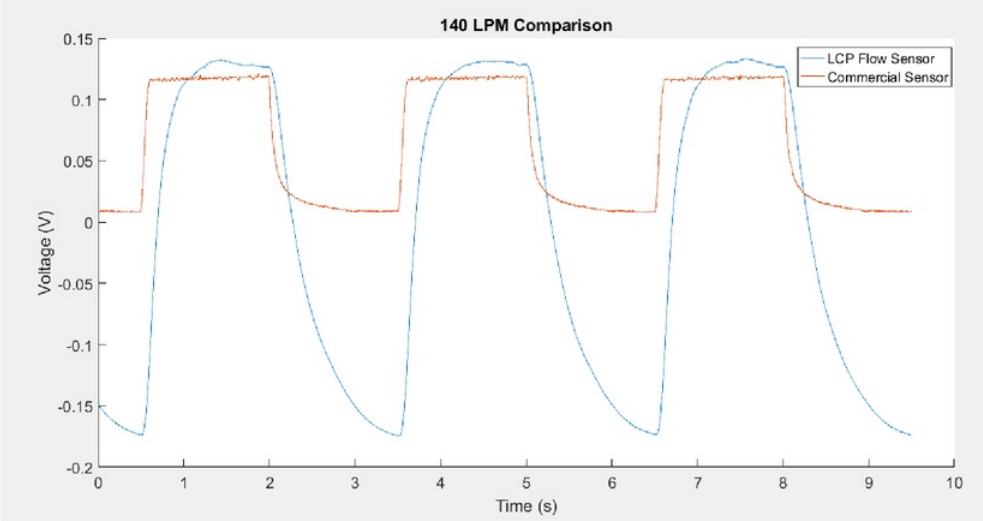

Figure 5.23: Comparison Plot 140LPM

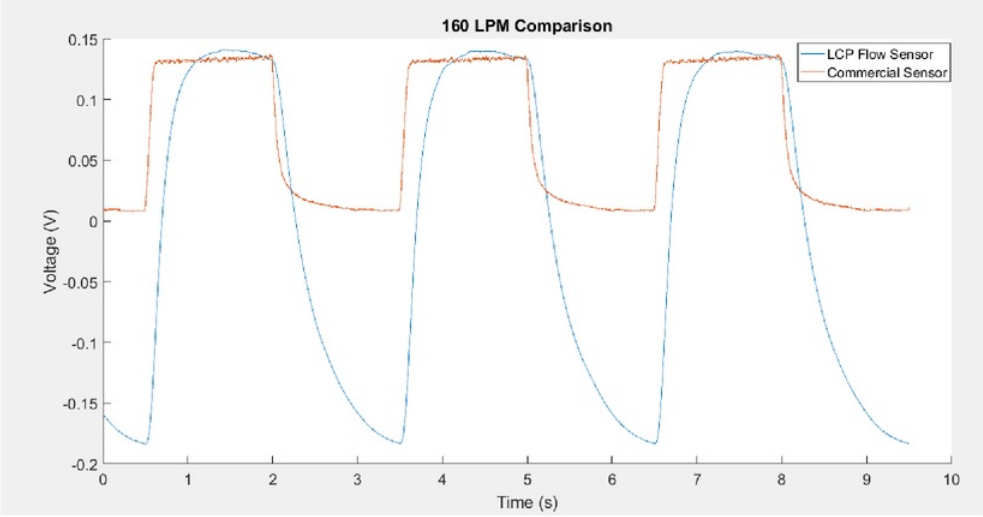

Figure 5.24: Comparison Plot 160LPM

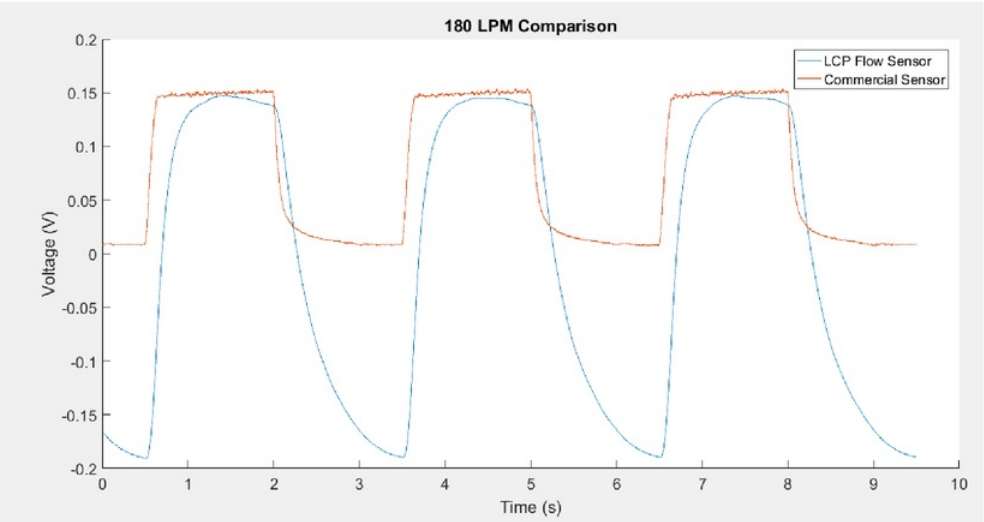

Figure 5.25: Comparison Plot 180LPM

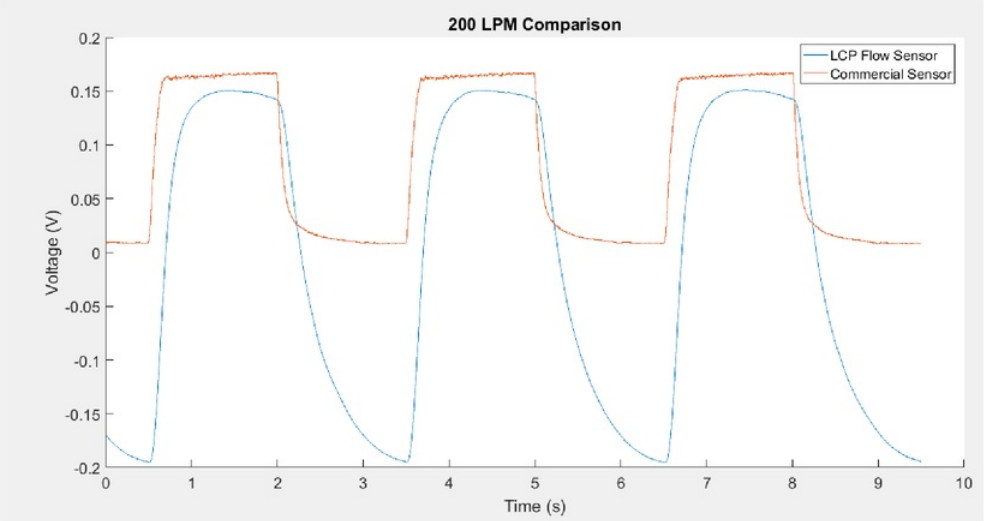

Figure 5.26: Comparison Plot 200LPM

5.6.3 Flow Flow Rate Sensing

The data collected and plotted in Figure 5.26 below demonstrates that the LCP flow sensor has capabilities of detecting, with a clear signal, the flow rates of 8LPM from the CPAP device, furthermore this plot also clearly demonstrates that the LCP flow sensors' superiority in its low velocity detection capabilities compared to the commercial flow sensor used in the pump itself.

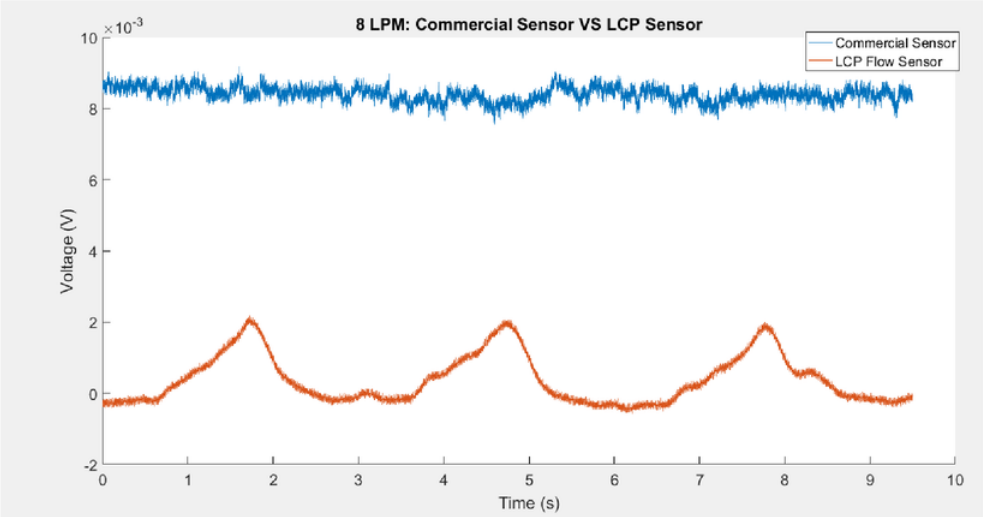

Figure 5.27: Comparison Plot 8LPM

5.6.4 Sensitivity/Resolution

Similarly, to the first design, there is a measurable difference in response from flow rate changes of 1LPM

There is an observed response change at the peaks somewhere in the order of 1mV - 10mV difference and therefore may be difficult to identify and distinguish which exact flow rate is generating a fluid flow without sufficient amplifiers and filters or other equipment needed to pick up low voltage fluctuations.

Figure 5.27 shows the sensitivity at 8 - 10LPM, Figure 5.28 shows the sensitivity between 47 - 50LPM, Figure 5.29 shows the sensitivity between 97 - 100LPM, Figure 5.30 shows the sensitivity between 147 - 150LPM, Figure 5.31 shows the sensitivity between 197 - 200LPM.

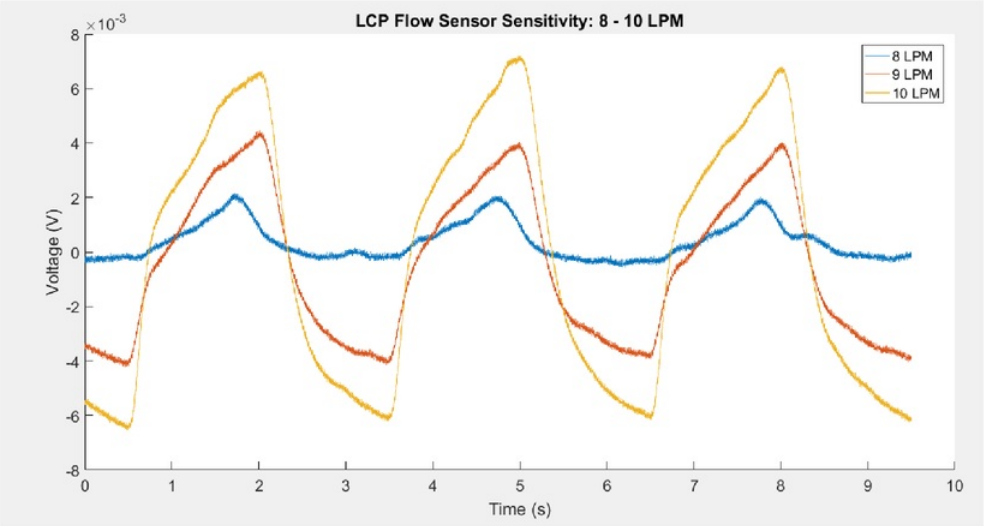

Figure 5.28: Flow Sensor Sensitivity 8-10LPM

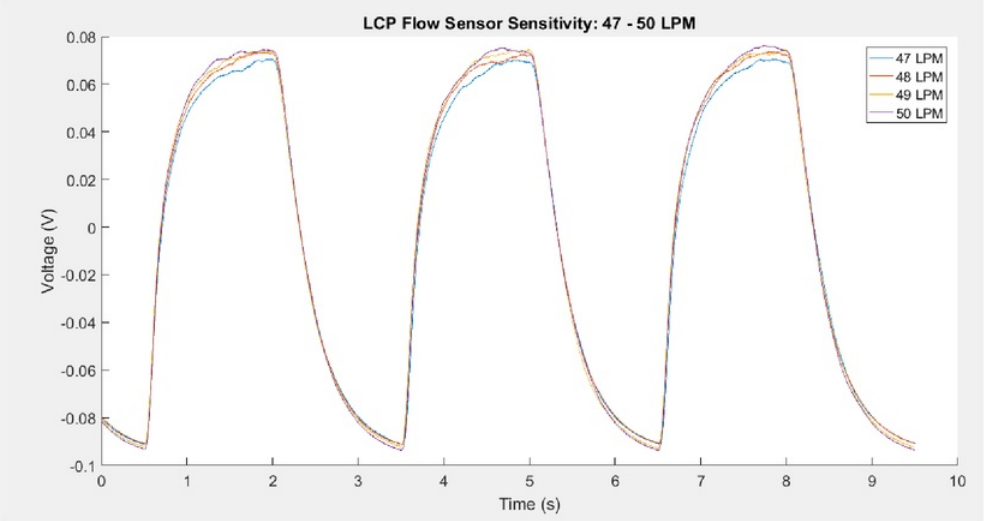

Figure 5.29: Flow Sensor Sensitivity 47-50LPM

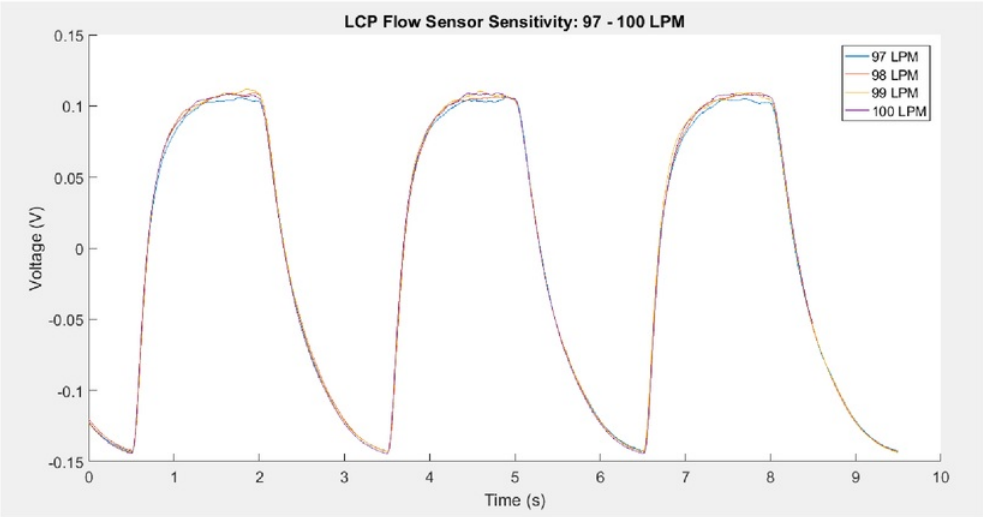

Figure 5.30: Flow Sensor Sensitivity 97-100LPM

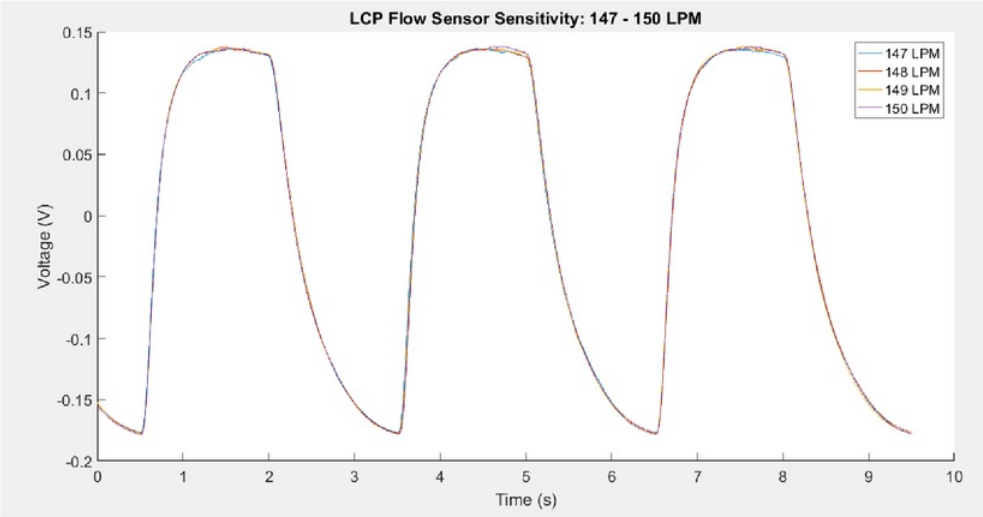

Figure 5.31: Flow Sensor Sensitivity 147-150LPM

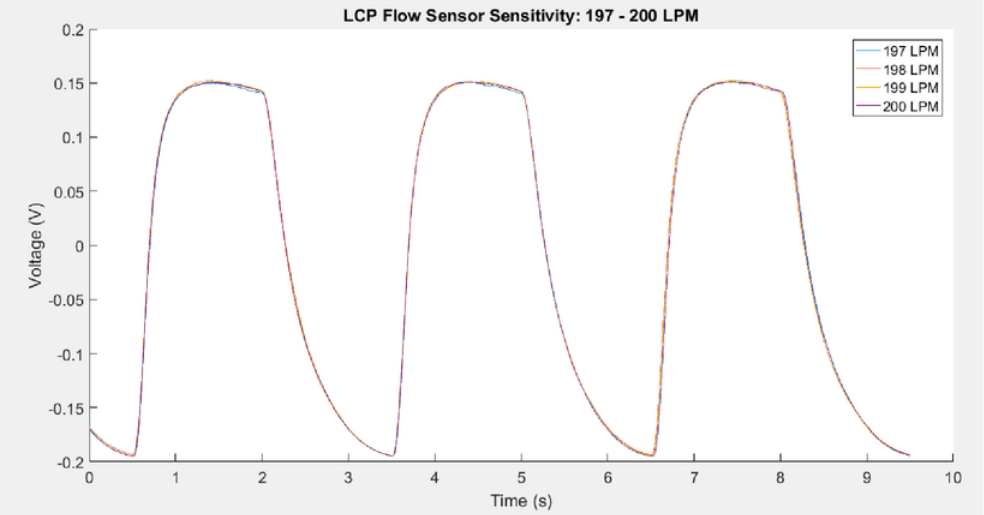

Figure 5.32: Flow Sensor Sensitivity 197-200LPM

5.6.5 Band Gap/Response Time

From the data collected and plotted in Figures 5.32 - 5.36 we can see the response times for the LCP flow sensor at varying flow rates. We can see that the response time is slower at lower flow velocities due to the time it takes for the standing structure to reach its maximum deflection from drag forces created between the structure and the fluid flow.

Table 5.1 below compares the response times of the LCP flow sensor against the commercial sensor. We can see from the table that the commercial sensor again remains consistent in its response times for each varying flow rate that it is able to detect and that the LCP flow sensor requires more time to reach its maximum deflection at lower flow velocities due to the nature of the mechanical properties of the sensor.

Flow Rate (LPM)	Flow Sensor Response (s)	Commercial Sensor Time (s)
10	1.5	N/A
50	0.7	0.15
100	0.7	0.1
150	0.5	0.1
200	0.5	0.1

Table 5.1: Response Time of Sensors

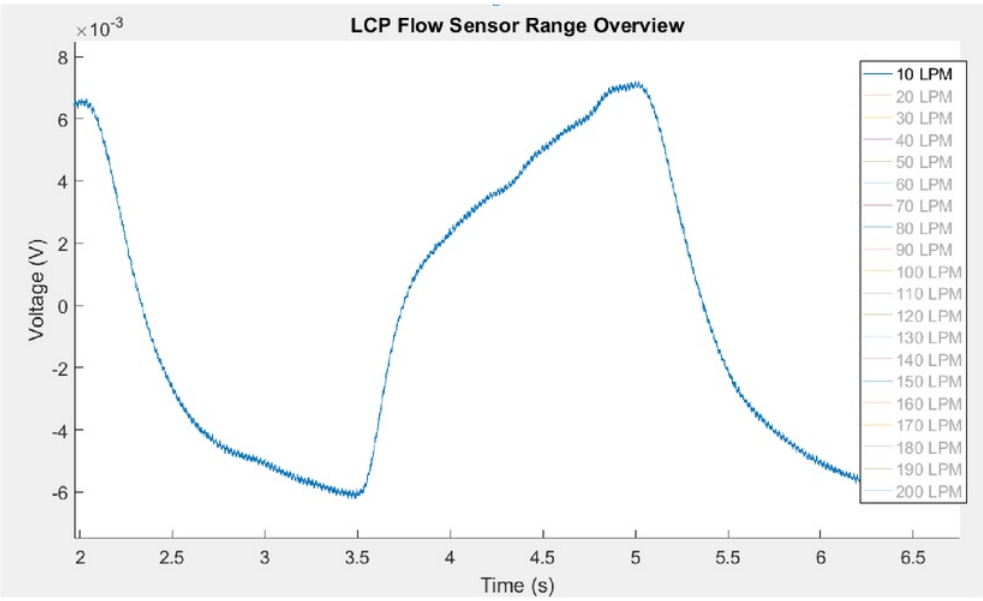

Figure 5.33: Flow Sensor Response Time 10LPM

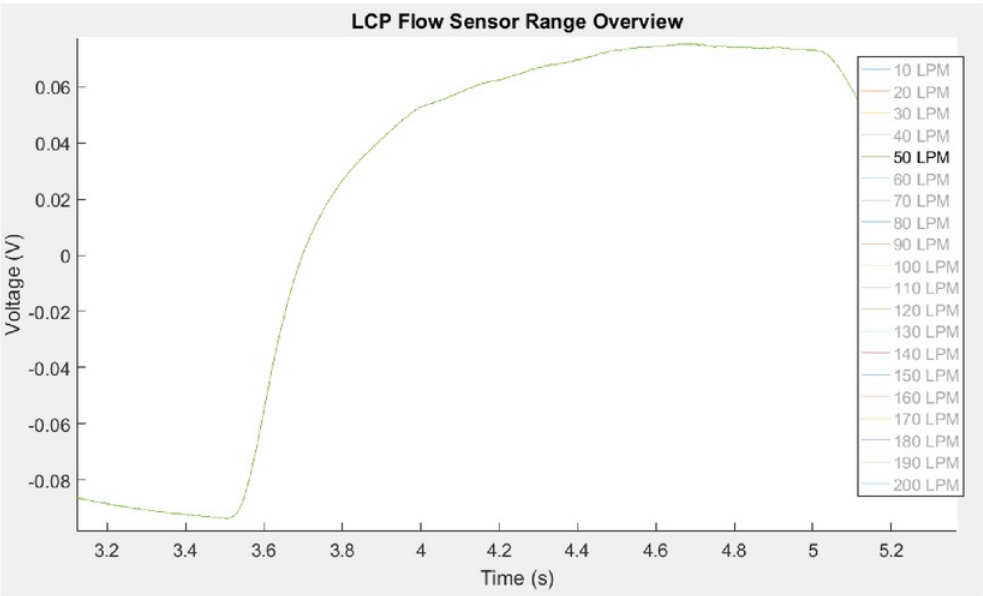

Figure 5.34: Flow Sensor Response Time 50LPM

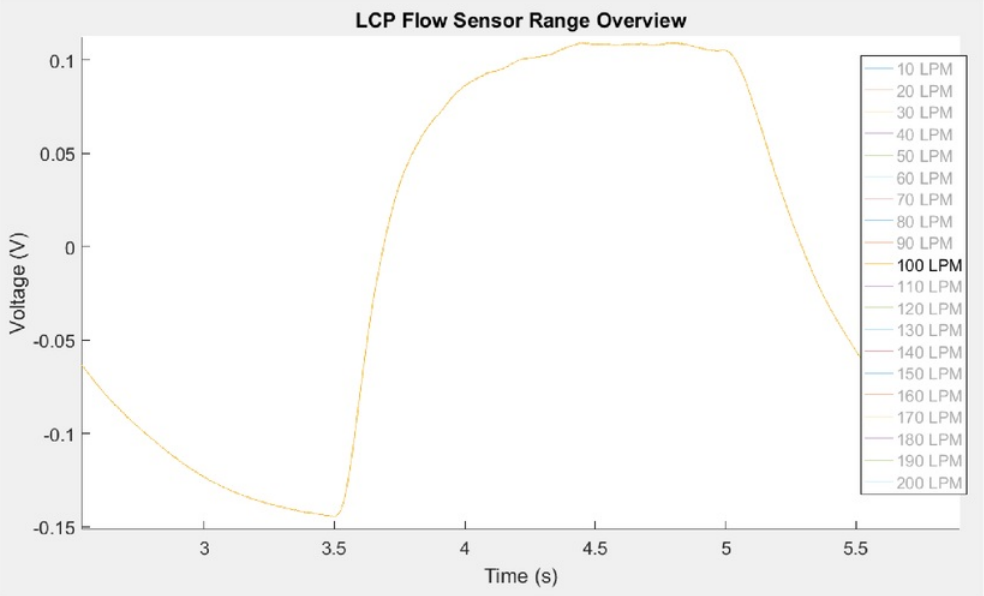

Figure 5.35: Flow Sensor Response Time 100LPM

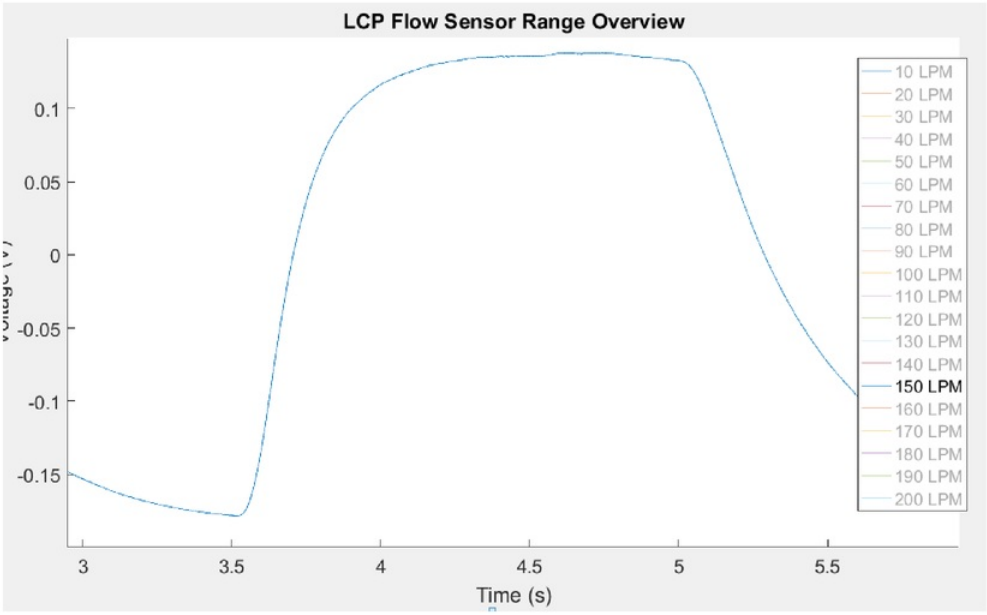

Figure 5.36: Flow Sensor Response Time 150LPM

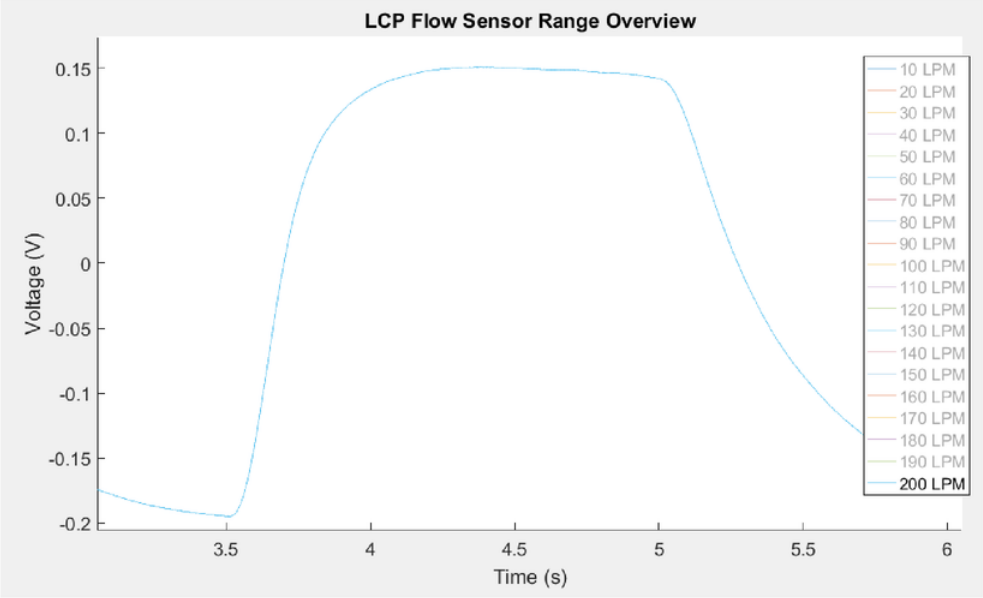

Figure 5.37: Flow Sensor Response Time 200LPM

5.6.6 Summary of Experimental Work

A number of tests have been conducted to compare the properties of the LCP MEMS flow sensor against a commercially available flow sensor. The main focus of study for these experiments have been directed at the flow range sensing abilities, resolution of detection in flow rate changes, accuracy and response time of the LCP sensor. We can see from the results that the sensor is capable of detecting air flow rates from 10 - 200LPM with relative clarity and minimal signal noise, it has also been demonstrated that the LCP flow sensor has capabilities of detecting as low as 8LPM. From the calibration plot we can see an average voltage response of 0.0016V per 1LPM flow rate change with an average standard deviation of 0.0015 across flow rates of 10 - 200LPM; the data collected has also demonstrates that there is a range of 1 - 10mV variation when detecting 1LPM flow variations. It has also been demonstrated that the response time is 5 - 7 times slower than that of the commercial sensor due to times required for the mechanical properties of the flow sensor to reach its maximum membrane displacement.

The results attained from experimental work can be further improved upon with greater access to sensor packaging tools which would mitigate some of the issues experienced in the packaging process of this sensor into the housing, the issues and differences between the pressure sensor and flow sensor configurations will be explained in greater detail in the next chapter of this thesis.

Chapter 6

Discussion

In the previous chapters, we have presented both simulated work and real-world experimental results of two LCP MEMS configurations, the first, by utilizing the LCP sensor as it was originally designed - as a pressure sensor, through simulation and testing, its performance the performance was measured and compared against a commercial sensor readily available in the medical industry. The design was changed, and the sensor was altered for use as a flow sensor and again simulation and testing was performed and its performance compared against the commercial sensor. In this section a comparison between the two configurations is discussed along with the limitation or issues that arose throughout the project work.

6.1 LCP Pressure Sensor Vs. LCP Flow Sensor

6.1.1 Simulated Comparison

From the simulation standpoint, the advantages of the pressor sensor configuration is that the system is not subjected to the backflow occurring at the back of the cross beam and therefore the system response is not reduced or influenced due to this, compared to the flow sensor configuration where the standing structure, which causes the membrane to deform, is subjected to the flow velocities and turbulence that occurs due to these backflows. Furthermore, in the pressure sensor configuration, the system is also less affected by boundary layers forming from the cross beam due to its position on the beam as well at the centre of the membrane is positioned above any boundary layers that may form from the beam itself, compared to the flow sensor configuration where there will always be some boundary layer influencing the amount of drag force generated and ultimately affecting the moment force about the base of the standing structure causing membrane displacement.

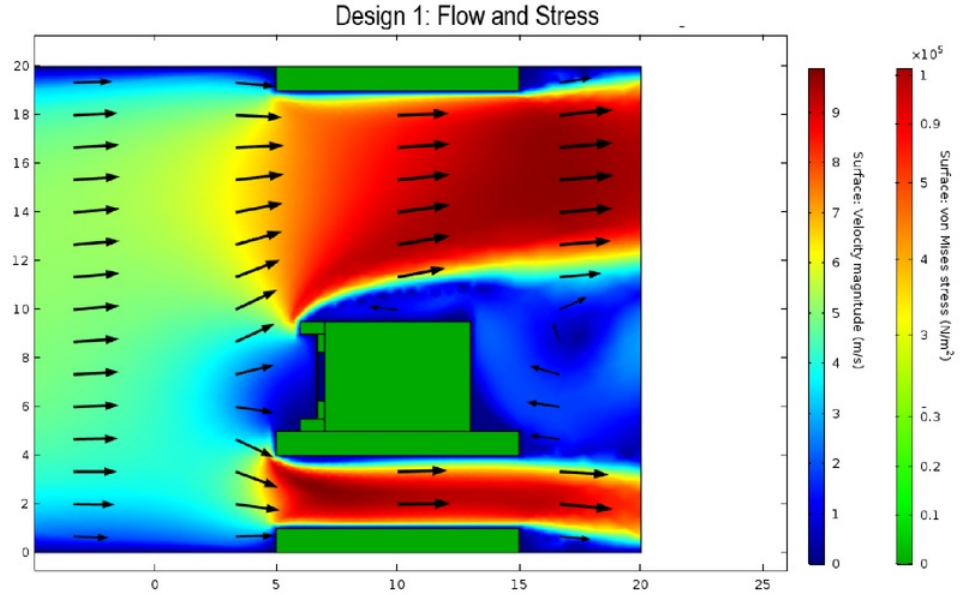

Figure 6.1: Flow and Stress: Pressure Sensor

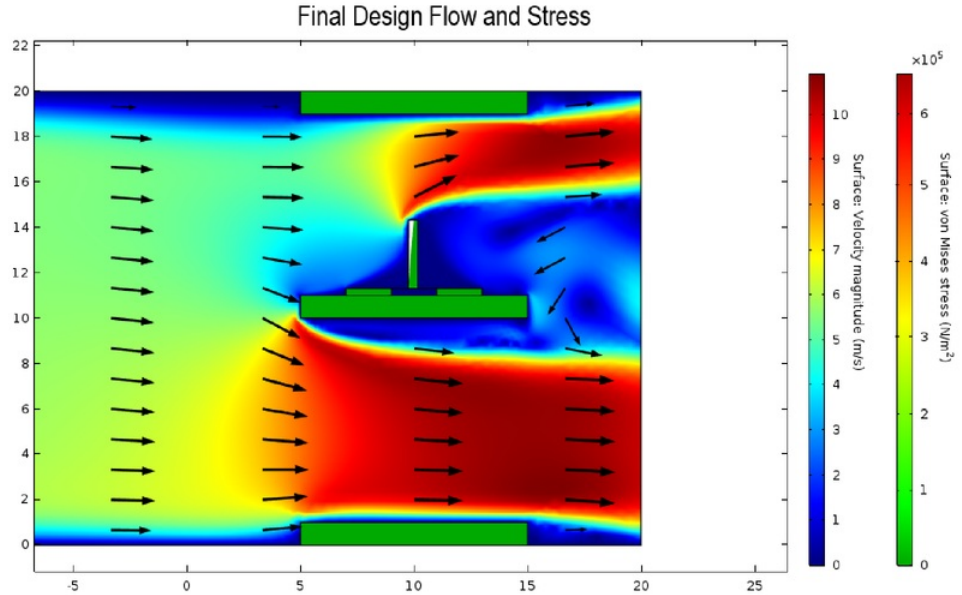

Figure 6.2: Flow and Stress: Flow Sensor

Based on the area of displacement that occurs on the membrane at 100LPM, the standing structure should have an increase system response of approximately 14%, however as previously stated in earlier chapters, this simulation is created in 2D space and therefore the ability for 2D simulated results may not be actualized in 3D space.

This can be seen in the difference between the pressure sensor configuration and the flow sensor configuration. In the pressure sensor configuration, the membrane is subjected to near uniform force generated by the flow velocity which translates to a near uniform membrane deformation across the entire membrane, this allows the maximum amount of gold strain gauges to be subjected to stress which is then translated into a change in resistance.

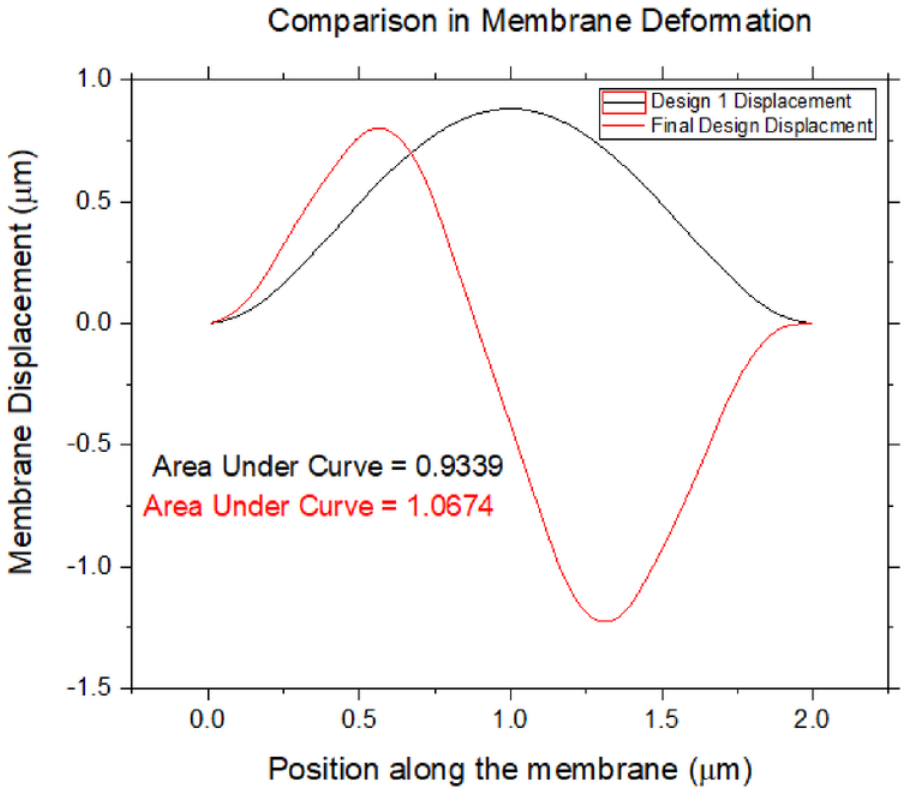

Figure 6.3: Membrane Displacement: Pressure Sensor Vs. Flow Sensor

This principle of the sensor does not hold true for the flow sensor configuration, as the displacement along the membrane is not symmetrical as seen in the 2D simulation, however this symmetrical deformation will not apply across the entirety of the membrane

due to the fixed constraints at the edges of the membrane, and therefore the simulation only shows a slice of the peak deformation occurring on either side of the standing structure but does not account for the rapid decrease in deformation radiating away from the standing structure towards the fixed edges of the circular membrane; the mathematics behind this deformation is outside the scope of this project and therefore was not calculated, however this idea translates to an asymmetrical stress applied to the tangential strain gauges at the edges of the membrane (where the most gold strain gauges are located) which will result in overall a decrease in the amount of strain gauges utilized for the change in resistance, however the strain gauges that are utilized may be subjected to higher levels of stress which may result in a higher resistance change and therefore may balance this inequality.

6.2 Experimental Results

6.2.1 Calibration Plot

When comparing the calibration plots against each other, based on a linear line of best fit it is demonstrated that the pressure sensor configuration is more sensitive per 1LPM flow change with a 0.0026 V/LPM compared to 0.0016 V/LPM this 1mV difference between the two sensitivities while measurable, could be considered a negligible difference when used as a means for determining the exactly flow rate given the sensitivities at peak values range from 1 10mV shown in the previous chapters. It is also important to observe that the both plots are only relatively linear in middle flow velocity rates (between 30 - 140 LPM flow rates). Based on the mechanical properties of the sensor, there will always be a maximum displacement the sensor can be subjected to due to limitations of mechanical strain, we see this however occur sooner in the flow sensor configuration from 180LPM onwards, therefore this may mean there are limitations to the standing structures ability to send higher flow velocities that may be required in sleep apnea devices.

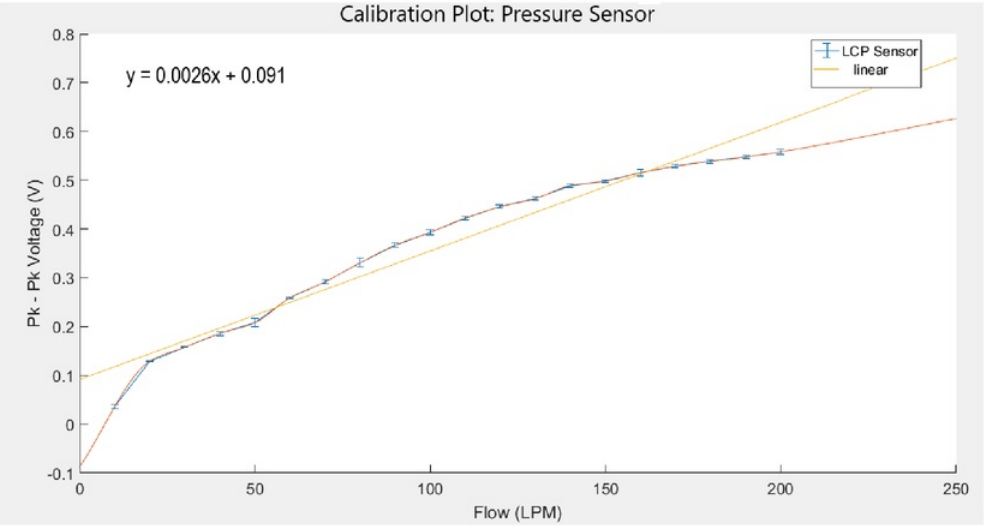

Figure 6.4: LCP Pressure Sensor Calibration Plot

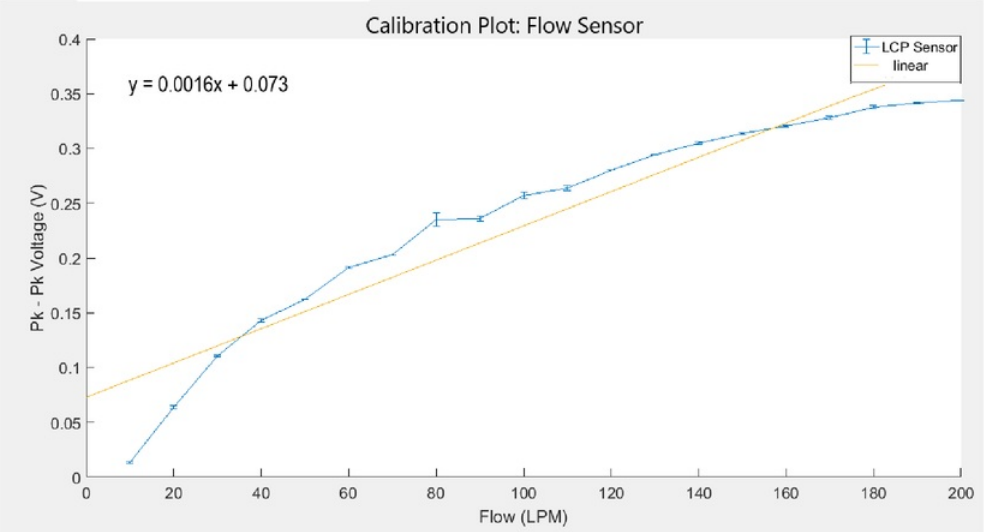

Figure 6.5: LCP Flow Sensor Calibration Plot

6.2.2 Sensitivity

We can see from the direct comparison below that the system response from the pressure sensor has higher peak to peak values that that of the flow sensor configuration, however the signal from the flow sensor configuration has less noise and the peaks are would be easier to distinguish from a controllers standpoint.

When comparing the higher flow velocities seen in Figures 6.8 - 6.11, we can again see that there is less noise in the system in the flow sensor configuration, even though the peak to peak values are almost half in size. These peak to peak voltage difference is not a pressing concern as a microcontroller can be adjusted to a lower peak value for each flow rate, therefore a clearer signal being sent to such a controller would be valued higher in priority from a sensitivity detection standpoint.

When comparing the clarity/resolution of each peak to peak value between each 1LPM change, both systems may face challenges in determining the exact flow rate passing through the system due to the small voltage differences between each flow rate (0.0026V/LPM and 0.0016V/LPM) however with a sufficient amplifier and signal processing, this issue can be mitigated and thus reinforcing the need to have a clearer signal over the size in peak to peak values.

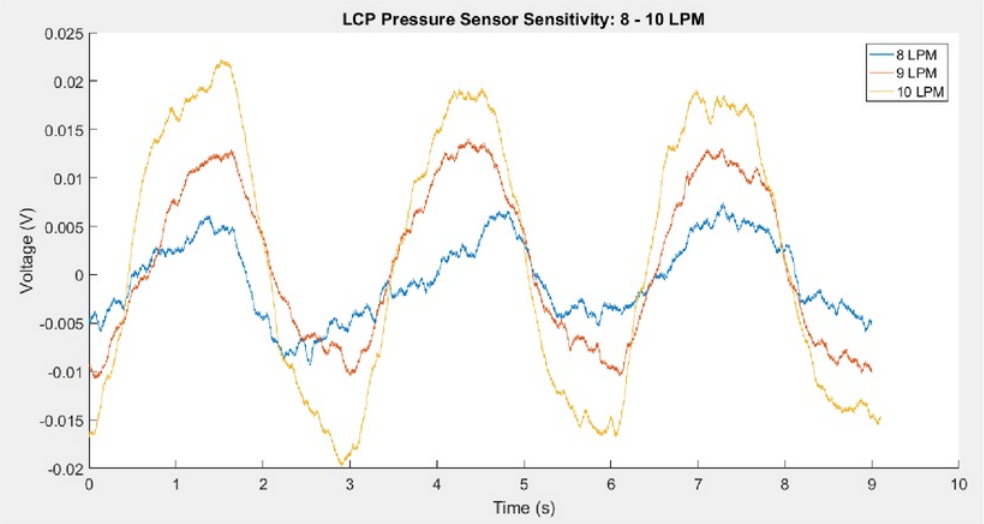

Figure 6.6: LCP Pressure Sensor Sensitivity 8-10LPM

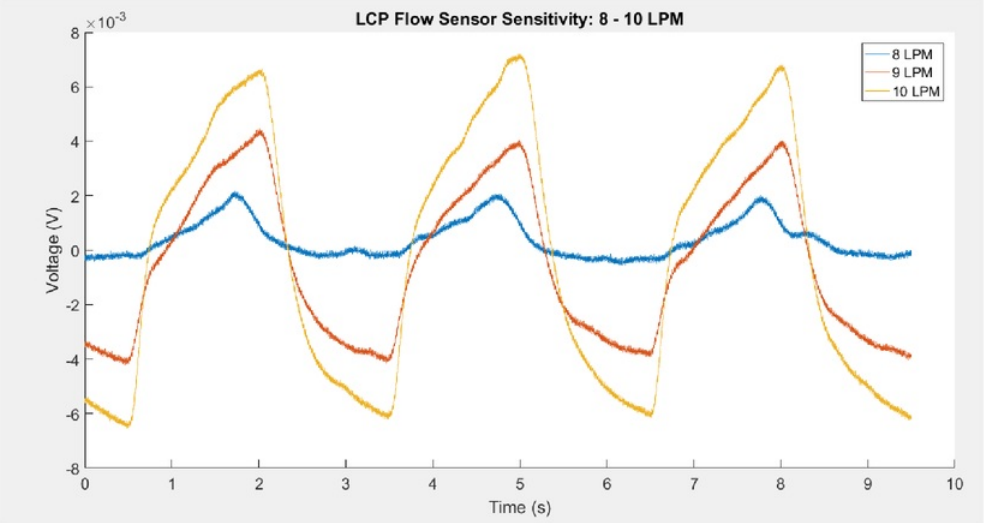

Figure 6.7: LCP Flow Sensor Sensitivity 8-10LPM

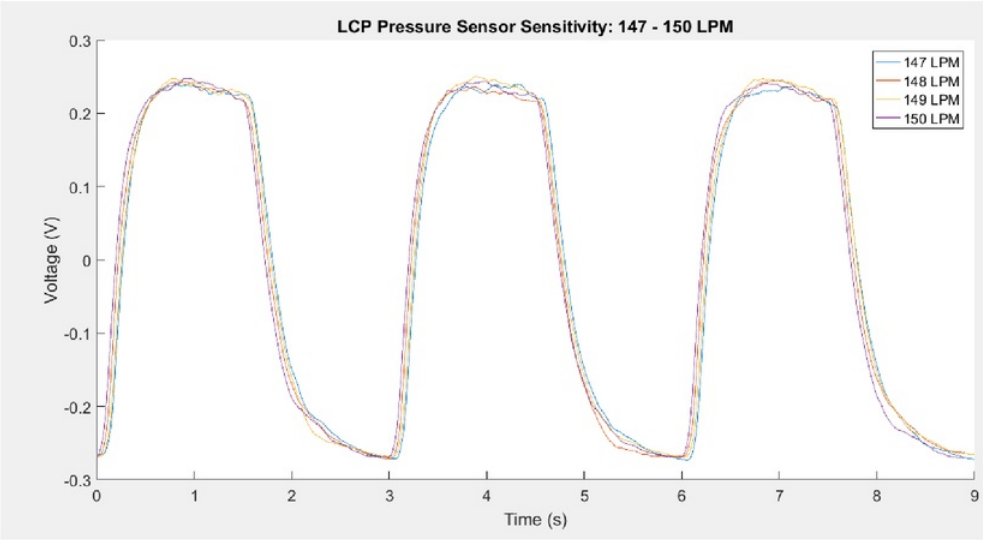

Figure 6.8: LCP Pressure Sensor Sensitivity 147-150LPM

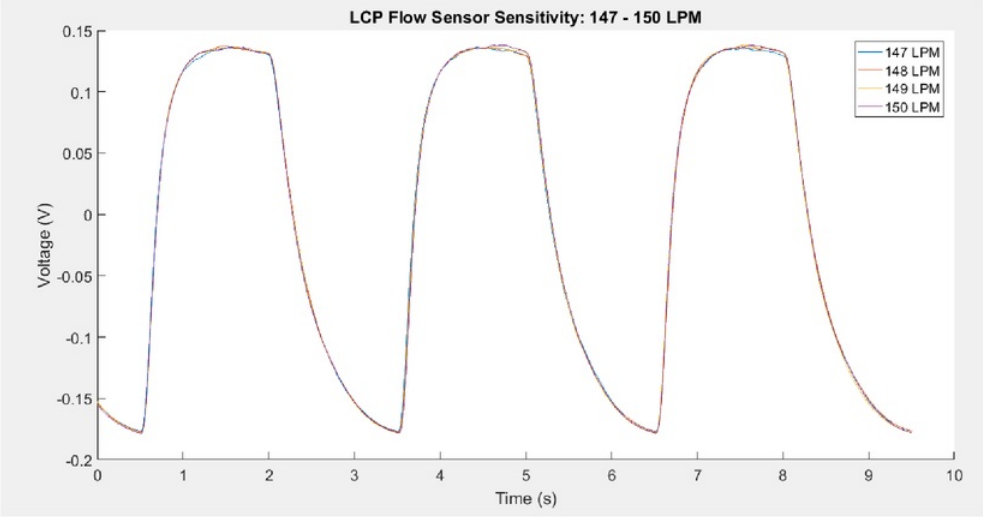

Figure 6.9: LCP Flow Sensor Sensitivity 147-150LPM

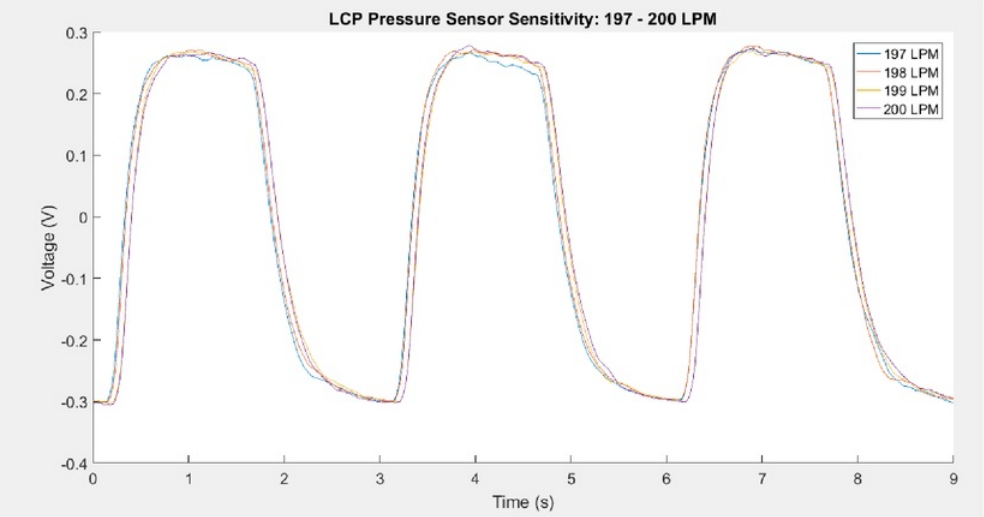

Figure 6.10: LCP Pressure Sensor Sensitivity 197-200LPM

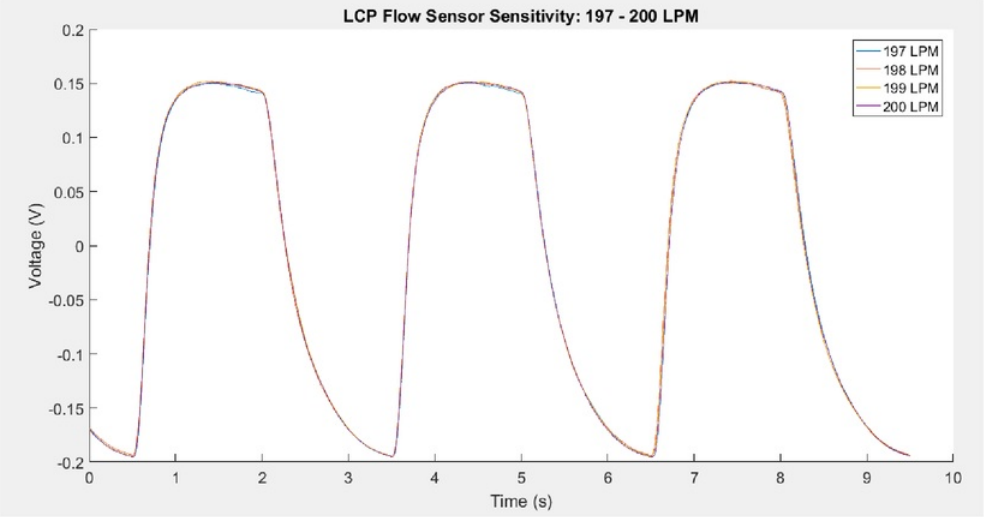

Figure 6.11: LCP Flow Sensor Sensitivity 197-200LPM

6.2.3 Low Flow Rate Sensing

When comparing the lowest flow velocity both configurations were able to sense, again we see this improvement in signal clarity from the flow sensor configuration compared to the pressure sensor despite the lower voltage peaks. Both sensor configurations are significantly better than the commercial sensors response which mostly consists of signal noise.

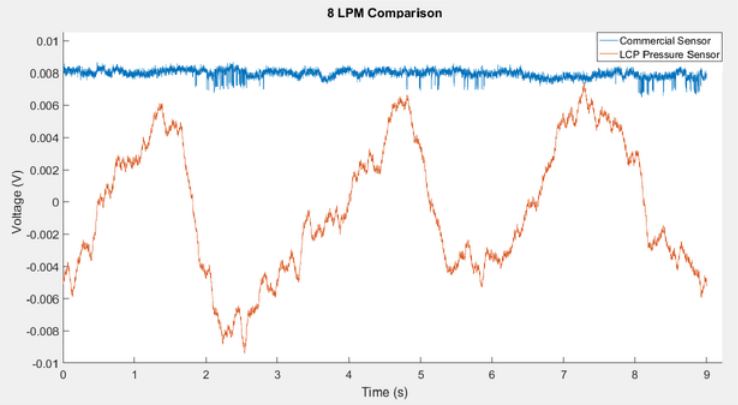

Figure 6.12: LCP Pressure Sensor Comparison 8LPM

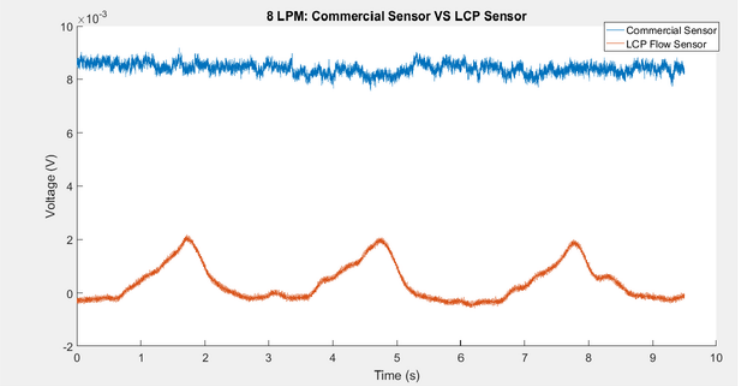

Figure 6.13: LCP Flow Sensor Comparison 8LPM

When comparing low flow rate with the whole data set collected up to 200LPM, as seen in the calibration plot, we can see a slower, more consistent gradient change in the flow sensor configuration than the pressure sensor configuration; it can be theorised that with a steadier gradient in peak to peak voltage responses from the flow sensor, this could indicate a more consistent and reliable system at detecting low flow velocities.

6.2.4 Response Time

When comparing the response times of both configurations against the commercial sensor, the response time of both LCP membrane bases sensors are significantly slower due to the mechanical properties and the time required to realise the mechanical stress into voltage change. Furthermore, the sensors are fundamentally different in that the sensor inside the flow generator utilised active sensing or better known as thermal bases sensor whereas LCP MEMS sensors use passive or non-thermal sensing capabilities and therefore require more time for sensing.

When comparing the pressure sensor configuration against the flow sensor configuration, we can see there is a delay in response due to the time required to create a drag force between the standing structure and the fluid flow, this time gap therefor may be a direct result of additional mechanical interactions required for the flow sensor to work. This gap in time reduces as the flow velocities increase further reinforcing the idea that the time delay is due to time required to generate sufficient drag force to bend the standing structure.

Flow Rate (LPM)	Pressure Sensor (s)	Flow Sensor (s)	Commercial Sensor (s)
10	1	1.5	N/A
50	0.4	0.7	0.15
100	0.4	0.7	0.1
150	0.4	0.5	0.1
200	0.4	0.5	0.1

Table 6.1: Response Time of Sensors

6.2.5 Conclusion

It is important to note that both configurations have provided useful information regarding their properties, advantages and constraints in their usability in air flow generators used to treat sleep apnea and more broadly, their use in the medical industry.
There is however differences and issues between the two sensor configurations which may explain the similarities in system response and shed some light as to the potential the flow sensor configuration has for use in future works.

The LCP MEMS sensors that were used in both configurations are two different sensors, in terms of their base resistances. When the LCP sensor used in the pressure sensor was tested using a multimeter, it had a resistance of 838Ω compared to the flow sensor configurations LCP sensor which had a resistance of 1053Ω, this 25% difference in resistance plays a significant impact on the peak to peak values that are displayed in the results above, which may account for the size of the peak to peak values of the flow sensor configuration.

Additionally, the assembly and packaging of the flow sensor experienced a variety of issues due to a lack of specialist tools required to correctly package the sensor into the housing. Some of the issues that may impact the flow systems performance is the requirement to have an exact two-part epoxy required to adhere the wires to the gold contact pads on the sides of the sensor, any variation in the mix would significantly affect the conductivity through the epoxy; since both sensors were not made at the same time, there is a high likelihood that the conductivity through each epoxy applied would have different conductivity properties, affecting the overall response of the system. There were also difficulties in applying the epoxy to the wires and contact pads due to the scale of application and easily resulted in applying too much epoxy or due to the size, the wires would not stay in place during curing stages as shown in the picture below, one picture shows a sensor where the wire was dislodged during the curing stage and was unusable during the testing stages of the project, the other was used during testing.

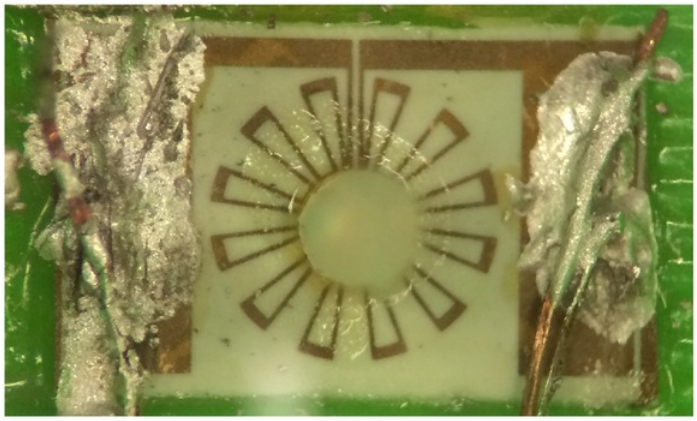

Figure 6.14: LCP Flow Sensor - Wire Issues

Other issues with the assembly stages of the flow sensor assembly included the standing structure, this standing structure had to be applied manually with the use of tweezers and a microscope, therefore a high likelihood of the standing structure not being perfectly perpendicular the membrane or aligned correctly to the exact middle of the membrane. Additionally, there was adhesive spill over during the assembly; this adhesive spill over as shown in the image below would also affect the pliability of the membrane, thus the membrane may have become more rigid which severely limits the membrane displacement and overall system response.

Given the near comparable system performance compared to the pressure sensor configuration, despite the standing structure assembly and packaging issues, there is significant room for improvement and further testing is required to fully realise the LCP MEMS capabilities as a flow sensor in air flow generators used in the medical field.

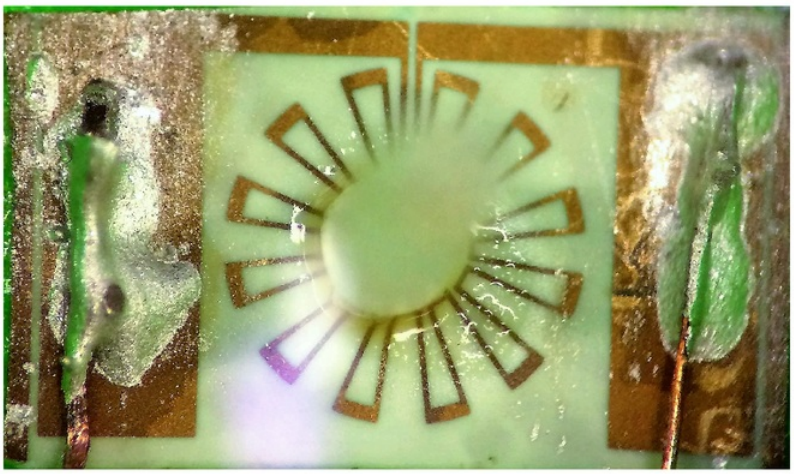

Figure 6.15: Working LCP Flow Sensor

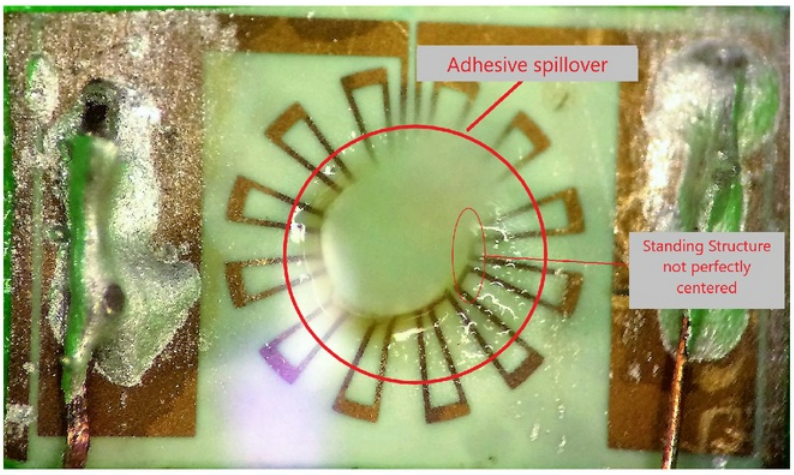

Figure 6.16: Issues with Working Flow Sensor

Chapter 7

Conclusion

The goal of this project was to design, simulate, test, and implement the most appropriate package and system configuration for the LCP MEMS sensor including any modifications to the sensor itself in order to enhance as well as demonstrate the sensors capabilities in the medical field, particularly through air flow, by subjecting the system to air flow velocities generated by a system used to treat sleep apnea.

A literature review was conducted to grasp an understanding of the LCP sensor itself, its working principle, the way it was fabricated, and the real-world applications is has already been subjected to in the past. Fundamental principles of fluid dynamics were explored such as Bernoullis principle, Hagen-Poiseuille flow, the viscosity properties of air and its interactions with solids.

Through this project the sensor was utilized as a pressure sensor and implemented into the system with a custom designed housing to allow the sensor to be fitted at the end of the tube where the flow generator is connected to the CPAP mask. The design was modelled using finite element analysis software and experimentally tested and data collected simultaneously with the data produced from the commercially available sensor fitted in the sleep apnea machine.

The results concluded that in all areas but response time the LCP pressure sensor configuration provided comparable system performance to the commercially available system through the use of passive sensing rather than active sensing techniques with advantages in low flow velocity detection sensitivity capabilities for 1LPM flow changes, however was slow in band gap/system response due the mechanical properties of the sensor.

Modifications were made to the LCP sensor and through the use of a standing structure the system was reconfigured to a flow sensor and housing was redesigned. This process again was done through FEA and experimental data collection; despite the limitations of the sensor due to lack of tools to professionally assemble and package the device, the

system was comparative to system performance of the LCP pressor sensor configuration with superiority in reduced signal noise but inferiority in system response.

The data collected from this thesis research has further contributed to the advancement in research in the field of LCP based piezoresistive sensors, evident by the journal article that is currently being written at the time of writing this thesis, with aims of it to be published in the near future.

Chapter 8

Future Work

In this chapter of the thesis, additional areas of research or refinement can be explored in future works related to this thesis or to the advancement of the LCP MEMS sensor.

8.1 Packaging and Assembly Refinement

As stated in previous chapters, there were issues in terms of assembly and packaging of the flow sensor configuration and therefore presents an ideal area for further research. The investment into packaging machines or methods to better assemble the standing structure or inhouse fabrication of the sensors themselves at Macquarie University for further testing of this configuration in order to determine if the issues brought up in this thesis did have any noteworthy impact on system performance and any future works with LCP MEMS sensors by future students and researchers.

Additional research can also be conducted into the implantation of two LCP flow sensors as a means for mitigating the slower response time; by implementing two standing structure LCP flow sensors a microcontroller can be used to detect the time difference in initial response (for example a particular percentage of the sensors response that is known at the particular flow rate) of the two sensors at a fixed distance, which could then be used to calculate the flow velocity passing through the system. By taking a fixed percentage, say 50% of the known full system voltage response, the time delay can be drastically reduced.

8.2 Improved Simulation

Due to modelling difficulties, limitations of computing power and time restrictions a 3D model was attempted but only successful in modelling fluid flow and not fluid-structure interaction. Therefore, future work can be done to complete this 3D modelling to gain a better understanding of the membrane deformation across the entire membrane that occurs due to buckling induced by the standing structure.

8.3 Redesign of Sensor

A redesign of the sensor could potentially yield promising results when implemented with the standing structure, for example thicker radial strain gauge deposits or more inner tangential ring based strain gauges could be implemented to better utilise the asymmetrical deformation that occurs due to buckling from the standing structure. As the original design was purposed for uniform pressure and uniform deformation, allowing for the tangential strain gauges at the edge of the membrane to be used.

8.4 Redesign of Standing Structure

Another area of research that can be implemented is the analysis in changing the standing structure. For example, by increasing the surface area of the standing structure, an increased drag force can be generated an applied to the membrane, giving a higher voltage response; furthermore, this could be used to detect lower flow velocities.

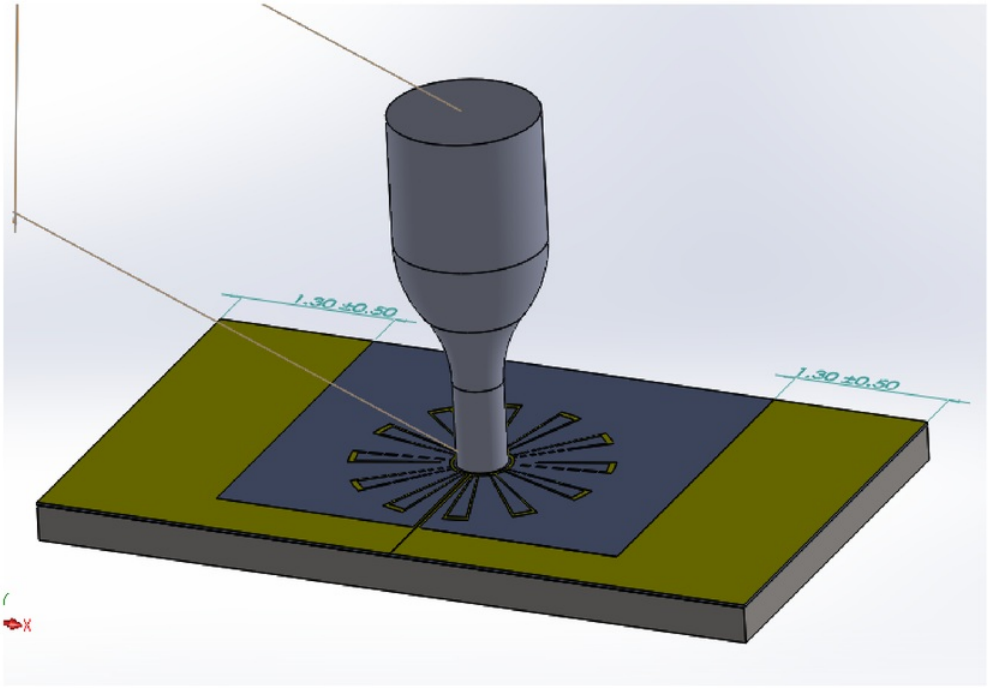

Figure 8.1: Redesign of Standing Structure

8.5 Further Areas for Airflow Testing

Further research and testing can be conducted into the sensors capabilities of detecting human breathing and air flow rates and the refinement of sensory application into medical devices pertained to human breath monitoring.

As a part of extra testing on the LCP sensor and the flow sensor configuration with a standing structure, this design was implemented into a 3D scaffold of a breathing nasal tube to determine if the sensor is capable of monitoring human breathing pattern.

As a part of the extra testing the setup was exactly the same as testing throughout the thesis in terms of using an amplifier, filter and recording data through NI-DAQ into Signal Express. The preliminary results attained from this can be seen in the following sections.

8.5.1 Inhale and Exhale Testing

Testing was also conducted to determine if the sensor would respond to the air flow changes made from the human respiratory system, the system was setup similarly to that of the thesis work conducted, however instead of using an air flow generator air was inhaled and exhaled manually and the data was collected.

Testing was carried out in three phases, the first, only inhaling took place into the piece to see if the sensor would respond, the second stage was exhale only into the system, and lastly normal slow breathing was performed into the system.

Preliminary setup can be seen in Figure 8.2 and 8.3 with results in Figures 8.4, 8.5 and 8.6.

As you can see in Figure 8.6, the response from inhaling is noticeably larger than the response from exhaling, this again is due to the material properties of the LCP membrane in the piezoresistive sensor, as previously mentioned, the material in the LCP sensors require time to rectify deformation that occurs due to air flow velocity, it can be hypothesised that maximum strain has occurred upon inhaling and therefore when exhaling immediately after, the sensor has not been given enough time to rectify deformation that has occurred during inhaling and thus the sensor has not returned to its normal state to response to the exhale portion of the breathing cycle. Alternatively, another reason for the difference in peaks between inhaling and exhaling is due to the human respiratory systems difference in pressure and flow rates of inhaling compared with exhaling [12].

This area of research can be explored into greater detail in future research projects with the LCP MEMS sensor.

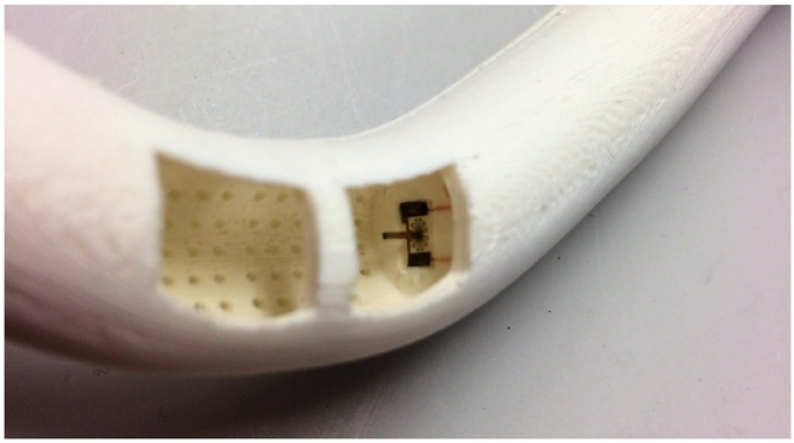

Figure 8.2: LCP Flow Sensor in Nasal Mask

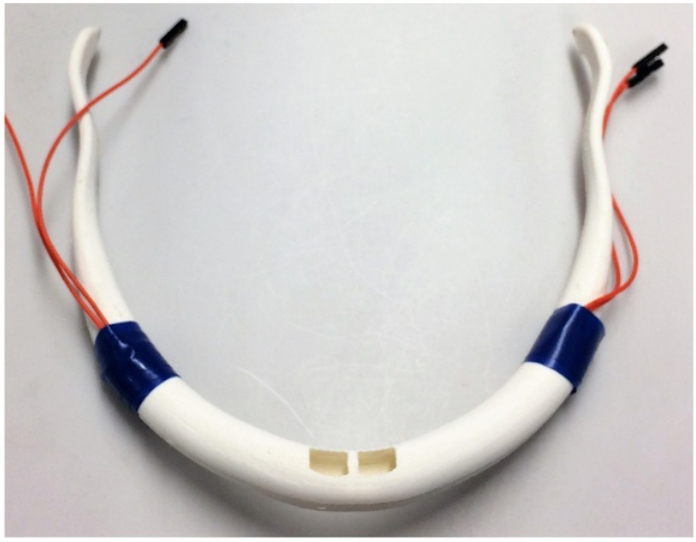

Figure 8.3: LCP Flow Sensor in Nasal Mask

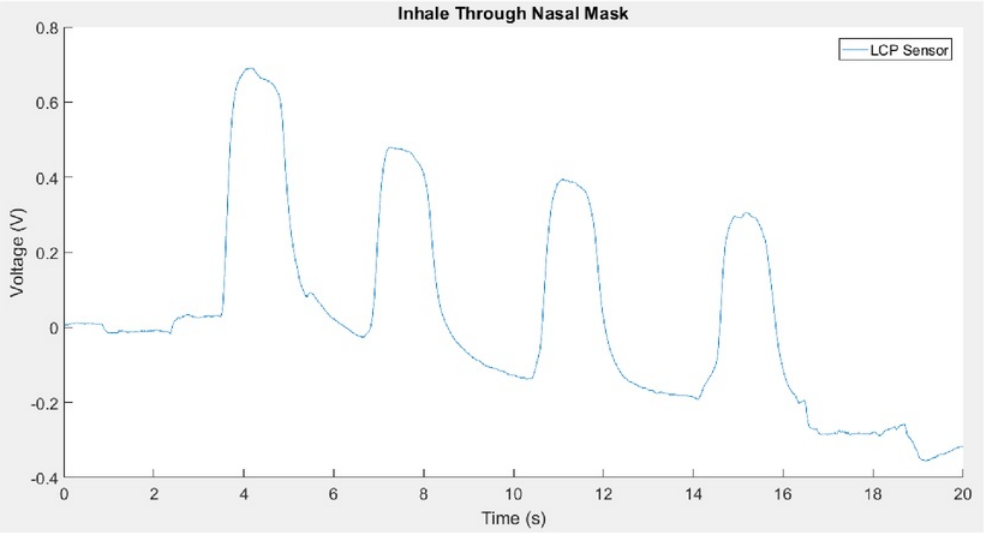

Figure 8.4: LCP Flow Sensor Nasal Mask Inhale Results

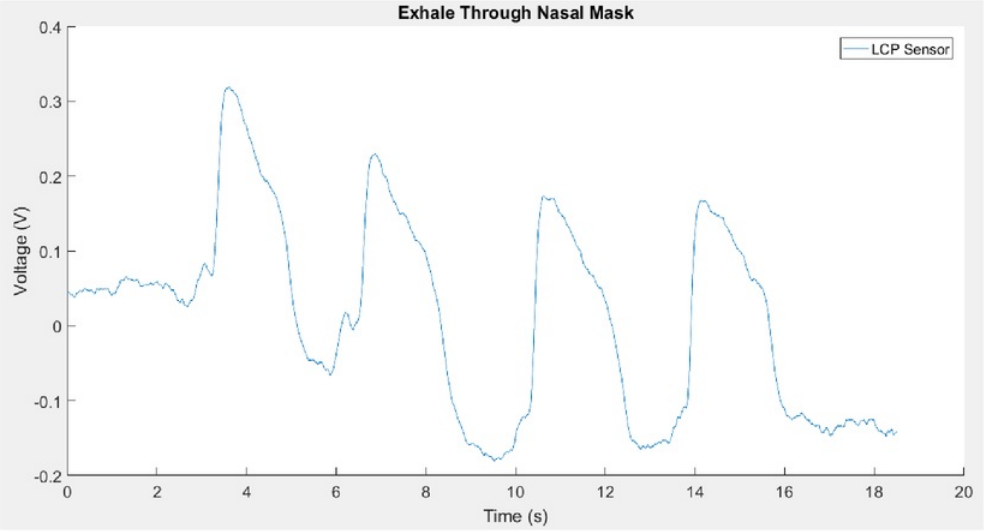

Figure 8.5: LCP Flow Sensor Nasal Mask Exhale Results

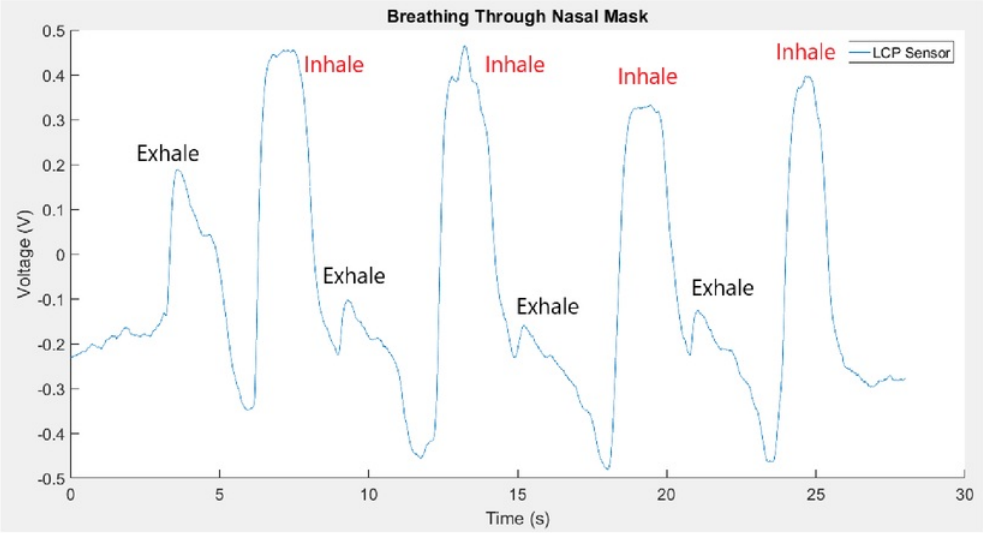

Figure 8.6: LCP Flow Sensor Nasal Mask Breathing Results

Chapter 9

Abbreviations

CAD	Computer Aided Design
CAE	Computer Aided Engineering
CPAP	Continuous Positive Airway Pressure
DAQ	Data Acquisition
DRIE	Deep Reactive Ion Etching
IV	Intravenous
KVO	Keep Vein Open
LCP	Liquid Crystal Polymer
MEMS	Micro-Electromechanical Systems
PLA	Polylactic Acid
PTFE	Polytetraflouroethelene
UNSW	University of New South Wales

Appendix A

Matlab Code

A.1 Overview

The two Matlab files written for the data collection throughout the thesis will be provided here for reference.

A.1.1 Matlab Code for Pressure Sensor

```
% %%%%%%%%%%%%%%%%%%%%%%%%%%%%%%%%%%%%%%%%%%%%%%%%%%
% LCP MEMS SENSOR AND PACKAGE DESIGN FOR CPAP Devices
%
% Author: William Thorby
% Department of Engineering, Macquarie University, Nov 2017
%
% Final year thesis project, Nov 2017
%
% This code was used to extract data collected from signal express to
% create meaningful graphs
% This data is from LCP Pressure Sensor Testing



%Copy Arrays so they can be manipulated

%Breathing through Mask
Breathing_Time = Breathing_TimeT;
Breathing_Voltage = Breathing_VoltageV;
Inhale_Time = Inhale_TimeT;
Inhale_Voltage = Inhale_VoltageV;
Exhale_Time = Exhale_TimeT;
```

```
23 Exhale_Voltage = Exhale_VoltageV;
24
25 %LCP
26 LCP_Time_008 = LCP_TimeT_008;
27 LCP_Voltage_008 = LCP_VoltageV_008;
28 LCP_Time_009 = LCP_TimeT_009;
29 LCP_Voltage_009 = LCP_VoltageV_009;
30 LCP_Time_010 = LCP_TimeT_010;
31 LCP_Voltage_010 = LCP_VoltageV_010;
32 LCP_Time_020 = LCP_TimeT_020;
33 LCP_Voltage_020 = LCP_VoltageV_020;
34 LCP_Time_030 = LCP_TimeT_030;
35 LCP_Voltage_030 = LCP_VoltageV_030;
36 LCP_Time_040 = LCP_TimeT_040;
37 LCP_Voltage_040 = LCP_VoltageV_040;
38 LCP_Time_047 = LCP_TimeT_047;
39 LCP_Voltage_047 = LCP_VoltageV_047;
40 LCP_Time_048 = LCP_TimeT_048;
41 LCP_Voltage_048 = LCP_VoltageV_048;
42 LCP_Time_049 = LCP_TimeT_049;
43 LCP_Voltage_049 = LCP_VoltageV_049;
44 LCP_Time_050 = LCP_TimeT_050;
45 LCP_Voltage_050 = LCP_VoltageV_050;
46 LCP_Time_060 = LCP_TimeT_060;
47 LCP_Voltage_060 = LCP_VoltageV_060;
48 LCP_Time_070 = LCP_TimeT_070;
49 LCP_Voltage_070 = LCP_VoltageV_070;
50 LCP_Time_080 = LCP_TimeT_080;
51 LCP_Voltage_080 = LCP_VoltageV_080;
52 LCP_Time_090 = LCP_TimeT_090;
53 LCP_Voltage_090 = LCP_VoltageV_090;
54 LCP_Time_097 = LCP_TimeT_097;
55 LCP_Voltage_097 = LCP_VoltageV_097;
56 LCP_Time_098 = LCP_TimeT_098;
57 LCP_Voltage_098 = LCP_VoltageV_098;
58 LCP_Time_099 = LCP_TimeT_099;
59 LCP_Voltage_099 = LCP_VoltageV_099;
60 LCP_Time_100 = LCP_TimeT_100;
61 LCP_Voltage_100 = LCP_VoltageV_100;
62 LCP_Time_110 = LCP_TimeT_110;
63 LCP_Voltage_110 = LCP_VoltageV_110;
64 LCP_Time_120 = LCP_TimeT_120;
65 LCP_Voltage_120 = LCP_VoltageV_120;
```

```
66  LCP_Time_130 = LCP_TimeT_130;
67  LCP_Voltage_130 = LCP_VoltageV_130;
68  LCP_Time_140 = LCP_TimeT_140;
69  LCP_Voltage_140 = LCP_VoltageV_140;
70  LCP_Time_147 = LCP_TimeT_147;
71  LCP_Voltage_147 = LCP_VoltageV_147;
72  LCP_Time_148 = LCP_TimeT_148;
73  LCP_Voltage_148 = LCP_VoltageV_148;
74  LCP_Time_149 = LCP_TimeT_149;
75  LCP_Voltage_149 = LCP_VoltageV_149;
76  LCP_Time_150 = LCP_TimeT_150;
77  LCP_Voltage_150 = LCP_VoltageV_150;
78  LCP_Time_160 = LCP_TimeT_160;
79  LCP_Voltage_160 = LCP_VoltageV_160;
80  LCP_Time_170 = LCP_TimeT_170;
81  LCP_Voltage_170 = LCP_VoltageV_170;
82  LCP_Time_180 = LCP_TimeT_180;
83  LCP_Voltage_180 = LCP_VoltageV_180;
84  LCP_Time_190 = LCP_TimeT_190;
85  LCP_Voltage_190 = LCP_VoltageV_190;
86  LCP_Time_197 = LCP_TimeT_197;
87  LCP_Voltage_197 = LCP_VoltageV_197;
88  LCP_Time_198 = LCP_TimeT_198;
89  LCP_Voltage_198 = LCP_VoltageV_198;
90  LCP_Time_199 = LCP_TimeT_199;
91  LCP_Voltage_199 = LCP_VoltageV_199;
92  LCP_Time_200 = LCP_TimeT_200;
93  LCP_Voltage_200 = LCP_VoltageV_200;
94
95  %RES
96  RES_Time_008 = RES_TimeT_008;
97  RES_Voltage_008 = RES_VoltageV_008;
98  RES_Time_009 = RES_TimeT_009;
99  RES_Voltage_009 = RES_VoltageV_009;
100 RES_Time_010 = RES_TimeT_010;
101 RES_Voltage_010 = RES_VoltageV_010;
102 RES_Time_020 = RES_TimeT_020;
103 RES_Voltage_020 = RES_VoltageV_020;
104 RES_Time_030 = RES_TimeT_030;
105 RES_Voltage_030 = RES_VoltageV_030;
106 RES_Time_040 = RES_TimeT_040;
107 RES_Voltage_040 = RES_VoltageV_040;
108 RES_Time_047 = RES_TimeT_047;
```

```
109 RES_Voltage_047 = RES_VoltageV_047;
110 RES_Time_048 = RES_TimeT_048;
111 RES_Voltage_048 = RES_VoltageV_048;
112 RES_Time_049 = RES_TimeT_049;
113 RES_Voltage_049 = RES_VoltageV_049;
114 RES_Time_050 = RES_TimeT_050;
115 RES_Voltage_050 = RES_VoltageV_050;
116 RES_Time_060 = RES_TimeT_060;
117 RES_Voltage_060 = RES_VoltageV_060;
118 RES_Time_070 = RES_TimeT_070;
119 RES_Voltage_070 = RES_VoltageV_070;
120 RES_Time_080 = RES_TimeT_080;
121 RES_Voltage_080 = RES_VoltageV_080;
122 RES_Time_090 = RES_TimeT_090;
123 RES_Voltage_090 = RES_VoltageV_090;
124 RES_Time_097 = RES_TimeT_097;
125 RES_Voltage_097 = RES_VoltageV_097;
126 RES_Time_098 = RES_TimeT_098;
127 RES_Voltage_098 = RES_VoltageV_098;
128 RES_Time_099 = RES_TimeT_099;
129 RES_Voltage_099 = RES_VoltageV_099;
130 RES_Time_100 = RES_TimeT_100;
131 RES_Voltage_100 = RES_VoltageV_100;
132 RES_Time_110 = RES_TimeT_110;
133 RES_Voltage_110 = RES_VoltageV_110;
134 RES_Time_120 = RES_TimeT_120;
135 RES_Voltage_120 = RES_VoltageV_120;
136 RES_Time_130 = RES_TimeT_130;
137 RES_Voltage_130 = RES_VoltageV_130;
138 RES_Time_140 = RES_TimeT_140;
139 RES_Voltage_140 = RES_VoltageV_140;
140 RES_Time_147 = RES_TimeT_147;
141 RES_Voltage_147 = RES_VoltageV_147;
142 RES_Time_148 = RES_TimeT_148;
143 RES_Voltage_148 = RES_VoltageV_148;
144 RES_Time_149 = RES_TimeT_149;
145 RES_Voltage_149 = RES_VoltageV_149;
146 RES_Time_150 = RES_TimeT_150;
147 RES_Voltage_150 = RES_VoltageV_150;
148 RES_Time_160 = RES_TimeT_160;
149 RES_Voltage_160 = RES_VoltageV_160;
150 RES_Time_170 = RES_TimeT_170;
151 RES_Voltage_170 = RES_VoltageV_170;
```

```
152 RES_Time_180 = RES_TimeT_180;
153 RES_Voltage_180 = RES_VoltageV_180;
154 RES_Time_190 = RES_TimeT_190;
155 RES_Voltage_190 = RES_VoltageV_190;
156 RES_Time_197 = RES_TimeT_197;
157 RES_Voltage_197 = RES_VoltageV_197;
158 RES_Time_198 = RES_TimeT_198;
159 RES_Voltage_198 = RES_VoltageV_198;
160 RES_Time_199 = RES_TimeT_199;
161 RES_Voltage_199 = RES_VoltageV_199;
162 RES_Time_200 = RES_TimeT_200;
163 RES_Voltage_200 = RES_VoltageV_200;
164
165
166
167 %Clip to appropraite intevals
168 %LCP
169 LCP_Time_008 = LCP_Time_008(LCP_Time_008<11.8);
170 LCP_Voltage_008 = LCP_Voltage_008(LCP_Time_008<11.8);
171  LCP_Time_009 = LCP_Time_009(LCP_Time_009<13.2);
172  LCP_Voltage_009 = LCP_Voltage_009(LCP_Time_009<13.2);
173  LCP_Time_010 = LCP_Time_010(LCP_Time_010<9.4);
174  LCP_Voltage_010 = LCP_Voltage_010(LCP_Time_010<9.4);
175  LCP_Time_020 = LCP_Time_020(LCP_Time_020<10.6);
176  LCP_Voltage_020= LCP_Voltage_020(LCP_Time_020<10.6);
177  LCP_Time_030 = LCP_Time_030(LCP_Time_030<9.6);
178  LCP_Voltage_030 = LCP_Voltage_030(LCP_Time_030<9.6);
179  LCP_Time_040 = LCP_Time_040(LCP_Time_040<9.24);
180  LCP_Voltage_040 = LCP_Voltage_040(LCP_Time_040<9.24);
181  LCP_Time_047 = LCP_Time_047(LCP_Time_047<9.5);
182  LCP_Voltage_047 = LCP_Voltage_047(LCP_Time_047<9.5);
183  LCP_Time_048 = LCP_Time_048(LCP_Time_048<9.4);
184  LCP_Voltage_048 = LCP_Voltage_048(LCP_Time_048<9.4);
185  LCP_Time_049 = LCP_Time_049(LCP_Time_049<11.4);
186  LCP_Voltage_049 = LCP_Voltage_049(LCP_Time_049<11.4);
187  LCP_Time_050 = LCP_Time_050(LCP_Time_050<10.2);
188  LCP_Voltage_050 = LCP_Voltage_050(LCP_Time_050<10.2);
189  LCP_Time_060 = LCP_Time_060(LCP_Time_060<11.8);
190  LCP_Voltage_060 = LCP_Voltage_060(LCP_Time_060<11.8);
191  LCP_Time_070 = LCP_Time_070(LCP_Time_070<11.6);
192  LCP_Voltage_070 = LCP_Voltage_070(LCP_Time_070<11.6);
193  LCP_Time_080 = LCP_Time_080(LCP_Time_080<14.1);
194  LCP_Voltage_080 = LCP_Voltage_080(LCP_Time_080<14.1);
```

```
195 LCP_Time_090 = LCP_Time_090(LCP_Time_090<9.3);
196 LCP_Voltage_090 = LCP_Voltage_090(LCP_Time_090<9.3);
197 LCP_Time_097 = LCP_Time_097(LCP_Time_097<9.1);
198 LCP_Voltage_097 = LCP_Voltage_097(LCP_Time_097<9.1);
199 LCP_Time_098 = LCP_Time_098(LCP_Time_098<11.3);
200 LCP_Voltage_098 = LCP_Voltage_098(LCP_Time_098<11.3);
201 LCP_Time_099 = LCP_Time_099(LCP_Time_099<9.8);
202 LCP_Voltage_099 = LCP_Voltage_099(LCP_Time_099<9.8);
203 LCP_Time_100 = LCP_Time_100(LCP_Time_099<10);
204 LCP_Voltage_100 = LCP_Voltage_100(LCP_Time_099<10);
205 LCP_Time_110 = LCP_Time_110(LCP_Time_110<11.5);
206 LCP_Voltage_110 = LCP_Voltage_110(LCP_Time_110<11.5);
207 LCP_Time_120 = LCP_Time_120(LCP_Time_120<10.1);
208 LCP_Voltage_120 = LCP_Voltage_120(LCP_Time_120<10.1);
209 LCP_Time_130 = LCP_Time_130(LCP_Time_130<11.6);
210 LCP_Voltage_130 = LCP_Voltage_130(LCP_Time_130<11.6);
211 LCP_Time_140 = LCP_Time_140(LCP_Time_140<10);
212 LCP_Voltage_140 = LCP_Voltage_140(LCP_Time_140<10);
213 LCP_Time_147 = LCP_Time_147(LCP_Time_147<9.8);
214 LCP_Voltage_147 = LCP_Voltage_147(LCP_Time_147<9.8);
215 LCP_Time_148 = LCP_Time_148(LCP_Time_148<10.9);
216 LCP_Voltage_148 = LCP_Voltage_148(LCP_Time_148<10.9);
217 LCP_Time_149 = LCP_Time_149(LCP_Time_149<14.2);
218 LCP_Voltage_149 = LCP_Voltage_149(LCP_Time_149<14.2);
219 LCP_Time_150 = LCP_Time_150(LCP_Time_150<12.4);
220 LCP_Voltage_150 = LCP_Voltage_150(LCP_Time_150<12.4);
221 LCP_Time_160 = LCP_Time_160(LCP_Time_160<10.3);
222 LCP_Voltage_160 = LCP_Voltage_160(LCP_Time_160<10.3);
223 LCP_Time_170 = LCP_Time_170(LCP_Time_170<9.2);
224 LCP_Voltage_170 = LCP_Voltage_170(LCP_Time_170<9.2);
225 LCP_Time_180 = LCP_Time_180(LCP_Time_180<10);
226 LCP_Voltage_180 = LCP_Voltage_180(LCP_Time_180<10);
227 LCP_Time_190 = LCP_Time_190(LCP_Time_190<11.9);
228 LCP_Voltage_190 = LCP_Voltage_190(LCP_Time_190<11.9);
229 LCP_Time_197 = LCP_Time_197(LCP_Time_197<10.1);
230 LCP_Voltage_197 = LCP_Voltage_197(LCP_Time_197<10.1);
231 LCP_Time_198 = LCP_Time_198(LCP_Time_198<11.5);
232 LCP_Voltage_198 = LCP_Voltage_198(LCP_Time_198<11.5);
233 LCP_Time_199 = LCP_Time_199(LCP_Time_199<11.8);
234 LCP_Voltage_199 = LCP_Voltage_199(LCP_Time_199<11.8);
235 LCP_Time_200 = LCP_Time_200(LCP_Time_200<9.8);
236 LCP_Voltage_200 = LCP_Voltage_200(LCP_Time_200<9.8);
237
```

```
238
239 %RES
240   RES_Time_008 = RES_Time_008(RES_Time_008<11.8);
241   RES_Voltage_008 = RES_Voltage_008(RES_Time_008<11.8);
242   RES_Time_009 = RES_Time_009(RES_Time_009<13.2);
243   RES_Voltage_009 = RES_Voltage_009(RES_Time_009<13.2);
244   RES_Time_010 = RES_Time_010(RES_Time_010<9.4);
245   RES_Voltage_010 = RES_Voltage_010(RES_Time_010<9.4);
246   RES_Time_020 = RES_Time_020(RES_Time_020<10.6);
247   RES_Voltage_020= RES_Voltage_020(RES_Time_020<10.6);
248   RES_Time_030 = RES_Time_030(RES_Time_030<9.6);
249   RES_Voltage_030 = RES_Voltage_030(RES_Time_030<9.6);
250   RES_Time_040 = RES_Time_040(RES_Time_040<9.24);
251   RES_Voltage_040 = RES_Voltage_040(RES_Time_040<9.24);
252   RES_Time_047 = RES_Time_047(RES_Time_047<9.5);
253   RES_Voltage_047 = RES_Voltage_047(RES_Time_047<9.5);
254   RES_Time_048 = RES_Time_048(RES_Time_048<9.4);
255   RES_Voltage_048 = RES_Voltage_048(RES_Time_048<9.4);
256   RES_Time_049 = RES_Time_049(RES_Time_049<11.4);
257   RES_Voltage_049 = RES_Voltage_049(RES_Time_049<11.4);
258   RES_Time_050 = RES_Time_050(RES_Time_050<10.2);
259   RES_Voltage_050 = RES_Voltage_050(RES_Time_050<10.2);
260   RES_Time_060 = RES_Time_060(RES_Time_060<11.8);
261   RES_Voltage_060 = RES_Voltage_060(RES_Time_060<11.8);
262   RES_Time_070 = RES_Time_070(RES_Time_070<11.6);
263   RES_Voltage_070 = RES_Voltage_070(RES_Time_070<11.6);
264   RES_Time_080 = RES_Time_080(RES_Time_080<14.1);
265   RES_Voltage_080 = RES_Voltage_080(RES_Time_080<14.1);
266   RES_Time_090 = RES_Time_090(RES_Time_090<9.3);
267   RES_Voltage_090 = RES_Voltage_090(RES_Time_090<9.3);
268   RES_Time_097 = RES_Time_097(RES_Time_097<9.1);
269   RES_Voltage_097 = RES_Voltage_097(RES_Time_097<9.1);
270   RES_Time_098 = RES_Time_098(RES_Time_098<11.3);
271   RES_Voltage_098 = RES_Voltage_098(RES_Time_098<11.3);
272   RES_Time_099 = RES_Time_099(RES_Time_099<9.8);
273   RES_Voltage_099 = RES_Voltage_099(RES_Time_099<9.8);
274   RES_Time_100 = RES_Time_100(RES_Time_099<10);
275   RES_Voltage_100 = RES_Voltage_100(RES_Time_099<10);
276   RES_Time_110 = RES_Time_110(RES_Time_110<11.5);
277   RES_Voltage_110 = RES_Voltage_110(RES_Time_110<11.5);
278   RES_Time_120 = RES_Time_120(RES_Time_120<10.1);
279   RES_Voltage_120 = RES_Voltage_120(RES_Time_120<10.1);
280   RES_Time_130 = RES_Time_130(RES_Time_130<11.6);
```

```
281 RES_Voltage_130 = RES_Voltage_130(RES_Time_130<11.6);
282 RES_Time_140 = RES_Time_140(RES_Time_140<10);
283 RES_Voltage_140 = RES_Voltage_140(RES_Time_140<10);
284 RES_Time_147 = RES_Time_147(RES_Time_147<9.8);
285 RES_Voltage_147 = RES_Voltage_147(RES_Time_147<9.8);
286 RES_Time_148 = RES_Time_148(RES_Time_148<10.9);
287 RES_Voltage_148 = RES_Voltage_148(RES_Time_148<10.9);
288 RES_Time_149 = RES_Time_149(RES_Time_149<14.2);
289 RES_Voltage_149 = RES_Voltage_149(RES_Time_149<14.2);
290 RES_Time_150 = RES_Time_150(RES_Time_150<12.4);
291 RES_Voltage_150 = RES_Voltage_150(RES_Time_150<12.4);
292 RES_Time_160 = RES_Time_160(RES_Time_160<10.3);
293 RES_Voltage_160 = RES_Voltage_160(RES_Time_160<10.3);
294 RES_Time_170 = RES_Time_170(RES_Time_170<9.2);
295 RES_Voltage_170 = RES_Voltage_170(RES_Time_170<9.2);
296 RES_Time_180 = RES_Time_180(RES_Time_180<10);
297 RES_Voltage_180 = RES_Voltage_180(RES_Time_180<10);
298 RES_Time_190 = RES_Time_190(RES_Time_190<11.9);
299 RES_Voltage_190 = RES_Voltage_190(RES_Time_190<11.9);
300 RES_Time_197 = RES_Time_197(RES_Time_197<10.1);
301 RES_Voltage_197 = RES_Voltage_197(RES_Time_197<10.1);
302 RES_Time_198 = RES_Time_198(RES_Time_198<11.5);
303 RES_Voltage_198 = RES_Voltage_198(RES_Time_198<11.5);
304 RES_Time_199 = RES_Time_199(RES_Time_199<11.8);
305 RES_Voltage_199 = RES_Voltage_199(RES_Time_199<11.8);
306 RES_Time_200 = RES_Time_200(RES_Time_200<9.8);
307 RES_Voltage_200 = RES_Voltage_200(RES_Time_200<9.8);
308
309
310
311 %STepINFO
312 LCP_graph008LPM = stepinfo(LCP_Voltage_008, LCP_Time_008);
313 RES_graph008LPM = stepinfo(RES_Voltage_008, RES_Time_008);
314 LCP_graph009LPM = stepinfo(LCP_Voltage_009, LCP_Time_009);
315 RES_graph009LPM = stepinfo(RES_Voltage_009, RES_Time_009);
316 LCP_graph010LPM = stepinfo(LCP_Voltage_010, LCP_Time_010);
317 RES_graph010LPM = stepinfo(RES_Voltage_010, RES_Time_010);
318 LCP_graph020LPM = stepinfo(LCP_Voltage_020, LCP_Time_020);
319 RES_graph020LPM = stepinfo(RES_Voltage_020, RES_Time_020);
320 LCP_graph030LPM = stepinfo(LCP_Voltage_030, LCP_Time_030);
321 RES_graph030LPM = stepinfo(RES_Voltage_030, RES_Time_030);
322 LCP_graph040LPM = stepinfo(LCP_Voltage_040, LCP_Time_040);
323 RES_graph040LPM = stepinfo(RES_Voltage_040, RES_Time_040);
```

```
LCP_graph050LPM = stepinfo(LCP_Voltage_050, LCP_Time_050);
RES_graph050LPM = stepinfo(RES_Voltage_050, RES_Time_050);
LCP_graph060LPM = stepinfo(LCP_Voltage_060, LCP_Time_060);
RES_graph060LPM = stepinfo(RES_Voltage_060, RES_Time_060);
LCP_graph070LPM = stepinfo(LCP_Voltage_070, LCP_Time_070);
RES_graph070LPM = stepinfo(RES_Voltage_070, RES_Time_070);
LCP_graph080LPM = stepinfo(LCP_Voltage_080, LCP_Time_080);
RES_graph080LPM = stepinfo(RES_Voltage_080, RES_Time_080);
LCP_graph090LPM = stepinfo(LCP_Voltage_090, LCP_Time_090);
RES_graph090LPM = stepinfo(RES_Voltage_090, RES_Time_090);
LCP_graph100LPM = stepinfo(LCP_Voltage_100, LCP_Time_100);
RES_graph100LPM = stepinfo(RES_Voltage_100, RES_Time_100);
LCP_graph110LPM = stepinfo(LCP_Voltage_110, LCP_Time_110);
RES_graph110LPM = stepinfo(RES_Voltage_110, RES_Time_110);
LCP_graph120LPM = stepinfo(LCP_Voltage_120, LCP_Time_120);
RES_graph120LPM = stepinfo(RES_Voltage_120, RES_Time_120);
LCP_graph130LPM = stepinfo(LCP_Voltage_130, LCP_Time_130);
RES_graph130LPM = stepinfo(RES_Voltage_130, RES_Time_130);

%GET SETTLING MIN
LCP_SettlingMin008 = LCP_graph008LPM.SettlingMin;
RES_SettlingMin008 = RES_graph008LPM.SettlingMin;
LCP_SettlingMin009 = LCP_graph009LPM.SettlingMin;
RES_SettlingMin009 = RES_graph009LPM.SettlingMin;
LCP_SettlingMin010 = LCP_graph010LPM.SettlingMin;
RES_SettlingMin010 = RES_graph010LPM.SettlingMin;
LCP_SettlingMin020 = LCP_graph020LPM.SettlingMin;
RES_SettlingMin020 = RES_graph020LPM.SettlingMin;
LCP_SettlingMin030 = LCP_graph030LPM.SettlingMin;
RES_SettlingMin030 = RES_graph030LPM.SettlingMin;
LCP_SettlingMin040 = LCP_graph040LPM.SettlingMin;
RES_SettlingMin040 = RES_graph040LPM.SettlingMin;
LCP_SettlingMin050 = LCP_graph050LPM.SettlingMin;
RES_SettlingMin050 = RES_graph050LPM.SettlingMin;
LCP_SettlingMin060 = LCP_graph060LPM.SettlingMin;
RES_SettlingMin060 = RES_graph060LPM.SettlingMin;
LCP_SettlingMin070 = LCP_graph070LPM.SettlingMin;
RES_SettlingMin070 = RES_graph070LPM.SettlingMin;
LCP_SettlingMin080 = LCP_graph080LPM.SettlingMin;
RES_SettlingMin080 = RES_graph080LPM.SettlingMin;
LCP_SettlingMin090 = LCP_graph090LPM.SettlingMin;
RES_SettlingMin090 = RES_graph090LPM.SettlingMin;
LCP_SettlingMin100 = LCP_graph100LPM.SettlingMin;
```

```
367 RES_SettlingMin100 = RES_graph100LPM.SettlingMin;
368 LCP_SettlingMin110 = LCP_graph110LPM.SettlingMin;
369 RES_SettlingMin110 = RES_graph110LPM.SettlingMin;
370 LCP_SettlingMin120 = LCP_graph120LPM.SettlingMin;
371 RES_SettlingMin120 = RES_graph120LPM.SettlingMin;
372 LCP_SettlingMin130 = LCP_graph130LPM.SettlingMin;
373 RES_SettlingMin130 = RES_graph130LPM.SettlingMin;
374
375
376 %Get pk to pk statistics into array
377 pkpk010 = [0.04,0.038,0.0335,0.032];
378 pkpk020 = [0.129,0.128,0.13,0.128];
379 pkpk030 = [0.157,0.158,0.158,0.158];
380 pkpk040 = [0.188,0.185,0.190,0.180];
381 pkpk050 = [0.22,0.21,0.20,0.21,0.20];
382 pkpk060 = [0.257,0.26,0.259,0.260];
383 pkpk070 = [0.295,0.286,0.293,0.293];
384 pkpk080 = [0.318,0.33,0.335,0.34];
385 pkpk090 = [0.37,0.365,0.371,0.368,0.36];
386 pkpk100 = [0.40,0.394,0.387,0.390,0.396];
387 pkpk110 = [0.426,0.419,0.422,0.423];
388 pkpk120 = [0.44,0.449,0.447,0.446,0.445];
389 pkpk130 = [0.46,0.46,0.462,0.468];
390 pkpk140 = [0.488,0.495,0.488,0.488,0.486];
391 pkpk150 = [0.493,0.50,0.498,0.499,0.50];
392 pkpk160 = [0.523,0.52,0.51,0.51];
393 pkpk170 = [0.531,0.532,0.529,0.524,0.527];
394 pkpk180 = [0.537,0.540,0.541,0.543,0.532];
395 pkpk190 = [0.547,0.544,0.551,0.548];
396 pkpk200 = [0.561,0.560,0.560,0.560,0.550];
397
398 pkpkavg010 = mean(pkpk010);
399 pkpkavg020 = mean(pkpk020);
400 pkpkavg030 = mean(pkpk030);
401 pkpkavg040 = mean(pkpk040);
402 pkpkavg050 = mean(pkpk050);
403 pkpkavg060 = mean(pkpk060);
404 pkpkavg070 = mean(pkpk070);
405 pkpkavg080 = mean(pkpk080);
406 pkpkavg090 = mean(pkpk090);
407 pkpkavg100 = mean(pkpk100);
408 pkpkavg110 = mean(pkpk110);
409 pkpkavg120 = mean(pkpk120);
```

```
410 pkpkavg130 = mean(pkpk130);
411 pkpkavg140 = mean(pkpk140);
412 pkpkavg150 = mean(pkpk150);
413 pkpkavg160 = mean(pkpk160);
414 pkpkavg170 = mean(pkpk170);
415 pkpkavg180 = mean(pkpk180);
416 pkpkavg190 = mean(pkpk190);
417 pkpkavg200 = mean(pkpk200);
418
419 std010 = std(pkpk010);
420 std020 = std(pkpk020);
421 std030 = std(pkpk030);
422 std040 = std(pkpk040);
423 std050 = std(pkpk050);
424 std060 = std(pkpk060);
425 std070 = std(pkpk070);
426 std080 = std(pkpk080);
427 std090 = std(pkpk090);
428 std100 = std(pkpk100);
429 std110 = std(pkpk110);
430 std120 = std(pkpk120);
431 std130 = std(pkpk130);
432 std140 = std(pkpk140);
433 std150 = std(pkpk150);
434 std160 = std(pkpk160);
435 std170 = std(pkpk170);
436 std180 = std(pkpk180);
437 std190 = std(pkpk190);
438 std200 = std(pkpk200);
439
440
441 %plot data - phase shift and put on zero x-axis
442 %LCP
443 figure (1)
444 hold on
445 title('LCP Pressure Sensor Range Overview');
446 set(gca,'FontSize',14); %Font Size
447 xlabel('Time (s)');
448 ylabel('Voltage (V)');
449 plot(LCP_Time_010(LCP_Time_010>0.3)-0.3,LCP_Voltage_010(
       LCP_Time_010>0.3));
450 plot(LCP_Time_020(LCP_Time_020>1.6)-1.6,LCP_Voltage_020(
       LCP_Time_020>1.6));
```

```
451 plot(LCP_Time_030(LCP_Time_030>0.45)-0.45,LCP_Voltage_030(
        LCP_Time_030>0.45));
452 plot(LCP_Time_040(LCP_Time_040>0.2)-0.2,LCP_Voltage_040(
        LCP_Time_040>0.2));
453 plot(LCP_Time_050(LCP_Time_050>1.2)-1.2,LCP_Voltage_050(
        LCP_Time_050>1.2));
454 plot(LCP_Time_060(LCP_Time_060>2.8)-2.8,LCP_Voltage_060(
        LCP_Time_060>2.8));
455 plot(LCP_Time_070(LCP_Time_070>2.5)-2.5,LCP_Voltage_070(
        LCP_Time_070>2.5));
456 plot(LCP_Time_080(LCP_Time_080>5)-5,LCP_Voltage_080(
        LCP_Time_080>5));
457 plot(LCP_Time_090(LCP_Time_090>0.3)-0.3,LCP_Voltage_090(
        LCP_Time_090>0.3));
458 plot(LCP_Time_100(LCP_Time_100>1)-1,LCP_Voltage_100(
        LCP_Time_100>1));
459 plot(LCP_Time_110(LCP_Time_110>2.5)-2.5,LCP_Voltage_110(
        LCP_Time_110>2.5));
460 plot(LCP_Time_120(LCP_Time_120>0.9)-0.9,LCP_Voltage_120(
        LCP_Time_120>0.9));
461 plot(LCP_Time_130(LCP_Time_130>2.5)-2.5,LCP_Voltage_130(
        LCP_Time_130>2.5));
462 plot(LCP_Time_140(LCP_Time_140>0.9)-0.9,LCP_Voltage_140(
        LCP_Time_140>0.9));
463 plot(LCP_Time_150(LCP_Time_150>3.3)-3.3,LCP_Voltage_150(
        LCP_Time_150>3.3));
464 plot(LCP_Time_160(LCP_Time_160>1.2)-1.2,LCP_Voltage_160(
        LCP_Time_160>1.2));
465 plot(LCP_Time_170(LCP_Time_170>0.1)-0.1,LCP_Voltage_170(
        LCP_Time_170>0.1));
466 plot(LCP_Time_180(LCP_Time_180>1)-1,LCP_Voltage_180(
        LCP_Time_180>1));
467 plot(LCP_Time_190(LCP_Time_190>2.9)-2.9,LCP_Voltage_190(
        LCP_Time_190>2.9));
468 plot(LCP_Time_200(LCP_Time_200>0.8)-0.8,LCP_Voltage_200(
        LCP_Time_200>0.8));
469 legend('10 LPM','20 LPM','30 LPM','40 LPM','50 LPM','60 LPM','
        70 LPM','80 LPM','90 LPM','100 LPM','110 LPM','120 LPM','130
         LPM','140 LPM','150 LPM','160 LPM','170 LPM','180 LPM','190
         LPM','200 LPM');
470
471 %RES
472 figure(2)
```

```
473 hold on
474 title('Commercial Flow Sensor Range Overview');
475 set(gca,'FontSize',14); %Font Size
476 xlabel('Time (s)');
477 ylabel('Voltage (V)');
478 plot(RES_Time_010(RES_Time_010>0.3)-0.3,RES_Voltage_010(
    RES_Time_010>0.3));
479 plot(RES_Time_020(RES_Time_020>1.6)-1.6,RES_Voltage_020(
    RES_Time_020>1.6));
480 plot(RES_Time_030(RES_Time_030>0.45)-0.45,RES_Voltage_030(
    RES_Time_030>0.45));
481 plot(RES_Time_040(RES_Time_040>0.2)-0.2,RES_Voltage_040(
    RES_Time_040>0.2));
482 plot(RES_Time_050(RES_Time_050>1.2)-1.2,RES_Voltage_050(
    RES_Time_050>1.2));
483 plot(RES_Time_060(RES_Time_060>2.8)-2.8,RES_Voltage_060(
    RES_Time_060>2.8));
484 plot(RES_Time_070(RES_Time_070>2.5)-2.5,RES_Voltage_070(
    RES_Time_070>2.5));
485 plot(RES_Time_080(RES_Time_080>5)-5,RES_Voltage_080(
    RES_Time_080>5));
486 plot(RES_Time_090(RES_Time_090>0.3)-0.3,RES_Voltage_090(
    RES_Time_090>0.3));
487 plot(RES_Time_100(RES_Time_100>1)-1,RES_Voltage_100(
    RES_Time_100>1));
488 plot(RES_Time_110(RES_Time_110>2.5)-2.5,RES_Voltage_110(
    RES_Time_110>2.5));
489 plot(RES_Time_120(RES_Time_120>0.9)-0.9,RES_Voltage_120(
    RES_Time_120>0.9));
490 plot(RES_Time_130(RES_Time_130>2.5)-2.5,RES_Voltage_130(
    RES_Time_130>2.5));
491 plot(RES_Time_140(RES_Time_140>0.9)-0.9,RES_Voltage_140(
    RES_Time_140>0.9));
492 plot(RES_Time_150(RES_Time_150>3.3)-3.3,RES_Voltage_150(
    RES_Time_150>3.3));
493 plot(RES_Time_160(RES_Time_160>1.2)-1.2,RES_Voltage_160(
    RES_Time_160>1.2));
494 plot(RES_Time_170(RES_Time_170>0.1)-0.1,RES_Voltage_170(
    RES_Time_170>0.1));
495 plot(RES_Time_180(RES_Time_180>1)-1,RES_Voltage_180(
    RES_Time_180>1));
496 plot(RES_Time_190(RES_Time_190>2.9)-2.9,RES_Voltage_190(
    RES_Time_190>2.9));
```

```
497  plot(RES_Time_200(RES_Time_200>0.8)-0.8,RES_Voltage_200(
       RES_Time_200>0.8));
498  legend('10 LPM','20 LPM','30 LPM','40 LPM','50 LPM','60 LPM','
       70 LPM','80 LPM','90 LPM','100 LPM','110 LPM','120 LPM','130
        LPM','140 LPM','150 LPM','160 LPM','170 LPM','180 LPM','190
        LPM','200 LPM');
499
500
501
502 %Plots of LCP Vs RES (With Gain)
503 figure(3)
504 hold on
505 title('10 LPM Comparison')
506 set(gca,'FontSize',14); %Font Size
507 xlabel('Time (s)');
508 ylabel('Voltage (V)');
509 plot(LCP_Time_010(LCP_Time_010>0.3)-0.3,LCP_Voltage_010(
       LCP_Time_010>0.3));
510 plot(RES_Time_010(RES_Time_010>0.3)-0.3,RES_Voltage_010(
       RES_Time_010>0.3));
511 legend('LCP Pressure Sensor','Commercial Sensor');
512
513 figure(4)
514 hold on
515 title('20 LPM Comparison')
516 set(gca,'FontSize',14); %Font Size
517 xlabel('Time (s)');
518 ylabel('Voltage (V)');
519 plot(LCP_Time_020(LCP_Time_020>1.6)-1.6,LCP_Voltage_020(
       LCP_Time_020>1.6));
520 plot(RES_Time_020(RES_Time_020>1.6)-1.6,RES_Voltage_020(
       RES_Time_020>1.6));
521 legend('LCP Pressure Sensor','Commercial Sensor');
522
523
524 figure(5)
525 hold on
526 title('30 LPM Comparison')
527 set(gca,'FontSize',14); %Font Size
528 xlabel('Time (s)');
529 ylabel('Voltage (V)');
530 plot(LCP_Time_030(LCP_Time_030>0.45)-0.45,LCP_Voltage_030(
       LCP_Time_030>0.45));
```

```
531 plot(RES_Time_030(RES_Time_030>0.45)-0.45,RES_Voltage_030(
    RES_Time_030>0.45));
532 legend('LCP Pressure Sensor','Commercial Sensor');
533
534 figure(6)
535 hold on
536 title('40 LPM Comparison')
537 set(gca,'FontSize',14); %Font Size
538 xlabel('Time (s)');
539 ylabel('Voltage (V)');
540 plot(LCP_Time_040(LCP_Time_040>0.2)-0.2,LCP_Voltage_040(
    LCP_Time_040>0.2));
541 plot(RES_Time_040(RES_Time_040>0.2)-0.2,RES_Voltage_040(
    RES_Time_040>0.2));
542 legend('LCP Pressure Sensor','Commercial Sensor');
543
544
545 figure(7)
546 hold on
547 title('60 LPM Comparison')
548 set(gca,'FontSize',14); %Font Size
549 xlabel('Time (s)');
550 ylabel('Voltage (V)');
551 plot(LCP_Time_060(LCP_Time_060>2.8)-2.8,LCP_Voltage_060(
    LCP_Time_060>2.8));
552 plot(RES_Time_060(RES_Time_060>2.8)-2.8,RES_Voltage_060(
    RES_Time_060>2.8));
553 legend('LCP Pressure Sensor','Commercial Sensor');
554
555 figure(8)
556 hold on
557 title('80 LPM Comparison')
558 set(gca,'FontSize',14); %Font Size
559 xlabel('Time (s)');
560 ylabel('Voltage (V)');
561 plot(LCP_Time_080(LCP_Time_080>5)-5,LCP_Voltage_080(LCP_Time_080
    >5));
562 plot(RES_Time_080(RES_Time_080>5)-5,RES_Voltage_080(RES_Time_080
    >5));
563 legend('LCP Pressure Sensor','Commercial Sensor');
564
565
566 figure(9)
```

```
567 hold on
568 title('100 LPM Comparison')
569 set(gca,'FontSize',14); %Font Size
570 xlabel('Time (s)');
571 ylabel('Voltage (V)');
572 plot(LCP_Time_100(LCP_Time_100>1)-1,LCP_Voltage_100(LCP_Time_100
    >1));
573 plot(RES_Time_100(RES_Time_100>1)-1,RES_Voltage_100(RES_Time_100
    >1));
574 legend('LCP Pressure Sensor','Commercial Sensor');
575
576 figure(10)
577 hold on
578 title('120 LPM Comparison')
579 set(gca,'FontSize',14); %Font Size
580 xlabel('Time (s)');
581 ylabel('Voltage (V)');
582 plot(LCP_Time_120(LCP_Time_120>0.9)-0.9,LCP_Voltage_120(
    LCP_Time_120>0.9));
583 plot(RES_Time_120(RES_Time_120>0.9)-0.9,RES_Voltage_120(
    RES_Time_120>0.9));
584 legend('LCP Pressure Sensor','Commercial Sensor');
585
586
587 figure(11)
588 hold on
589 title('140 LPM Comparison')
590 set(gca,'FontSize',14); %Font Size
591 xlabel('Time (s)');
592 ylabel('Voltage (V)');
593 plot(LCP_Time_140(LCP_Time_140>0.9)-0.9,LCP_Voltage_140(
    LCP_Time_140>0.9));
594 plot(RES_Time_140(RES_Time_140>0.9)-0.9,RES_Voltage_140(
    RES_Time_140>0.9));
595 legend('LCP Pressure Sensor','Commercial Sensor');
596
597 figure(12)
598 hold on
599 title('160 LPM Comparison')
600 set(gca,'FontSize',14); %Font Size
601 xlabel('Time (s)');
602 ylabel('Voltage (V)');
```

```
603 plot(LCP_Time_160(LCP_Time_160>1.2)-1.2,LCP_Voltage_160(
    LCP_Time_160>1.2));
604 plot(RES_Time_160(RES_Time_160>1.2)-1.2,RES_Voltage_160(
    RES_Time_160>1.2));
605 legend('LCP Pressure Sensor','Commercial Sensor');
606
607
608 figure(13)
609 hold on
610 title('180 LPM Comparison')
611 set(gca,'FontSize',14); %Font Size
612 xlabel('Time (s)');
613 ylabel('Voltage (V)');
614 plot(LCP_Time_180(LCP_Time_180>1)-1,LCP_Voltage_180(LCP_Time_180
    >1));
615 plot(RES_Time_180(RES_Time_180>1)-1,RES_Voltage_180(RES_Time_180
    >1));
616 legend('LCP Pressure Sensor','Commercial Sensor');
617
618 figure(14)
619 hold on
620 title('200 LPM Comparison')
621 set(gca,'FontSize',14); %Font Size
622 xlabel('Time (s)');
623 ylabel('Voltage (V)');
624 plot(LCP_Time_200(LCP_Time_200>0.8)-0.8,LCP_Voltage_200(
    LCP_Time_200>0.8));
625 plot(RES_Time_200(RES_Time_200>0.8)-0.8,RES_Voltage_200(
    RES_Time_200>0.8));
626 legend('LCP Pressure Sensor','Commercial Sensor');
627
628
629 %Lowest Reading From LCP 8LPM:
630 figure(15)
631 hold on
632 title('8 LPM Comparison');
633 set(gca,'FontSize',14); %Font Size
634 xlabel('Time (s)');
635 ylabel('Voltage (V)');
636 plot(RES_Time_008(RES_Time_008>2.8)-2.8,RES_Voltage_008(
    RES_Time_008>2.8));
637 plot(LCP_Time_008(LCP_Time_008>2.8)-2.8,LCP_Voltage_008(
    LCP_Time_008>2.8));
```

```
638 legend('Commercial Sensor','LCP Pressure Sensor');
639
640
641 %Sensitivity of LCP
642 % 8 - 10LPM
643 figure(16)
644 hold on
645 title('LCP Pressure Sensor Sensitivity: 8 - 10 LPM');
646 set(gca,'FontSize',14); %Font Size
647 xlabel('Time (s)');
648 ylabel('Voltage (V)');
649 plot(LCP_Time_008(LCP_Time_008>2.8)-2.8,LCP_Voltage_008(
       LCP_Time_008>2.8));
650 plot(LCP_Time_009(LCP_Time_009>4.2)-4.2,LCP_Voltage_009(
       LCP_Time_009>4.2));
651 plot(LCP_Time_010(LCP_Time_010>0.3)-0.3,LCP_Voltage_010(
       LCP_Time_010>0.3));
652 legend('8 LPM','9 LPM','10 LPM');
653
654
655 figure(17)
656 hold on
657 title('LCP Pressure Sensor Sensitivity: 47 - 50 LPM');
658 set(gca,'FontSize',14); %Font Size
659 xlabel('Time (s)');
660 ylabel('Voltage (V)');
661 plot(LCP_Time_047(LCP_Time_047>0.5)-0.5,LCP_Voltage_047(
       LCP_Time_047>0.5));
662 plot(LCP_Time_048(LCP_Time_048>0.4)-0.4,LCP_Voltage_048(
       LCP_Time_048>0.4));
663 plot(LCP_Time_049(LCP_Time_049>2.4)-2.4,LCP_Voltage_049(
       LCP_Time_049>2.4));
664 plot(LCP_Time_050(LCP_Time_050>1.2)-1.2,LCP_Voltage_050(
       LCP_Time_050>1.2));
665 legend('47 LPM','48 LPM','49 LPM','50 LPM');
666
667
668 figure(18)
669 hold on
670 set(gca,'FontSize',14); %Font Size
671 title('LCP Pressure Sensor Sensitivity: 97 - 100 LPM');
672 xlabel('Time (s)');
673 ylabel('Voltage (V)');
```

```
674 plot(LCP_Time_097(LCP_Time_097>0.1)-0.1,LCP_Voltage_097(
        LCP_Time_097>0.1));
675 plot(LCP_Time_098(LCP_Time_098>2.3)-2.3,LCP_Voltage_098(
        LCP_Time_098>2.3));
676 plot(LCP_Time_099(LCP_Time_099>0.8)-0.8,LCP_Voltage_099(
        LCP_Time_099>0.8));
677 plot(LCP_Time_100(LCP_Time_100>1)-1,LCP_Voltage_100(LCP_Time_100
        >1));
678 legend('97 LPM','98 LPM','99 LPM','100 LPM');
679
680
681 figure(19)
682 hold on
683 set(gca,'FontSize',14); %Font Size
684 title('LCP Pressure Sensor Sensitivity: 147 - 150 LPM');
685 xlabel('Time (s)');
686 ylabel('Voltage (V)');
687 plot(LCP_Time_147(LCP_Time_147>0.8)-0.8,LCP_Voltage_147(
        LCP_Time_147>0.8));
688 plot(LCP_Time_148(LCP_Time_148>2)-2,LCP_Voltage_148(LCP_Time_148
        >2));
689 plot(LCP_Time_149(LCP_Time_149>5.2)-5.2,LCP_Voltage_149(
        LCP_Time_149>5.2));
690 plot(LCP_Time_150(LCP_Time_150>3.5)-3.5,LCP_Voltage_150(
        LCP_Time_150>3.5));
691 legend('147 LPM','148 LPM','149 LPM','150 LPM');
692
693
694 figure(20)
695 hold on
696 set(gca,'FontSize',14); %Font Size
697 title('LCP Pressure Sensor Sensitivity: 197 - 200 LPM');
698 xlabel('Time (s)');
699 ylabel('Voltage (V)');
700 plot(LCP_Time_197(LCP_Time_197>1.1)-1.1,LCP_Voltage_197(
        LCP_Time_197>1.1));
701 plot(LCP_Time_198(LCP_Time_198>2.5)-2.5,LCP_Voltage_198(
        LCP_Time_198>2.5));
702 plot(LCP_Time_199(LCP_Time_199>2.8)-2.8,LCP_Voltage_199(
        LCP_Time_199>2.8));
703 plot(LCP_Time_200(LCP_Time_200>0.8)-0.8,LCP_Voltage_200(
        LCP_Time_200>0.8));
704 legend('197 LPM','198 LPM','199 LPM','200 LPM');
```

```
705
706 figure(21)
707 hold on
708 set(gca,'FontSize',14); %Font Size
709 title('Inhale Through Nasal Mask');
710 xlabel('Time (s)');
711 ylabel('Voltage (V)');
712 plot(Inhale_Time,Inhale_Voltage);
713 legend('LCP Sensor');
714
715 figure(22)
716 hold on
717 set(gca,'FontSize',14); %Font Size
718 title('Exhale Through Nasal Mask');
719 xlabel('Time (s)');
720 ylabel('Voltage (V)');
721 plot(Exhale_Time,Exhale_Voltage);
722 legend('LCP Sensor');
723
724 figure(23)
725 hold on
726 set(gca,'FontSize',14); %Font Size
727 title('Breathing Through Nasal Mask');
728 xlabel('Time (s)');
729 ylabel('Voltage (V)');
730 plot(Breathing_Time,Breathing_Voltage);
731 legend('LCP Sensor');
732
733 figure(24)
734 hold on
735 set(gca,'FontSize',14); %Font Size
736 title('Calibration Plot LCP  Pressure Sensor');
737 xlabel('Flow (LPM)');
738 ylabel('Pk - Pk Voltage (V)');
739 CalibrationFlow =
      [10,20,30,40,50,60,70,80,90,100,110,120,130,140,150,160,170,180,190,200];

740 err = [std010, std020, std030, std040, std050,std060, std070,
      std080, std090, std100, std110, std120, std130, std140,
      std150, std160, std170, std180, std190, std200];
741 CalibrationPkPk = [pkpkavg010,pkpkavg020,pkpkavg030,pkpkavg040,
      pkpkavg050,pkpkavg060,pkpkavg070,pkpkavg080,pkpkavg090,
      pkpkavg100,pkpkavg110,pkpkavg120,pkpkavg130,pkpkavg140,
```

```
    pkpkavg150 , pkpkavg160 , pkpkavg170 , pkpkavg180 , pkpkavg190 ,
    pkpkavg200 ] ;
errorbar ( CalibrationFlow , CalibrationPkPk , err ) ;
fit = polyval ( polyfit ( CalibrationFlow , CalibrationPkPk ,1) ,1) ;
plot ( fit ) ;
legend ( 'LCP Pressure Sensor ' ) ;
```

A.1.2 Matlab Code for Flow Sensor

```
% %%%%%%%%%%%%%%%%%%%%%%%%%%%%%%%%%%%%%%%%%%%%%%
% LCP MEMS SENSOR AND PACKAGE DESIGN FOR CPAP Devices
%
% Author: William Thorby
% Department of Engineering , Macquarie University , Nov 2017
%
% Final year thesis project , Nov 2017
%
% This code was used to extract data collected from signal
    express to
% create meaningful graphs
% This data is from LCP Pressure Sensor Testing


%Copy Arrays so they can be manipulated

%LCP
LCP_Time_008 = LCP_TimeT_008;
LCP_Voltage_008 = LCP_VoltageV_008;
LCP_Time_009 = LCP_TimeT_009;
LCP_Voltage_009 = LCP_VoltageV_009;
LCP_Time_010 = LCP_TimeT_010;
LCP_Voltage_010 = LCP_VoltageV_010;
LCP_Time_020 = LCP_TimeT_020;
LCP_Voltage_020 = LCP_VoltageV_020;
LCP_Time_030 = LCP_TimeT_030;
LCP_Voltage_030 = LCP_VoltageV_030;
LCP_Time_040 = LCP_TimeT_040;
LCP_Voltage_040 = LCP_VoltageV_040;
LCP_Time_047 = LCP_TimeT_047;
LCP_Voltage_047 = LCP_VoltageV_047;
LCP_Time_048 = LCP_TimeT_048;
LCP_Voltage_048 = LCP_VoltageV_048;
LCP_Time_049 = LCP_TimeT_049;
LCP_Voltage_049 = LCP_VoltageV_049;
```

```
35 LCP_Time_050 = LCP_TimeT_050;
36 LCP_Voltage_050 = LCP_VoltageV_050;
37 LCP_Time_060 = LCP_TimeT_060;
38 LCP_Voltage_060 = LCP_VoltageV_060;
39 LCP_Time_070 = LCP_TimeT_070;
40 LCP_Voltage_070 = LCP_VoltageV_070;
41 LCP_Time_080 = LCP_TimeT_080;
42 LCP_Voltage_080 = LCP_VoltageV_080;
43 LCP_Time_090 = LCP_TimeT_090;
44 LCP_Voltage_090 = LCP_VoltageV_090;
45 LCP_Time_097 = LCP_TimeT_097;
46 LCP_Voltage_097 = LCP_VoltageV_097;
47 LCP_Time_098 = LCP_TimeT_098;
48 LCP_Voltage_098 = LCP_VoltageV_098;
49 LCP_Time_099 = LCP_TimeT_099;
50 LCP_Voltage_099 = LCP_VoltageV_099;
51 LCP_Time_100 = LCP_TimeT_100;
52 LCP_Voltage_100 = LCP_VoltageV_100;
53 LCP_Time_110 = LCP_TimeT_110;
54 LCP_Voltage_110 = LCP_VoltageV_110;
55 LCP_Time_120 = LCP_TimeT_120;
56 LCP_Voltage_120 = LCP_VoltageV_120;
57 LCP_Time_130 = LCP_TimeT_130;
58 LCP_Voltage_130 = LCP_VoltageV_130;
59 LCP_Time_140 = LCP_TimeT_140;
60 LCP_Voltage_140 = LCP_VoltageV_140;
61 LCP_Time_147 = LCP_TimeT_147;
62 LCP_Voltage_147 = LCP_VoltageV_147;
63 LCP_Time_148 = LCP_TimeT_148;
64 LCP_Voltage_148 = LCP_VoltageV_148;
65 LCP_Time_149 = LCP_TimeT_149;
66 LCP_Voltage_149 = LCP_VoltageV_149;
67 LCP_Time_150 = LCP_TimeT_150;
68 LCP_Voltage_150 = LCP_VoltageV_150;
69 LCP_Time_160 = LCP_TimeT_160;
70 LCP_Voltage_160 = LCP_VoltageV_160;
71 LCP_Time_170 = LCP_TimeT_170;
72 LCP_Voltage_170 = LCP_VoltageV_170;
73 LCP_Time_180 = LCP_TimeT_180;
74 LCP_Voltage_180 = LCP_VoltageV_180;
75 LCP_Time_190 = LCP_TimeT_190;
76 LCP_Voltage_190 = LCP_VoltageV_190;
77 LCP_Time_197 = LCP_TimeT_197;
```

```
78 LCP_Voltage_197 = LCP_VoltageV_197;
79 LCP_Time_198 = LCP_TimeT_198;
80 LCP_Voltage_198 = LCP_VoltageV_198;
81 LCP_Time_199 = LCP_TimeT_199;
82 LCP_Voltage_199 = LCP_VoltageV_199;
83 LCP_Time_200 = LCP_TimeT_200;
84 LCP_Voltage_200 = LCP_VoltageV_200;
85
86 %RES
87 RES_Time_008 = RES_TimeT_008;
88 RES_Voltage_008 = RES_VoltageV_008;
89 RES_Time_009 = RES_TimeT_009;
90 RES_Voltage_009 = RES_VoltageV_009;
91 RES_Time_010 = RES_TimeT_010;
92 RES_Voltage_010 = RES_VoltageV_010;
93 RES_Time_020 = RES_TimeT_020;
94 RES_Voltage_020 = RES_VoltageV_020;
95 RES_Time_030 = RES_TimeT_030;
96 RES_Voltage_030 = RES_VoltageV_030;
97 RES_Time_040 = RES_TimeT_040;
98 RES_Voltage_040 = RES_VoltageV_040;
99 RES_Time_047 = RES_TimeT_047;
100 RES_Voltage_047 = RES_VoltageV_047;
101 RES_Time_048 = RES_TimeT_048;
102 RES_Voltage_048 = RES_VoltageV_048;
103 RES_Time_049 = RES_TimeT_049;
104 RES_Voltage_049 = RES_VoltageV_049;
105 RES_Time_050 = RES_TimeT_050;
106 RES_Voltage_050 = RES_VoltageV_050;
107 RES_Time_060 = RES_TimeT_060;
108 RES_Voltage_060 = RES_VoltageV_060;
109 RES_Time_070 = RES_TimeT_070;
110 RES_Voltage_070 = RES_VoltageV_070;
111 RES_Time_080 = RES_TimeT_080;
112 RES_Voltage_080 = RES_VoltageV_080;
113 RES_Time_090 = RES_TimeT_090;
114 RES_Voltage_090 = RES_VoltageV_090;
115 RES_Time_097 = RES_TimeT_097;
116 RES_Voltage_097 = RES_VoltageV_097;
117 RES_Time_098 = RES_TimeT_098;
118 RES_Voltage_098 = RES_VoltageV_098;
119 RES_Time_099 = RES_TimeT_099;
120 RES_Voltage_099 = RES_VoltageV_099;
```

```
121 RES_Time_100 = RES_TimeT_100;
122 RES_Voltage_100 = RES_VoltageV_100;
123 RES_Time_110 = RES_TimeT_110;
124 RES_Voltage_110 = RES_VoltageV_110;
125 RES_Time_120 = RES_TimeT_120;
126 RES_Voltage_120 = RES_VoltageV_120;
127 RES_Time_130 = RES_TimeT_130;
128 RES_Voltage_130 = RES_VoltageV_130;
129 RES_Time_140 = RES_TimeT_140;
130 RES_Voltage_140 = RES_VoltageV_140;
131 RES_Time_147 = RES_TimeT_147;
132 RES_Voltage_147 = RES_VoltageV_147;
133 RES_Time_148 = RES_TimeT_148;
134 RES_Voltage_148 = RES_VoltageV_148;
135 RES_Time_149 = RES_TimeT_149;
136 RES_Voltage_149 = RES_VoltageV_149;
137 RES_Time_150 = RES_TimeT_150;
138 RES_Voltage_150 = RES_VoltageV_150;
139 RES_Time_160 = RES_TimeT_160;
140 RES_Voltage_160 = RES_VoltageV_160;
141 RES_Time_170 = RES_TimeT_170;
142 RES_Voltage_170 = RES_VoltageV_170;
143 RES_Time_180 = RES_TimeT_180;
144 RES_Voltage_180 = RES_VoltageV_180;
145 RES_Time_190 = RES_TimeT_190;
146 RES_Voltage_190 = RES_VoltageV_190;
147 RES_Time_197 = RES_TimeT_197;
148 RES_Voltage_197 = RES_VoltageV_197;
149 RES_Time_198 = RES_TimeT_198;
150 RES_Voltage_198 = RES_VoltageV_198;
151 RES_Time_199 = RES_TimeT_199;
152 RES_Voltage_199 = RES_VoltageV_199;
153 RES_Time_200 = RES_TimeT_200;
154 RES_Voltage_200 = RES_VoltageV_200;
155
156
157
158 %Clip to appropraite intevals
159 %LCP
160  LCP_Time_008 = LCP_Time_008(LCP_Time_008<12);
161  LCP_Voltage_008 = LCP_Voltage_008(LCP_Time_008<12);
162  LCP_Time_009 = LCP_Time_009(LCP_Time_009<12);
163  LCP_Voltage_009 = LCP_Voltage_009(LCP_Time_009<12);
```

```
164 LCP_Time_010 = LCP_Time_010(LCP_Time_010<11.8);
165 LCP_Voltage_010 = LCP_Voltage_010(LCP_Time_010<11.8);
166 LCP_Time_020 = LCP_Time_020(LCP_Time_020<11.95);
167 LCP_Voltage_020= LCP_Voltage_020(LCP_Time_020<11.95);
168 LCP_Time_030 = LCP_Time_030(LCP_Time_030<11);
169 LCP_Voltage_030 = LCP_Voltage_030(LCP_Time_030<11);
170 LCP_Time_040 = LCP_Time_040(LCP_Time_040<10.7);
171 LCP_Voltage_040 = LCP_Voltage_040(LCP_Time_040<10.7);
172 LCP_Time_047 = LCP_Time_047(LCP_Time_047<11.25);
173 LCP_Voltage_047 = LCP_Voltage_047(LCP_Time_047<11.25);
174 LCP_Time_048 = LCP_Time_048(LCP_Time_048<10.24);
175 LCP_Voltage_048 = LCP_Voltage_048(LCP_Time_048<10.24);
176 LCP_Time_049 = LCP_Time_049(LCP_Time_049<9.64);
177 LCP_Voltage_049 = LCP_Voltage_049(LCP_Time_049<9.64);
178 LCP_Time_050 = LCP_Time_050(LCP_Time_050<11.85);
179 LCP_Voltage_050 = LCP_Voltage_050(LCP_Time_050<11.85);
180 LCP_Time_060 = LCP_Time_060(LCP_Time_060<11.71);
181 LCP_Voltage_060 = LCP_Voltage_060(LCP_Time_060<11.71);
182 LCP_Time_070 = LCP_Time_070(LCP_Time_070<11.47);
183 LCP_Voltage_070 = LCP_Voltage_070(LCP_Time_070<11.47);
184 LCP_Time_080 = LCP_Time_080(LCP_Time_080<11.39);
185 LCP_Voltage_080 = LCP_Voltage_080(LCP_Time_080<11.39);
186 LCP_Time_090 = LCP_Time_090(LCP_Time_090<10.06);
187 LCP_Voltage_090 = LCP_Voltage_090(LCP_Time_090<10.06);
188 LCP_Time_097 = LCP_Time_097(LCP_Time_097<11.11);
189 LCP_Voltage_097 = LCP_Voltage_097(LCP_Time_097<11.11);
190 LCP_Time_098 = LCP_Time_098(LCP_Time_098<10.91);
191 LCP_Voltage_098 = LCP_Voltage_098(LCP_Time_098<10.91);
192 LCP_Time_099 = LCP_Time_099(LCP_Time_099<9.93);
193 LCP_Voltage_099 = LCP_Voltage_099(LCP_Time_099<9.93);
194 LCP_Time_100 = LCP_Time_100(LCP_Time_099<9.59);
195 LCP_Voltage_100 = LCP_Voltage_100(LCP_Time_099<9.59);
196 LCP_Time_110 = LCP_Time_110(LCP_Time_110<10.67);
197 LCP_Voltage_110 = LCP_Voltage_110(LCP_Time_110<10.67);
198 LCP_Time_120 = LCP_Time_120(LCP_Time_120<10.94);
199 LCP_Voltage_120 = LCP_Voltage_120(LCP_Time_120<10.94);
200 LCP_Time_130 = LCP_Time_130(LCP_Time_130<11.74);
201 LCP_Voltage_130 = LCP_Voltage_130(LCP_Time_130<11.74);
202 LCP_Time_140 = LCP_Time_140(LCP_Time_140<11.18);
203 LCP_Voltage_140 = LCP_Voltage_140(LCP_Time_140<11.18);
204 LCP_Time_147 = LCP_Time_147(LCP_Time_147<9.81);
205 LCP_Voltage_147 = LCP_Voltage_147(LCP_Time_147<9.81);
206 LCP_Time_148 = LCP_Time_148(LCP_Time_148<12.1);
```

```
207 LCP_Voltage_148 = LCP_Voltage_148(LCP_Time_148<12.1);
208 LCP_Time_149 = LCP_Time_149(LCP_Time_149<10.01);
209 LCP_Voltage_149 = LCP_Voltage_149(LCP_Time_149<10.01);
210 LCP_Time_150 = LCP_Time_150(LCP_Time_150<9.96);
211 LCP_Voltage_150 = LCP_Voltage_150(LCP_Time_150<9.96);
212 LCP_Time_160 = LCP_Time_160(LCP_Time_160<10.74);
213 LCP_Voltage_160 = LCP_Voltage_160(LCP_Time_160<10.74);
214 LCP_Time_170 = LCP_Time_170(LCP_Time_170<10.44);
215 LCP_Voltage_170 = LCP_Voltage_170(LCP_Time_170<10.44);
216 LCP_Time_180 = LCP_Time_180(LCP_Time_180<11.96);
217 LCP_Voltage_180 = LCP_Voltage_180(LCP_Time_180<11.96);
218 LCP_Time_190 = LCP_Time_190(LCP_Time_190<11.95);
219 LCP_Voltage_190 = LCP_Voltage_190(LCP_Time_190<11.95);
220 LCP_Time_197 = LCP_Time_197(LCP_Time_197<11.04);
221 LCP_Voltage_197 = LCP_Voltage_197(LCP_Time_197<11.04);
222 LCP_Time_198 = LCP_Time_198(LCP_Time_198<11.06);
223 LCP_Voltage_198 = LCP_Voltage_198(LCP_Time_198<11.06);
224 LCP_Time_199 = LCP_Time_199(LCP_Time_199<12.32);
225 LCP_Voltage_199 = LCP_Voltage_199(LCP_Time_199<12.32);
226 LCP_Time_200 = LCP_Time_200(LCP_Time_200<10.25);
227 LCP_Voltage_200 = LCP_Voltage_200(LCP_Time_200<10.25);
228
229
230 %RES
231 RES_Time_008 = RES_Time_008(RES_Time_008<12);
232 RES_Voltage_008 = RES_Voltage_008(RES_Time_008<12);
233 RES_Time_009 = RES_Time_009(RES_Time_009<12);
234 RES_Voltage_009 = RES_Voltage_009(RES_Time_009<12);
235 RES_Time_010 = RES_Time_010(RES_Time_010<11.8);
236 RES_Voltage_010 = RES_Voltage_010(RES_Time_010<11.8);
237 RES_Time_020 = RES_Time_020(RES_Time_020<11.95);
238 RES_Voltage_020= RES_Voltage_020(RES_Time_020<11.95);
239 RES_Time_030 = RES_Time_030(RES_Time_030<11);
240 RES_Voltage_030 = RES_Voltage_030(RES_Time_030<11);
241 RES_Time_040 = RES_Time_040(RES_Time_040<10.7);
242 RES_Voltage_040 = RES_Voltage_040(RES_Time_040<10.7);
243 RES_Time_047 = RES_Time_047(RES_Time_047<11.25);
244 RES_Voltage_047 = RES_Voltage_047(RES_Time_047<11.25);
245 RES_Time_048 = RES_Time_048(RES_Time_048<10.24);
246 RES_Voltage_048 = RES_Voltage_048(RES_Time_048<10.24);
247 RES_Time_049 = RES_Time_049(RES_Time_049<9.64);
248 RES_Voltage_049 = RES_Voltage_049(RES_Time_049<9.64);
249 RES_Time_050 = RES_Time_050(RES_Time_050<11.85);
```

```
250 RES_Voltage_050 = RES_Voltage_050(RES_Time_050<11.85);
251 RES_Time_060 = RES_Time_060(RES_Time_060<11.71);
252 RES_Voltage_060 = RES_Voltage_060(RES_Time_060<11.71);
253 RES_Time_070 = RES_Time_070(RES_Time_070<11.47);
254 RES_Voltage_070 = RES_Voltage_070(RES_Time_070<11.47);
255 RES_Time_080 = RES_Time_080(RES_Time_080<11.39);
256 RES_Voltage_080 = RES_Voltage_080(RES_Time_080<11.39);
257 RES_Time_090 = RES_Time_090(RES_Time_090<10.06);
258 RES_Voltage_090 = RES_Voltage_090(RES_Time_090<10.06);
259 RES_Time_097 = RES_Time_097(RES_Time_097<11.11);
260 RES_Voltage_097 = RES_Voltage_097(RES_Time_097<11.11);
261 RES_Time_098 = RES_Time_098(RES_Time_098<10.91);
262 RES_Voltage_098 = RES_Voltage_098(RES_Time_098<10.91);
263 RES_Time_099 = RES_Time_099(RES_Time_099<9.93);
264 RES_Voltage_099 = RES_Voltage_099(RES_Time_099<9.93);
265 RES_Time_100 = RES_Time_100(RES_Time_099<9.59);
266 RES_Voltage_100 = RES_Voltage_100(RES_Time_099<9.59);
267 RES_Time_110 = RES_Time_110(RES_Time_110<10.67);
268 RES_Voltage_110 = RES_Voltage_110(RES_Time_110<10.67);
269 RES_Time_120 = RES_Time_120(RES_Time_120<10.94);
270 RES_Voltage_120 = RES_Voltage_120(RES_Time_120<10.94);
271 RES_Time_130 = RES_Time_130(RES_Time_130<11.74);
272 RES_Voltage_130 = RES_Voltage_130(RES_Time_130<11.74);
273 RES_Time_140 = RES_Time_140(RES_Time_140<11.18);
274 RES_Voltage_140 = RES_Voltage_140(RES_Time_140<11.18);
275 RES_Time_147 = RES_Time_147(RES_Time_147<9.81);
276 RES_Voltage_147 = RES_Voltage_147(RES_Time_147<9.81);
277 RES_Time_148 = RES_Time_148(RES_Time_148<12.1);
278 RES_Voltage_148 = RES_Voltage_148(RES_Time_148<12.1);
279 RES_Time_149 = RES_Time_149(RES_Time_149<10.01);
280 RES_Voltage_149 = RES_Voltage_149(RES_Time_149<10.01);
281 RES_Time_150 = RES_Time_150(RES_Time_150<9.96);
282 RES_Voltage_150 = RES_Voltage_150(RES_Time_150<9.96);
283 RES_Time_160 = RES_Time_160(RES_Time_160<10.74);
284 RES_Voltage_160 = RES_Voltage_160(RES_Time_160<10.74);
285 RES_Time_170 = RES_Time_170(RES_Time_170<10.44);
286 RES_Voltage_170 = RES_Voltage_170(RES_Time_170<10.44);
287 RES_Time_180 = RES_Time_180(RES_Time_180<11.96);
288 RES_Voltage_180 = RES_Voltage_180(RES_Time_180<11.96);
289 RES_Time_190 = RES_Time_190(RES_Time_190<11.95);
290 RES_Voltage_190 = RES_Voltage_190(RES_Time_190<11.95);
291 RES_Time_197 = RES_Time_197(RES_Time_197<11.04);
292 RES_Voltage_197 = RES_Voltage_197(RES_Time_197<11.04);
```

```
293  RES_Time_198 = RES_Time_198(RES_Time_198<11.06);
294  RES_Voltage_198 = RES_Voltage_198(RES_Time_198<11.06);
295  RES_Time_199 = RES_Time_199(RES_Time_199<12.32);
296  RES_Voltage_199 = RES_Voltage_199(RES_Time_199<12.32);
297  RES_Time_200 = RES_Time_200(RES_Time_200<10.25);
298  RES_Voltage_200 = RES_Voltage_200(RES_Time_200<10.25);
299
300
301
302 %STepINFO
303 LCP_graph008LPM = stepinfo(LCP_Voltage_008, LCP_Time_008);
304 RES_graph008LPM = stepinfo(RES_Voltage_008, RES_Time_008);
305 LCP_graph009LPM = stepinfo(LCP_Voltage_009, LCP_Time_009);
306 RES_graph009LPM = stepinfo(RES_Voltage_009, RES_Time_009);
307 LCP_graph010LPM = stepinfo(LCP_Voltage_010, LCP_Time_010);
308 RES_graph010LPM = stepinfo(RES_Voltage_010, RES_Time_010);
309 LCP_graph020LPM = stepinfo(LCP_Voltage_020, LCP_Time_020);
310 RES_graph020LPM = stepinfo(RES_Voltage_020, RES_Time_020);
311 LCP_graph030LPM = stepinfo(LCP_Voltage_030, LCP_Time_030);
312 RES_graph030LPM = stepinfo(RES_Voltage_030, RES_Time_030);
313 LCP_graph040LPM = stepinfo(LCP_Voltage_040, LCP_Time_040);
314 RES_graph040LPM = stepinfo(RES_Voltage_040, RES_Time_040);
315 LCP_graph050LPM = stepinfo(LCP_Voltage_050, LCP_Time_050);
316 RES_graph050LPM = stepinfo(RES_Voltage_050, RES_Time_050);
317 LCP_graph060LPM = stepinfo(LCP_Voltage_060, LCP_Time_060);
318 RES_graph060LPM = stepinfo(RES_Voltage_060, RES_Time_060);
319 LCP_graph070LPM = stepinfo(LCP_Voltage_070, LCP_Time_070);
320 RES_graph070LPM = stepinfo(RES_Voltage_070, RES_Time_070);
321 LCP_graph080LPM = stepinfo(LCP_Voltage_080, LCP_Time_080);
322 RES_graph080LPM = stepinfo(RES_Voltage_080, RES_Time_080);
323 LCP_graph090LPM = stepinfo(LCP_Voltage_090, LCP_Time_090);
324 RES_graph090LPM = stepinfo(RES_Voltage_090, RES_Time_090);
325 LCP_graph100LPM = stepinfo(LCP_Voltage_100, LCP_Time_100);
326 RES_graph100LPM = stepinfo(RES_Voltage_100, RES_Time_100);
327 LCP_graph110LPM = stepinfo(LCP_Voltage_110, LCP_Time_110);
328 RES_graph110LPM = stepinfo(RES_Voltage_110, RES_Time_110);
329 LCP_graph120LPM = stepinfo(LCP_Voltage_120, LCP_Time_120);
330 RES_graph120LPM = stepinfo(RES_Voltage_120, RES_Time_120);
331 LCP_graph130LPM = stepinfo(LCP_Voltage_130, LCP_Time_130);
332 RES_graph130LPM = stepinfo(RES_Voltage_130, RES_Time_130);
333
334 %GET SETTLING MIN
335 LCP_SettlingMin008 = LCP_graph008LPM.SettlingMin;
```

```
336 RES_SettlingMin008 = RES_graph008LPM.SettlingMin;
337 LCP_SettlingMin009 = LCP_graph009LPM.SettlingMin;
338 RES_SettlingMin009 = RES_graph009LPM.SettlingMin;
339 LCP_SettlingMin010 = LCP_graph010LPM.SettlingMin;
340 RES_SettlingMin010 = RES_graph010LPM.SettlingMin;
341 LCP_SettlingMin020 = LCP_graph020LPM.SettlingMin;
342 RES_SettlingMin020 = RES_graph020LPM.SettlingMin;
343 LCP_SettlingMin030 = LCP_graph030LPM.SettlingMin;
344 RES_SettlingMin030 = RES_graph030LPM.SettlingMin;
345 LCP_SettlingMin040 = LCP_graph040LPM.SettlingMin;
346 RES_SettlingMin040 = RES_graph040LPM.SettlingMin;
347 LCP_SettlingMin050 = LCP_graph050LPM.SettlingMin;
348 RES_SettlingMin050 = RES_graph050LPM.SettlingMin;
349 LCP_SettlingMin060 = LCP_graph060LPM.SettlingMin;
350 RES_SettlingMin060 = RES_graph060LPM.SettlingMin;
351 LCP_SettlingMin070 = LCP_graph070LPM.SettlingMin;
352 RES_SettlingMin070 = RES_graph070LPM.SettlingMin;
353 LCP_SettlingMin080 = LCP_graph080LPM.SettlingMin;
354 RES_SettlingMin080 = RES_graph080LPM.SettlingMin;
355 LCP_SettlingMin090 = LCP_graph090LPM.SettlingMin;
356 RES_SettlingMin090 = RES_graph090LPM.SettlingMin;
357 LCP_SettlingMin100 = LCP_graph100LPM.SettlingMin;
358 RES_SettlingMin100 = RES_graph100LPM.SettlingMin;
359 LCP_SettlingMin110 = LCP_graph110LPM.SettlingMin;
360 RES_SettlingMin110 = RES_graph110LPM.SettlingMin;
361 LCP_SettlingMin120 = LCP_graph120LPM.SettlingMin;
362 RES_SettlingMin120 = RES_graph120LPM.SettlingMin;
363 LCP_SettlingMin130 = LCP_graph130LPM.SettlingMin;
364 RES_SettlingMin130 = RES_graph130LPM.SettlingMin;
365
366
367 %Get pk to pk statistics into array
368 pkpk010 = [0.013,0.014,0.014,0.012];
369 pkpk020 = [0.063,0.066,0.062,0.064];
370 pkpk030 = [0.111,0.110,0.111,0.110];
371 pkpk040 = [0.142,0.142,0.144,0.144];
372 pkpk050 = [0.162,0.162,0.162,0.163,0.162];
373 pkpk060 = [0.191,0.191,0.191,0.192];
374 pkpk070 = [0.203,0.203,0.203,0.203];
375 pkpk080 = [0.230,0.240,0.230,0.240];
376 pkpk090 = [0.235,0.235,0.235,0.235,0.240];
377 pkpk100 = [0.255,0.260,0.255,0.255,0.260];
378 pkpk110 = [0.260,0.265,0.265,0.265];
```

```
379 pkpk120 = [0.280,0.280,0.280,0.280,0.280];
380 pkpk130 = [0.294,0.295,0.294,0.294];
381 pkpk140 = [0.304,0.306,0.306,0.304,0.304];
382 pkpk150 = [0.314,0.312,0.314,0.314,0.314];
383 pkpk160 = [0.320,0.320,0.322,0.320];
384 pkpk170 = [0.328,0.326,0.328,0.330,0.328];
385 pkpk180 = [0.338,0.340,0.338,0.336,0.336];
386 pkpk190 = [0.340,0.342,0.342,0.342];
387 pkpk200 = [0.344,0.344,0.344,0.344,0.344];
388
389 pkpkavg010 = mean(pkpk010);
390 pkpkavg020 = mean(pkpk020);
391 pkpkavg030 = mean(pkpk030);
392 pkpkavg040 = mean(pkpk040);
393 pkpkavg050 = mean(pkpk050);
394 pkpkavg060 = mean(pkpk060);
395 pkpkavg070 = mean(pkpk070);
396 pkpkavg080 = mean(pkpk080);
397 pkpkavg090 = mean(pkpk090);
398 pkpkavg100 = mean(pkpk100);
399 pkpkavg110 = mean(pkpk110);
400 pkpkavg120 = mean(pkpk120);
401 pkpkavg130 = mean(pkpk130);
402 pkpkavg140 = mean(pkpk140);
403 pkpkavg150 = mean(pkpk150);
404 pkpkavg160 = mean(pkpk160);
405 pkpkavg170 = mean(pkpk170);
406 pkpkavg180 = mean(pkpk180);
407 pkpkavg190 = mean(pkpk190);
408 pkpkavg200 = mean(pkpk200);
409
410 std010 = std(pkpk010);
411 std020 = std(pkpk020);
412 std030 = std(pkpk030);
413 std040 = std(pkpk040);
414 std050 = std(pkpk050);
415 std060 = std(pkpk060);
416 std070 = std(pkpk070);
417 std080 = std(pkpk080);
418 std090 = std(pkpk090);
419 std100 = std(pkpk100);
420 std110 = std(pkpk110);
421 std120 = std(pkpk120);
```

```
422 std130 = std(pkpk130);
423 std140 = std(pkpk140);
424 std150 = std(pkpk150);
425 std160 = std(pkpk160);
426 std170 = std(pkpk170);
427 std180 = std(pkpk180);
428 std190 = std(pkpk190);
429 std200 = std(pkpk200);
430
431
432 %plot data - phase shift and put on zero x-axis
433 %LCP
434 figure (1)
435 hold on
436 title('LCP Flow Sensor Range Overview');
437 set(gca,'FontSize',14); %Font Size
438 xlabel('Time (s)');
439 ylabel('Voltage (V)');
440 plot(LCP_Time_010(LCP_Time_010>2.3)-2.3,LCP_Voltage_010(
      LCP_Time_010>2.3));
441 plot(LCP_Time_020(LCP_Time_020>2.45)-2.45,LCP_Voltage_020(
      LCP_Time_020>2.45));
442 plot(LCP_Time_030(LCP_Time_030>1.5)-1.5,LCP_Voltage_030(
      LCP_Time_030>1.5));
443 plot(LCP_Time_040(LCP_Time_040>1.2)-1.2,LCP_Voltage_040(
      LCP_Time_040>1.2));
444 plot(LCP_Time_050(LCP_Time_050>2.35)-2.35,LCP_Voltage_050(
      LCP_Time_050>2.35));
445 plot(LCP_Time_060(LCP_Time_060>2.21)-2.21,LCP_Voltage_060(
      LCP_Time_060>2.21));
446 plot(LCP_Time_070(LCP_Time_070>1.97)-1.97,LCP_Voltage_070(
      LCP_Time_070>1.97));
447 plot(LCP_Time_080(LCP_Time_080>1.89)-1.89,LCP_Voltage_080(
      LCP_Time_080>1.89));
448 plot(LCP_Time_090(LCP_Time_090>0.56)-0.56,LCP_Voltage_090(
      LCP_Time_090>0.56));
449 plot(LCP_Time_100(LCP_Time_100>1.09)-1.09,LCP_Voltage_100(
      LCP_Time_100>1.09));
450 plot(LCP_Time_110(LCP_Time_110>1.17)-1.17,LCP_Voltage_110(
      LCP_Time_110>1.17));
451 plot(LCP_Time_120(LCP_Time_120>1.44)-1.44,LCP_Voltage_120(
      LCP_Time_120>1.44));
452 plot(LCP_Time_130(LCP_Time_130>2.24)-2.24,LCP_Voltage_130(
```

```
    LCP_Time_130>2.24));
453 plot(LCP_Time_140(LCP_Time_140>1.68)-1.68,LCP_Voltage_140(
    LCP_Time_140>1.68));
454 plot(LCP_Time_150(LCP_Time_150>0.46)-0.46,LCP_Voltage_150(
    LCP_Time_150>0.46));
455 plot(LCP_Time_160(LCP_Time_160>1.24)-1.24,LCP_Voltage_160(
    LCP_Time_160>1.24));
456 plot(LCP_Time_170(LCP_Time_170>0.94)-0.94,LCP_Voltage_170(
    LCP_Time_170>0.94));
457 plot(LCP_Time_180(LCP_Time_180>2.46)-2.46,LCP_Voltage_180(
    LCP_Time_180>2.46));
458 plot(LCP_Time_190(LCP_Time_190>2.45)-2.45,LCP_Voltage_190(
    LCP_Time_190>2.45));
459 plot(LCP_Time_200(LCP_Time_200>0.75)-0.75,LCP_Voltage_200(
    LCP_Time_200>0.75));
460 legend('10 LPM','20 LPM','30 LPM','40 LPM','50 LPM','60 LPM','
    70 LPM','80 LPM','90 LPM','100 LPM','110 LPM','120 LPM','130
     LPM','140 LPM','150 LPM','160 LPM','170 LPM','180 LPM','190
     LPM','200 LPM');
461
462 %RES
463 figure(2)
464 hold on
465 title('Commercial Flow Sensor Range Overview');
466 set(gca,'FontSize',14); %Font Size
467 xlabel('Time (s)');
468 ylabel('Voltage (V)');
469 plot(RES_Time_010(RES_Time_010>2.3)-2.3,RES_Voltage_010(
    RES_Time_010>2.3));
470 plot(RES_Time_020(RES_Time_020>2.45)-2.45,RES_Voltage_020(
    RES_Time_020>2.45));
471 plot(RES_Time_030(RES_Time_030>1.5)-1.5,RES_Voltage_030(
    RES_Time_030>1.5));
472 plot(RES_Time_040(RES_Time_040>1.2)-1.2,RES_Voltage_040(
    RES_Time_040>1.2));
473 plot(RES_Time_050(RES_Time_050>2.35)-2.35,RES_Voltage_050(
    RES_Time_050>2.35));
474 plot(RES_Time_060(RES_Time_060>2.21)-2.21,RES_Voltage_060(
    RES_Time_060>2.21));
475 plot(RES_Time_070(RES_Time_070>1.97)-1.97,RES_Voltage_070(
    RES_Time_070>1.97));
476 plot(RES_Time_080(RES_Time_080>1.89)-1.89,RES_Voltage_080(
    RES_Time_080>1.89));
```

```
477  plot(RES_Time_090(RES_Time_090>0.56)-0.56,RES_Voltage_090(
         RES_Time_090>0.56));
478  plot(RES_Time_100(RES_Time_100>1.09)-1.09,RES_Voltage_100(
         RES_Time_100>1.09));
479  plot(RES_Time_110(RES_Time_110>1.17)-1.17,RES_Voltage_110(
         RES_Time_110>1.17));
480  plot(RES_Time_120(RES_Time_120>1.44)-1.44,RES_Voltage_120(
         RES_Time_120>1.44));
481  plot(RES_Time_130(RES_Time_130>2.24)-2.24,RES_Voltage_130(
         RES_Time_130>2.24));
482  plot(RES_Time_140(RES_Time_140>1.68)-1.68,RES_Voltage_140(
         RES_Time_140>1.68));
483  plot(RES_Time_150(RES_Time_150>0.46)-0.46,RES_Voltage_150(
         RES_Time_150>0.46));
484  plot(RES_Time_160(RES_Time_160>1.24)-1.24,RES_Voltage_160(
         RES_Time_160>1.24));
485  plot(RES_Time_170(RES_Time_170>0.94)-0.94,RES_Voltage_170(
         RES_Time_170>0.94));
486  plot(RES_Time_180(RES_Time_180>2.46)-2.46,RES_Voltage_180(
         RES_Time_180>2.46));
487  plot(RES_Time_190(RES_Time_190>2.45)-2.45,RES_Voltage_190(
         RES_Time_190>2.45));
488  plot(RES_Time_200(RES_Time_200>0.75)-0.75,RES_Voltage_200(
         RES_Time_200>0.75));
489  legend('10 LPM','20 LPM','30 LPM','40 LPM','50 LPM','60 LPM','
       70 LPM','80 LPM','90 LPM','100 LPM','110 LPM','120 LPM','130
        LPM','140 LPM','150 LPM','160 LPM','170 LPM','180 LPM','190
        LPM','200 LPM');
490
491
492
493 %Plots of LCP Vs RES (With Gain)
494 figure(3)
495 hold on
496 title('10 LPM Comparison')
497 set(gca,'FontSize',14); %Font Size
498 xlabel('Time (s)');
499 ylabel('Voltage (V)');
500 plot(LCP_Time_010(LCP_Time_010>2.3)-2.3,LCP_Voltage_010(
      LCP_Time_010>2.3));
501 plot(RES_Time_010(RES_Time_010>2.3)-2.3,RES_Voltage_010(
      RES_Time_010>2.3));
502 legend('LCP Flow Sensor','Commercial Sensor');
```

```
503
504 figure(4)
505 hold on
506 title('20 LPM Comparison')
507 set(gca,'FontSize',14); %Font Size
508 xlabel('Time (s)');
509 ylabel('Voltage (V)');
510 plot(LCP_Time_020(LCP_Time_020>2.45)-2.45,LCP_Voltage_020(
      LCP_Time_020>2.45));
511 plot(RES_Time_020(RES_Time_020>2.45)-2.45,RES_Voltage_020(
      RES_Time_020>2.45));
512 legend('LCP Flow Sensor','Commercial Sensor');
513
514
515 figure(5)
516 hold on
517 title('30 LPM Comparison')
518 set(gca,'FontSize',14); %Font Size
519 xlabel('Time (s)');
520 ylabel('Voltage (V)');
521 plot(LCP_Time_030(LCP_Time_030>1.5)-1.5,LCP_Voltage_030(
      LCP_Time_030>1.5));
522 plot(RES_Time_030(RES_Time_030>1.5)-1.5,RES_Voltage_030(
      RES_Time_030>1.5));
523 legend('LCP Flow Sensor','Commercial Sensor');
524
525 figure(6)
526 hold on
527 title('40 LPM Comparison')
528 set(gca,'FontSize',14); %Font Size
529 xlabel('Time (s)');
530 ylabel('Voltage (V)');
531 plot(LCP_Time_040(LCP_Time_040>1.2)-1.2,LCP_Voltage_040(
      LCP_Time_040>1.2));
532  plot(RES_Time_040(RES_Time_040>1.2)-1.2,RES_Voltage_040(
       RES_Time_040>1.2));
533 legend('LCP Flow Sensor','Commercial Sensor');
534
535
536 figure(7)
537 hold on
538 title('60 LPM Comparison')
539 set(gca,'FontSize',14); %Font Size
```

```
540 xlabel('Time (s)');
541 ylabel('Voltage (V)');
542 plot(LCP_Time_060(LCP_Time_060>2.21)-2.21,LCP_Voltage_060(
    LCP_Time_060>2.21));
543 plot(RES_Time_060(RES_Time_060>2.21)-2.21,RES_Voltage_060(
    RES_Time_060>2.21));
544 legend('LCP Flow Sensor','Commercial Sensor');
545
546 figure(8)
547 hold on
548 title('80 LPM Comparison')
549 set(gca,'FontSize',14); %Font Size
550 xlabel('Time (s)');
551 ylabel('Voltage (V)');
552 plot(LCP_Time_080(LCP_Time_080>1.89)-1.89,LCP_Voltage_080(
    LCP_Time_080>1.89));
553 plot(RES_Time_080(RES_Time_080>1.89)-1.89,RES_Voltage_080(
    RES_Time_080>1.89));
554 legend('LCP Flow Sensor','Commercial Sensor');
555
556
557 figure(9)
558 hold on
559 title('100 LPM Comparison')
560 set(gca,'FontSize',14); %Font Size
561 xlabel('Time (s)');
562 ylabel('Voltage (V)');
563 plot(LCP_Time_100(LCP_Time_100>1.09)-1.09,LCP_Voltage_100(
    LCP_Time_100>1.09));
564  plot(RES_Time_100(RES_Time_100>1.09)-1.09,RES_Voltage_100(
     RES_Time_100>1.09));
565 legend('LCP Flow Sensor','Commercial Sensor');
566
567 figure(10)
568 hold on
569 title('120 LPM Comparison')
570 set(gca,'FontSize',14); %Font Size
571 xlabel('Time (s)');
572 ylabel('Voltage (V)');
573 plot(LCP_Time_120(LCP_Time_120>1.44)-1.44,LCP_Voltage_120(
    LCP_Time_120>1.44));
574  plot(RES_Time_120(RES_Time_120>1.44)-1.44,RES_Voltage_120(
     RES_Time_120>1.44));
```

```
575 legend('LCP Flow Sensor','Commercial Sensor');
576
577
578 figure(11)
579 hold on
580 title('140 LPM Comparison')
581 set(gca,'FontSize',14); %Font Size
582 xlabel('Time (s)');
583 ylabel('Voltage (V)');
584 plot(LCP_Time_140(LCP_Time_140>1.68)-1.68,LCP_Voltage_140(
      LCP_Time_140>1.68));
585  plot(RES_Time_140(RES_Time_140>1.68)-1.68,RES_Voltage_140(
       RES_Time_140>1.68));
586 legend('LCP Flow Sensor','Commercial Sensor');
587
588 figure(12)
589 hold on
590 title('160 LPM Comparison')
591 set(gca,'FontSize',14); %Font Size
592 xlabel('Time (s)');
593 ylabel('Voltage (V)');
594 plot(LCP_Time_160(LCP_Time_160>1.24)-1.24,LCP_Voltage_160(
      LCP_Time_160>1.24));
595  plot(RES_Time_160(RES_Time_160>1.24)-1.24,RES_Voltage_160(
       RES_Time_160>1.24));
596 legend('LCP Flow Sensor','Commercial Sensor');
597
598
599 figure(13)
600 hold on
601 title('180 LPM Comparison')
602 set(gca,'FontSize',14); %Font Size
603 xlabel('Time (s)');
604 ylabel('Voltage (V)');
605 plot(LCP_Time_180(LCP_Time_180>2.46)-2.46,LCP_Voltage_180(
      LCP_Time_180>2.46));
606  plot(RES_Time_180(RES_Time_180>2.46)-2.46,RES_Voltage_180(
       RES_Time_180>2.46));
607 legend('LCP Flow Sensor','Commercial Sensor');
608
609 figure(14)
610 hold on
611 title('200 LPM Comparison')
```

```
612 set(gca,'FontSize',14); %Font Size
613 xlabel('Time (s)');
614 ylabel('Voltage (V)');
615 plot(LCP_Time_200(LCP_Time_200>0.75)-0.75,LCP_Voltage_200(
      LCP_Time_200>0.75));
616  plot(RES_Time_200(RES_Time_200>0.75)-0.75,RES_Voltage_200(
       RES_Time_200>0.75));
617 legend('LCP Flow Sensor','Commercial Sensor');
618
619
620 %Lowest Reading From LCP 8LPM:
621 figure(15)
622 hold on
623 title('8 LPM: Commercial Sensor VS LCP Sensor');
624 set(gca,'FontSize',14); %Font Size
625 xlabel('Time (s)');
626 ylabel('Voltage (V)');
627 plot(RES_Time_008(RES_Time_008>2.5)-2.5,RES_Voltage_008(
      RES_Time_008>2.5));
628 plot(LCP_Time_008(LCP_Time_008>2.5)-2.5,LCP_Voltage_008(
      LCP_Time_008>2.5));
629 legend('Commercial Sensor','LCP Flow Sensor');
630
631
632 %Sensitivity of LCP
633 % 8 - 10LPM
634 figure(16)
635 hold on
636 title('LCP Flow Sensor Sensitivity: 8 - 10 LPM');
637 set(gca,'FontSize',14); %Font Size
638 xlabel('Time (s)');
639 ylabel('Voltage (V)');
640 plot(LCP_Time_008(LCP_Time_008>2.5)-2.5,LCP_Voltage_008(
      LCP_Time_008>2.5));
641 plot(LCP_Time_009(LCP_Time_009>2.5)-2.5,LCP_Voltage_009(
      LCP_Time_009>2.5));
642 plot(LCP_Time_010(LCP_Time_010>2.3)-2.3,LCP_Voltage_010(
      LCP_Time_010>2.3));
643 legend('8 LPM','9 LPM','10 LPM');
644
645
646 figure(17)
647 hold on
```

```
title('LCP Flow Sensor Sensitivity: 47 - 50 LPM');
set(gca,'FontSize',14); %Font Size
xlabel('Time (s)');
ylabel('Voltage (V)');
plot(LCP_Time_047(LCP_Time_047>1.75)-1.75,LCP_Voltage_047(
    LCP_Time_047>1.75));
plot(LCP_Time_048(LCP_Time_048>0.74)-0.74,LCP_Voltage_048(
    LCP_Time_048>0.74));
plot(LCP_Time_049(LCP_Time_049>0.14)-0.14,LCP_Voltage_049(
    LCP_Time_049>0.14));
plot(LCP_Time_050(LCP_Time_050>2.35)-2.35,LCP_Voltage_050(
    LCP_Time_050>2.35));
legend('47 LPM','48 LPM','49 LPM','50 LPM');


figure(18)
hold on
set(gca,'FontSize',14); %Font Size
title('LCP Flow Sensor Sensitivity: 97 - 100 LPM');
xlabel('Time (s)');
ylabel('Voltage (V)');
plot(LCP_Time_097(LCP_Time_097>1.61)-1.61,LCP_Voltage_097(
    LCP_Time_097>1.61));
plot(LCP_Time_098(LCP_Time_098>1.41)-1.41,LCP_Voltage_098(
    LCP_Time_098>1.41));
plot(LCP_Time_099(LCP_Time_099>0.43)-0.43,LCP_Voltage_099(
    LCP_Time_099>0.43));
plot(LCP_Time_100(LCP_Time_100>1.09)-1.09,LCP_Voltage_100(
    LCP_Time_100>1.09));
legend('97 LPM','98 LPM','99 LPM','100 LPM');


figure(19)
hold on
set(gca,'FontSize',14); %Font Size
title('LCP Flow Sensor Sensitivity: 147 - 150 LPM');
xlabel('Time (s)');
ylabel('Voltage (V)');
plot(LCP_Time_147(LCP_Time_147>0.31)-0.31,LCP_Voltage_147(
    LCP_Time_147>0.31));
plot(LCP_Time_148(LCP_Time_148>2.6)-2.6,LCP_Voltage_148(
    LCP_Time_148>2.6));
plot(LCP_Time_149(LCP_Time_149>0.51)-0.51,LCP_Voltage_149(
```

```
    LCP_Time_149>0.51));
plot(LCP_Time_150(LCP_Time_150>0.46)-0.46,LCP_Voltage_150(
    LCP_Time_150>0.46));
legend('147 LPM','148 LPM','149 LPM','150 LPM');


figure(20)
hold on
set(gca,'FontSize',14); %Font Size
title('LCP Flow Sensor Sensitivity: 197 - 200 LPM');
xlabel('Time (s)');
ylabel('Voltage (V)');
plot(LCP_Time_197(LCP_Time_197>1.54)-1.54,LCP_Voltage_197(
    LCP_Time_197>1.54));
plot(LCP_Time_198(LCP_Time_198>1.56)-1.56,LCP_Voltage_198(
    LCP_Time_198>1.56));
plot(LCP_Time_199(LCP_Time_199>2.82)-2.82,LCP_Voltage_199(
    LCP_Time_199>2.82));
plot(LCP_Time_200(LCP_Time_200>0.75)-0.75,LCP_Voltage_200(
    LCP_Time_200>0.75));
legend('197 LPM','198 LPM','199 LPM','200 LPM');

% figure(21)
% hold on
% set(gca,'FontSize',14); %Font Size
% title('Inhale Through Nasal Mask');
% xlabel('Time (s)');
% ylabel('Voltage (V)');
% plot(Inhale_Time,Inhale_Voltage);
% legend('LCP Sensor');

% figure(22)
% hold on
% set(gca,'FontSize',14); %Font Size
% title('Exhale Through Nasal Mask');
% xlabel('Time (s)');
% ylabel('Voltage (V)');
% plot(Exhale_Time,Exhale_Voltage);
% legend('LCP Sensor');
%
% figure(23)
% hold on
% set(gca,'FontSize',14); %Font Size
```

```
718 % title('Breathing Through Nasal Mask');
719 % xlabel('Time (s)');
720 % ylabel('Voltage (V)');
721 % plot(Breathing_Time,Breathing_Voltage);
722 % legend('LCP Sensor');
723
724 figure(24)
725 hold on
726 set(gca,'FontSize',14); %Font Size
727 title('Calibration Plot LCP Flow Sensor');
728 xlabel('Flow (LPM)');
729 ylabel('Pk - Pk Voltage (V)');
730 CalibrationFlow =
      [10,20,30,40,50,60,70,80,90,100,110,120,130,140,150,160,170,180,190,200];

731 err = [std010, std020, std030, std040, std050,std060, std070,
      std080, std090, std100, std110, std120, std130, std140,
      std150, std160, std170, std180, std190, std200];
732 CalibrationPkPk = [pkpkavg010,pkpkavg020,pkpkavg030,pkpkavg040,
      pkpkavg050,pkpkavg060,pkpkavg070,pkpkavg080,pkpkavg090,
      pkpkavg100,pkpkavg110,pkpkavg120,pkpkavg130,pkpkavg140,
      pkpkavg150,pkpkavg160,pkpkavg170,pkpkavg180,pkpkavg190,
      pkpkavg200];
733 errorbar(CalibrationFlow,CalibrationPkPk,err);
734 fit = polyval(polyfit(CalibrationFlow, CalibrationPkPk,1),1);
735 plot(fit);
736 legend('LCP Flow Sensor');
```

Appendix B

Weekly Meeting Attendance

Form for weekly attendance is located in this section:

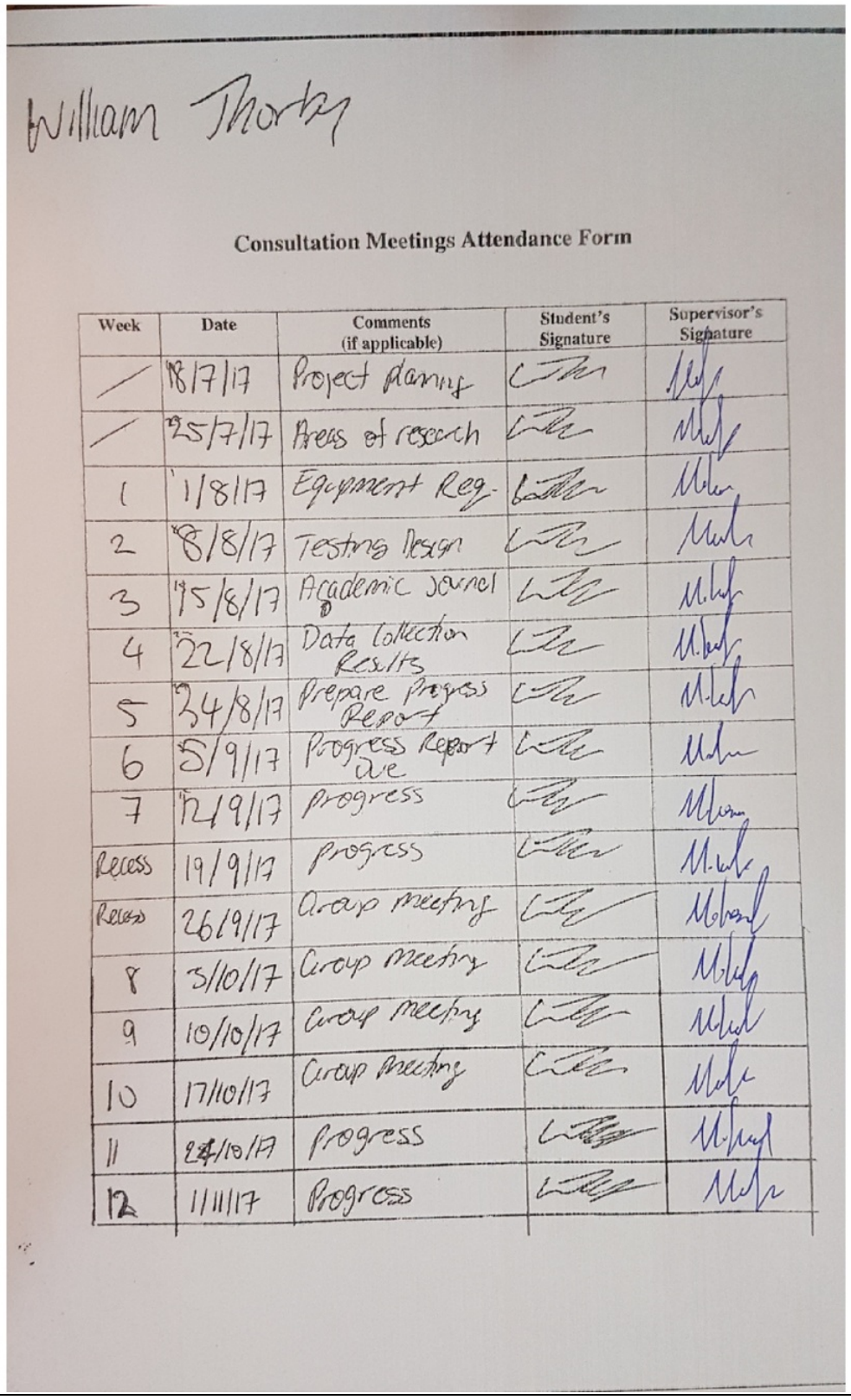

William Thorby

Consultation Meetings Attendance Form

Week	Date	Comments (if applicable)	Student's Signature	Supervisor's Signature
/	18/7/17	Project planning		
/	25/7/17	Areas of research		
1	1/8/17	Equipment Req.		
2	8/8/17	Testing Design		
3	15/8/17	Academic Journal		
4	22/8/17	Data Collection Results		
5	29/8/17	Prepare Progress Report		
6	5/9/17	Progress Report due		
7	12/9/17	Progress		
Recess	19/9/17	Progress		
Recess	26/9/17	Group meeting		
8	3/10/17	Group Meeting		
9	10/10/17	Group Meeting		
10	17/10/17	Group Meeting		
11	24/10/17	Progress		
12	1/11/17	Progress		

Bibliography

[1] L. Clancy, *Aerodynamics*. Wiley, 1975.

[2] A. G. P. Kottapalli, M. Asadnia, J. M. Miao, G. Barbastathis, and M. S. Triantafyllou, "A flexible liquid crystal polymer mems pressure sensor array for fish-like underwater sensing," *Smart Materials and Structures*, vol. 21, no. 11, p. 115030, 2012. [Online]. Available: http://stacks.iop.org/0964-1726/21/i=11/a=115030

[3] A. G. P. Kottapalli, M. Asadnia, J. M. Miao, and M. S. Triantafyllou, "Biomimetic polymer mems haircells with high-aspect ratio for high accuracy flow sensing," in *2013 Transducers Eurosensors XXVII: The 17th International Conference on Solid-State Sensors, Actuators and Microsystems (TRANSDUCERS EUROSENSORS XXVII)*, June 2013, pp. 976–979.

[4] A. G. P. Kottapalli, Z. Shen, M. Asadnia, S. Tian, K. Tao, J. Miao, and M. S. Triantafyllou, "Polymer mems sensor for flow monitoring in biomedical device applications," in *2017 IEEE 30th International Conference on Micro Electro Mechanical Systems (MEMS)*, Jan 2017, pp. 632–635.

[5] A. G. P. Kottapalli, C. W. Tan, M. Olfatnia, J. M. Miao, G. Barbastathis, and M. Triantafyllou, "A liquid crystal polymer membrane mems sensor for flow rate and flow direction sensing applications," *Journal of Micromechanics and Microengineering*, vol. 21, no. 8, p. 085006, 2011. [Online]. Available: http://stacks.iop.org/0960-1317/21/i=8/a=085006

[6] F. Mailly, A. Giani, R. Bonnot, P. Temple-Boyer, F. Pascal-Delannoy, A. Foucaran, and A. Boyer, "Anemometer with hot platinum thin film," *Sensors and Actuators A: Physical*, vol. 94, no. 1, pp. 32 – 38, 2001. [Online]. Available: http://www.sciencedirect.com/science/article/pii/S0924424701006689

[7] M. Mirjany, T. Preuss, and D. S. Faber, "Role of the lateral line mechanosensory system in directionality of goldfish auditory evoked escape response," *Journal of Experimental Biology*, vol. 214, no. 20, pp. 3358–3367, 2011. [Online]. Available: http://jeb.biologists.org/content/214/20/3358

[8] J. Montgomery, S. Coombs, and M. Halstead, "Biology of the mechanosensory lateral line in fishes," *Reviews in Fish Biology and Fisheries*, vol. 5, no. 4, pp. 399–416, Dec 1995. [Online]. Available: https://doi.org/10.1007/BF01103813

[9] T. Neda, K. Nakamura, and T. Takumi, "A polysilicon flow sensor for gas flow meters," *Sensors and Actuators A: Physical*, vol. 54, no. 1, pp. 626 – 631, 1996. [Online]. Available: http://www.sciencedirect.com/science/article/pii/S0924424797800271

[10] M. Schrope, "Whale deaths caused by us navy's sonar," *Nature*, vol. 415, no. 6868, p. 106, Jan 10 2002, name - Navy-US; Copyright - Copyright Macmillan Journals Ltd. Jan 10, 2002; Last updated - 2017-10-31; CODEN - NATUAS. [Online]. Available: http://simsrad.net.ocs.mq.edu.au/login?url=https://search-proquest-com.simsrad.net.ocs.mq.edu.au/docview/204517787?accountid=12219

[11] Y.-C. Tai and R. S. Muller, "Lightly-doped polysilicon bridge as a flow meter," *Sensors and Actuators*, vol. 15, no. 1, pp. 63 – 75, 1988. [Online]. Available: http://www.sciencedirect.com/science/article/pii/0250687488850182

[12] J. W. Tang, A. D. Nicolle, C. A. Klettner, J. Pantelic, L. Wang, A. B. Suhaimi, A. Y. L. Tan, G. W. X. Ong, R. Su, C. Sekhar, D. D. W. Cheong, and K. W. Tham, "Airflow dynamics of human jets: Sneezing and breathing - potential sources of infectious aerosols," *PLoS One*, vol. 8, no. 4, 04 2013, copyright - 2013 Tang et al. This is an open-access article distributed under the terms of the Creative Commons Attribution License, which permits unrestricted use, distribution, and reproduction in any medium, provided the original author and source are credited: Tang JW, Nicolle AD, Klettner CA, Pantelic J, Wang L, et al. (2013) Airflow Dynamics of Human Jets: Sneezing and Breathing - Potential Sources of Infectious Aerosols. PLoS ONE 8(4): e59970. doi:10.1371/journal.pone.0059970; Last updated - 2013-04-27. [Online]. Available: http://simsrad.net.ocs.mq.edu.au/login?url=https://search-proquest-com.simsrad.net.ocs.mq.edu.au/docview/1330900614?accountid=12219

[13] X. Wang, J. Engel, and C. Liu, "Liquid crystal polymer (lcp) for mems: processes and applications," *Journal of Micromechanics and Microengineering*, vol. 13, no. 5, p. 628, 2003. [Online]. Available: http://stacks.iop.org/0960-1317/13/i=5/a=314